AEROSOL IN THE TROPICAL TROPOPAUSE LAYER

A thesis submitted to the University of Manchester
for the degree of Doctor of Philosophy
in the Faculty of Engineering and Physical Sciences

2010

By
David Alan Waddicor
School of Earth, Atmospheric and Environmental Sciences

Contents

List of Tables

List of Figures

Abstract

An abstract of the thesis of David A. Waddicor, PhD, December 16, 2010.

Title: Aerosol in the Tropical Tropopause Layer.

This thesis details the ACTIVE campaign in the tropics of northern Australia during 2005-2006 (based in Darwin). The focus of the campaign was to find the influence of tropical convection on the aerosol and chemical content of the Tropical Tropopause Layer [TTL] and the cirrus cloud cover in the area, which is important for the global energy budget. This study details the background climatology of the Darwin region with statistical categorisation of the trace gases and particles. The TTL had regions of extremely high aerosol number concentration, much higher than that of the PBL. The 10 to 1000 nm particle concentrations were as high as 25,000 cm^{-3} and 100 to 1000 nm were as high as 1000 cm^{-3}. High aerosol concentrations were usually found in cloud-free conditions; cloudy regions were typically low in aerosol number. Wind data and trajectories (BADC) were used to find the origin of the high particle concentrations. Aerosols were found to be nucleating in outflow regions of convective anvils. SO_2 oxidation to H_2SO_4 is a widely accepted mechanism for nucleation. A binary mechanism (H_2O-H_2SO_4), with SO_2 as the precursor, was found to be inadequate in explaining the nucleation and growth rates – tested using an aerosol sectional model. However, it was found, via back trajectory analysis, that the climatology of Darwin was influenced by local and long-range sources, including advection from Indonesia and the Tropical Warm Pool. These distant sources could have introduced condensable matter, with aerosol precursor properties (certain organic compounds). The aerosol model found a condensable precursor concentration of at least 300 pptv was necessary to replicate the observations.

Declaration

No portion of the work referred to in this thesis has been submitted in support of an application for another degree or qualification of this or any other university or other institute of learning.

Copyright

Acknowledgements

I would like to thank my supervisors Geraint Vaughan and Thomas Choularton for continual support and advice; the ACTIVE consortium and all of the collaborators, in particular: Grant Allen, Keith Bower, Hugh Coe, Mike Flynn, Martin Gallagher, William Heyes, Lorenzo Labrador and Paul Williams. Further thanks must be extended to the whole Centre for Atmospheric Science (CAS) at Manchester and my officemates in particular since help has been obtained from many of my colleagues through formal and informal discussions throughout my time in the department. In particular, I would like to thank my colleagues Hugo Ricketts and Daniel Grosvenor who, despite not being involved in ACTIVE, often provided me help with computer programming, Endnote/bibtex, general atmospheric knowledge, etc. I need to thank Elena Fuentes for her constant support and hard work in supporting me through the PhD, finding many papers, researching and making suggestions for my work and discussing difficult concepts – despite being a busy Postdoc – you were invaluable to my progress – I thank you deeply. I thank NERC for the opportunity to be involved in ACTIVE and the financial support they gave me. Lastly, I would like to thank my Parents for continual support in my academic career.

Chapter 1

The Tropics and the TTL

1.1 Tropical Dynamics

This thesis describes data from a large, broad-scoped and well-equipped campaign in the tropics of northern Australia: the Aerosol and Chemical Transport in tropIcal conVEction [ACTIVE] (Vaughan et al., 2008; May et al., 2008). Based in Darwin, Northern Territory, the campaign used aircraft, sondes and ground systems to survey tropical convection, cloud particles, aerosols and chemical species in the region.

The tropics are a driving force for many of the Earth's climatological and meteorological phenomena. A combination of high solar irradiance, high moisture and a low Coriolis force provides unique conditions for atmospheric phenomena. 50% of the Earth's surface lies between 30°N and 30°S. The tropics can have a global impact beyond the boundaries of the tropics and tend to show great temporal and spatial variation, meridionally and zonally. For example, summer monsoons affect South Asia as high as 30°N but to only 20°N in West Africa, while in late summer and autumn tropical hurricanes may affect 'extra-tropical' areas of East Asia and eastern North America. Furthermore, not only do tropical boundaries seasonally extend poleward, but in zones between major subtropical high-pressure cells there are frequent interactions between temperate and tropical disturbances (Barry and Chorley, 2003). A number of basic parameters shape tropical climatology. First, the Coriolis force approaches zero at the equator, meaning winds can significantly depart from geostrophic balance. The pressure

gradients are generally weak, except where tropical storms form. Second, temperature gradients are also rather weak. Spatial and temporal variations in moisture content is a more typical factor in determining tropical climate. Third, diurnal land/sea breezes play an important role in tropical meteorology and storm formation, as a result of the almost constant day length and high solar irradiance. Due to these factors, the tropics are a region of high convective activity and net uplifting regime across the tropical troposphere. Significantly for the present study, large convective storms in the tropics can lift air and its chemical and particulate constituents into the higher reaches of the troposphere and the stratosphere where it can be transported globally. The thermal structure of the tropical troposphere is determined by radiative-convective equilibrium up to 12 - 14 km, which is the level of maximum outflow from convective storms (Vaughan et al., 2008). Above this level, convective outflow drops off with altitude, and at the cold point tropopause, the outflow is very much reduced. The layer of the tropical atmosphere between the main convective outflow and the cold point tropopause is known as the tropical tropopause layer (TTL). At some altitude within it, the net radiative heating changes from cooling to warming. This is around 15 km in clear air, though it depends quite sensitively on the cloud cover in and below the TTL. Above this altitude, large-scale dynamics dominate and the corresponding vertical diabatic transport is a slow background on top of which rapid adiabatic oscillations occur. Air will tend to ascend slowly into the tropical middle stratosphere, although there is some isentropic exchange with the extratropical lowermost stratosphere. This part of the TTL forms the base of the Brewer-Dobson circulation, determining the eventual composition of the global stratosphere (Vaughan et al., 2008). Therefore, the TTL can be seen to be not only the interface between two dynamical regimes but also as an entrance point to the stratosphere for atmospheric tracers such as water vapour and Very Short Lived Substances (VSLS), which all have an impact on atmospheric chemistry (Fueglistaler et al., 2009).

1.2 Global circulations

Global circulation refers to the large-scale wind and pressure patterns that persist throughout the year or recur seasonally. The primary driving force is the imbalance in solar irradiance from lower to higher latitudes but it is also important to appreciate the methods by which energy is transferred in the atmosphere. Unequal heating of the earth and its atmosphere generates potential energy, some of which is then converted into kinetic energy by rising, warm, low-density air and the sinking of cooler air – a convective cell circulation. The kinetic energy of moving air, on all scales, is typically dissipated by frictional effects and small-scale turbulent eddies (due to internal viscosity). The rates of kinetic energy generation and dissipation are estimated to be 2 Wm^{-2}, which amounts to only 1 per cent of the globally absorbed energy budget from solar radiation – in effect the atmosphere is an inefficient heat engine (Barry and Chorley, 2003). A second controlling factor is the conservation of angular momentum. This is the tendency for the atmosphere to move with the earth as it rotates beneath it. Since the angular momentum is proportional to the angular velocity and the square of the distance from the axis of rotation. This means that angular momentum decreases from a maximum at the equator to zero at the poles. Conservation of angular momentum requires that an air parcel travelling meridionally will change its angular velocity in order to conserve angular momentum. This effect has very important consequences for circulation in the atmosphere. Moving air will acquire lateral velocity as it travels poleward; this effect is also known as the Coriolis force and it has a major role in zonal wind flow and cyclogenesis. The continual poleward transport of momentum can be appreciated by the maintenance of the mid-latitude westerlies. The earth's frictional effect would soon lead to the dissipation of the westerlies unless there is a continuous transport of angular momentum from lower latitude regions.

There are two possible ways in which the atmosphere can transport heat and momentum. The first is by transport in the vertical plane as in figure 1.1, which has 3 meridional cells in each hemisphere. This is based on the concept of convective cells and was first proposed as a atmospheric mechanism by G.Hadley in 1735. Warm air near the equator was thought to rise and then return towards the equator via a low-level flow. Hadley suggested that the low-level flow

would attain a deflection cue to the earth's rotation, thus explaining the north-east and southeast trades. W.Ferrel expanded this model, in 1856, by considering conservation of angular momentum as an explanation for the easterlies because the Coriolis force would be too small in the tropics. Poleward counter-currents would complete the low-latitude cell, with the air sinking at about 30° due to radiative cooling (Barry and Chorley, 2003). This theory was not completely correct because the fact that solar radiation is incident on all the earth's surface, not just the equator, was neglected. Also, the trade winds are not continuous around the globe and the upper poleward flow occurs mainly at the western ends of the subtropical high cells aloft (Barry and Chorley, 2003). Figure 1.1 shows the presence of a polar cell with descending cool air from a polar high pressure. This is likely to be a simplified model of the global circulation, in particular, in the polar cell. The intermediate Ferrel cell is thermally indirect and is driven by the other two cells. Momentum considerations would indicate the necessity for easterlies aloft in the Ferrel cells but it was found that westerly winds existed in the midlatitude upper troposphere. Rossby modified the three cell model to propose that westerly momentum was transferred to the middle latitudes from the upper flows of the high and low latitude cells – troughs and ridges in the upper flow could provide this westerly flow (Barry and Chorley, 2003). This theory held popular opinion until about 1948 when it was calculated that heat and momentum could be transported by horizontal circulations (cyclonic and anti-cyclonic cells). It was shown that midlatitude horizontal circulation transported most of the required heat and momentum poleward. This mechanism works through a series of quasi-stationary highs and travelling highs and lows near the surface acting together with their associated wave patterns at the upper troposphere/stratosphere boundary (Rossby waves). This eddy-like energy transport is the modern view of the zonal wind patterns, ultimately derived from travelling waves. In the lower latitudes, eddy transport is not sufficient to explain the total energy transport required for energy balance. This is the reason that the mean Hadley cell representation of general circulation (figure 1.1) is still used. The tropical circulation is considered to be complex, with large-scale vertical transport produced by large cumulonimbus clouds. These disturbances occur in the tropical low pressure trough, which is located on average 5°S in January and 10°N in July (Barry and Chorley, 2003). The Hadley cell of the winter hemisphere is by far the most important, since it allows low-level transequatorial flow

into the summer hemisphere. The traditional global circulation model of twin symmetrical cells only exists in spring/autumn. Longitudinally the Hadley cells are linked with the monsoon regimes of the summer hemisphere. Rising air over South Asia (and also South America and Indonesia) is associated with east-west (zonal) outflow, these systems are known as *Walker circulations*. The poleward return transport of the meridional Hadley cells takes place in troughs that extend into low latitudes from midlatitude westerlies. This tends to occur at the western ends of the upper tropospheric subtropical high-pressure cells. Horizontal mixing predominates in the higher and midlatitudes, although there is thought to exist a weak cell in the midlatitudes but on a reduced scale to that envisaged in the three cell model (Barry and Chorley, 2003).

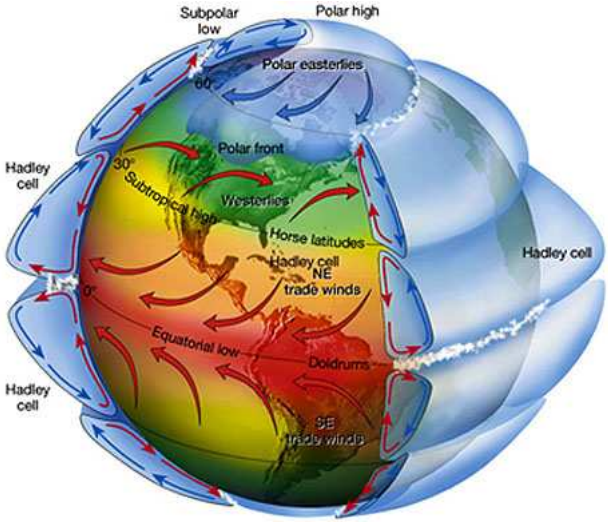

Figure 1.1: Global circulation model. The polar cells are centred over the two poles and the Ferrel cells are intermediate between the Hadley and polar cells, in the midlatitudes. Source: Barry and Chorley (2003), adapted from NASA.

1.3 Walker circulations

As the Hadley circulations represent a meridional (north - south) link in the general atmospheric circulation, so the Walker circulation (see figure 1.2) represents the large-scale zonal (east - west) link in the tropics. Tropical weather differs from midlatitude climate due to a much weaker Coriolis force (zero at the equator),with a resulting departure from geostrophic winds. The Walker circulation is

driven by zonal pressure gradients caused by differences in vertical motion (Barry and Chorley, 2003). Spatial and temporal variations in moisture, and continental and oceanic heating develop the Walker circulation. Areas of enhanced heating, typically over continental regions (lower heat capacity) but also certain warmer parts of the ocean, produce rising air mass. On the other hand, air subsides over cooler parts of the oceans, over continental regions where deep high pressure systems have become established, and in association with subtropical high pressure cells.

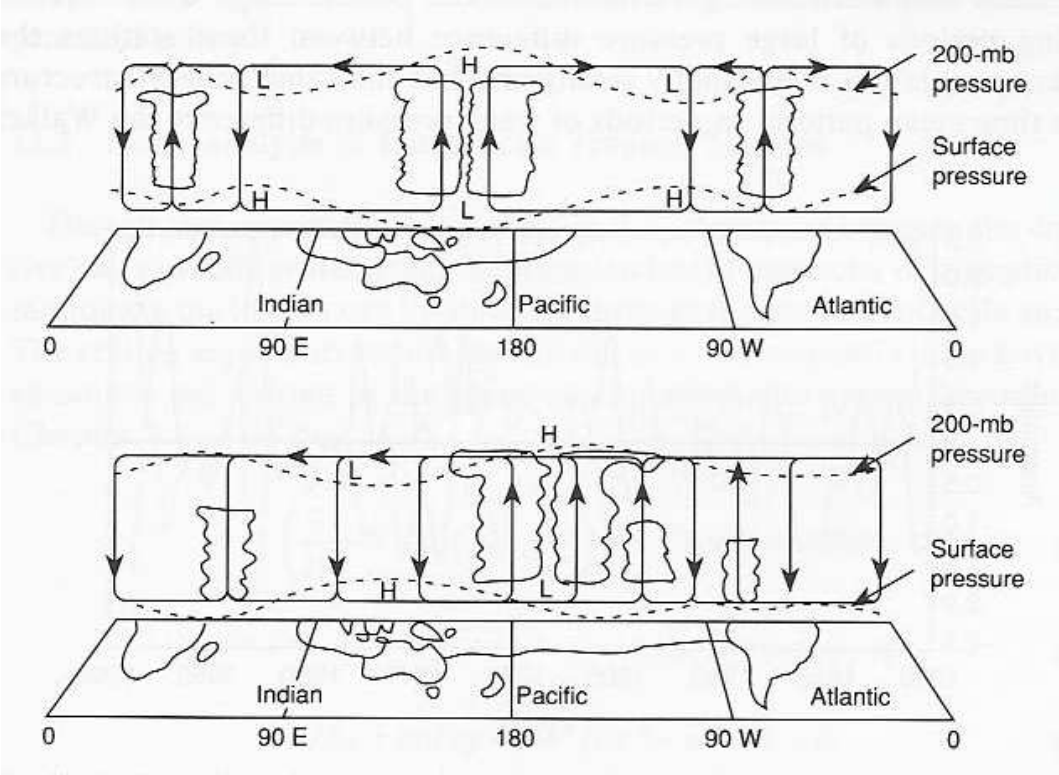

Figure 1.2: The Walker circulation. *Top* is non-ENSO; *bottom* ENSO. Source: Barry and Chorley (2003).

The effect was first noticed by Sir Gilbert Walker from 1922 to 1923 by his discovery of an inverse correlation between the pressure over the eastern Pacific Ocean and Indonesia (Barry and Chorley, 2003). The strength and phase of this is called the *Southern Oscillation* and is commonly measured by the pressure difference between Tahiti (18°S, 150°W) and Darwin, Australia (12°S, 130°E). The Southern Oscillation Index (SOI) has two extreme phases:

- *positive* when there is a strong high pressure in the southeast Pacific and a

low centred over Indonesia with ascending air and convective precipitation;

- *negative* (or low) when the area of low pressure is displaced eastwards towards the central Pacific.

Positive [negative] SOI implies strong easterly trade winds [low-level equatorial westerlies] over the central-western Pacific. These Walker circulations are subjected to fluctuations in which an oscillation (El Niño/Southern Oscillation – ENSO) between high phases (non-ENSO events) and low phases (ENSO events) is of great impact:

- *High phase* (top panel, figure 1.2) This consists of 4 major zones of rising low pressure air and increase precipitation over Amazonia, central Africa and Indonesia/India. Conversely there is subsidising high pressure limbs and decreased precipitation over the eastern Pacific, South Atlantic and western Indian Ocean. During this phase low-level easterlies strengthen over the Pacific and subtropical westerly jet streams in both hemispheres weaken, as does the Pacific Hadley cell.

- *Low phase* (lower panel, figure 1.2) This phase has five major zonal cells involving rising low pressure air and increased precipitation over the South Atlantic, the western Indian Ocean, the western Pacific and the eastern Pacific. Subsidising air and decreased precipitation is found over Amazonia, central Africa, Indonesia/India and the central Pacific. Low-level westerlies and high-level easterlies dominate over the Pacific and subtropical westerly jet streams in both hemispheres intensify, as does the Pacific Hadley cell (Barry and Chorley, 2003).

The ENSO events are believed to be caused by shifting oceanic circulations. The vast heat reservoir of the Pacific Ocean switches gradient like a giant 'see-saw'. In this regime, the sea surface temperatures in the eastern Pacific increase (a sea surface temperature > 27 °C is conducive for marine convection); the higher surface temperatures in the eastern ocean 'skew' the Walker circulation, so that low pressure rising is found over the Pacific ocean - particularly near the coast of Peru and Ecuador. Conversely, there is subsiding high pressure air in the central-western Pacific. It was a high phase SOI during ACTIVE 2005/2006, with a positive value for most of the latter part of 2005 and early 2006 (see table 1.1). There was one exception during November 2005 when a weak low phase event of

-2.7 occurred.

Year	Jan	Feb	Mar	Oct	Nov	Dec
2005	–	–	–	10.9	-2.7	0.6
2006	12.7	0.1	13.8	–	–	–

Table 1.1: S.O.I. – Southern Oscillation Index for ACTIVE related period. *Data from the Australian Bureau of Meteorology (BoM)*

1.4 The importance of aerosols and the TTL

Tropical convection has often been considered an important source of aerosol in the upper tropopause (above 10 km) and the TTL (e.g. Junge et al., 1961; Rosen et al., 1978; Perry and Hobbs, 1994; Brock et al., 1995; Schröder and Ström, 1997; Twohy et al., 2002). The troposphere and the stratosphere both have distinct features and the Tropical Tropopause Layer (TTL) is the transition region between the two where features of both are observable. Quantities such as altitude, temperature variability, ozone, potential temperature and vorticity and even convective outflow are all used to define the TTL region, thus leading to a different definitions of the TTL in the literature (Fueglistaler et al., 2009). At about 200 hPa (350K/12.5 km), the meridional temperature gradient reverses sign, which is also the level of the core of the subtropical jet. The lower bound of the TTL is typically taken to be above the level of main convective outflow (Fueglistaler et al., 2009), i.e. at about 150 hPa (355 K/14 km). Below, air is radiatively cooling (subsiding), and ascent occurs predominantly in moist convection. Above that level, air is radiatively heated under all sky conditions. The level of zero radiative heating (LZRH) under clear sky conditions is slightly higher, at about 125 hPa (360K/15.5 km) as shown by the dashed line in figure 1.3. The upper bound of the TTL is set at about 70 hPa (425 K/18.5 km), and laterally the TTL is bounded by the position of the underlying subtropical jets (i.e. equatorwards of about 30° latitude) (Tuck et al., 2004; Fueglistaler et al., 2009). In the lower part of the TTL, meridional transport is limited by the large gradients in potential vorticity associated with the subtropical jets. In the upper part of the TTL, rapid horizontal transport to higher latitudes and mixing into the tropics from higher latitudes is observed (Tuck et al., 2004; Fueglistaler et al., 2009).

Above the TTL (above 60 hPa/450 K), the inner tropics become relatively isolated (the tropical pipe). The definition of the TTL is primarily motivated by the observed large-scale dynamical structures. The horizontal circulation and temperature structure of the TTL are strongly influenced by the distribution of convection in the troposphere, while vertical motion is increasingly dominated by eddy driven circulations typical of the stratosphere. Detrainment of deep convective clouds may occur throughout the TTL, and likely has an impact on tracer concentrations, and perhaps the heat budget, of the TTL (Fueglistaler et al., 2009) – as investigated during the ACTIVE (and the cooperative SCOUT-O3 and TWP-ICE) campaign.

The tropics climatology (Reid and Gage, 1996) is dominated by large thunderstorm (cumulonimbus) that can uplift vast amounts of boundary layer air into the upper troposphere (UT) and possibly the TTL (Dessler, 2002). The content of the air could have a large impact on the chemistry of the atmosphere and the evolution of the cloud; there is also the potential to inject aerosols or aerosol precursor material into the cold, dry TTL – ideal for aerosol formation (nucleation) to occur (Ekman et al., 2004; Lee et al., 2004). The TTL is also believed to act as a transition region with the lower stratosphere, as seen in figure 1.3, by Fueglistaler et al. (2009).

Fast convection can also inject short-lived species, with a high degree of mass conservation, from the Planetary Boundary Layer (PBL), such as source gases for halogen radicals – that can destroy ozone in the TTL and LS (e.g. Fueglistaler et al., 2009; Larin and Yermakov, 2010; Mebarki et al., 2010). Cumulonimbus clouds are typically areas of intense lightning activity that produce large amounts of nitrogen oxides (NO_x) (Huntrieser et al., 2002). Uplifted CO and hydrocarbons from the polluted boundary layers can react with NO_x in the UT/LS to produce ozone [see equations 2.8, 2.9 and 2.10 in section 2.3.2]. Ozone in the stratosphere is a very important global species that absorbs much of the incoming UV radiation and also initiates many photochemical reactions [e.g. SO_2 oxidation, see section 2.3.2 for example]. Aerosols are also expected to influence the moisture balance in the TTL and stratosphere (Smith et al., 2006) – moisture levels can affect ozone chemistry in the stratosphere. Furthermore, the TTL is an area that links the troposphere to the stratosphere and the circulatory winds therein. The TTL is found at the limit of the uplift region of the Hadley cells; this potentially allows

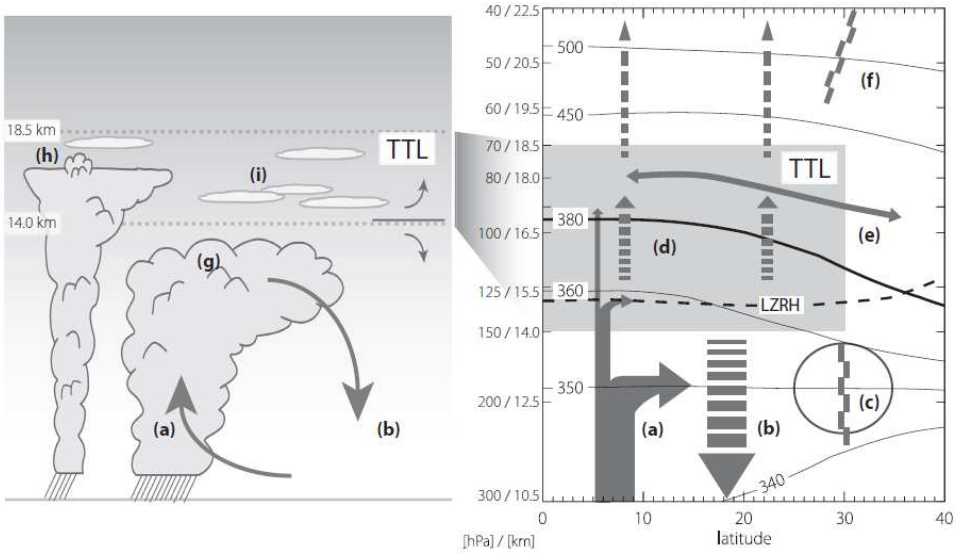

Figure 1.3: Schematic of cloud processes and transport *left* and zonal mean circulation *right*. Source: Fueglistaler et al. (2009). Arrows indicate circulation, black dashed line indicates *clear sky* level of zero net radiative heating. (a) Deep convection: Main outflow around 200 hPa, outflow rapidly decays with height in TTL, rare penetrations of tropopause. Fast vertical transport of tracers from boundary layer into the TTL. (b) Radiative cooling (subsidence). (c) Subtropical jets, limit quasi-isentropic exchange between troposphere and stratosphere (transport barrier). (d) Radiative heating, balances forced diabatic ascent. (e) Rapid meridional transport of tracers, mixing. (f) Edge of the 'tropical pipe', relative isolation of tropics and stirring over extratropics ('the surf zone'). (g) Deep convective cloud. (h) Convective core overshooting its level of neutral buoyancy. (i) Ubiquitous optically (and geometrically) thin, horizontally extensive cirrus clouds, often formed *in situ*. Note: The height-pressure-potential temperature relations shown are based on tropical annual mean temperature fields, with height values rounded to the nearest 0.5 K.

the transport of TTL air and its constituents into the subtropical stratosphere and beyond. A residual wind called the Brewer-Dobson circulation (e.g. Holton et al., 1995; Fueglistaler et al., 2009) provides a meridional link between the tropics and the polar regions through the lower stratosphere. Within this context, the motivation for the ACTIVE project was to improve understanding of the aerosol and chemical processes that occur in the TTL and the tropics.

1.5 Aerosol and radiation

Aerosols are known to play a significant role in the absorption, reflection and scattering of solar and terrestrial radiation (IPCC, 2007; Kiehl and Trenberth, 1997). The Sun, with a surface temperature of roughly 6000 K, has a black-body radiation curve shifted to smaller wavelengths – visible and ultraviolet – and with a greater integrated energy flux than the Earth (the Sun has a super-high temperature plasma [corona] which is theoretically 10^6 K; this alters the output spectrum somewhat from that expected of an ideal black-body (Tobiska et al., 2000)). The Earth has an average surface temperature of $\sim$ 298 K and therefore has a radiation flux of much lower energy and shifted towards infrared wavelengths. The amount of incoming solar and outgoing terrestrial radiation absorbed is determined by the composition of the Earth's atmosphere (chemistry, cloud, aerosol, etc.) and the density and size of these components – figure 1.4 shows a schematic of the global and annual radiation balance.

Aerosol and radiation interaction is defined by four broad categories. Black carbon absorbs solar radiation and can as a result affect the vertical temperature gradient. Water-soluble inorganic species (SO_2, NO_3, NH_4) - have a backscattering effect on solar radiation; furthermore, they indirectly have an effect on the reflection of solar radiation by acting as cloud condensation nuclei (CCN) – cloud properties and lifetime are determined to a large degree by the aerosols. Condensed organic species also behave with similar radiative properties to the inorganic species. Finally, the larger mineral dust particles can absorb and backscatter solar radiation, act as ice nuclei and therefore aid cloud formation, and absorb/emit infra-red radiation.

Sulphate aerosols are predicted to cause a global radiative forcing of -0.4 W m^{-2}; biomass burning aerosols produce a forcing of -0.1 W m^{-2} (fossil fuel organic carbon) and fossil fuel black carbon yields a +0.2 W m^{-2} forcing. Mineral dust has a more variable and unpredictable effect on the global radiation budget. The current estimates for the direct effect are 0.5 to -0.6 W m^{-2} and for the indirect effects on cloud particle production, 0 to -2.0 W m^{-2} (Andronache et al., 1999). The overall effect of aerosol acting as CCN on radiation forcing is not very well

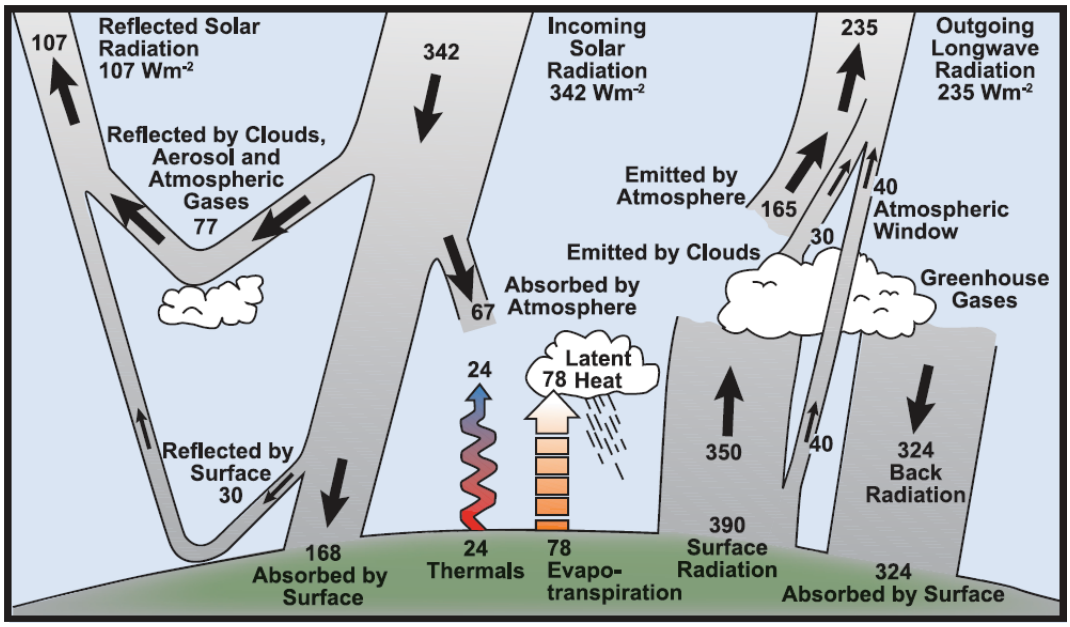

Figure 1.4: Schematic of global and annual mean energy balance, including radiation (units in Wm^{-2}). Figure from IPCC (2007) [schematic originally from Kiehl and Trenberth (1997)].

defined but expected to be cooling. A ±15% change in CCN in marine stratus cloud, which covers about 25% of the Earth's surface, could provide ±1 W m^{-2} to the global energy budget.

Cirrus cloud is 'wispy' ice cloud that is formed in the high altitude (on a global average, higher than 4 km), cold regions of the UT/TTL. Tropical convection cloud begins to glaciate (ice crystals) as the updraught columns rise. As the cloud top reaches equilibrium, the outflow region of the cumulonimbus spreads out into a characteristic 'anvil' form. This anvil is of utmost importance to the global radiative budget because high speed winds circulate over great distances and can spread the cloud over many hundreds of kilometres. Cirrus cloud (Seifert et al., 2004a; Gallagher et al., 2005; Wang, 2005a,b; Choularton et al., 2008) can reflect solar radiation in the visible spectrum and re-emit infrared at shifted frequencies (Chou and Neelin, 1999; Sherwood et al., 1994; Hartmann et al., 2001a,b) back towards the Earth.

There is also an increased understanding of the influence of subvisible cirrus cloud;

these low number concentration clouds can still have a major impact on the radiative forcing in the UT/TTL (Lawson et al., 2008); these clouds form in the TTL cold point [$\sim$ 17 km] (Dinelli et al., 2009; Vaughan et al., 2008). In the study by Thomas et al. (2002), a high altitude aircraft (the Russian Geophysica) was used to sample subvisible cloud, at 17 km, 190 K temperature; significant findings were: 1) the horizontal extent of the clouds were in the hundreds of kilometres; 2) they persisted for at least three hours and 3) had geometric thickness of 100 - 400 m. The particle size range was 0.4 to 23 μm with typical concentrations of 0.1 to 0.3 cm^{-3}. The Costa Rican CR-AVE campaign (Lawson et al., 2008) measured subvisible cirrus cloud in the TTL and found much larger ice crystal sizes than other experiments: typical ice crystal diameters were 100 μm, with sizes extending up to 165 μm. The ACTIVE campaign was joined by two collaborating experiments, SCOUT-O3 and TWP-ICE (see section 5.1 and references Brunner et al. (2009); May et al. (2008)), that yielded a large dataset of in situ cirrus cloud measurements (anvil, aged, thin, etc.) – a thorough discussion of cirrus cloud is found in the references. However, the exact production mechanism is still not fully understood; despite this, they are strongly believed to play a role in the tropical, and even global, radiative forcing (e.g. radiative and dynamic model, Durran et al., 2009). The importance of subvisible cirrus is that they exhibit much wider extent than visible cirrus. Jensen et al. (1999) also concluded that the humidity of deep convection allowed subvisible cirrus to form in the TTL. It was concluded that the outgoing longwave radiative flux is reduced by 1 - 2 W m^{-2}, with an accompanying increasing in the radiative heating of the UT/TTL.

Chapter 2

Introduction - Aerosols

2.1 Aerosols in the Atmosphere

Aerosols are described as well dispersed suspended particles of liquid or solid constitution, some being a complex mixture of both phases. They are found in most environments around the world and their generation, origin and composition is studied by a broad range of disciplines: physics, meteorology, chemistry, etc. Particles have been detected in the tropics, arctic, in marine environments, from the Planetary Boundary Layer (PBL) to the upper Troposphere/lower Stratosphere (UT/LS). They are ubiquitous in the earth's atmosphere and play a key role in the climate. Aerosols can directly effect incoming and outgoing radiation by reflection and scattering and indirectly by their role in cloud formation – this contributes to global climate forcing, to an as yet unknown degree.

Aerosols can be produced by the mechanical action of wind and erosion, such as sea salt droplets from the action of wind on the surface of the sea and the erosion of rock and sand – referred to as primary aerosols. They can be produced naturally, such as organic plant matter, or by anthropogenic means, such as sulphur based pollution from power stations and soot from coal burning. Particles can also form from precursor gases, where molecular clusters form stable nuclei on which further condensation and coagulation can occur (see figure 2.4) – referred to as secondary aerosols. Aged aerosol also undergo oxidation and become progressively more internally mixed (composed of various compound fractions),

particularly organic aerosol (Alfarra et al., 2006; Duplissy et al., 2008). The larger, supermicron aerosols, such as mineral dust, tend to sediment out of the atmosphere in fairly short timescales ($\sim$ 2 days). The sub-micron sulphate and nitrate dominated aerosols have an important and intrinsic role to play in the evolution and chemical composition of cloud and of the atmosphere in general.

Aerosols can grow through condensation of vapour and coagulation. These are very dependent on size, composition and atmospheric conditions. Atmospheric water vapour hydrates aerosol particles and eventually lets the particles grow into cloud droplets. At supersaturated conditions, aerosols that grow beyond the so-called activation diameter (Köhler theory) are typically called Cloud Condensation Nuclei (CCN) and are very important for the formation of clouds and the climate in general.

This thesis will attempt to further the understanding of aerosols' role in the atmosphere, particularly in the UT/TTL. To do this, a comprehensive dataset of airborne measurements, from a large tropical campaign, will be presented and discussed. The Aerosol and Chemical Transport in tropIcal conVEction [ACTIVE] (Vaughan et al., 2008; May et al., 2008) was a broad scoped and well-equipped campaign in the tropics of northern Australia that yielded a wealth of scientific data and information.

2.1.1 Aerosol size, composition and mass distribution

The size, mass and volume modes for aerosol populations tend to be defined in 4 literature categories: Nucleation mode (less than 3 nm – although very hard to detect with current technology), Aitken mode (typically, 10 to 100 nm), accumulation (100 to 1000 nm) and the supermicron (greater than 1 μm) coarse mode. There is some variability in the definitions but the general definitions are: nuclei mode are the initial aerosol regime produced from molecular clusters; Aitken mode are removed relatively quickly by deposition and growth; accumulation mode, as the name suggests, are usually harder to remove from the atmosphere (reduced Brownian motion due to their intermediate size); the coarse mode generally has a low lifetime, because of its high mass, it settles out of the atmosphere

through sedimentation. The relative distribution of these modes is usually described by log-normal distributions. The location (marine, urban, rural, etc.), the height and the age of the air mass determines to a large degree the number, size, mass and chemical composition of aerosol population.

Zaizen et al. (2004) surveyed the aerosol size distribution in the free troposphere (above the boundary layer – altitude greater than 2 km) of the North West Pacific Ocean region (example of the size distribution is given in figure 2.1), including areas with continental Asian outflow. They found that the aerosol number concentration and size distribution were different in different air masses – divided by fronts in the subtropics. In the extratropical region there was a low fine aerosol (less than 150 nm) population fraction, a large accumulation mode fraction (150 to 500 nm) and a large modal radius (30 to 60 nm); the air was found to be aged pollution from the Asian continent with a mixture of sulphates and soot – the aged nature of the aerosols explains the increased modal radii. In the more convectively active subtropical region there was a high number of fine aerosol, below 150 nm; this produced a small modal radius in this region: 10 to 30 nm. The accumulation mode was significantly lower in concentration than in the extratropical regions: less than 10 cm^{-3} (STP), showing a less aged aerosol loading. The study also found that there was an increase in fine aerosols (up to 3000 cm^{-3} STP) with altitude, up to 11 km, in the region 15 to 31 °N. They theorised that this is due to homogeneous nucleation (section 2.3) occurring in the UT from the high mixing ratios of SO_2 (0.25 to 0.50 ppbv at 11 km) in the Asian Pacific atmosphere. Further discussion of the transport mechanism of the pollutant SO_2 is not discussed but other studies go into more depth and explain convective uplift as a quick input route into the UT/TTL.

Froyd et al. (2009) undertook an aircraft campaign from 2004 to 2006 in the UT/TTL over Costa Rica. They found some distinctive aerosol population regions that were often defined by convective activity in the area. The maritime influence was found to increase the burden of acidic, sulphate-rich aerosols in the convective outflow regions up to 12 km. Continental air tended to loft organic rich particles and precursors into the TTL (see also, Murphy et al. (2007)); these organics had undergone some degree of oxidation, many also contained nitrates.

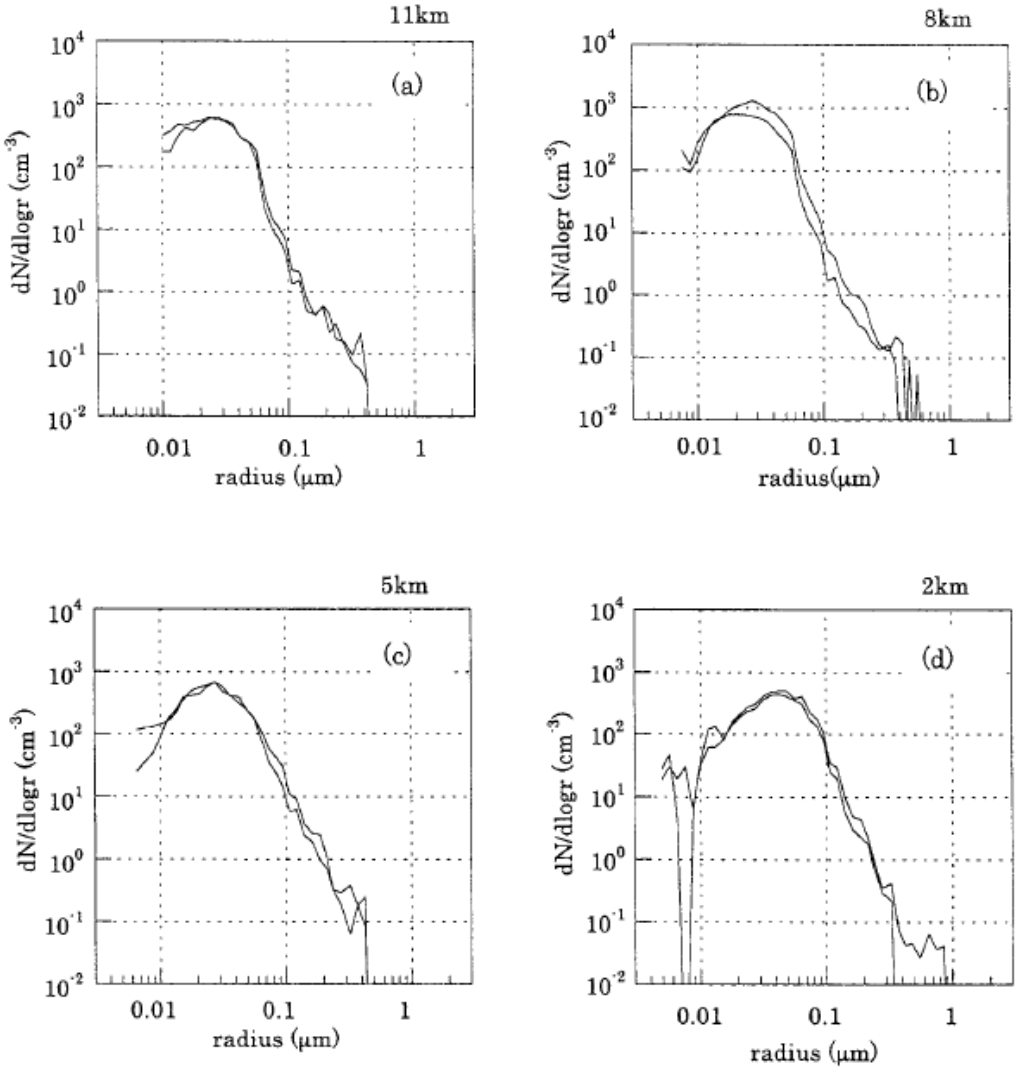

Figure 2.1: Size distribution over Saipan Island (15° N, 145° E), Northwestern Pacific Ocean. Figure from Zaizen et al. (2004).

Above the tropopause the regime returned to a sulphate dominated aerosol population. Regardless of recent convective input, the TTL aerosol composition was remarkably consistent. Accumulation mode particles were internal mixtures of highly oxidized organic material and partially or fully neutralized sulfate. In this case it was discovered that maritime convection, over the Pacific, even recent, had only a weak influence on TTL aerosol properties: it was much more influenced by continental input from South America. Organics are believed to play a role in the nucleation and hygroscopic growth of aerosol particles, in some cases reducing hydration, in some cases increasing water uptake (Andreae et al., 2001; Andreae

and Merlet, 2001; Sjogren et al., 2007). However, the interplay between organic and inorganic compounds and their effect on aerosol particle's surface tension, hygroscopic uptake and particle generation (nucleation) properties are believed to be very complex, with variations from species to species.

Liu et al. (2005) performed a modelling study into the composition of aerosols in the different size modes, in a global aerosol model. Using a method of moments and modes – two modes for sulphate aerosols: nucleation and accumulation – the model predicted high sulphate aerosol number concentrations in the nucleation mode ($> 10^4$ cm^{-3}) particularly in the tropical upper troposphere. The concentration of larger accumulation mode aerosols was found to be in the range 50 to 500 cm^{-3} anywhere in the free troposphere. 80% of global sulphate by mass exists as pure sulfate aerosols (9.7% in nuclei and 69.8% in accumulation mode), with 14.3% on carbonaceous aerosol, 3.3% on dust, and 2.7% on sea salt. However, they found that in the planetary boundary region there was a 40% sulphate association with non-sulphate aerosols, whereas in the upper troposphere it was less than 10%. Investigating the mass fraction of carbonaceous-sulphate aerosols, it was found that carbonaceous aerosols are generally internally mixed with sulphate in most of the troposphere; this provided the aerosols with a degree of hygroscopicity. The exception was close to source regions where the carbonaceous emissions were unaged – mixed mass fraction in this case was less than 5% – and were hydrophobic. They found an average carbonaceous aerosol lifetime of 3 - 4 days. It has been shown in previous studies, such as in the Amazon (Andreae et al., 2001; Andreae and Merlet, 2001; Jones et al., 2001), that biomass burning by-products (acetonitryl, methyl chloride, hydrocarbons, etc.) are prevalent in the UT/TTL. They found correlation with recent convective activity and biomass burning episodes and the high loading of the UT with aerosols, organics, NO, O_3, CO, CO_2, etc. These studies demonstrate the complexities that exist when there are many source regions that contribute to an aerosol population. In Darwin there were various influences on the regional climatology that changed with the monsoon winds: there was a dry season (pre-monsoon) with biomass burning (soot/carbonaceous organics), oceanic input from the Indian and Pacific Oceans, pollution from the built-up areas of Australia and Indonesia and organic compounds from the rural/forested areas of these land masses. ACTIVE provided an opportunity to investigate the effect of these background sources on the tropospheric climatology and storm dynamics.

2.2 Aerosol in the Upper Troposphere and TTL

A wide range of aerosol population concentrations have been observed in the TTL during field campaigns. Brock et al. (1995) presented data from the UT which suggested that aerosol production was taking place in situ from binary homogeneous nucleation of sulphuric acid and water, H_2O-H_2SO_4. Homogeneous nucleation of H_2O-H_2SO_4 particles near the tropical tropopause and vertical transport/mixing, was put forward as an explanation for the relative uniformity of the aerosol composition in the lower stratosphere. The paper finds maximum aerosol concentrations of 30,000 cm^{-3} from direct measurements in the TTL over Fuji.

An aircraft survey over Western Europe in summer 1994 (Schröder and Ström, 1997) detected aerosols throughout the troposphere and into the lower stratosphere. High concentrations of aerosols (diameter greater than 18 nm) were found in the troposphere (above 4 km), with maxima as high as 2×10^4 cm^{-3} and medians of 1400 cm^{-3} (all values in STP values – standard temperature and pressure, 273.15 K and 1013.25 hPa); these high maxima were similar to the TTL number concentrations seen by Brock et al. (1995) and other later campaigns and were seen to increase with altitude up to about 10 km. The smaller nucleation mode was seen to be very variable throughout the troposphere, this is an expected effect due to the sudden and relatively localised nature of nucleation bursts. There were measurements of almost zero aerosol concentrations and maxima up to 10^4 cm^{-3}, with a median of 300 cm^{-3}. Above the tropopause there were lower number densities of aerosols greater than 18 nm in diameter; concentrations were between 10^2 and 10^3 cm^{-3} with a median of 400 cm^{-3}. The nucleation mode was observed in similar quantities to that in the troposphere. The results revealed that nucleation mode aerosols became more abundant the higher the altitude, concluding that the UT was the most effective source region for nucleation bursts and aerosol generation by sulphate gas-to-particle conversion – these bursts had horizontal extents of 10 to 30 km. Accumulation mode aerosols (greater than 120 nm in this study) were found to be more prevalent where coagulation, condensation and cloud processing were more important, in

the lower troposphere (below 6 km). Interestingly, there was not found to be any solid link between clean, low preexisting aerosol number, environments and high nucleation mode, $\sim$ 7 nm, aerosols (Strom et al., 1999; Clement et al., 2006; Boy et al., 2008). There was no anti-correlation between the nucleation mode particles and the accumulation mode; furthermore, there were not any significant reductions in accumulation mode particles in the vicinity of nucleation bursts, in contrast to other experiments (e.g. Clement et al., 2002; Young et al., 2007; Boy et al., 2008). Andreae et al. (2001) found that cloud inhibited aerosol generation and caused aerosol removal; 85 - 90% of the accumulation were removed by convective transport. It was suggested that the removal of the accumulation mode benefited the production of nucleation mode aerosols when precursor gases were detrained from storms into the UT/TTL.

Secondary aerosol particle generation in the atmosphere is a result of gas-to-particle conversion; the precursors involved and the exact mechanism is not fully understood but sulphate chemistry is known to be very important in this process. Dimethyl sulphide (DMS) has been argued to be an important source of SO_2 over the remote oceans for the Marine Boundary Layer (MBL) and the free troposphere. SO_2 can be further oxidised to sulphuric acid, H_2SO_4 – sulphuric acid is known to be a prime, aerosol forming, precursor gas because of its low vapour pressure. Thornton et al. (1997) presented DMS and SO_2 concentrations for the western Pacific Ocean, using aircraft data from the Pacific Exploratory Mission-West(PEM-West), and considered its origin and role in aerosol generation. In the same way as aerosol was found to increase with altitude in Schröder and Ström (1997), the vertical concentration of SO_2 was found to increase with height. This was explained as a result of its detrainment from continental convective storms and then long-range transport to the western Pacific Ocean. This campaign found elevated numbers of aerosol in regions of high SO_2 and NO. With concentrations of NO reaching 1000 pptv and UV upwelling above cloud tops, the OH levels could be enhanced significantly. It is stated by Thornton et al. (1997) that levels of SO_2 could reach 100 pptv in the UT with 8×10^6 cm^{-3} OH molecules; this would be sufficient to produce sulphuric acid in such quantities as to drive aerosol nucleation in the UT with concentrations of 10^4 nuclei within a few hours. In conclusion, Thornton et al. (1997) found that DMS, during the west Pacific Ocean campaign (PEM-West), was not a major source of SO_2 in the UT and the

majority of SO_2 was due to volcanic emission and anthropogenic sources. DMS on average only provided 1% of overall SO_2 production during 1991; in 1994, the main sources were again volcanic and anthropogenic emissions with <10% DMS – the fact that the DMS contribution was higher in 1994 was due to the fact that overall SO_2 levels were considerably lower during that time. The high UT concentrations of SO_2 were found to be a result of convective uplift and long-range transport; coinciding with these high levels of SO_2 were large numbers of nucleation mode aerosols ($\sim$ 7 nm, 10^4 cm^{-3}) – also of importance was the high concentrations of NO (possibly lightning produced in convective storms) and its involvement in OH production (see section 2.3 for a more detailed discussion about nucleation and chemistry).

The Stratosphere-Troposphere Experiment by Aircraft Measurements (STREAM) took place in July 1994 (Strom et al., 1999). It was a campaign over north western Europe that looked at cumulonimbus properties, the associated ice crystals, trace gases and aerosols. High CO concentrations, above 130 ppbv, were seen inside convective anvil cloud; CO was anticorrelated with ozone and was used as a tracer of convectively influenced air. Other studies have shown raised CO and ozone in anvil cloud; this has been explained as convective air mixing with high ozone concentration stratospheric air but it depends on the height of the convection and the degree of tropopause disturbance (Smith et al., 2006). Strom et al. (1999) also confirmed that the condition of the boundary layer plays an important role in shaping the UT/TTL composition during quick convective injection; CO was correlated to boundary layer variations from day to day. Higher aerosol concentrations were found in areas of lower crystal ice number (cloud), conjectured to be an effect of cloud particle scavenging of aerosols. The coagulation of aerosols and cloud particles would be sufficient to remove any local maxima. The cloud ice crystal number densities reached as high as 100 cm^{-3} (STP) – cloud water content of 1 g m^{-3} – in the cumulonimbus, furthermore, the convection was intense enough to pierce the tropopause and inject water vapour, CO and aerosols into the stratosphere – demonstrating the potential of convection to influence the composition of the photochemically active lower stratosphere. The high CO, convectively influenced air, was found to contain $\sim$ 15,000 cm^{-3} (STP) particles larger than 18 nm and as high as 20,000 cm^{-3} particles larger than 7 nm (typical nucleation mode). Strom et al. (1999) suggested that the these aerosol particles

could be generated during convective uplift or in the anvil outflows. However, it is expected (e.g. Pirjola, 1999; Wang and Prinn, 2000; Clement et al., 2002; Twohy et al., 2002; Clement et al., 2006) that such small nucleation particles could not form in a highly scavenging environment of cloud particles (liquid drops and ice crystals).

De Reus et al. (1998) presented data from the STREAM-96 campaign, which flew tropopause missions above Britain and Ireland in May-June 1996. The study showed that water vapour mixing ratios and aerosol concentration correlated, showing the importance of convective and frontal uplift, and cloud particle evaporation for moisture in the UT and subsequent nucleation. Nucleation was modelled for UT conditions and was found to be dependent on a lower threshold of preexisting particle number density, above which aerosols would not be produced. Mixing of tropospheric and stratospheric air were seen to influence the aerosol concentrations and possibly activate aerosol nucleation. The measured aerosol concentrations were 500 to 2000 cm^{-3}, with isolated events up to 10,000 cm^{-3} (STP).

The CARIBIC programme (Heintzenberg et al., 2003; Hermann et al., 2003; Brenninkmeijer et al., 2007) placed air sampling equipment on commercial flights between Germany and southern Africa and also over the Middle East to the Indian subcontinent – destinations also included the east coast of China (Guangzhou, 2006). These flights crossed the convectively active equatorial tropics, over land that had undergone considerable biomass burning. Heintzenberg et al. (2003) found many aerosol nucleation events in the TTL: particles with diameters between 4 and 12 nm had concentrations in the range 10,000 to 30,000 cm^{-3} (STP) and those with diameters between 12 and 18 nm had an overall campaign median concentration of 9000 cm^{-3} (STP). Figure 2.2 shows the aerosol time line for a flight between Munich and Colombo, 5 June 1998; it can be seen that aerosol number concentrations are consistently above 10,000 cm^{-3} in the tropics. In the UT over the eastern seaboard of China (Brenninkmeijer et al., 2007) there were even examples of $\sim$ 140,000 cm^{-3}, in both size groups, $>$ 4 nm and $>$ 12 nm. Nucleation was found to be linked to convective activity, particularly in the tropics and subtropics; the Guangzhou case showed particularly high aerosol loadings

that are expected to be a result of high concentrations of anthropogenic pollution, with subsequent particle formation in the UT. Similarly, Twohy et al. (2002) studied the outflow from a mesoscale convective system in the USA. They found extremely large concentrations of aerosol downwind of the storm: 45,000 cm^{-3} (STP) for particle sizes $\geq$ 25 nm, spread over a 600 to 800 km horizontal region, 2 km vertical depth. These high particle concentrations were highly correlated with various trace gases, such as methane, carbon monoxide, nitrogen oxides and hydroxyl radicals. These gases were detected in similar ratios inside the convective cloud region, indicating the air had passed through the storm before being outgassed into the tropopause. No correlation was found with the cloud particles, suggesting that the aerosol production was independent of the cloud formation/evaporation. This study shows the potential for convective uplift to produce high number concentrations of aerosols in the UT – however, the precise mechanics of the nucleation are still not fully understood.

Young et al. (2007) investigated enhanced aerosol numbers in the northern midlatitude tropopause. Measurements were made with aircraft during the NSF/NCAR GV Progressive Science Missions, December 2005. Number concentrations and size distributions were made between 4 and 2000 nm (N_{4-2000}) diameters in order to detect signs of air mass mixing and associated nucleation events – nucleation events were found to coincide with tropopause folds, when stratospheric air mixes with upper tropospheric air. In agreement with other studies, Young et al. (2007) believe that the UT/LS are prime regions for particle production due to low temperature, low surface area density of preexisting aerosols and high sun exposure. The nucleation mechanism is still uncertain, with a number of possible candidates identified (see section 2.3): binary, ternary, ion induced and organic induced. In the low temperature UT/LS there is expected to be almost barrierless nucleation (Kulmala et al., 1998). Barrierless nucleation derives from the Gibbs free energy equations (see section 3.2); this equation describes the balance between the sum of the chemical potentials of the species and the surface tension of a liquid drop. It is the surface tension and the creation of 'new surface area' that forms an energy barrier to particle formation. Curtius (2006) derived an expression for the critical radius of a stable nucleation cluster for a single species. Working from Gibbs free energy expression,

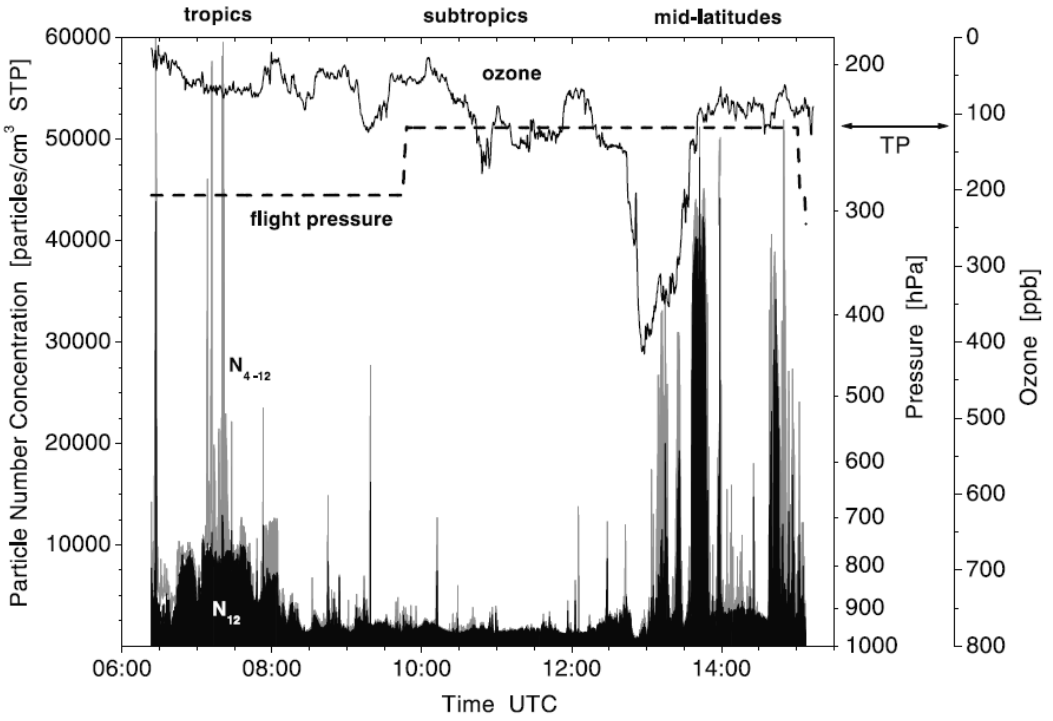

Figure 2.2: Particle number concentrations from the CARIBIC flight Colombo-Munich on 5 June 1998. N_{12} (black area) indicates the Aitken plus accumulation mode (i.e. greater than 12 nm). N_{4-12} (gray area) indicates the ultrafine/nucleation aerosols. The thick dashed line is flight pressure and the thin solid line is the ozone mixing ratio. TP indicates the tropopause. Data and figure from Hermann et al. (2003).

$$\Delta G = -\frac{4}{3}\pi R^3 \frac{kT}{v_l} \ln(S) + 4\pi R^2 \sigma, \tag{2.1}$$

where S is the saturation ratio, $S = p_A/p_{A\infty}$ (p_A is the vapour pressure of A and $p_{A\infty}$ is the pressure over a flat surface of liquid A), k is the Boltzmann constant, T is the temperature, v_l is the volume occupied per molecule, and σ is the surface tension. Differentiation of ΔG with respect to R and setting to zero will give the maximum for the energy curve and hence the energy barrier and the critical radius for stable cluster formation. After differentiation, the energy barrier is given by,

$$\Delta G^* = \frac{4\pi}{3}\sigma R^2 = \frac{4\pi}{3}\sigma \left(\frac{2\sigma v_l}{kT \ln(S)} \right)^2. \tag{2.2}$$

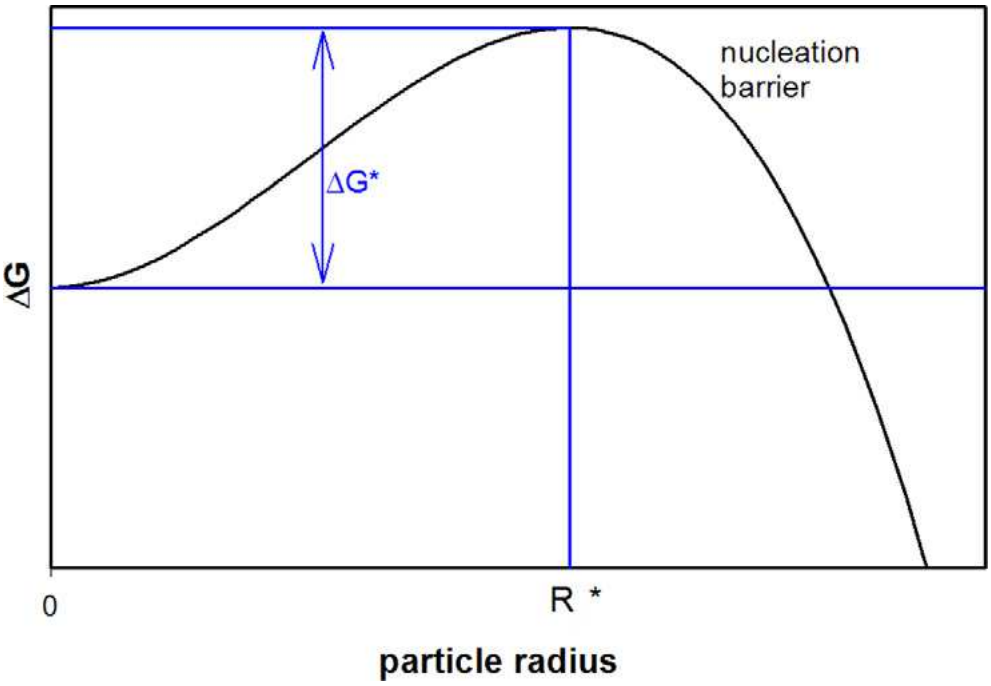

Figure 2.3: Thermodynamic representation of aerosol nucleation. A nucleation barrier of height Δ G* exists. The critical cluster size R* is defined by the maximum of the barrier. Figure from Curtius (2006).

The energy barrier and critical radius are shown graphically in figure 2.3. Studies (e.g. Lushnikov and Kulmala, 1995; Kulmala et al., 1998; Clement and Ford, 1999a,b) have demonstrated that at colder temperatures, such as in the TTL, the critical radius approaches molecular dimension and the energy barrier becomes smaller – this is ultimately due to the saturation vapour pressure decreasing with temperature.

The uncertainty in understanding nucleation processes has led to many differing aerosol concentrations being detected in the UT/LS and varying explanations for their origin. Several observations in the free troposphere showed that new particle formation can be activated by convection (De Reus et al., 1998, 2000; Clement et al., 2002; Twohy et al., 2002; Lee et al., 2004; Kulmala et al., 2006b), due to the uplifting of large concentraions of SO_2 and SO_2 precursors from the PBL up to the UT/LS. Agreeing with the importance of convection, Young et al. (2007) also state that further nucleation can be activated in the lower stratosphere when a tropopause folds occur, allowing air mixing. The numbers detected are somewhat lower than those detected by other studies (Twohy et al. (2002), for

example), particularly those in the TTL; average N_{4-9} concentrations were 460 to 490 cm^{-3} and N_{4-2000} were 620 - 730 cm^{-3}. In the enhanced particle production tropopause fold regions there were 700 to 3960 cm^{-3} N_{4-9} particles and 1000 to 3990 cm^{-3} N_{4-2000} particles (all non-STP) – emphasizing the importance of mixing of air with differing humidities, particle and gas loading for aerosol nucleation.

The question of whether short or long-range influences effect the local tropopause composition is still uncertain. In the Froyd et al. (2009) study there were seen to be many influences on the aerosol population throughout the troposphere and lower stratosphere. It was seen that there were both long-range and short-range chemical signatures in the aerosol composition and an overall external mixture throughout the troposphere. The aerosol properties in the tropics were defined by their source and ultimately the tropical dynamics. With higher organic content coming from continental sources, in particular trajectories that crossed the Amazon, more sulphate dominated aerosol from maritime convection and industrial plumes, and biomass from rural/jungle areas, it is apparent that there are many varied sources that can affect the tropical troposphere composition. Transit times from convective systems were $\sim$ 5 to 10 days, indicating that lofted material spent several days in the free troposphere without further boundary layer influence. Froyd et al. (2009) also reached the same conclusion concerning the origin of fresh regions of ultrafine particle: that maritime convection in remote regions promotes new particle formation in the upper troposphere from convective lofting of aerosol precursors. Continental convection was seen to inject aerosol and precursor gases into the TTL and even into the lower stratosphere – a significant motivation for the ACTIVE campaign. Despite the sporadic and localized nature of convection, the TTL residence time is considerably higher than the lower troposphere and for zonal transport. A final conclusion is that intense convection can seed the TTL and LS with primary aerosols and secondary aerosol material (precursor gases, SO_2, DMS, organics, etc.) The long residency times, nucleation and gas-phase accumulation in the TTL act to decouple the aerosols' characteristics from its sources.

Heyes et al. (2009) also found long-range transport was more influential for background TTL composition than local convective input during ACTIVE. Using

ozone data and back trajectory analysis, it was shown that the high variability in TTL ozone concentrations, except during active monsoon conditions, was due to variability in the origin of long-range sources. High ozone concentrations were advected from Indonesia and Asia whilst much lower concentrations typically came from the remote Pacific; the advection was generally found to ascend the 500 hPa level $\sim$ 5 days before in situ measurements took place around Darwin – the air would be mostly unchanged during this upper tropospheric transport. Overall, it was concluded that the TTL over Darwin was governed by the composition of the wider Tropical Warm Pool (TWP) region rather than just local boundary layer injection through convection. On the other hand, there were clear signs of local boundary layer input into the TTL, when vigorous convection is in the vicinity; the anvils and cloud outflows from these regular storms did contain signature CO boundary layer ratios. This paper supports the idea that the tropical tropopause layer is influenced by many varied sources across a wide hemispheric range. Similar conclusions were reached in Mari et al. (2000): there was found to be low concentrations of PBL gas in convective outflows. A 'ladder' effect was envisaged as air was entrained and detrained at different levels and phases of the clouds growth, in effect, air was entrained from throughout the free troposphere.

In summary it can be seen that there has been direct detection of high numbers of aerosols in the troposphere and particularly in the UT/TTL; for aerosols greater than 7 nm diameter there are found concentrations of the order 10^3 to 10^4 cm^{-3}. These high concentrations were typically found in cloud-free areas but in air that had recently been affected by convective activity. This activity had been seen, in numerous campaigns, to loft high concentrations of known precursor gases (such as, SO_2) into the UT/TTL. It is still unknown what gases play a role in aerosol nucleation, what exact mechanism is involved and what are the threshold conditions required for nucleation; the survivability of aerosols formed in the PBL and transported through convection is also not fully known. There seems to be a consensus on the importance of clean air with low preexisting aerosol loading, high humidity, and precursor gases where nucleation occurs. Cloud particles are also generally seen to be inhibitive for aerosol generation but some studies (e.g. Kulmala et al., 2006b; Kazil et al., 2007) propose that small 'seed' nuclei (insoluble organics) could exist interstitially in cloud and then become activated in the cold TTL after detraining from cloud. This thesis aims to increase the dataset

and knowledge of TTL aerosol population and generation.

2.3 Aerosol nucleation and growth

2.3.1 Basics of Nucleation

Nucleation is the production of particles, of the order of a few nanometers, from the binding of free-molecular gases (Curtius, 2006). Aerosols are often emitted as primary sources (e.g. direct aerosol production, from industrial combustion); when gases are emitted into the environment, by anthropogenic or natural means, they can become 'processed' (reactions) by the environment and can then develop into compounds ideally suited to aerosol nucleation. When involved in the nucleation process, gases are referred to as 'precursor' and the aerosols are considered secondary source. An aerosol particle is initially formed as a stable nucleus; it can vary in size and composition depending on the environment and vapour concentrations present. Gases that are thought to be major precursors include: H_2SO_4 which is often formed from dimethyl sulphide (DMS) and sulphur dioxide (SO_2). Ammonia is a very soluble, reactive and condensable gas that has many global sources – e.g. agricultural fertilisers, microbial action and plant processes. Ammonia and its related compound, ammonium (NH_4^+), also play an important role in aerosol and cloud processing (e.g. Napari et al., 2002b). Many other atmospheric compounds (e.g. organics) are considered as possible nucleation precursors, either as a nuclei themselves or through their interaction with other inorganic/organic compounds (e.g. Alfarra et al., 2006; Laaksonen et al., 2008b).

DMS, which is often released in coastal and marine environments (e.g. Davis et al., 1998, 1999; O'Dowd et al., 2007) and SO_2, which has both natural (e.g. volcanoes, DMS) and anthropogenic (e.g. industrial burning of fossil fuels) sources, can be oxidised to sulphuric acid (H_2SO_4) which is believed to be a major precursor of homogeneous (meaning direct from gas-phase with no surface interactions) binary nucleation (Viisanen et al., 1997; Hellmuth, 2006). The chemistry, reactivity and water affinity of the gases are of prime importance when considering their

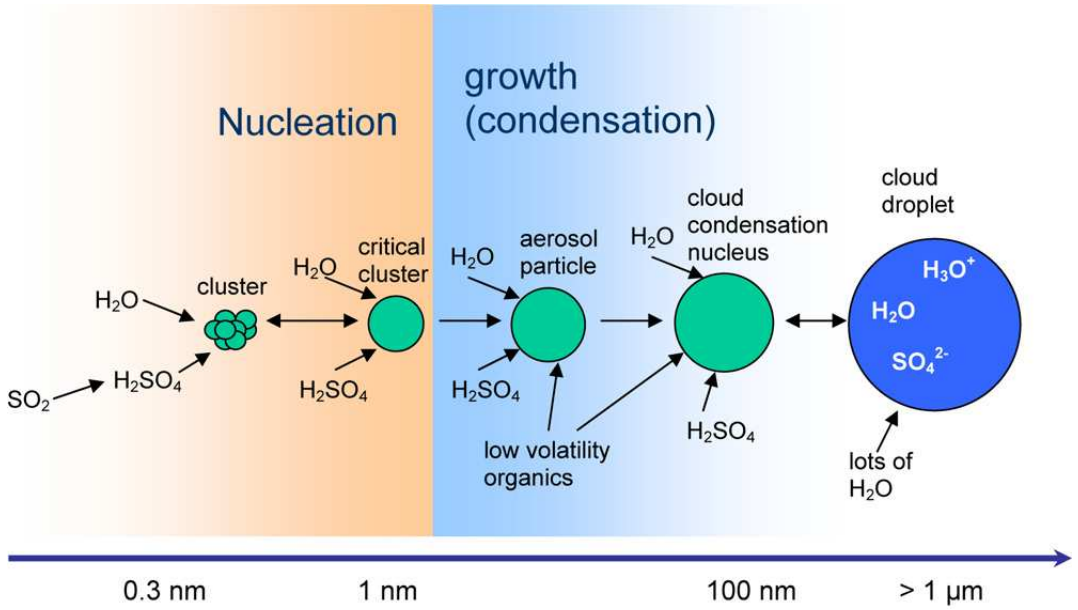

Figure 2.4: Schematic of aerosol nucleation and growth. Figure from Curtius (2006).

suitability for particle production. Because of the many potential sources and the complexity of the chemistry, aerosol nucleation is still not fully understood. Theoretically, many models describe the nucleus using macroscopic concepts such as density and surface tension, rather than a more laborious but accurate quantum chemistry model. These uncertainties manifest themselves in the aerosol number concentration and composition in theoretical models. The dominant nucleation processes are debated in the current literature, with 4 major mechanisms all competing; these are: binary, ternary, ion recombination (Wilhelm et al., 2004; Sorokin et al., 2006; Sorokin and Arnold, 2007) and organic compounds (Kulmala et al., 2006b). Furthermore, the last 2 models are thought to interact with the binary and ternary mechanisms and aid or hinder the production and growth of particles. Once a nucleus is formed, growth can ensue via condensation and coagulation (Kulmala et al., 2004, 2006a).

2.3.2 Binary Nucleation

In the binary hypothesis, sulphuric acid and water, H_2O-H_2SO_4, form molecular clusters that are sufficiently energetically stable (critically sized cluster) for continuous vapour deposition to occur (Viisanen et al., 1997; Laaksonen et al.,

2000; Arnold et al., 2006); this growth will continue into detectable aerosol size ranges ($\sim$ 3 nm), provided there is an adequate supply of condensable material (Clement et al., 2006; Boy et al., 2008; Iida et al., 2008). Some studies have determined a critical cluster size: Curtius (2006) concluded, from experimental derived parameterisations, that $\sim$ 8 sulphuric acid molecules are needed to reach the critical number, for typical boundary layer temperatures and pressures (293K, 1013 hPa).

In the case of TTL nucleation, the low temperature and low saturation vapour pressure of sulphuric acid make for ideal nucleation conditions – nucleation is considered to be barrierless (a stable monomer nuclei) (Kulmala et al., 1998; Clement and Ford, 1999b; Clement et al., 2002; Curtius et al., 2001), with a production rate only 10 times less than the classical binary collision rate (Kulmala et al., 1998).

Sulphuric acid is typically produced by the oxidation of SO_2(e.g. Clement and Ford, 1999a,b; Clement et al., 2002; Twohy et al., 2002; Berglen et al., 2004). The following set of equations show the possible pathway for H_2SO_4 production in the UT/TTL. Ozone and NO_x compounds are very important components in the chemical cycle of the UT/TTL and they play an vital role in H_2SO_4 production, as seen in the reaction equations.

$$SO_2 + OH + M \rightarrow HOSO_2 + M, \qquad k_{SO_2}{}^* \simeq 7.848 \times 10^{-13} \qquad (2.3)$$

for average oxygen and nitrogen (air [M]) molecular concentrations at P = 200 hPa

$$HOSO_2 + O_2 \rightarrow HO_2 + SO_3, \qquad k_{HOSO_2}{}^* = 1.3 \times 10^{-12} e^{-\frac{300}{T}} \qquad (2.4)$$

$k_{HOSO_2} = 3.37 \times 10^{-13}$, for T = 222 K

$$SO_3 + 2H_2O \rightarrow H_2SO_4 + H_2O, \qquad k_{SO_3}{}^* = 8.5 \times 10^{-41} e^{\frac{6540}{T}} [H_2O]^2 \qquad (2.5)$$

$$k_{SO_3} \simeq 21 s^{-1}$$

, for T = 222 K and 2×10^{14} cm^{-3} of H_2O

where the second H_2O molecule acts by association. This reaction is very dependent on the moisture in the atmosphere, which is usually low in the UT and LS (lower stratosphere), unless there is an uplifting mechanism such as convection. Deep convective thunderstorms can provide localised areas of high relative humidity that can promote chemical reactions in the UT/LS (Wang and Prinn, 2000).

* References for rate constants: 2.3, 2.4 and 2.5 – Atkinson et al. (1989); Pirjola and Kulmala (1998); 2.6 – Bahe et al. (1979); 2.7 – Atkinson et al. (1992); Pirjola and Kulmala (1998). Rate coefficient (K) is s^{-1} for unimolecular reactions and cm^3 $molecule^{-1}$ s^{-1} for others.

$$O_3 + h\nu(\lambda < 320 \text{ nm}) \rightarrow O_2 + O(^1D), \qquad J_{O_3}{}^{\dagger} = \int_{\lambda_1}^{\lambda_2} \sigma(\lambda,T)\phi(\lambda,T)I(\lambda)\mathrm{d}\lambda \tag{2.6}$$

λ is wavelength, σ is cross-section,
ϕ is quantum yield
and I is Irradiance ($\mathrm{Js^{-1}m^{-2}Sr^{-1}Hz^{-1}}$)
$J_{O_3} \simeq 0.7 - 20 \times 10^{-6}\mathrm{s^{-1}}, \lambda = 306$ nm
depending on solar zenith angle, etc.

$$O(^1D) + H_2O \rightarrow 2OH, \qquad k_{O(^1D)}{}^{\dagger} = 1.63 \times 10^{-10} e^{\frac{60}{T}} \tag{2.7}$$

$$k_{O(^1D)} = 2.1358 \times 10^{-10}, \text{ for T} = 222 \text{ K}$$

The production of OH radicals via this primary route mechanism (equations 2.6 and 2.7) is dependent on the degree of photodissociation by daytime solar radiation – which in the TTL is invariably high – and the moisture content.

This was theoretically considered the primary route to the hydroxy radical, OH, (Levy, 1971) but in the past 15 years HO_x (OH and peroxy, HO_2) detection has been possible. Three campaigns in the 1990s were amongst the first to detect OH in situ in the UT and TTL: STRAT, SUCCESS and SONEX (Jaeglé et al., 2001). The data revealed that concentrations were up to 4 times higher than that expected solely from ozone dissociation; a 24 hour average gave values of 1.6, 5.2, 0.95 pptv, respectively for the three campaigns. This suggested that the UT was more photochemically active than previously thought (Jaeglé et al., 2001) and that there was a more important role for ozone, due to anthropogenic emissions of nitrogen oxides ($NO_x = NO$ and NO_2) and various hydrocarbons such as acetone (Jaeglé et al., 2001), which increased the overall OH production rate. An increased ozone, and OH, production rate would also increase the oxidation

† References for rate constants: 2.3, 2.4 and 2.5 – Atkinson et al. (1989); Pirjola and Kulmala (1998); 2.6 – Bahe et al. (1979); 2.7 – Atkinson et al. (1992); Pirjola and Kulmala (1998). Rate coefficient (K) is $\mathrm{s^{-1}}$ for unimolecular reactions and $\mathrm{cm^3}$ $\mathrm{molecule^{-1}}$ $\mathrm{s^{-1}}$ for others.

rate of sulphur dioxide (SO_2), ultimately producing sulphuric acid (H_2SO_4 (g)), which is a major precursor of atmospheric aerosols (e.g. Russell et al., 1994; Viisanen et al., 1997; Laaksonen et al., 2000)

$$\mathrm{CO + OH + (\ O_2) \rightarrow CO_2 + HO_2}, \quad k_{CO-OH}{}^{\ddagger} = 2.4 \times 10^{-13} \tag{2.8}$$

$$\mathrm{HO_2 + NO \rightarrow OH + NO_2}, \qquad k_{HO_2-NO}{}^{\ddagger} = 3.7 \times 10^{-12} e^{\frac{240}{T}} \tag{2.9}$$
$$k_{HO_2-NO} = 1.09 \times 10^{-11}, \text{ for T} = 222 \text{ K}$$

$$\mathrm{NO_2 + h\nu(\lambda < 410\ nm) + (O_2) \rightarrow NO + O_3}, \qquad k_{NO_2}{}^{\ddagger} \simeq 9 - 30\mathrm{s}^{-1} \tag{2.10}$$
depending on solar zenith angle

NO_x (e.g. Pirjola and Kulmala, 1998; Wang and Prinn, 2000; Jaeglé et al., 2001) has anthropogenic and natural sources (e.g. soil and plants). Lightning NO_x (Huntrieser et al., 2002; Labrador et al., 2004), from thunderstorms, is one of most important source of NO_x in the free troposphere; it can be produced in the high altitude columns of cumulonimbus and can thus influence the chemistry of the UT. However, its global annual production rate has not been precisely defined and the uncertainty in this measurement affects the accuracy of tropospheric chemistry models. Furthermore, there is also evidence that NO_x can be transported throughout the TTL with lifetimes up to 5 days when widespread convection (typical in monsoon conditions) is present (Labrador et al., 2009). NO_x interacts with and acts as a precursor for ozone, O_3; therefore an increased concentration of NO_x should theoretically produce an increase in O_3 through photochemical reactions [see Atkinson and Lloyd (1984); Atkinson et al. (1984, 1986, 1989, 1990, 1992) and Simpson (1992) for a full list of reactions and rate constants; or Pirjola and Kulmala (1998) for a summary]. Equations 2.8, 2.9 and

‡ References for rate constants: 2.8 and 2.9 – Atkinson et al. (1992); Pirjola and Kulmala (1998); 2.10 – Seinfeld (1986). Rate coefficient (K) is s^{-1} for unimolecular reactions and cm^3 $molecule^{-1}$ s^{-1} for others.

2.10 show the reactions involving NO_x that lead to the production of ozone; note that the OH radical is not lost (shown in equation 2.9), therefore conserving the OH reservoir and its role in sulphuric acid formation (equation 2.5).

Aqueous phase chemistry is important in warm clouds and significant chemical reactions take place in cloud particles. In particular, SO_2 oxidation can take place with hydrogen peroxide (H_2O_2) in aqueous phase (Jaeglé et al., 2001; Berglen et al., 2004). This cloud processing is considered a significant mechanism for chemical reactions and aerosol processing. This has been seen in the Marine Boundary Layer (MBL) when cloud evaporates (Coe et al., 2000). Scavenging of trace gases was modelled by Mari et al. (2000); the study found that although trace gases, such as SO_2, H_2O_2 and HNO_3, were efficiently scavenged in warm (low level) clouds, glaciated cloud often released H_2O_2 due to low retention efficiency of ice. This was used to explain why some trace gases, such as HNO_3, were depleted in convective outflow and others, such as H_2O_2, were enhanced. Mari et al. (2000) showed that the scavenging of trace gases in convective cloud is dependent on temperature of the cloud, cloud phase and maturity, the chemical species involved and the concentrations uplifted and entrained in the cloud. Ultimately there is a complex relationship between the amount of trace gas in the PBL and free troposphere and the amount outgassed in the convective outflow. Entrainment and detrainment were seen to be very important in the lifecycle of trace gases; very little PBL gas reached the UT due to low level (warm cloud) detrainment (also, Heyes et al., 2009). High level (glaciated cloud) entrainment was also an important factor that effected the concentration at outflow. Instead, Mari et al. (2000) propose a ladder effect where midlevel outflow during the convective growing phase is re-entrained into the convective plume as the cloud glaciates and matures. Therefore outflow gases may have both local and long-range origins (also, Heyes et al., 2009), as they are entrained from all levels of the free troposphere.

The rate of nucleation has been formulated with theory and parametrization. It is believed that in certain conditions, in the cold UT/TTL for example, that a kinetic regime exists whereby single sulphuric acid molecules are sufficiently stable to act as nucleation nuclei (Kulmala et al., 2006a; Sihto et al., 2006; Boy et al.,

2008); this is a form of barrierless activation that yields a nucleation rate that is proportional to the square of the vapour concentration $[H_2SO_4]^2$. The alternative to the kinetic regime is the activation regime (Kulmala et al., 2006a; Sihto et al., 2006; Boy et al., 2008). In this mechanism, stable molecular clusters exist that contain one sulphuric acid molecule; the 'activation' can occur through heterogenous chemical reactions, for example. The presence of a single sulphuric acid molecule means that there is a linear dependence to the nucleation rate (J): $J \propto [H_2SO_4]$. This is thought to be more relevant to the PBL where higher temperatures require stable clusters to form before aerosol 'activation' can occur. The observations show power-law dependencies with an exponent, n, ($J \propto [H_2SO_4]^n$) somewhere between 1 and 2 (Kulmala et al., 2006a; Riipinen et al., 2007). Close correlations between H_2SO_4 and nucleation mode particles (size range: 3 to 6 nm) were also found during QUEST (Hyytiälä, Finland, March-April 2003 and Heidelberg, Germany, March-April 2004). The percentage contribution of sulphuric acid to particle growth, in these two PBL locations, was below 10% and to initial growth, below 20% (Fiedler et al., 2005). Furthermore, the growth rate from 1 nm to a detectable 3 nm was inferred by the time lag between H_2SO_4 concentration plots and the 3 nm concentration curve. The time lag was 20 minutes and 100 minutes for Riipinen et al. (2007) and Fiedler et al. (2005), respectively, giving a growth rates of 6 and 1.2 nm h^{-1} for the initial nuclei growth (in PBL, forested, conditions).

The binary scheme is based on classical theory with the sulphate aerosols treated as liquid droplets. Vehkamäki et al. (2002) recently developed parameterised equations for the sulphuric acid-water nucleation under atmospheric conditions, in which nucleation was a function of the surface tension, density of the solution and equilibrium vapour pressures of both sulphuric acid and water above the solution. This parameterisation is a revision of the initial work of Kulmala et al. (1995), Kulmala et al. (1998) and Viisanen et al. (1997); it corrected the activity coefficients and errors made in the kinetic assumptions in the previous parameterisation. However, the original theoretical framework was formulated by Wilemski (1984). The new parameterisation of the nucleation rate was shown to be in good agreement with theoretical rates for the temperatures between 230 and 300 K, relative humidities (RH) between 0.01% and 100% and for total sulphuric acid concentrations between 10^4 and 10^{11} cm^{-3}. However, the parameterisation

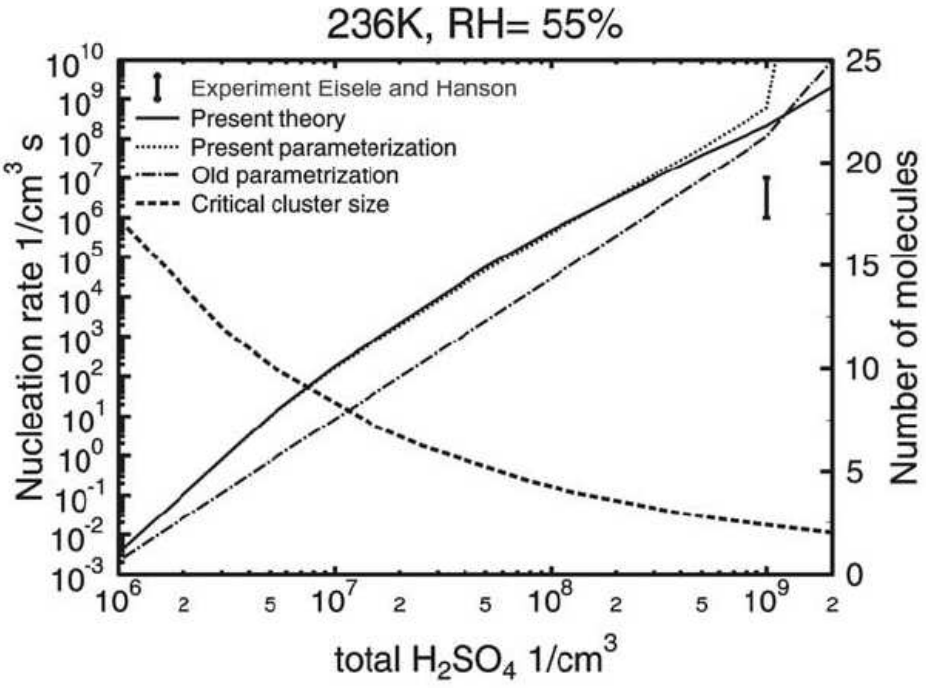

Figure 2.5: Nucleation rates as a function of sulphuric acid concentrations, at 236 K and 55% humidity. The experimental data are from Eisele and Hanson (2000) and the old parameterisation is based on Kulmala et al. (1998). The theoretical size of the critical cluster is also shown. Figure and data from Vehkamäki et al. (2002).

was limited by the number of molecules in the critical cluster: if it exceeded 25 there was poor agreement between the complete theoretical model and the parameterised values.

One of the main problems with binary theory is the discrepancy between observed concentrations of condensable vapour (H_2SO_4) and the theoretical threshold for nucleation to begin. In some cases atmospheric nucleation occurs at H_2SO_4 concentrations 2 - 4 orders of magnitude lower than the binary nucleation rate would suggest (Laaksonen et al., 2008a). In the PBL it represents a major obstacle to the satisfactory explanation of nucleation. In the PBL temperatures are typically above 250 K, at this temperature stable nuclei are believed to require a significant number of sulphuric acid molecules (8 according to Curtius (2006)). The most popular explanation is that a third compound is involved such as ammonia (see ternary nucleation) but recent research (Berndt et al., 2005; Laaksonen et al.,

2008a) has suggested that the formation of free radicals, HSO_5, in pace with H_2SO_4, during SO_2 oxidation can provide a stabilising effect on the nuclei. The theory proposes that the HSO_5 reacts with an, as yet unspecified, atmospheric species that then provide heterogeneous sites for H_2SO_4 nucleation and vapour growth. In the case of the UT/TTL, the temperatures are considered too low for HSO_5 radicals to form in sufficient numbers to interfere with H_2SO_4 nucleation.

2.3.3 Ternary Nucleation

It has been found in certain circumstances that nucleation rates have been much higher than that predicted by a binary mechanism. This suggested the role of a third component (Napari et al., 2002b,c); the obvious candidate is ammonia. Ammonia is one of the most abundant tropospheric compounds; it also has the property of lowering the vapour pressure of H_2SO_4 above the solution surface (H_2O-H_2SO_4-NH_3). Laboratory work and modelling (Napari et al., 2002b,c) have suggested that ternary nucleation could increase the homogeneous nucleation rate by several orders of magnitude compared to binary. Merikanto et al. (2007) used a more up-to-date parameterisation to produce lower nucleation rates that match more closely the observed values: at UT temperatures their parameterisation produced 10^6 to 10^7 cm^{-3} s^{-1}. Napari et al. (2002a) tested a hypothesis whereby H_2SO_4 was replaced by other inorganic acids in the ternary process: nitric acid, hydrochloric acid, methane sulfonic acid. The study found that the replacement acids yield nucleation rates only marginally higher than that for binary nucleation and H_2O-H_2SO_4-NH_3 ternary reactions still presented the most likely mechanism for quick nucleation. Furthermore, sensitivity analysis of the parameters showed that a varying NH_3 mixing ratio, above 100 pptv, had no significant effect on the nucleation rate except at very low sulphuric acid concentrations (Holmes, 2007). The parameterised model was found to fit between the limits of the full models calculations but was limited in the low ammonia regime because the mole fraction of the critical cluster changes rapidly, causing the classical theory to fail.

The ternary process is a mechanism that is applied more often to the boundary layer; this is due to the fact that ammonia is mainly emitted from agriculture

processes, fertilisers, plant and microbial action.

Like binary theory, the ternary mechanism has shown discrepancies when compared to observation. Standard H_2O-H_2SO_4-NH_3 cluster formation is predicted to produce orders, or even tens of orders, of magnitude higher nucleation rates than that typically seen in the environment for given vapour concentrations. The ternary theory, in some conditions, predicted that cluster formation would even surpass that of kinetic collision rate, which is obviously impossible. Therefore, ternary nucleation theory, as it stands, cannot be a complete explanation for all situations, particularly in the relatively high temperatures of the PBL. Anttila et al. (2005) noticed that the original theory (Napari et al., 2002b,c) neglected the formation of ammonium bisulphate compounds, which have a similar effect to hydrate formation, in that ammonium bisulphate and hydrate clusters have a smaller nucleation potential than free sulphuric acid. This adapted ternary nucleation mechanism produces nucleation rates orders of magnitude lower than traditional ternary predicts and in greater agreement with the available observations.

Due to its high solubility, ammonia based ternary nucleation is not expected to be particulary relevant in the TTL (Barth et al., 2001). Most of the ammonia would have been absorbed into cloud droplets and then washed out during precipitation. Therefore, a pathway that involves binary nucleation, with the possible assistance of ions (Yu and Turco, 2001; Laakso et al., 2002, 2003, 2007) and/or organic compounds (Kulmala et al., 2006b; Sihto et al., 2006), is expected to dominate in the TTL.

2.3.4 Aerosol Nucleation in the TTL

Kulmala et al. (2006b) and Sihto et al. (2006) propose a hypothesis that aerosol is produced in cloud by water insoluble trace gases. The reduced levels of sulphuric acid inside clouds (due to cloud particle uptake) would greatly inhibit the role of binary, ternary and ion nucleation. With typical SO_2 concentrations of the order of 10^8 - 10^{10} cm^{-3} out of cloud, an in cloud concentration would be 10^2

- 10^5 cm^{-3}, due to the SO_2 sink in/on cloud particles. In most current binary nucleation theories, this is taken to be far too low for nucleation to occur inside cloud. This does not however curtail sulphuric acid production and aerosol nucleation in outflow regions of convection when unscavenged SO_2 survives in-cloud transport and is then outgassed into the TTL. The insoluble compounds would have a saturation ratio 1 or 2 orders of magnitude higher in the upper troposphere compared to the boundary layer, due to cooling of 50 - 60 K. Major candidates for this role are water insoluble organic compounds [possible candidates were not identified in the study]. Organics may survive the transport process within the cloud or they may help contribute to the growth rate once the molecular clusters form (Kulmala et al., 2006b; Henson, 2007). Sorjamaa and Laaksonen (2007) proposed a new theoretical framework in which the traditional Köhler theory, which is based on soluble or partially soluble compounds, is extended to include a term for insoluble species. The growth and activation of such particles was described by substituting the solute effect in Köhler theory by a term that can be obtained from any multilayer adsorption model. With this revision, and under certain conditions, activation could be achieved for insoluble 100 nm particles – ultimately this work provides some theoretical basis for the insoluble particle hypothesis. The survival of the water insoluble gases and aerosols, in the cloud, would allow the formation of small clusters that are not significantly scavenged by the cloud particles. Once the the particles are in cloud-free air, any sulphuric acid, can begin to nucleate into aerosol particles. But in this hypothesis there is the added influence of the surviving water insoluble clusters that can be used as nuclei upon which the sulphuric acid and water molecules are able to condense. Lee et al. (2004) also found high levels (up to 3000 cm^{-3}) of ultrafine (3 - 9 nm) particles existing interstitially within cirrus cloud. Kulmala et al. (2006b) ultimately conclude that there is some alternative mechanism to H_2O/H_2SO_4 binary nucleation occurring in the UT/TTL that works either solely to nucleate aerosols or enhances the binary process. Furthermore, high aerosol concentrations near convective cloud outflow show very short particle production timescales; these timescales are expected to be too short for SO_2 oxidation to H_2SO_4, in sufficient quantities – strongly supporting their hypothesis.

2.4 Modelling of Aerosol nucleation and growth

Modelling simulations have been used to gain an insight into the process of aerosol nucleation (Clement et al., 2006; Boy et al., 2008; Iida et al., 2008). These simulations provide a way of testing hypotheses and determining controlling parameters. The limited number of precise, in-situ observations of aerosol nucleation and growth, in the TTL, has meant that computer models have proven a convenient method for testing theories. The difficulty in location and instrument detection limitations has meant that there is still a lot of uncertainty concerning aerosol production. The role of other species, such as organics, is still not fully known nor is the relative importance of the acid concentration, SO_2 and OH concentrations (Boy et al., 2008) and the condensational sinks (preexisting aerosol). The sensitivity of nucleation growth rates to the change in a given parameter can be simulated in models. A number of important controlling factors have been found in these studies. For instance, the preference of nucleation to occur in 'clean' (low preexisting aerosol population) environments rather than polluted. Other important factors include the acid production rate (from SO_2 oxidation) and the growth rate of the newly formed particles: as the aerosol particles become large enough they begin to compete for condensable vapour and thus inhibit further nucleation (Clement et al. 2006).

Clement et al. (2006) looked, analytically and numerically, at the rate of nucleation and its controlling factors. The model was set up to show a transition in acid production – via SO_2 and OH radicals – throughout the day. The OH production maximum occurred at midday, when the photodissociation of ozone to OH is greatest, and the production was halted at nighttime (7 hours in their simulation). This was parameterised as a maximum H_2SO_4 production rate of 10^5 $cm^{-3}s^{-1}$ from an estimated SO_2 concentration of 1 ppb. Their analysis showed that after 21 minutes a nucleation mode ($\sim$ 3 nm) burst appeared. After 1 hour, a 'shoulder' appeared in the size distribution as condensational growth continued on the nucleated particles and coagulation occurred (see figure 2.6). The nucleation peak remains large as long as acid production remains high. The simulations by Clement et al. (2006) showed that levels of aerosol produced (see figure 2.6) were typically 10^3 - 10^4 cm^{-3}, for sizes above 20 nm; the total aerosol concentration (sized over 3 nm) was between 10^4 - 10^6 cm^{-3} - this was from a

H_2SO_4 production rate of 10^5 $cm^{-3}s^{-1}$. The final number of aerosol produced is found to be independent of the initial number of nucleated particles and is related more to the acid production rate. This production will only occur in the daylight; beyond this, the nucleation mode aerosol will coagulate into the larger size ranges and the remaining acid will condense onto aerosol particles. Clement et al. (2006) suggest that the nucleation events will be cut-off when the background aerosol concentration is above a certain value. This will be lower for low SO_2 and acid source rates and higher for high SO_2 and acid concentrations. This is logical, due to the high solubility of the acid sources: aerosols and cloud droplets will scavenge the trace gases as they grow. Therefore, evaporating cloud regions of the storm outflow would be the best areas for nucleation to occur. The release of trace gases and the cleansing of the air (reduced background aerosol content) would provide ideal conditions for aerosol production from H_2SO_4/H_2O clusters. The Aitken mode aerosol (typically defined as 10 to 100 nm size range) is expected to grow more efficiently into the accumulation mode (100 to 1000 nm) by coagulation rather than H_2SO_4-H_2O condensation alone (Ekman et al., 2004) - this is a result of the surface tension (Kelvin effect) reducing condensation for smaller radii particles.

The growth rates of nucleated aerosol, during simulation, are typically 1 - 3 nm h^{-1} (Boy et al., 2008; Nishita et al., 2008). Boy et al. (2008) is more specific and defines a growth rate of 3.96 nm h^{-1}, for particles between 1 and 15 nm; for particles greater than 15 nm, the growth rate dropped slightly to 3.02 nm h^{-1}. Boy et al. (2008) also found that sulphuric acid contributed 5 - 25%, by number, to the growth of nucleation mode aerosol (3 - 20 nm); this contribution dropped as the particle grew into the Aitken mode (10 - 100 nm). Up to 3 nm, however, there is expected to be a 10 - 35%, by molecular number, dependence on sulphuric acid deposition for growth of sulphuric acid molecules in the formation of energetically stable clusters. The percentage of water molecules to acid in the aerosol nuclei is determined by the relative humidity and relative acidity in the atmosphere (Jaecker-voirol and Mirabel, 1988; Kulmala et al., 1998).

Ion-ion recombination (Laakso et al., 2002, 2003, 2007) or ion mediated nucleation (Yu and Turco, 2000), is expected to play a significant role in nucleation, especially as cosmic rays are more penetrative into the lower stratosphere/upper

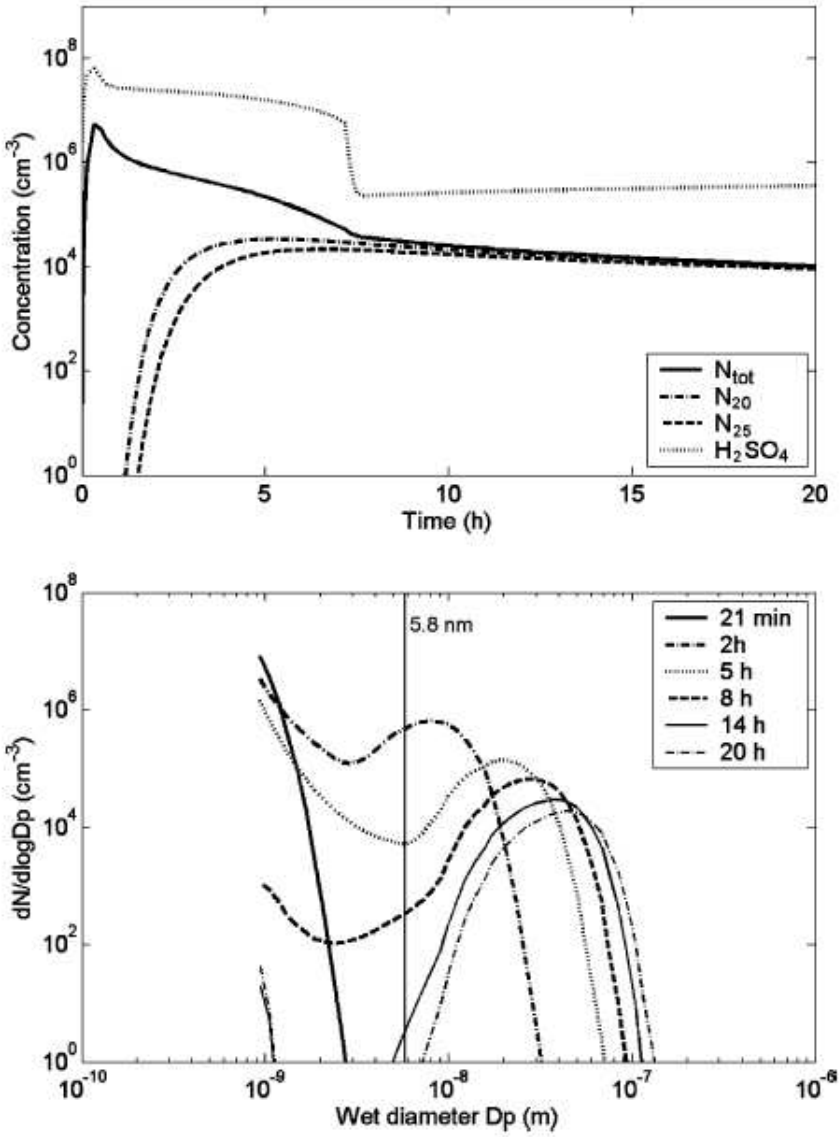

Figure 2.6: Numerical calculations of size distribution with time. Figure from Clement et al. (2006).

troposphere than the lower troposphere and PBL (Kazil et al., 2006). The number of nucleation particles ($\sim$ 3nm) produced are expected to increase in the case of an ion-assisted mechanism; Laakso et al. (2003) also found a growth rate of $\sim$ 1 nm h^{-1}, for 3 nm nucleated particles.

Chapter 3

Binary nucleation: theory and modelling

As mentioned previously, nucleation is the production of particle clusters from gas phase precursors. For nucleation to occur an energetically stable 'embryo' must form, upon which further gas phase particles can bind – condensation, in macroscopic language. Herein lies one of the great problems of current nucleation models: whether to treat nucleation with a more accurate but computationally intensive quantum chemistry theory or use macroscopic concepts, such as density and surface tension to simplify the numerical calculations. The basis of most nucleation models involves a thorough analysis of gas-to-particle thermodynamics and in particular the Gibbs free energy parameter, for a mixed vapour-liquid phase population. The benefit of Gibbs free energy analysis is that the main variables, pressure and temperature, are readily measurable. This macroscopic treatment was used in this analysis and is discussed in section 3.2. The Gibbs free energy method has been used with some accuracy to replicate experimental and analytical work (e.g. Wilemski, 1984; Jaecker-voirol et al., 1987; Jaecker-voirol and Mirabel, 1988; Kulmala et al., 1998; Clement et al., 2006) and was therefore chosen as a reasonably accurate and timesaving numerical model for use in this study.

The conceptual model applied in this study encompassed a compartmentalised system whereby nucleation, nucleation rate, condensation and coagulation were

all treated in discrete modelling blocks: operational splitting of tasks. The simulation was simplified to a box-model (1D) that ignored wind shear, turbulence, mixing and any other type of translational motion in the air mass – the outflow was assumed to be in freestream laminar flow in the UT/TTL. Therefore, a Brownian motion scheme was chosen to simulate the effect of diffusional coagulation in the box-model (chap.11, Pruppacher and Klett, 1997). The calculation of the critical nucleus size and nucleation rate are typically some of the most computationally intensive components of an aerosol model. This model therefore made use of a number of parameterisations (Kulmala et al., 1998) for the nuclei modelling section. Condensational growth was represented by standard vapour-liquid interface theory, embodied in the Köhler equation; this equation combines the Kelvin effect (surface tension for droplets) and the Raoult term, which describes the vapour pressure of an ideal solution (Kulmala, 1993). This is dependent on the vapour pressure of each chemical component and the mole fraction of the components present in the solution; in this study there was a binary water-sulphuric acid mixture. Coagulation was modelled as Brownian diffusion, which is largely dependent on the cross-sectional areas of the two incident particles and their relative difference in area (chap.11, Pruppacher and Klett, 1997). These components were then integrated into a sectional size distribution: a set number of fixed size bins containing a fixed number of sulphuric acid molecules. This was different to other models that use a number of shifting log-normal distributions (usually 3 or 4 to model the nucleation, Aitken, accumulation and coarse modes). The system was evolved using an Eulerian forward differencing time step. The numerical methodology was programmed in Fortran 90 and the verbatim code can be viewed in appendix A.

First, the fundamentals of the model will be discussed, together with the chemical species that were incorporated.

3.1 Chemical species

The formulae that follow were used in the modelling study and are basic binary theory for nucleation and growth; a sectional model is used to describe the aerosol size distribution, based on the AEROFOR methodology (Pirjola and Kulmala, 1998). A number of size bins are used to divide the size distribution in to bins

of a set size width, each bin also has a set number of sulphuric acid molecules per particle (the model considers the dry radius only). To start with, the mass balance of a given chemical species, c_i, is:

$$\frac{\mathrm{d}c_i}{\mathrm{d}t} = p_i - l_i c_i + \frac{e_i}{h} - \frac{v_d c_i}{h}, \tag{3.1}$$

where c_i is the concentration of species i, p_i is the chemical production rate, $l_i c_i$ is the chemical loss rate, e_i is the direct emission rate, v_d is the deposition velocity and h is the height of the mixing layer as emissions and depletions are only relevant in the PBL (Pirjola and Kulmala, 1998). In the case of the nuclei precursor sulphuric acid (N_a is the number concentration), the mass balance equation is:

$$\frac{\mathrm{d}N_a}{\mathrm{d}t} = Q_a - n_a^* J - N_a \sum_{i=1}^{n_{class}} C_i N_i - \frac{v_d}{h} N_a, \tag{3.2}$$

where Q_a is the chemical net effect of production and loss in the gas phase. n_a^* is the number of sulphuric acid molecules in the critical cluster, C_i is the condensation rate of sulphuric acid onto particles in size class i and N_i is the total number concentration of particles in class i (Pirjola, 1999).

A kinetic rate equation for the production of H_2SO_4 is presented in Clement et al. (2002) and is used in the AEROFOR model for this study:

$$Q_a = 10^{-18}[OH][SO_2]\mathrm{cm}^{-3}\mathrm{s}^{-1}, \tag{3.3}$$

where [OH] = n(air)c(OH) and [SO_2] = n(air)c(SO_2), with the concentrations c being the observed mixing ratios. The rate coefficient is calculated by Clement et al. (2002) at a typical TTL temperature of 215 K.

The nucleation rate, J, as discussed already, is a complex concept to model; the simplest way is to treat it as a classical macroscopic problem rather than a detailed quantum chemistry model. Computation time is greatly reduced by using parameterisation for modelling nuclei and production rates (Wilemski, 1984; Jaecker-voirol and Mirabel, 1988; Kulmala et al., 1998). The parameterisation

by Vehkamäki et al. (2002), which built on previous works, has been shown to agree well with more detailed nucleation models, up to a point of 25 sulphuric acid molecules in the critical cluster – such large clusters are not expected to be necessary in the cold TTL environment for stability. The model is therefore based on the revised parameterisation work from (Wilemski, 1984) which is thermodynamically correct and takes into account the effect of hydrate formation (Jaecker-voirol et al., 1987). The critical cluster is also parameterised to save computational time; it is a function of temperature, relative humidity and relative acidity, as described in Kulmala et al. (1998).

3.2 Critical cluster parameterisation

Microscopically, for a cluster to form, there must initially be a binding of two molecules. The binding or sticking probability (Clement et al., 1996) is determined by the internal energy of the vapour mixture. The internal energy is the total energy (kinetic and potential) contained by a thermodynamic system. Kinetic energy encompasses the translational, rotational and vibrational energy of the molecules; potential energy is associated with the static constituents of matter, static forces (in lattice crystals, for example) and electromagnetic forces related to molecular 'sticking'. Electromagnetic intermolecular forces (such as electron cloud fluctuations: van der Waals force) are ultimately responsible for the binding of molecules into clusters. Two-body collisions between incident molecules in which energy and momentum are exchanged must result in molecular sticking rather than reflection, for the cluster to form; naturally, the thermal (kinetic) energy of the molecules plays an important role in this matter. If molecules do manage to bind, their bind energies are usual small and are still therefore susceptible to break-up due to thermal agitation. However, if a vapour is supersaturated there is an excess of gas-phase molecules with a resulting pressure increase caused by the high particle number density. This reduction in mean free path results in an increase in particle collisions and hence an increased likelihood of a successful binding occurring; this in effect reduces the pressure in the system and returns it to equilibrium. Furthermore, polar molecules (such as sulphuric acid, ammonia and water) have an increased possibility of successfully binding

due to the presences of opposing charges on the 'poles' of a single molecule. Polar charges are a result of electron cloud disturbance caused by nuclear force effects in the molecule; typically a larger nucleus, such as an oxygen nucleus in a water molecule, attract electrons more strongly (higher electronegativity) than the two hydrogen nuclei. This produces a distinct polar effect, where the oxygen atom appears to have a slight negative charge and the two hydrogens have a resulting positive charge.

The molecular model is macroscopically and theoretically described using the statistical thermodynamic concept of Gibbs free energy for fluctuating particle populations (see for example, chapter 7, Pruppacher and Klett (1997)). With temperature and pressure fixed, a closed thermodynamic system will be in equilibrium when the Gibbs free energy is minimal. If a substance is supersaturated in the gas phase and far away from any other surfaces on which the gas-phase molecules could condense on, the system is metastable and the vapour molecules would generally prefer to undergo a phase transition to the condensed phase as a lower value of G (Gibbs free energy) could be obtained due to the lower chemical potential of the bulk liquid. In the case of water and sulphuric acid the Gibbs free energy is given by:

$$\Delta G = n_w \Delta\mu_w + n_a \Delta\mu_a + A\sigma, \tag{3.4}$$

where ΔG is the change in Gibbs free energy when n_w molecules of species w and n_a molecules of species a shift from vapour to liquid phase. $\Delta\mu_w$ and $\Delta\mu_a$ are the differences in the chemical potential for a water and acid phase change from vapour to liquid; A and σ denote the surface area and the surface tension of the droplet (see Wilemski (1984) and Kulmala et al. (1998) for a more thorough derivation). Graphically, Δ G, for a single species, is shown by figure 2.3. The figure clearly shows that for the aerosol embryo to become stable, a critical radius must be reached; this is dependant on the thermodynamic properties of the closed system. However, for the binary mixture considered here, the critical nucleus is found by locating the three-dimensional saddle point on the ΔG, n_w and n_a surface, that is, setting $(\mathrm{d}\Delta G/\mathrm{d}\ n_i)_{n_j} = 0$ – this is equivalent to the R* point in figure 2.3 (if the system contained only a single species [2D]). Note that technically $n_i = n_{il} + n_{is}$, where n_{il} is the number of molecules of species i that are within the surface of tension and n_{is} is the surface excess number of molecules that corrects

for the difference between the density profiles of our uniform droplet model and the actual cluster. Continuing with the derivation of saddle point and hence the critical radius,

$$(d\Delta G/dn_i)_{n_j} = \left(\Delta\mu_i + \sigma\frac{\partial A}{\partial n_i}\right) dn_i + n_i d\mu_{il} + n_j d\mu_{jl} + A d\sigma = 0. \tag{3.5}$$

Using the Gibbs-Duhem relation (Kulmala et al., 1998),

$$n_{il} d\mu_{il} + n_{jl} d\mu_{jl} = 0, \tag{3.6}$$

and the Gibbs adsorption isotherm,

$$n_{is} d\mu_{il} + n_{js} d\mu_{jl} + A d\sigma = 0 \qquad (i = a, w), \tag{3.7}$$

the Kelvin equations can be derived:

$$\Delta\mu_i + \frac{2\sigma v_i}{r^*} = 0 \qquad (i = a, w), \tag{3.8}$$

where v_i is the partial molecular volume for species i the asterisk denotes critical nucleus. The two equations in 3.8 can then become:

$$v_a \Delta\mu_w = v_w \Delta\mu_a. \tag{3.9}$$

The free energy of formation of the critical cluster is given by:

$$\Delta G^* = \frac{4}{3}\pi r^{*2}\sigma. \tag{3.10}$$

The chemical potential for species i is:

$$\Delta\mu_i = -kT \ln \frac{A_{iv}}{A_{il}}, \tag{3.11}$$

where $A_{il} = p_{i,sol}/p_{i,s}$ and $A_{iv} = p_i/p_{i,s}$, p_i, $p_{i,s}$ and $p_{i,sol}$ denote the partial pressure, saturation vapour pressure and the pressure over the surface of the

binary solution, respectively. The saturation pressures can be found using the following equations:

$$p_{w,s} = \exp\{77.3449129 - 7235.42465/T - 8.2\ln T + T(5.711 \times 10^{-3})\}, \quad (3.12)$$

for water, and for sulphuric acid,

$$p_{a,s} = \exp\{27.7849206 - 1015.0/T\}. \quad (3.13)$$

The activity of the liquid drop is a function of the mole fraction of sulphuric acid in the nuclei, $A_{il} = \gamma_i X_{il}$, where γ_i is a coefficient that is related to Raoult's law, it can be found parametrically (Kulmala et al., 1998):

$$\log_{10}(\gamma_w) = \frac{A_{11}X_{al}^2}{(X_{al} + B_{11}X_{wl})^2 T}, \quad (3.14)$$

and,

$$\log_{10}(\gamma_a) = \frac{A_{12}X_{wl}^2}{(X_{wl} + B_{12}X_{al})^2 T}, \quad (3.15)$$

where,

$$A_{11} = 2.989 \times 10^3 - \frac{2.147 \times 10^6}{T} + \frac{2.33 \times 10^8}{T^2}, \quad (3.16)$$

$$A_{12} = 5.672 \times 10^3 - \frac{4.047 \times 10^6}{T} + \frac{4.421 \times 10^3}{T^2}, \quad (3.17)$$

and finally,

$$B_{11} = 0.527 = 1/B_{12}. \quad (3.18)$$

To find the molar fraction we use another parameterisation from Kulmala et al. (1998):

$$X_{al} = 1.2233 - \frac{0.0154RA}{RA + RH} + 0.0102 \ln N_{av} - 0.0415 \ln N_{wv} + 0.0016T, \quad (3.19)$$

where N_{av} and N_{wv} are the vapour concentrations cm^{-3} for sulphuric acid and water vapour, respectively. RA (partial pressure over saturation pressure, $p_a/p_{a,s}$) is the relative acidity and RH ($p_w/p_{w,s}$) is the relative humidity, divided by 100%. This equation is very important for the nucleation model because many of the parameterisations depend on it.

The number of sulphuric acid molecules in the critical cluster can be calculated from the mole fraction parameterisation:

$$n_a^* = \frac{\frac{4}{3}\pi r^{*3}\rho}{M_a + \frac{1-X_{al}}{X_{al}} M_w}, \quad (3.20)$$

where ρ is the density of the droplet (parameterised), M_a and M_w are the masses of a sulphuric acid and water molecule, respectively. $V = X_{al}V_a + (1 - X_{al})V_w$ is the average volume of a molecule in a droplet.

3.2.1 Hydrate correction factor

Hydrates are clusters of water molecules around a single sulphuric acid molecule; clusters are expected to have no more than 10 water molecules. The theory of hydrates was developed by Jaecker-voirol et al. (1987) to explain lower nucleation rates than expected with a standard binary mechanism (H_2O-H_2SO_4). Hydrates have an affinity to form clusters; these clusters can affect sulphuric acid vapour activity. With a hydrate correction (from Jaecker-voirol et al. (1987)), the acid activities become:

$$\left(\ln \frac{A_{av}}{A_{al}} \right)_{cor} = \ln \frac{A_{av}}{A_{al}} + \ln C, \quad (3.21)$$

where the hydration correction factor, C, is given by,

$$C = \left[\frac{1 + K_1 p_{w,sol} + ... + K_1 K_2 \times ... \times K_k p_{w,sol}^k}{1 + K_1 p_w + ... + K_1 K_2 \times ... \times K_k p_w^k} \right]^{n_a}, \tag{3.22}$$

where w and a refer to water and sulphuric acid. K_k is the equilibrium constant for formation of hydrate containing k water molecules. It can be safely assumed that the occurrence of hydrates with more than 10 water molecules is negligible (Jaecker-voirol et al., 1987), that is $k \leq 10$.

Jaecker-voirol et al. (1987) gave an approximate expression for K_k:

$$\ln(K_k) = \ln \frac{A_{wv}}{A_{wl}} - \frac{2\sigma v_w}{kTr_k}, \tag{3.23}$$

where r_k is the radius of the, assumed spherical, hydrate cluster. To determine the composition and size of the critical nucleus, the corrected chemical potential (equation 3.21) is used for sulphuric acid – from this, the critical radius (equation 3.8) can be determined. Surface tension, σ, and density, ρ, of the nuclei are required in the critical nuclei parameterisation. This requires some quite lengthy equations; they can be found in the appendix of Kulmala et al. (1998). The final step required to solve equation 3.8 is to input the molecular volume for sulphuric acid (taken to be 8.844×10^{-29} m^{-3}, from density considerations); this then allows the critical radius to be found and thus the Gibbs free energy of the critical cluster (equation 3.10).

3.3 Nucleation rate

The binary nucleation equation is expressed as:

$$J = N_v A B_{AV} Z \exp(-\Delta G/kT), \tag{3.24}$$

$N_v = N_{wv} + N_{av} + \sum_{h=1,10} N_h$ is the total number density of the vapour phase, A is the surface area of the nucleus, B_{AV} is the average growth rate, and Z is the Zeldovich non-equilibrium factor. The vapour is assumed to consist of water

monomers, sulphuric acid monomers, and hydrates containing 1 acid and 1 to 10 water molecules. The average growth rate is then given by:

$$B_{AV} = \frac{B_w B_a - (\sum_h B_h)^2}{B_w \sin^2\Theta + B_a \cos^2\Theta - 2\sum_h B_h \sin\Theta\cos\Theta}, \tag{3.25}$$

where Θ is the angle between the n_w axis and the direction of growth at the saddle point in the three-dimensional space $(\Delta G, n_w, n_a)$. The condensation rates of the monomers are taken from kinetic gas theory (Kulmala et al., 1998):

$$B_i = N_{iv}\sqrt{\frac{k_B T}{2\pi}\left(\frac{1}{m_i} - \frac{1}{m^*}\right)} \qquad (i = a, w), \tag{3.26}$$

m_i is the molecular mass of species i and m^* is the mass of the critical nucleus; k_B is the Boltzmann constant. The condensation rate of the hydrates is given by:

$$B_i = N_h\sqrt{\frac{k_B T}{2\pi}\left(\frac{1}{m_h} - \frac{1}{m^*}\right)} \qquad (h = 1, ..., 10), \tag{3.27}$$

where $m_h = m_a + hm_a$.

The growth angle, Θ, is found by the angle of steepest descent:

$$\tan\Theta \approx X_{al}/X_{wl}. \tag{3.28}$$

The Zeldovich factor is calculated by considering the critical nucleus as consisting of fictitious 'average' monomers with volume $V_{AV} = X_{wl}V_w + X_{al}V_a$; this reduces the calculation to one-component nucleation:

$$Z = \sqrt{\frac{\sigma}{k_B T}}\frac{V_{AV}}{2\pi r^{*2}}. \tag{3.29}$$

The pre-exponential is the most likely source of error in numerical calculations of nucleation rate. The errors produced by the growth angle and Zeldovich factor expressions used here are expected to result in no more than 1 order of magnitude error in the final nucleation rate (Viisanen et al., 1997; Kulmala et al., 1998).

3.4 Sectional model

This model is a sectional, rather than modal, representation of an aerosol size distribution. It is based on work by Pirjola and Kulmala (1998) and Pirjola (1999) called AEROFOR that incorporates nucleation, condensational growth and coagulation (dry deposition and emission can be included but it is only significant in the PBL, not in the high altitude TTL). The chemical model (equations 3.1 and 3.2) can be made more complicated by including chemical species other than SO_2 and OH (such as acetone, NO_x, ozone, etc.) and a detailed solar radiation model (UV flux, photochemistry, sinusoidal daylight variation, etc.); Pirjola and Kulmala (1998) used AEROFOR together with a full (67 compounds) chemical scheme. The calculations presented later in this thesis used a simple SO_2 and OH kinetic rate equation (Clement et al., 2002) for the production of H_2SO_4. The model can represent the effect of pre-existing aerosol or it can be used with only fresh nucleation as the particle source. The sections divide the size range into log-scale classes with fixed lower and upper bounds; the classes (or bins) also contain a fixed number of sulphuric acid molecules, considering a 100% acid composition (dry radius only).

For the sectional model, the number of sections, n_{class}, between $r_{min} = 0.5\times10^{-9}$ and $r_{max} = 1\times10^{-6}$ m, was set at 27. The lower bound of each section (dry radius of droplet r_i) is determined logarithmically by:

$$\log_{10}(r_i) = \log_{10}(r_{min}) + \frac{\log_{10}(r_{max}) - \log_{10}(r_{min})}{n_{class}}(i-1). \tag{3.30}$$

The sectional boundaries are therefore time invariant, as opposed to a moving modal scheme. The drops in a given section $[r_i,\ r_{i+1}]$ have a fixed number of H_2SO_4 molecules:

$$n_i = \frac{4}{3}\pi r_i^3 \rho_a / M_a, \tag{3.31}$$

where ρ_a is the density of pure liquid sulphuric acid.

The time evolution of the particle number concentration in section i is given by Raes and Janssens (1986):

$$\begin{aligned}\frac{\mathrm{d}N_i(t)}{\mathrm{d}t} &= J\frac{n^* - n_{i-1}}{n_i - n_{i-1}}\delta_{n^*,]n_{i-1},n_i]} + J\frac{n_{i+1} - n^*}{n_{i+1} - n_i}\delta_{n^*,]n_i,n_{i+1}]} \\ &+\frac{C_{i-1}}{n_i - n_{i-1}}N_{i-1}(t)N_a(t) - \frac{C_i}{n_{i+1} - n_i}N_i(t)N_a(t) \\ &+\sum_{j=1}^{i}\sum_{k=j}^{i}\frac{K_{j,k}}{1+\delta_{j,k}}N_j(t)N_k(t)\frac{((n_j+n_k)-n_{i-1})}{(n_i - n_{i-1})}\delta_{n_j+n_k,]n_{i-1},n_i]} \\ &+\sum_{j=1}^{i}\sum_{k=j}^{i}\frac{K_{j,k}}{1+\delta_{j,k}}N_j(t)N_k(t)\frac{(n_{i+1}-(n_j+n_k))}{(n_{i+1} - n_i)}\delta_{n_j+n_k,]n_i,n_{i+1}]} \\ &-N_i(t)\sum_{j=1}^{n_{class}}K_{i,j}N_j(t) - \lambda^i_{dep}N_i(t).\end{aligned} \tag{3.32}$$

J is the nucleation rate, C_i is the rate of condensational growth for droplets in section i, $K_{i,j}$ is the Brownian coagulation coefficient between particles in section i and j (e.g. Pirjola and Kulmala, 1998; Pirjola, 1999). Kronecker's delta is:

$$\delta_{n_j+n_k,]n_i,n_{i+1}]} = \begin{cases} 0, \notin]\, n_i < n_j + n_k \leq n_{i+1}, \\ 1, \in]\, n_i < n_j + n_k \leq n_{i+1}. \end{cases} \tag{3.33}$$

The dry deposition of particles in section i is given by λ^i_{dep}; it is controlled by Brownian diffusion and interception (Schack et al., 1985). The dry deposition is neglected for the current study since the deposition velocity is negligible for TTL altitudes.

3.4.1 Condensational growth

Since the water vapour concentration is so much higher than sulphuric acid vapour, the new droplet solution is soon in equilibrium with water vapour (Pirjola

and Kulmala, 1998). The vapour pressure of H_2SO_4 above the droplet surface is assumed to be zero to maximise the condensation flux. The complete condensational growth equation, C_i, is given by:

$$C_i = \frac{4\pi\beta D}{k_B T N_a}(p_a - p_{a,kelvin}) \tag{3.34}$$

where $p_{a,kelvin}$ is the sulphuric acid vapour pressure above the spherical droplet surface,

$$p_{a,kelvin} = p_{a,sol} \exp\left(\frac{2v_{frac}\sigma_{drop}}{RTr_{drop}}\right), \tag{3.35}$$

where the exponential is the Kelvin term for spherical surface (tension) effects. v_{frac} is the molar fraction of sulphuric acid, σ_{drop} is the surface tension for a droplet of radius r_{drop} and R is the gas constant (8.3145 J/mol.K). $p_{a,sol}$ is the pressure above the, flat, solution surface (Raoult effect). However, this equation is not required in most cases, as $p_{a,kelvin}$ is much smaller than p_a, and it was assumed to be zero for the current study. Thus, equation 3.34 reduces to:

$$C_i = \frac{4\pi\beta D p_a}{k_B T N_a}, \tag{3.36}$$

where $p_a/k_B T N_a$ cancels (since N_a is in units volume^{-1}), to leave,

$$C_i = 4\pi\beta D. \tag{3.37}$$

D is the diffusion coefficient of sulphuric acid in air and β is the transitional correction factor (Pirjola and Kulmala, 1998):

$$\beta = \frac{K_n + 1}{0.377K_n + 1 + \frac{4}{3}\alpha^{-1}K_n^2 + \frac{4}{3}\alpha^{-1}K_n} \tag{3.38}$$

α is the sticking coefficient, which is usually assumed to be 1 (Clement and Ford, 1999a). The Knudsen number is $K_n = \lambda_v/r$, with the mean free path given by:

$$\lambda_v = 3\sqrt{\frac{\pi M_a}{8k_B T}}D. \tag{3.39}$$

The diffusion coefficient is a semi-empirical equation with the following form:

$$D = 0.00143T^{1.75}\frac{\sqrt{M_{air}^{-1} + M_{vap}^{-1}}}{P\left(D_{x,air}^{1/3} + D_{x,vap}^{1/3}\right)^2}, \tag{3.40}$$

the units are cm^2s^{-1}, M_{air} and M_{vap} are the masses of air and sulphuric acid molecules, P is the atmospheric pressure in bar, $D_{x,air} = 19.7$ and $D_{x,vap} = 51.66$ are the diffusion volumes for air and sulphuric acid molecules respectively.

3.4.2 Coagulation

Coagulation is the increase in particle size by the accumulation of smaller particles to make larger particles; smaller particles are greatly affected by Brownian motion and can as a result collide and stick to larger particles. The collisions and subsequent sticking of particles result in a reduction in overall particle concentration but an increase in the size distribution as increasing-sized particles are coagulated. Particles undergoing relative Brownian diffusion have a finite probability of colliding and sticking to one another; i.e., they may experience thermal or spontaneous coagulation. The sticking probability or sticking efficiency of aerosol particles is a complicated function of their shape and surface conditions (roughness, absorbed vapors, etc.), the relative humidity of the air, the presence of foreign vapours in the air, and other factors. Although little is known quantitatively about the sticking efficiency of aerosol particles, the fact that the kinetic energy of the colliding particles is very small makes bounce-off unlikely (chap. 11, Pruppacher and Klett, 1997).

Table 3.1 gives an impression of the the effect of particle size and concentration on coagulation rates. For monodisperse particle populations, it can be seen that decreasing size increases the rate of coagulation due to the increased effect of Brownian motion. An increased particle concentration also intuitively increases the coagulation rate because of the greater chance of particle collisions occurring. The coagulation mechanism turns out to be more efficient between particles of greater size difference; the coagulation coefficient, $K_{i,j}$ is an expression of the efficiency of collision and sticking of particles of size i and j. The following theory

Table 3.1: Coagulation times $t_{1/2}$ for aerosols of a given uniform size, r, and concentration, n, for 15°C and 1000 mb. Data taken from Pruppacher and Klett (1997) in order to given an impression of the effect of size and concentration on coagulation rates. d = days, h = hours, m = minutes.

r (μm)	1.0	1.0	0.1	0.1	0.01	0.01
n (cm^{-3})	10^4	10^3	10^4	10^2	10^5	10^4
C_c [a]	1.0926	1.0926	1.993	1.993	12.8	12.8
$t_{1/2}$ [b]	85.6 h	35.6 d	46.8 h	195.2 d	43.8 m	7.6 h

[a] The Cunningham correction factor (see equation 3.44) is an empirically derived correction for smaller sized particles (below 1 μm). The factor is approximately unity for micron-sized particles and larger.

[b] $t_{1/2}$ is a measure of the time taken for the initial concentration to decrease by half its number.

is valid for all size regimes: free molecular ($K_n > 10$), transition ($1 < K_n \leq 10$) and continuum ($K_n \leq 1$) [much of this coagulation theory is taken from Pirjola and Kulmala (1998) and references therein, in particular Fuchs (1964)]:

$$K_{i,j} = \frac{K_C^B}{\frac{R_{ij}}{R_{ij}+\sigma_{ij}} + \frac{4D_{ij}}{\bar{c}_{ij}R_{ij}}}, \tag{3.41}$$

where,

$$K_C^B = 4\pi(R_i + R_j)(D_i + D_j), \tag{3.42}$$

$R_{ij} = R_i + R_j$ is the contact distance for particles in section i and j (radii R_i and R_j). The binary diffusion coefficient, assuming particles do not interfere with each others motion, can be expressed as $D_{ij} = D_i + D_j$.

$$D_i = \frac{k_B T C_C}{6\pi\mu_{visc} R_i}, \tag{3.43}$$

where the Cunningham correction factor is given by the following semi-empirical formula:

$$C_C = 1 + K_n(\alpha_1 + \alpha_2 \exp(-\alpha_3/K_n)), \tag{3.44}$$

with the values, $\alpha_1 = 1.142$, $\alpha_2 = 0.558$ and $\alpha_3 = 0.999$ (Pirjola and Kulmala, 1998); μ_{visc} is the gas dynamic viscosity for air. The mean relative thermal velocity between particles is:

$$\overline{c}_{ij} = \sqrt{\overline{c}_i^2 + \overline{c}_j^2}, \tag{3.45}$$

and:

$$\overline{c}_i = \sqrt{\frac{8k_BT}{\pi M_i}}, \tag{3.46}$$

is the mean velocity for a particle of class i and mass M_i. The two fluxes are matched at a distance given by:

$$\sigma_{ij} = \sqrt{\omega_{ij}^2 + \omega_{ji}^2}, \tag{3.47}$$

where:

$$\omega_{ij} = \frac{(R_{ij} + \gamma_i)^3 - (R_{ij}^2 + \gamma_i^2)^{3/2}}{3R_{ij}\gamma_i} - R_{ij}. \tag{3.48}$$

The final equation is expressed as:

$$\gamma_i = \frac{8D_i}{\pi \overline{c}_i} \tag{3.49}$$

Table 3.2 gives numerical values for the coagulation coefficient, $K_{i,j}$, for a selection of particle sizes. It can be seen that the coagulation coefficient is greater between particles with a greater size difference; for instance a collision of a 0.001 μm and a 1.0 μm particle is more likely, given the coefficient of 2.8×10^{-10}, than a collision with another 0.001 μm particle (the coefficient is 4.0×10^{-16} in this case).

These equations give a reasonably accurate simulation of the coagulation mechanism, when applied to an aerosol box-model with only Brownian motion under consideration and neglecting wind shear and turbulence.

Table 3.2: Coagulation coefficient, described by equation 3.41, for various particle diameters. This coefficient is dependent, amongst other parameters, on the size of the two incident particles. To model the TTL environment during convective outflow, the calculations used the following parameters: a temperature of 222 K, a pressure of 200 hPa and a sulphuric acid concentration of 1.3×10^{8} cm^{-3}. $K_{i,j}$ is expressed in standard units of m^{3}s^{-1}.

r (μm)	0.0005	0.001	0.01	0.05	0.1	0.5	1.0
0.0005	4.0×10^{-16}	8.5×10^{-16}	4.8×10^{-14}	8.3×10^{-13}	4.8×10^{-12}	8.8×10^{-11}	2.8×10^{-10}
0.001	8.5×10^{-16}	6.2×10^{-16}	1.4×10^{-14}	2.3×10^{-13}	1.3×10^{-12}	2.4×10^{-11}	7.6×10^{-11}
0.01	4.8×10^{-14}	1.4×10^{-14}	2.0×10^{-15}	1.0×10^{-14}	4.6×10^{-14}	7.4×10^{-13}	2.3×10^{-12}
0.05	8.3×10^{-13}	2.3×10^{-13}	1.0×10^{-14}	4.2×10^{-15}	8.8×10^{-15}	9.5×10^{-14}	2.8×10^{-13}
0.1	4.8×10^{-12}	1.3×10^{-12}	4.6×10^{-14}	8.8×10^{-15}	6.4×10^{-15}	3.2×10^{-14}	8.6×10^{-14}
0.5	8.8×10^{-11}	2.4×10^{-11}	7.4×10^{-13}	9.5×10^{-14}	3.2×10^{-14}	1.3×10^{-14}	2.0×10^{-14}
1.0	2.8×10^{-10}	7.6×10^{-11}	2.3×10^{-12}	2.8×10^{-13}	8.6×10^{-14}	2.0×10^{-14}	1.8×10^{-14}

3.4.3 Numerical estimation of the derivative

In order to calculate a time derivative numerically, iterative methods must be employed. There are many such techniques in the mathematical field of numerical analysis, for example, Runge-Kutta, Crank-Nicholson, Euler differencing, Jacobi method, etc. (see for example, Press (2007)). Each have advantages and drawbacks and the selection of one over the other can have major implications for the ease of implementation, programme speed, stability, truncation errors and accuracy.

We can rewrite the differential equation (3.32) as follows,

$$\frac{\mathrm{d}N_i(t)}{\mathrm{d}t} = F(t), \tag{3.50}$$

where $F(t)$ represents the right-hand side of equation 3.32. Using a finite element approach, we have,

$$\frac{\Delta N_i(t)}{\Delta t} = F(t). \tag{3.51}$$

If we expand the $\Delta N_i(t)$ term, we find,

$$N_i^{new}(t) - N_i^{old}(t) = F(t)\Delta t. \tag{3.52}$$

It can be seen that the derivation of the *new* value for $N_i(t)$ is dependent on the

old value and an incremental change in the differential equation, given by $F(t)$, and calculated at a time Δt. $F(t)$ could be calculated at time $-\Delta t$, $+\Delta t$ or some complex implicit combination of the variables in equation 3.52; this determines the nature and properties of the numerical methodology employed. Two of the more simple techniques are referred to as the forward Euler and the backward Euler methods. These use respectively the $F(t)$ value at the *start* of the time-step and at the *end* of the time-step. Therefore equation 3.52 becomes, for a forward differencing methodology,

$$N_i^{new}(t) = N_i^{old}(t) + F^{old}(t)\Delta t, \tag{3.53}$$

and for backward differencing,

$$N_i^{new}(t) = N_i^{old}(t) + F^{new}(t)\Delta t. \tag{3.54}$$

So as the time increment, Δt, is increased the calculation of $F(t)$ takes place at the start or at the end of the time change, depending on the particular Euler technique used. Despite their simplicity and similarity, there are inherent advantages and disadvantages between the two: forward differencing is easy to implement (since it is an *explicit* equation), however it is only first-order in Δt and suffers from stability issues that restrict the time-step; backward differencing has no such problems with time-step choice but also has problems with accuracy due to the first-order nature of Δt. Backward differencing also has a much more problematic implementation because of its implicit nature.

Eulerian forward differencing is a non-implicit methodology that is easier to implement and it was for this reason that it was employed in the numerical solver. Due to the time-step stability issues, the solver was run using a variety of time increments and the results were examined visually for signs of divergence. Also, into the Fortran programme, were written implicit accuracy, or tolerance, levels that caused a run-time error if the solver began to diverge. For these reasons, the required time-step for stability was easily determined – it was found that a time increment of 0.01 s produced a stable solver that did not adversely affect the run-time (see chapter 9 for model run outcomes).

Chapter 4

Climatology and Meteorology

4.1 The Planetary Boundary Layer (PBL) near Darwin

The climatology and meteorology in the Darwin region were well documented and analysed so that the ACTIVE dataset had a solid foundation. Because of the fast transport of Planetary Boundary Layer (PBL) air into the UT/TTL by tropical convection, it was necessary to examine composition of the PBL in detail. Uplifted aerosols and trace gases affect the constitution and chemistry of the UT/TTL (Dessler, 2002), which ultimately influences the cloud formation in the UT and the ozone levels in the stratosphere – all of which have important consequences for the radiative forcing on global climate. The ACTIVE campaign used a wide range of instrumentation (see the NERC Dornier aircraft description, section 5.2.3) with which to catalogue the aerosols and gas species in the PBL (Allen et al., 2008) and measure atmospheric conditions [e.g., ozonesondes to profile the atmosphere – Allen et al. (2008); Vaughan et al. (2008); Heyes et al. (2009)].

Six distinct climatological regimes were encountered during the two ACTIVE campaigns, 10 November to 10 December 2005 and 14 January to 14 February 2006. The campaign began during the dry season with a period of biomass burning.

Table 4.1: Distinct periods of climatology during ACTIVE, with relevant flights

Period	Prevailing Influence	Dornier Flights	Egrett Flights
13 - 19 Nov + 25 - 30 Nov	biomass burning	TD02-SD05 + AD08-AD09	AE03-AE06
20 - 24 Nov	mini-monsoon	SD06-SD07	–
1 - 11 Dec	premonsoon	AD10-AD12	AE07-AE13 + SE14
14 - 24 Jan	active monsoon	TD13-AD15	AE17-AE19
25 Jan - 3 Feb	inactive monsoon	AD16-SD18	AE20-AE21 + SE24
4 - 14 Feb	monsoon break	AD23-AD28	AE25-AE30

The biomass burning took place between 13 and 19 November and then again between 25 and 30 November. The biomass plumes were produced by dry grass and bush fires that had been ignited through lightning strikes or land clearance by local farmers; these fires were visible with the Moderate Resolution Imaging Spectroradiometer (MODIS) instrument on NASA's TERRA satellite and were widespread in the Northern Territory (NT) and Queensland (Allen et al., 2008). The low level winds were dominated by easterly flow at 700 mb (convective steering level) with wind speeds between 12 and 20 ms^{-1} (Allen et al., 2008). Sea breeze circulations at the surface generated convection, individual thunderstorms and squall lines ($\sim$ 100 km in size). Back trajectories analysis showed air parcels tracking over areas of biomass burning; these polluted air masses were then introduced into the Darwin area by the predominant easterly winds – biomass burning pollution was also sampled by the Dornier. In this period there was an enhanced level of gases and particles associated with biomass burning. CO concentrations were higher on average than at any point in the ACTIVE campaign; CO is commonly used as a marker for combustion and related emissions (hydrocarbons, etc.) – it is ideally suited to this role due to its long lifetime of $\sim$ 2 months and its associated release during biomass and fossil fuel combustion (Flocke et al., 1999; Edwards et al., 2006; Lopez et al., 2006). Organic compounds, such as ethyl benzene, monoterpenes, OVOCs, were detected in direct correlation with CO, suggesting a common source from biomass burning emissions. Furthermore,

the fine aerosols, defined as size 0.2 to 2.5 μm in Allen et al. (2008), were measured in greater number concentrations during the biomass period, with higher organic mass percentage and CO correlation. This high organic content in the atmosphere dropped steadily throughout the remainder of the two ACTIVE campaigns (it reached a low point during the active monsoon).

Between the two main biomass burning episodes, there was a period, 20 to 22 November, of intense convective activity named the 'mini-monsoon'. '*It was so named because of a deep westerly flow from 700 mb to 200 mb coincident with widespread oceanic convection. This reversal in the prevailing winds was associated with an unusually strong northward undulation of the subtropical jet stream and a significant westerly momentum injection to the free troposphere associated with a breaking Rossby wave*,' (Allen et al., 2008, 2009). The descending air acted as a pseudo-frontal system and enabled convective uplift to occur in the Darwin area without the presence of sea breeze circulation.

After the passing of the Rossby wave, the wind return to its prevalent easterly flow, with the meteorology following the same general pattern as before. There was however a reduction in the number of biomass fires detected by the MODIS system (Allen et al., 2008); this naturally resulted in a reduced atmospheric burden of trace gases, black soot particles and organic aerosols associated with biomass burning. However, the black carbon concentration remained steady with median mass concentrations between 0.2 and 0.3 μg m^{-3} (although the mass concentration was much more variable throughout the biomass burning period, with a maximum of about 1 μg m^{-3}); it accounted for about 6 % of the total organic mass throughout the biomass burning and premonsoon phases.

The active monsoon began on the 14 January during the second campaign when a monsoon trough formed to the south of Darwin, bring northwesterly air flow into the Top End of the Northern Territory (NT), between 300 mb and the surface. 5 day back trajectories confirmed that the flow into the Top End was dominated by maritime air. This triggered widespread maritime convection that was as deep as in the first campaign, reaching as high as the tropopause. This regime persisted until the 22 January when a monsoon low formed to the north of Darwin and then moved south to central Northern Territory. During this period of maritime air

flow there was a marked shift away from the organic, biomass burning, influences towards a sulphate dominated aerosol composition (59 % of total mass of the internally mix was sulphate).

The inactive monsoon occurred due to the monsoon low centred in the NT; the wind become stable and westerly across the Top End, suppressing deep convection and reducing storm cloud top heights to less than 10 km – this lasted until 3 February 2006. The air continued to have a low organic content, as in the active monsoon, and retained a high internal mix of sulphates, 57 %.

After 3 February 2006, the monsoon low disappeared and there was a return to the deep easterly flow, initially at 700 mb but descending to the surface, that was seen in the premonsoon period – this was termed the monsoon break period. This was marked by a reappearance of single-cellular deep convection, occurring first on the Tiwi Islands as Hector storms, but then spreading to mainland NT. The convection was similar to that seen in the premonsoon but the single-celled storms became more organised throughout the remainder of February until the end of the campaign on the 14 February. With the breaking of the monsoon wind circulation, there was a reduction in the maritime influence on the PBL air composition and with it a steady increase in the internal organic content of the aerosol population.

Furthermore, the nitrate and ammonium burden in the PBL was low for the duration of the two ACTIVE campaigns; although, the ammonium concentrations, when compared to the sulphate after averaging, indicated that the aerosols were mostly pH-neutral. Nitrate and ammonium are important atmospheric gases due to their influential role in aerosol production and growth, through homogeneous ternary nucleation (see section 2.3.3). A low level nitrate concentration in the Darwin area would have a major impact on the aerosol processing, or lack thereof, that took place during the ACTIVE campaign. This a factor that had to be considered when making any conclusions concerning the aerosol dataset in the TTL and the influence of precursor gases.

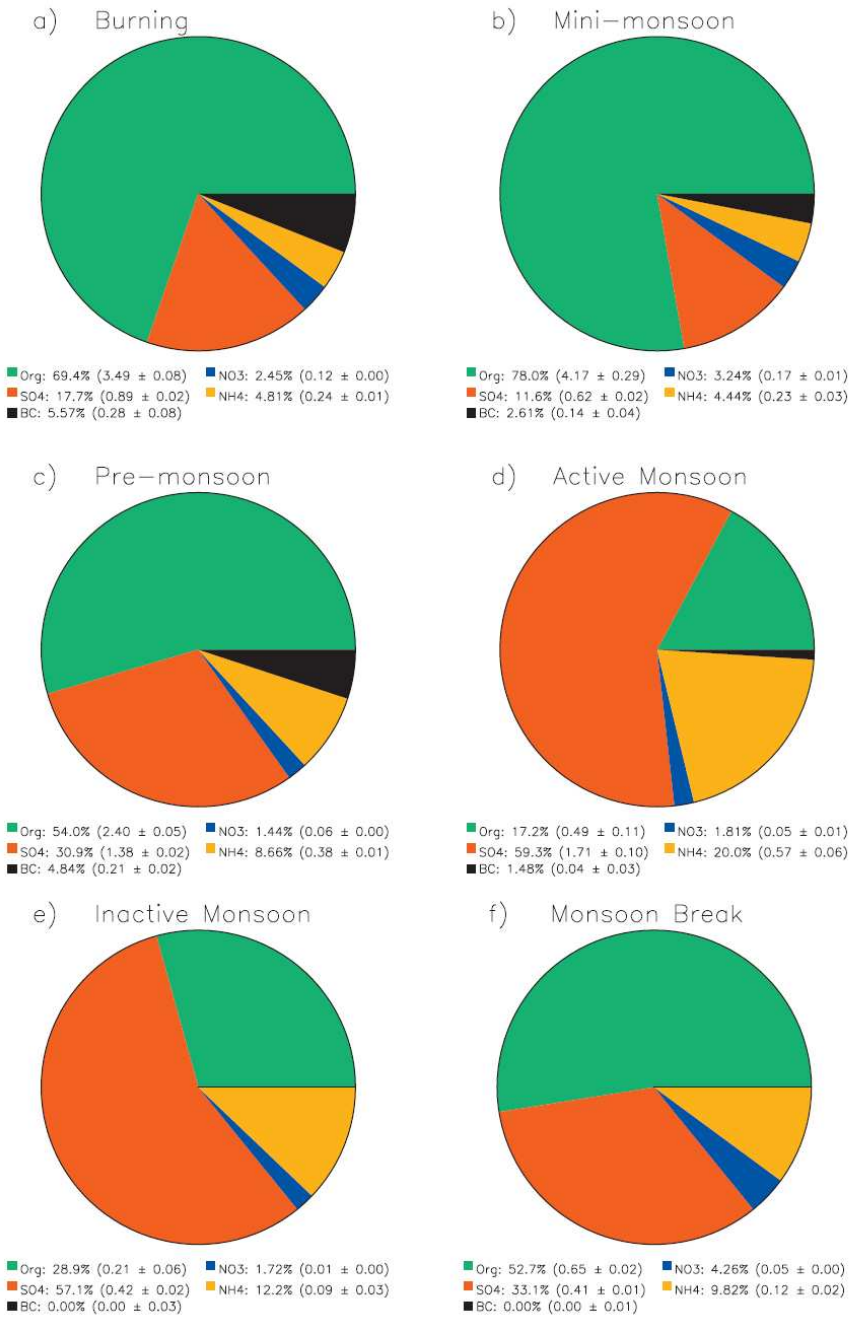

Figure 4.1: Submicron mass fraction, of the four main constituents (sulphate, nitrates, organics and ammonium) measured by the Dornier's AMS. The black carbon content is measured by the PSAP instrument. Data and figure from Allen et al. (2008).

4.2 Storm Dynamics and Microphysics

As mentioned earlier, the premonsoon and monsoon break periods were meteorologically dominated by single-cell storms, some of which were deep (up to the TTL $\sim$ 18 km) and with intense rainfalls. The active monsoon was a period of widespread convection, both inland continental and maritime in origin, that were typically less intense and shorter lived than the premonsoon/break regimes (May and Ballinger, 2007) – monsoon convection did however produce greater rainfall totals of any phase. One of the ACTIVE objectives was to find the effect of uplifted aerosols and chemicals on the storm intensity, lifetime and extent and the also on the small-scale cloud microphysics (such as ice crystal habits and crystal concentrations (for example, Gallagher et al., 2005)). This was primarily to improve the state of current cloud models and in particularly the climatology/meteorology forecasting in the tropics where intense convection has a high impact on the global cloud cover.

To achieve this – together with the aircraft mounted instruments – there were ground based radar stations strategically placed to observe convective activity in the NT; regular sonde launches, from Darwin airport and 5 others around the NT, measured the vertical thermodynamic and moisture profile of the atmosphere. While most of the other instruments were well suited to characterizing the environmental conditions, radar is an ideal technique for describing convection (see May et al. (2008) for a full description of the ACTIVE/TWP-ICE experiment and the categorization of the observed convection).

The sounding data were analysed routinely by the Australian Bureau of Meteorology operational forecasters to give estimates of Convective Available Potential Energy (CAPE) and Convective Inhibition (CIN). These two parameters are often very good indicators of storm intensity and uplift and the likelihood of convection taking place at all. CIN can act as a 'lid' on convective uplift; CIN is typically a result of a temperature inversion in the lower/mid ($\lesssim$ 700 hPa) troposphere (e.g. Beringer et al., 2001; Browning et al., 2007). The strength is determined by the CAPE; when a CIN lid is involved, the CAPE can build up like a pressure cooker and produce more vigourous and deeper convection. The Hector storms that form

on the Tiwi Islands have been investigated previously using modelling techniques (Golding, 1993; Crook, 1996; Keenan et al., 2000; Beringer et al., 2001). Using simulation and observed data from MCTEX 1995, Crook (1996) found that the surface wind speed and moisture content were the most important parameters in Hector generation, with gentler breezes being more conducive for deep convection. Convection was also found to form on the downwind coast of the islands (Keenan et al., 2000; Beringer et al., 2001). Storm initiation was confined to areas of boundary layer convergence lines (sea breeze or gust fronts) that were intensified more if there were interacting with non-precipitating cumulus clouds or degenerating thunderstorms – initiation could be delayed and even suppressed by strong shear winds, which prevent buoyant air from reaching the free troposphere (Keenan et al., 2000; Beringer et al., 2001). The dissipation of Hector occurred if it moved westwards over the ocean or occasionally inland over areas cooled by earlier storms. Keenan et al. (2000) and Beringer et al. (2001) described Hector suppression, low CAPE, as being caused by previous convective disturbances such as monsoon lows and squall lines; this was seen during the inactive phase of ACTIVE when a monsoon low formed in the central NT and strong westerlies cut off convection across the whole region. Higher CAPE did produce earlier and more intense storms during the computer simulations but the observations were not well correlated to CAPE – there were however slight increases in size and the maximum strength Crook (1996).

The radar has a C-pol 5.5 cm wavelength scanning polarimetric weather radar system located at Gunn Point (12.25° S, 131.04° E). The radar provided measurements of the reflectivity, differential reflectivity, absolute differential phase on propagation as well as its derivative in range, the Specific Differential Phase; and finally the correlation of the signals at the two polarisations. The polarimetric radar had two major advantages over conventional radar: firstly, it can resolve rainfall much better than using reflectivity alone; secondly, it had the capability to distinguish hydrometeor species. The radar's rain detecting and hydrometeor categorisation capabilities provided a method for defining storm size and intensity. May et al. (2008) used these data to analyse convection that was encountered during the second ACTIVE campaign (alongside TWP-ICE) and then to statistically classify the storms.

There was a clear signal found in the high CAPE cases: high CAPE average produced larger areas of rain, convection, wider anvils and more intense cells, albeit with a considerable spread in the data (May et al., 2008). Low CIN produced storms of higher rain and anvil area; convection which originated from high CIN conditions were found to have delayed initiation but more intense cells – the convective area was independent in this case. This increased intensity is a result of the 'lid' effect above the PBL allowing potential energy to build up before its release. The amount of forcing required to trigger convection during high CIN might also add to the overall strength of the storm. The maximum convective area in the low CIN cases were only marginally higher but the high CIN examples were significantly delayed in reaching their maximum. Finally, the last thermodynamic consideration in May et al. (2008) – wind shear – showed a strong suppression of storm activity and intensity with increased shear, in agreement with Keenan et al. (2000) and Beringer et al. (2001). As a result, the low shear cases produced substantially more rain than the high. Shear was also found to affect the organisation of storm lines; in Hector cases however, its main effect is to change the sea breeze orientation into shear perpendicular squall line configurations in the mature storm system phase (May et al., 2008).

4.3 CO profiles and convective influence on the UT/TTL

CO is a useful marker for pollution and air mass history. CO has a fairly long lifetime (of the order of 1 month) in the entire troposphere, allowing it to survive uplift in convection and long-range transportation. It is particularly useful as a convective tracer in areas with high gradients between the PBL and the background concentrations at the outflow. In this situation enhanced concentration spikes in the convective anvil are much more noticeable (Heyes et al., 2009) and have been detected in-cloud during convective research campaigns (Strom et al., 1999).

The CO analyser on the Egrett was used to produce profiles of the troposphere, including the UT (see chapter 5 for details of the instrumentation and quality

control). Only the take-off, ascent and UT/TTL sections of flight were used, since the descent data at times produced spurious readings. This was due to the evaporation and sublimation of water and other volatile compounds in instrument cavities and inlets during atmospheric warming on descent.

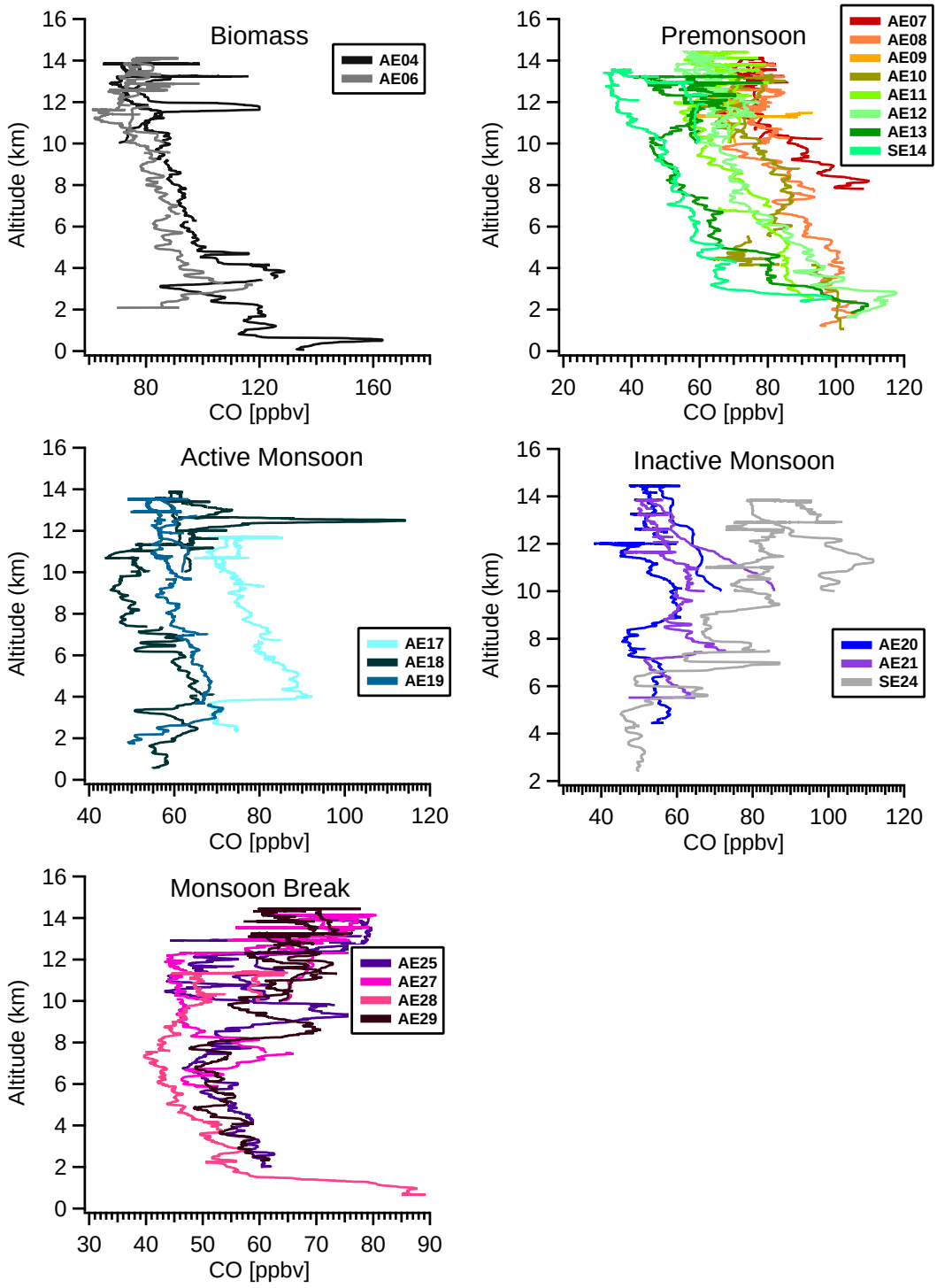

Figure 4.2: Egrett flights and their associated CO profiles, for 5 climatological phases.

The profiles are shown for the 5 phases that had concurrent Egrett flights (figure

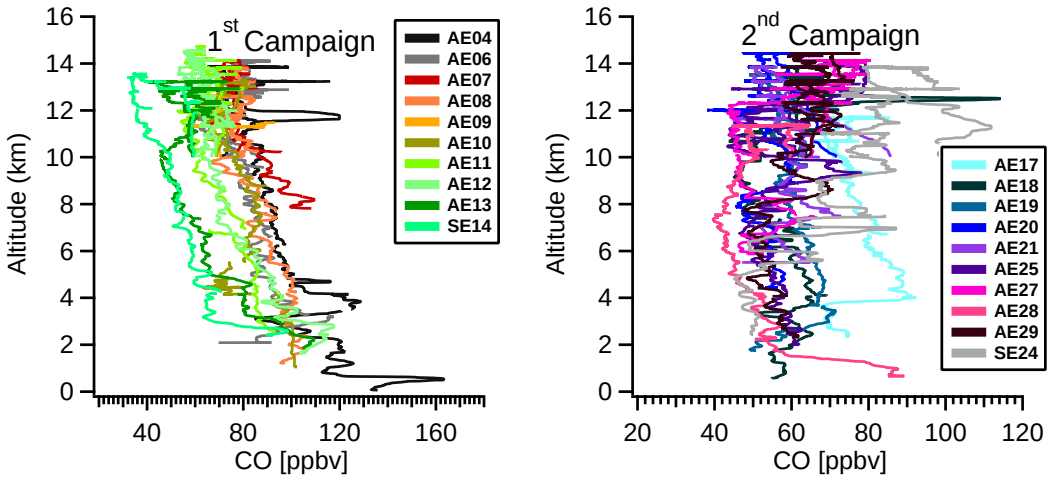

Figure 4.3: Egrett flight's CO profiles summarised for the 2 campaigns.

4.2). The profiles are categorised into 2 campaigns in figure 4.3. The CO profiles in the first campaign (in particular, the biomass and premonsoon periods) seem to follow the idealised shape that is useful for convection tracing: a high surface concentration and lower background levels in the UT. This suggests that areas of enhanced CO in the UT/TTL are due to convective uplift. The high altitude Geophysica research aircraft also showed this decreasing CO trend continued up to the tropopause and beyond into the stratosphere (Vaughan et al., 2008); CO concentrations ranging between 40 and 60 pptv were typically detected beyond the tropopause, during flights on the 23 and 30 November 2005. This is confirmed by higher CO being found in anvil cloud than in cloud-free air. The background CO concentrations in the UT/TTL were studied by Heyes et al. (2009) and were found to be mainly influenced by long-range transport from Indonesia (high concentrations) and the Tropical Warm Pool to the west (lower concentrations). The UT/TTL air with convective influences had a variety of origins, including the PBL around Darwin and from entrainment (Mari et al., 2000). The premonsoon showed a steady decrease in mean CO gradient with altitude; the standard deviation is remarkably similar throughout the troposphere. The relatively wide variability in the CO concentration would suggest that there were a number of influences on the constitution on the UT/TTL, including local convection. The second campaign showed a marked change in the local climatology as the monsoon began. During this time the profiles showed lower, or very similar, surface CO concentrations compared to the UT/TTL (particularly between 10 to 14 km).

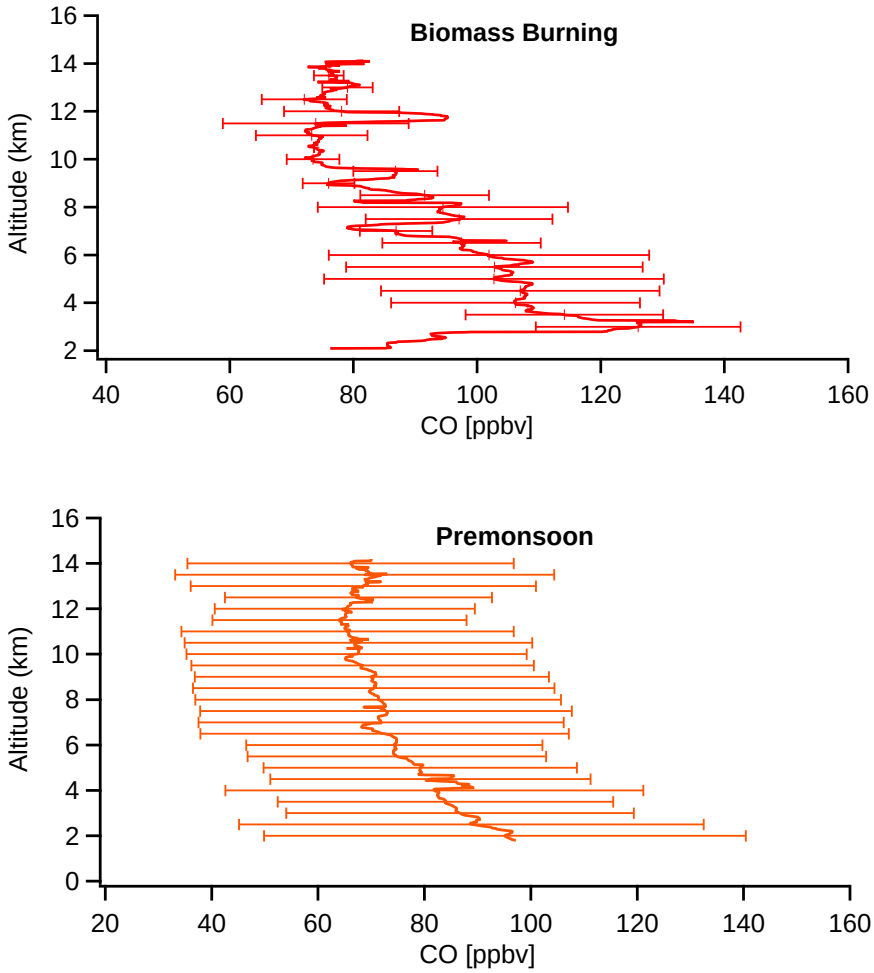

Figure 4.4: These plots show the mean profile for the biomass burning and premonsoon phases, with the standard deviation given as error bars. These occurred during the first ACTIVE campaign.

The lower surface CO concentrations reflected the cleansing effect of the monsoon winds on the biomass burning pollution that had previously dominated the local Darwin PBL. The low-level concentrations in the active monsoon were found by back trajectories to be of local, maritime origin (Allen et al., 2008; Heyes et al., 2009). The UT/TTL CO was also found to have a stronger convective influence, shown by the remarkable constant mean concentration profiles in the active monsoon (figures 4.2 and 4.5). However, due to the high variability in the UT/TTL values (see standard deviations in profile plots) during the second campaign and low surface concentrations, there was still a significant impact from

transportation of long-range sources on the UT/TTL composition (also, Heyes et al., 2009). The inactive monsoon returns to a more complex average profile with a large standard deviation throughout the troposphere. It should be mentioned that this phase included flight SE24 which flew a northern flight plan that took it close to the chemical boundary with Northern Hemisphere influenced pollution (see Dornier flight discussion: detection of the northern plume, figure 6.6). The effect of the pollution plume would be expected to produce high variability in the profiles. However, the high variance exists throughout the troposphere and indicates that there must have been a number of sources with possibly long-range origins. Furthermore, since this was the inactive monsoon there was an almost complete halt in convective activity in the local Darwin area; air masses would have been transported from other regions by long-range transportation in order to produce the disperse CO background levels encountered.

The monsoon break shows very little variation in CO concentration up to 10 km, at the same time as the mean CO gradient increases. Again this would suggest that local convection would not be the major influence on the UT/TTL composition. This phase showed a return to the isolated storm cells, such as Hector, that were prevalent in the premonsoon. Convection was occurring locally but the overall composition of the UT/TTL could not have been determined by this convection; the higher mean and variability in the UT/TTL would not have been possible with such low and invariable CO concentrations in the PBL. It appeared that the CO concentrations in the troposphere were just beginning to recover after the low of the monsoon and the impact of local convection was only slowly having an influence, after the inactive monsoon.

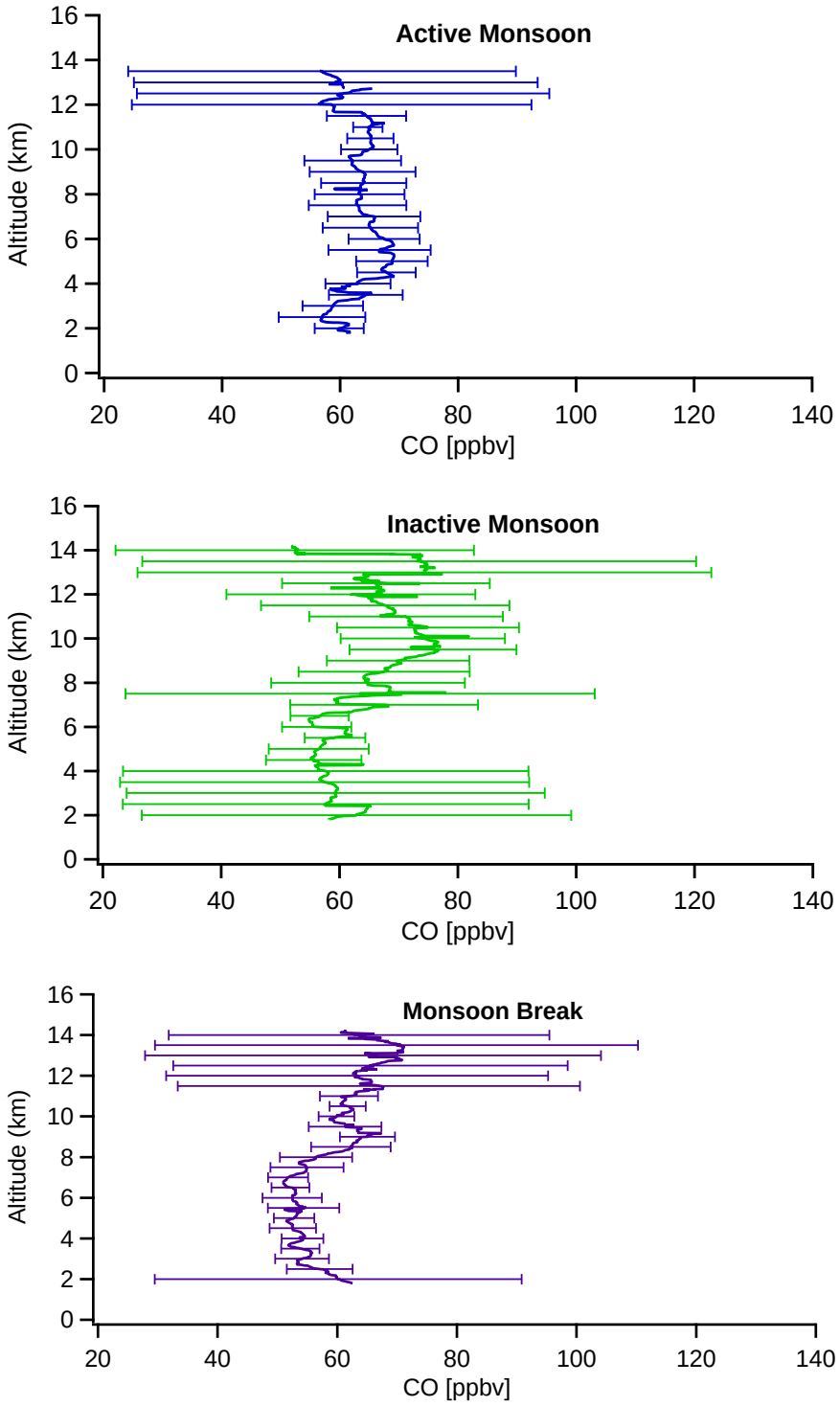

Figure 4.5: These plots show the mean profile for the active monsoon, inactive monsoon and the monsoon break, with the standard deviation given as error bars. These occurred during the second ACTIVE campaign.

Chapter 5

The ACTIVE Experiment

5.1 ACTIVE

The Aerosol and Chemical Transport in tropIcal conVEction [ACTIVE] took place over two campaigns in the tropics of the Northern Territory (NT), Australia (Vaughan et al., 2008; May et al., 2008). The northern sector of the Northern Territory, referred to as the Top End, was the region of climatological and meteorological interest for the ACTIVE campaign. Figure 5.1 shows the general focus of the ACTIVE campaign in the area around Darwin and the Tiwi Islands.

The focus of the campaign, as the title suggests, was to find the influence of tropical convection (through cumulonimbus thunderstorms) on the aerosol and chemical content of the TTL (between 14 and 18 km) and the cirrus cloud cover in the area. The base of the operation was Darwin (12.47°S, 130.85°E); the Tiwi Islands, 100 km, to the north were the focus of the campaign, due to their regular storms – called Hector. Hectors occured during the premonsoon and monsoon break climatological regimes – see chapter 4. The two campaigns took place during the 2005/2006 wet season (November February) after a period of considerable biomass burning (Allen et al., 2008). This area is very convectively active and is also influenced in the summer by monsoon winds and precipitation; a number of previous studies (both campaigns and models) have taken place in the Darwin area or focused on the climatology of the area (Golding, 1993; Crook, 1996; Keenan et al., 2000; Beringer et al., 2001; May and Ballinger, 2007). This is a

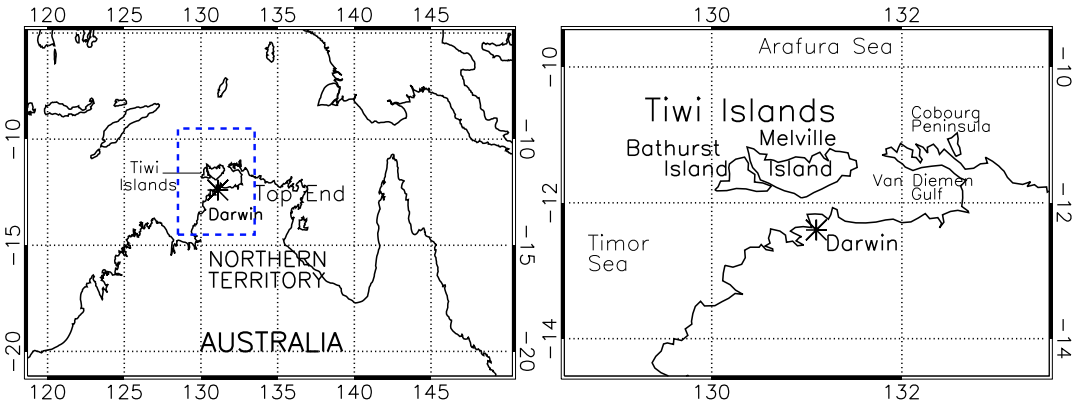

Figure 5.1: *left*: Map of northern Australia and the surrounding tropical warm pool. The Top End is the geographical name for the northernmost peninsula region of the Northern Territory. The blue dashed box indicates the area enlarged in the righthand image. *right*: The main focus of the ACTIVE campaign: the Tiwi Islands, Darwin, the surrounding seas and the Top End in general.

very coupled system with many aerosol processes (condensation growth, freezing, etc.) taking place inside cloud. The strength of the convection is also expected to be influenced by the aerosol and chemical loading in the PBL; for example, aerosol size, composition and number concentration can have an effect on the convective intensity and cloud formation (Wang, 2005a,b). This campaign was preceded by the EMERALD-I and II campaign in 2001 and 2004 respectively – undertaken by some of the participants of ACTIVE – it collected interesting data concerning cloud formation and chemical species in the area – EMERALD-I and II (Whiteway et al., 2004; Gallagher et al., 2005) found elevated ozone levels in anvils which could have been due to lightning NO_x production, but was ultimately unexplained. The campaigns also gathered, through particle imaging technology (Cloud Particle Imager, CPI), extensive data about ice crystal habits and their growth. In terms of the the scope and planning required to study thunderstorms in the Darwin area, the campaigns provided an invaluable background for the ACTIVE experiment. It provided an insight into the role aerosols play in cirrus generation but it did not specifically focus on the aerosol population in the TTL – ACTIVE aimed to build on the EMERALD dataset and also improve the aerosol data.

The campaign used a wide variety of aircraft and instrumentation in the boundary layer, mid-troposphere and upper troposphere/lower stratosphere in order to make as thorough an examination of the tropical region as possible. This thesis will reveal the characteristics of the aerosols dataset from the northern Australian tropics. It will aim to improve the understanding of aerosol and chemical transport, aerosol number concentrations, mechanisms for aerosol formation from precursors and lifetimes for aerosols in the UT/TTL. These are areas that are still not fully understood but are believed to have a very direct impact on the global cloud cover and hence the Earth's radiative budget. There has already been a number of publications that analyse and interpret the abundant ACTIVE dataset (e.g. Allen et al., 2008; Vaughan et al., 2008; Chemel et al., 2009; Heyes et al., 2009; Labrador et al., 2009; May et al., 2009).

5.1.1 SCOUT-O3 and TWP-ICE

ACTIVE was one part of a wider consortium that involved two other campaigns: the StratosphericClimate Links with Emphasis on the Upper Troposphere and Lower Stratosphere (SCOUT-O3), between 10 November 2005 and 10 December 2005, and the Tropical Warm Pool International Cloud Experiment (TWP-ICE), between 21 January and 14 February 2006.

SCOUT-O3 is a European integrated campaign that took place in the premonsoon season when single-cellular convection was more common. The focus of SCOUT-O3 was the effect of tropical convection on the chemistry, water vapour and aerosol content in the upper troposphere and lower stratosphere (UTLS), with an emphasis on ozone and climate change. Three objectives were outlined for the campaign: to better understand (1) the transport of trace gases through the TTL and into the stratosphere, (2) the role of deep convection in this process, and (3) dehydration processes in close to the TTL (Brunner et al., 2009). SCOUT-O3 made use of four main aircraft (figure 5.2) with remote sensing and in situ instrumentation; vertical profile measurements came from ozonesondes launches. There was a wide network of ground-based stations, including polarimetric weather radars and a lightning interferometer network. A more thorough

introduction to SCOUT-O3 is given by Vaughan et al. (2008) and Brunner et al. (2009); numerous papers have already been published and more are being prepared concerning SCOUT-O3 data (e.g. Corti et al., 2008; Spang et al., 2008; Ferretti and Gentile, 2009; Huntrieser et al., 2009).

TWP-ICE (May et al., 2008) focused on the cloud properties and their aerosol processing in the Darwin area, from 21 January to 14 February 2006, alongside the second ACTIVE campaign. It included a ship, five aircraft and numerous soundings. The improved accuracy of cloud resolving models was one of the main aims for the TWP-ICE campaign; cloud models and general circulation models (GCM) are a vital tool for forecasting in the convectively active tropics. To meet this task, the network of sounding stations were arranged to fit a typical GCM grid; a high temporal resolution was also achieved with 3-hourly balloon launches. Together with the aircraft and soundings, there were ground-based polarimetric weather radars that allowed the storm size, intensity and possible composition to be inferred. May et al. (2008) list the main directives for TWP-ICE. In brief, the campaign sought to quantify the effect of convectively uplifted aerosols and gases on the evolution, composition, microphysics and structure of cumulonimbus cloud. The ice crystal microphysics can affect the reflectivity of the cloud in the TTL. Ice crystal structure and composition can therefore influence the radiative forcing on the climate. Other objectives for TWP-ICE included the improvement of satellite and ground-based retrieval systems and possible detection of dynamic phenomena such as gravity waves. Again publications have already been released that use the ACTIVE/TWP-ICE dataset and more are planned (e.g. Frederick and Schumacher, 2008; May et al., 2009; Wang et al., 2009).

In summary, the ACTIVE/SCOUT-O3/TWP-ICE conglomerate shared a common objective to improve the understanding of the tropical climate system; cooperation was crucial in producing this extensive dataset.

5.2 Aircraft and Instrumentation

Figure 5.2 shows the aircraft that were used during the ACTIVE project. The two principle datasets used during this study came from the NERC Dornier-228 and the ARA Grob 520T Egrett (hereafter referred to as simply the Dornier and Egrett). The M-55 Geophysica, from SCOUT-O3, and the Twin Otter, from the TWP-ICE consortium (May et al., 2008), datasets were used to a lesser degree.

The Dornier is light twin-engine aircraft with an interior cabin modified to harbour a scientific payload. Ambient air was sampled through a purpose-built stainless steel, forward-facing, passive, isokinetic inlet positioned over the centre of the cockpit (Allen et al., 2008). This was directed to the cabin payload cabin payload; this included a CPC and three optical particle spectrometers for measuring particles of diameter > 200 nm. The aerosol inlet did not transmit particles greater than 2 μm diameter; however these were measured using an FSSP (forward scattering spectrometer probe) mounted on the wing. Also wing-mounted, was an AVENTECH AIMMS-20 meteorological probe. Full details of the Dornier payload may be found in Allen et al. (2008) and summarised in table 5.3. The Dornier has a ceiling of 4 km and was used to survey the PBL and the inflow climatology into convective storms.

The ARA Grob 520T Egrett is a single propeller-engined aircraft, capable of high-altitude work (ceiling of 15 km), that has been modified to carry instrumentation for atmospheric research. It can carry up to 750 kg of scientific equipment and has an endurance of 6 hours. The Egrett aircraft was used for measurements in the anvil outflow at 1214 km. Typical air speeds on science runs were 100 ms^{-1}. The equipment (see table 5.1) was fitted into fuselage bays and exposed wing pylons (port and starboard). The fuselage was augmented with removable U-bays that could be used as changeable instrument platforms. Of particular relevance to this work were two Condensation Particle Counters (CPC, see below) in the fuselage and cloud probes on the wings. The fuselage instrumentation drew air from a transportation pipe connected to the isokinetic inlet, which was mounted on the port wing pylon (see below for inlet details).

Figure 5.2: Montage of aircraft used in ACTIVE/SCOUT-O3 with a brief description of each. Figure from Vaughan et al. (2008).

5.2.1 Egrett payload

Table 5.1: Instrumentation payload for the ARA Egrett

Instrument	**Description**
Basic meteorology and position	Pressure, temperature, wind, GPS (1 Hz)
DMT Single Particle Soot Photometer (SP-2)*	Aerosol particle size distribution (0.2 - 1.0 μm), light absorbing fraction (LAP), carbon mass, metal.
2 x TSI-3010 Condensation Particle Counters (CPC)	(1) Total particles > 10 nm (10 nm has 50% detection efficiency) (2) 3 diffusion disks: > 41 nm; 50% efficiency increases to 100 nm at 200 hPa
DMT Cloud, Aerosol & Precipitation Spectrometer (CAPS)	Cloud droplet spectrum, aerosol/small particle asymmetry, aerosol refractive index, (0.3 < Dp < 2000 μm), Total Liquid Water Content
DMT Cloud Droplet Probe (CDP)	Particle size distribution (2 < Dp < 62 μm)
SPEC Cloud Particle Imager CPI-230	Cloud particle/ice CCD images, (10 < Dp < 2,300 μm)
Julich CO analyser	High precision (± 2 ppb), fast response (10 Hz) CO
Cambridge Miniature Gas-Chromatograph	Halocarbons (Cl, Br, I), 3-6 min, ± 5%
Buck Research CR-2 frost point hygrometer	Temperature, dew/ice point, 20 s, ± 0.1°
2x Tunable diode laser Hygrometer (SpectraSensors)	Water vapour, 1 Hz, ± 1 ppmv precision
TE-49C UV Ozone sensor	Ozone concentration (± 2 ppbv, 10 seconds)
Adsorbent tube carbon trap	C4-C9 nonmethane hydrocarbons, monoterpenes, OVOCs, aliphatics, acetone
NO and NO_2 chemiluminescent detector*	± 200 ppt @ 10 Hz; ± 30 ppt with 4 s integration

**Alternate usage, only one flown at any time*

5.2.2 Egrett missions

Table 5.2: Summary of Egrett flights

Flight Number	**Date**	**Description**
First Campaign		
AE04	16 November 2005	Biomass burning: Hector sampling
AE06	30 November	Biomass burning: Hector outflow sampling to the east of Melville Island
AE07	1 December	Premonsoon: Hector sampling
AE08	3 December	Premonsoon: Hector storm on Bathurst Island - flight to the west of island
AE09	4 December	Premonsoon: Hector outflow sampled, to the south of Bathurst Island
AE10	5 December	Premonsoon: Intercomparison with AD12. Then sampled aged cirrus cloud between Melville island and Coburg peninsula
AE11	6 December	Premonsoon: Large cirrus outflow sampled south of Bathurst and Melville Islands and west of Cape Gambier
AE12	8 December	Premonsoon: A sample of the large storm anvil remaining from the previous night
AE13	9 December	Premonsoon: Anvil spreading west from Bathurst Island. Egrett transects anvil at increasing distance from the core

SE14	10 December	Premonsoon: A sample flight during a Hector. This involved long straight legs of flight circumnavigating the whole Tiwi and Top End area. Aim to measure background conditions and make use of SP2 instrument

Flight Number	**Date**	**Description**
Second Campaign		
AE17	20 January 2006	Active Monsoon: Flight to investigate squall line progressing across the Tiwis and coast
AE18	22 January	Active Monsoon: Investigating a monsoon storm to the south of Darwin
AE19	23 January	Active Monsoon: Flight in Timor sea area to sample dissipating anvil
AE20	25 January	Inactive Monsoon: Egrett flew into aged cirrus anvil that drifted from mesoscale system in central NT
AE21	27 January	Inactive Monsoon: Again, aged cirrus anvil was sampled
SE24	3 February	Inactive Monsoon: No convection around Tiwi Islands for about 5 days. The Egrett does a sample flight with long level sections
AE25	6 February	Monsoon break: Flight into detached Hector anvil north and west of Melville Island
AE27	10 February	Monsoon break: A large Hector is formed - sampled by the Egrett
AE28	12 February	Monsoon break
AE29	13 February	Monsoon break

AE30	14 February	Monsoon break: intercomparison flight with AD28 in the lower 4 km troposphere around Darwin/Tiwi Islands

5.2.3 Dornier Payload

Table 5.3: Instrumentation payload for the NERC Dornier

Instrument	**Description**
Aventech AIMMS-20 probe	GPS position, pressure, temperature, relative humidity, winds, 1 Hz
Aerodyne aerosol mass spectrometer	Aerosol size and composition (30-2000* nm)
TSI-3010 condensation particle Counter (CPC)	Total particles $>$ 10 nm (10 nm has 50% detection efficiency), 1 Hz
Grimm optical particle counter model 1.108	Aerosol size distribution, (0.3-2* μm, bins 0.10.2 μm, 0.16 Hz)
Ultra-high-sensitivity aerosol spectrometer	Aerosol size distribution (0.1-0.8 μm, 7.5-nm bins, 1 Hz)
DMT aerosol spectrometer probe ASP-100	Aerosol size distribution (0.2-2* μm, bins 0.03-0.5 μm, 0.1 Hz)
Forward scattering spectrometer probe (FSSP)	Aerosol and cloud-droplet size distribution (0.5-32 μm, bin 0.8 μm, 0.1 Hz)
Particle soot absorption spectrometer (PSAP)	Black carbon concentration (aerosol) ($\pm$ 1 μg m^{-3}, 0.2 Hz)
Filters	Coarse aerosol composition, whole flight accumulation
2B technologies model 202 ozone monitor	Ozone concentration ($\pm$ 2 ppbv, 0.1 Hz)
Aerolaser AL5003	Carbon monoxide concentration ($\pm$ 1 ppbv, 1 Hz)
Automatic tube sampler (ATS), 15 samples per flight	C4-C9 nonmethane hydrocarbons, monoterpenes, oxygenated volatile organic compounds OVOCs
Chemiluminescence/catalysis	NO/NO$_x$/NO$_y$
Miniature gas chromatograph	Halocarbons (Cl, Br, I; 36 min, $\pm$ 5%)

** Upper bound limited by inlet efficiency (see e.g. Allen et al. (2008))*

5.3 Condensation Particle Counter (CPC)

5.3.1 Basic Operation of the TSI 3010 CPC

The aerosol measurements reported here are primarily based on TSI 3010 condensation particle counters (CPCs) (Sem, 2002), two of which were flown on the Egrett and one on the Dornier. The latter, and one of the Egrett CPCs, operated with a lower cut-off of 10 nm in particle diameter (this is the 50% point on the instrument detection efficiency curve).

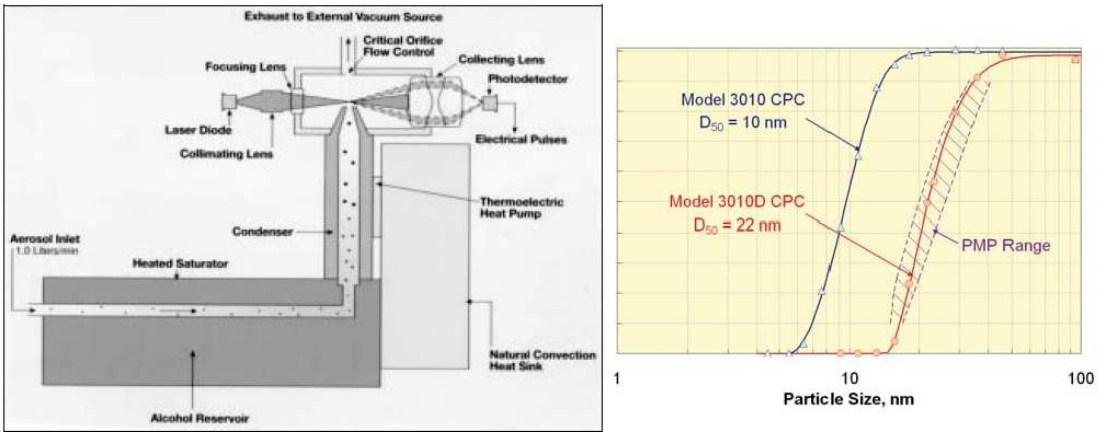

Figure 5.3: *left*: Schematic of the CPC operation, showing the saturator, condenser and photodetection system. *right*: The left-hand curve shows the efficiency of the TSI 3010 CPC (blue curve) against particle diameter.

The CPC has an operational flow rate of 1 litre/minute. Air passes through a heated saturator where alcohol is vapourised and allowed to diffuse into the sampled air, saturating it with alcohol vapour. The air/alcohol mixture then moves to a cooling condenser. As the air cools the alcohol becomes supersaturated (the partial pressure being greater than the equilibrium vapour pressure) in the air, therefore, the alcohol condenses onto the aerosol particles (which act as condensation nuclei, as in cloud droplet formation). The droplets grow, with further alcohol condensing onto the aerosol, until the droplets can be optically resolved. The CPC must maintain a steady and constant temperature difference between the saturator and the condenser, for the system to work as expected (17°C for a lower cut-off of 10 nm). The optical detection system is provided by a laser diode,

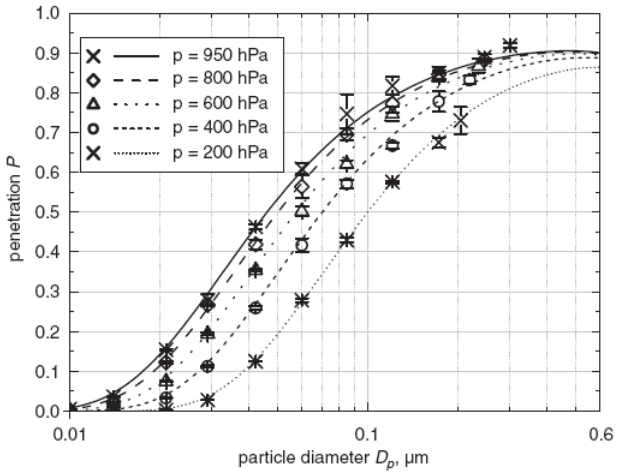

Figure 5.4: Efficiency curves for a TSI 3010 CPC fitted with 3 diffusion screens and running at a 1 litre/minute intake rate. The curves show theoretical particle penetration against particle size for various ambient pressures; the data points are taken from experiment. Work and figure taken from Feldpausch et al. (2006).

lenses, and photodetector set-up [see TSI. (2002) for full operational instructions; figure 5.3 shows the operation of the CPC and the efficiency curve].

The efficiency curve was described mathematically by Mertes et al. (1995), with the following formulae:

$$\begin{aligned} \eta_{cpc1} &= 1 - a\left(1 + \exp^{(D_p - D_1)/D_2}\right)^{-1}, \\ & D_p \geq D_0, \\ \eta_{cpc1} &= 1 \qquad\qquad D_p < D_0, \\ D_0 &= D_2 \ln(a-1) + D_1. \end{aligned} \tag{5.1}$$

η_{cpc1} yields a factor from 0 to 1 for the CPC detection efficiency. These formulae were used in the later modelling section to determine the point of initial CPC detection as an aerosol population increases in modal size (see chapter 9). Parameters of η_{cpc1} were determined by comparison with the measured particle detection efficiency of the TSI-3010 CPC (Mertes et al., 1995). For a temperature difference of $17°C$ between saturator and condenser, parameters were: a = 1.4, $D_1 = 8.9$ and $D_2 = 2.9$.

The second CPC used on the Egrett was fitted with 3 diffusion disks. Diffusion

disks (Knutson, 1999; Baron and Willeke, 2001; Feldpausch et al., 2006) are fine meshed screens that are fitted to the inlet of a CPC. The disks increase the lower cut-off point of the CPC by removing smaller aerosol from the flow. The disks work on the principle of deposition of aerosol (Baron and Willeke, 2001) on to the mesh screens; the more disk that are added, the higher the lower cut-off. In this case, there were 3 disks fitted, to give a lower cut-off, for the second CPC, of 40 nm at 1013 hPa (Feldpausch et al., 2006).

5.3.2 Quality assurance and control

The successful and reliable operation of an instrument is vital for the validity of the conclusions. In order to assess the quality of CPC data and to apply any quality controls, a thorough laboratory inspection was undertaken. The exact two CPCs that were present on the Egrett aircraft were run in parallel, under laboratory conditions, to check for consistent performance. The experiments allowed the two CPCs' efficiency curves to be derived and compared with the expected performance in the literature. The method used a Differential Mobility Particle Sizer (DMPS) set-up which contains the Differential Mobility Analyser (DMA) to select a monodisperse particle population and the CPCs to count the number density (Williams, 1999). A schematic of the experiment can be seen in figure 5.5 and the laboratory layout is shown in figure 5.6.

The set-up included a nebuliser to generate a polydisperse aerosol population, using butanol and an airflow to create aerosols via spray and surface bubble processes. This airflow was then dried using ammonium nitrate dissicate; next it was ionised using a radioactive source placed around a section of the flow pipes. The polydisperse aerosol population then enters the DMA in order to be size selected. A DMA separates charged particles due to their electrical mobility. Electrically charged particles move in the electrical field according to their electrical mobility. The DMA is a cylindrical capacitor consisting of an inner electrode (HV-Rod) and an outer electrode. The incoming sample flow containing the polydisperse aerosol was directed, together with laminar particle-free sheath air, parallel to the HV-Rod. Depending on their polarity the particles are accelerated either to the outer or the inner electrode. The particles whose deposition (at a certain voltage,

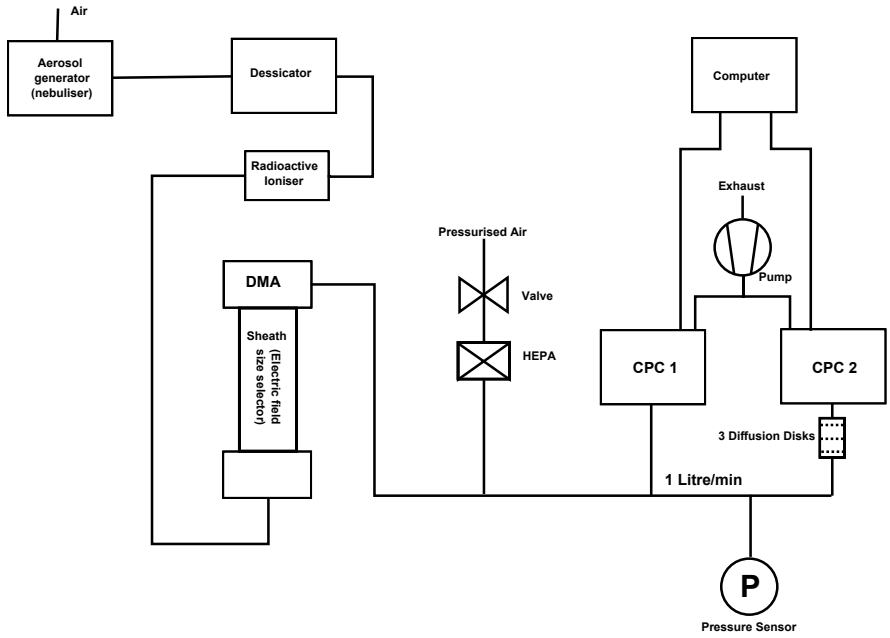

Figure 5.5: Schematic set-up for the CPC calibration experiment

i.e. electrical mobility) matched the position of the gap at the outlet of the DMA, pass through, and were therefore size classified. Following this, the monodisperse aerosol population exited the DMA and was then transported towards the CPCs. The air pressure at this stage is not usually sufficient to provide the 1 litre/minute needed for CPC usage. To augment the airflow an external air cylinder was used to increase the pressure. It was first cleaned using a HEPA filter and was then joined to the aerosol flow with a metal junction. A valve tap allowed the pressure of the external air source to be adjusted until the correct overall flow rate was achieved. The inflow was split into two branches: for the first CPC (CPC1) and the second, diffusion disk, CPC (CPC2) – the CPCs' exhausts were driven by a pump. The CPC particle count was then recorded on computer and the relevant flow rate was used to convert the count into a concentration per unit volume.

For a given size selection, the experiment was run for a minimum of 10 minutes in order to gain an average result and to reduce the standard deviation. For the smaller sizes (below $\sim$ 30 nm), this was complicated due to very low particle production rates from the nebuliser. The standard deviation was therefore higher in the lower particle sizes (below $\sim$ 30 nm). The average was taken for each size selection and then the ratio of the CPC1 average to the CPC2 average was calculated, together with the standard deviation. Figure 5.7 shows the data for

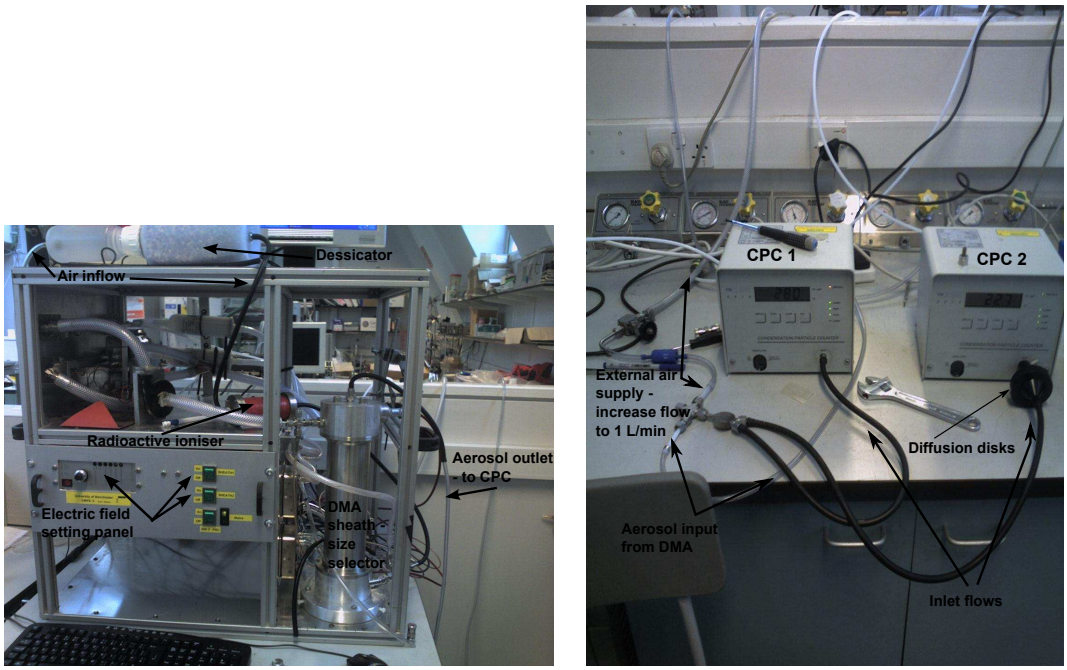

Figure 5.6: DMPA set-up experimental set-up. *Left*: Equipment used for aerosol generation including the DMA used for particle size selection. *Right*: Set-up of the two TSI 3010 CPCs during experimental tests.

the two CPCs when run in identical operation mode with no diffusion disks fitted (to CPC2).

This initial experiment demonstrates that the two CPCs were operating consistently throughout the 10 to 700 nm size range. The only divergence occurs towards 10 nm (50% detection efficiency for TSI 3010 CPC models) with on approximate 20% offset but with a very large experimental variance it is difficult to conclude that this is due to an intrinsic instrumentation offset.

Measuring the performance of the diffusion disks, in comparison to standard operation mode (no disks), was of vital importance for the ACTIVE dataset. The literature (Knutson, 1999; Baron and Willeke, 2001; Feldpausch et al., 2006) provided a value of 41 nm for the lower detection limit (50% efficiency) and is was necessary to replicate this in the laboratory for reliable subsequent data analysis.

Figure 5.8 shows the experimental effect of adding 3 diffusion disks to the second CPC - the ratio of CPC2 to CPC1 is shown as a function of particle size. The red dashed line indicates 41 nm, the expected lower (50% efficiency) detection limit, for standard temperature and pressure (1013 hPa, 297 K). It can be seen

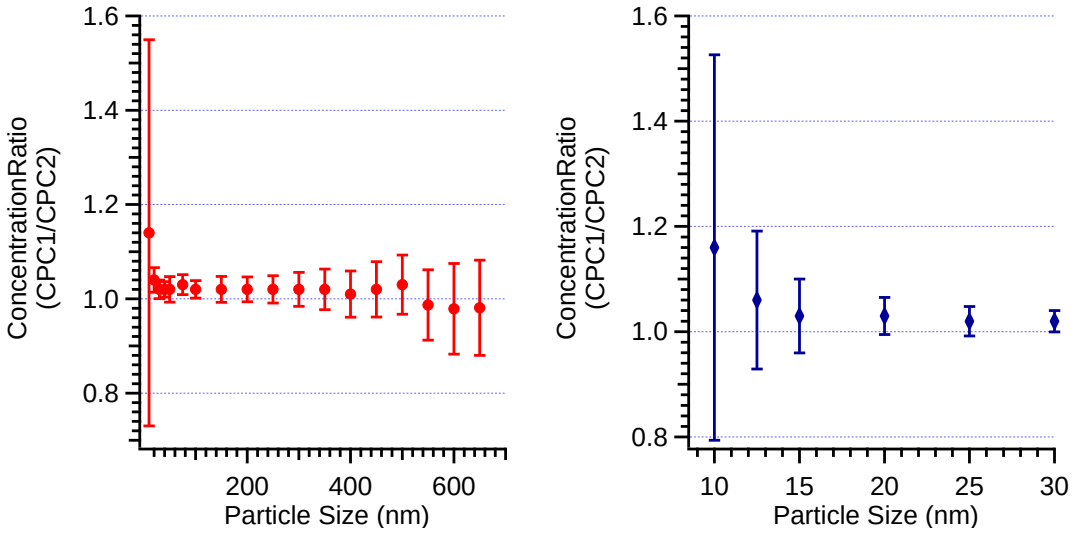

Figure 5.7: Plots from the CPC comparison laboratory experiments. Note that the two CPCs were run in identical operation mode: CPC2 was not fitted with 3 diffusion disks. *Left*: The ratio of measured CPC1 concentration to measured CPC2 concentration against size particle selection. *Right*: A more detailed examination of the lower sized particles (below 30 nm).

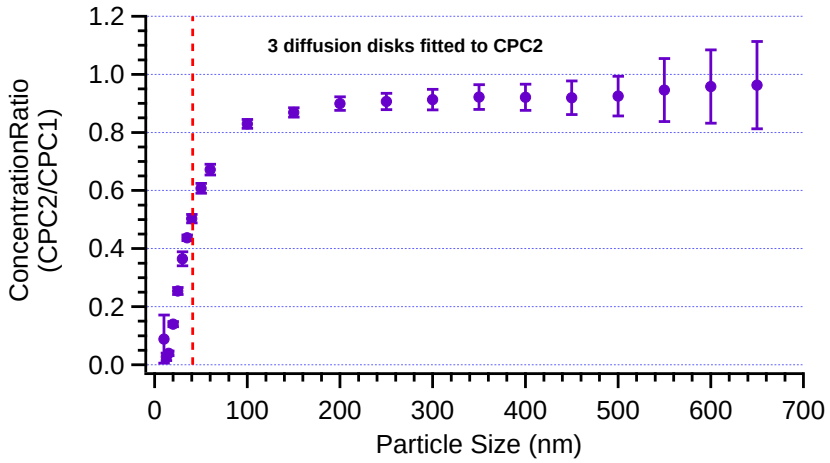

Figure 5.8: Plots from the CPC comparison laboratory experiments. In this case, CPC2 was fitted with 3 diffusion disks. The plot shows the ratio of measured CPC2 concentration to measured CPC1 concentration against size particle selection. The dashed red line shows 41 nm where the 50% detection efficiency level is expected (Knutson, 1999; Baron and Willeke, 2001; Feldpausch et al., 2006).

that the experimental data agreed well with the literature data (e.g. Feldpausch et al., 2006).

5.3.3 Pressure Correction

Low pressure, low temperatures and variability of moisture are all factors at high altitude that can affect the reliability of the CPC. Seifert et al. (2004b) conducted pressure chamber (AIDA) experiment to determine a count correction for the CPC, to account for low pressure efficiency loss:

$$\text{count efficiency}, \eta = 1 - a\exp(-bp/p_0) \tag{5.2}$$

where, $a = 1.627$, $b = 16.215$, $p_0 = 1013$ hPa, p (hPa) - is the ambient pressure. This formula is applicable over a pressure range of 100 to 1000 hPa with a precision of $\pm 2\%$. This expression (Seifert et al., 2004b) has been applied to the Egrett data and the pressure was derived from the Egrett positional data. It should be noted that for a typical UT/TTL pressure of 200 hPa, the CPC still works with a relatively high efficiency of $\sim 93\%$ compared to 1013 hPa operation.

For the second CPC, three diffusion disks were attached to increase the lower cut-off point of the CPC by removing smaller aerosol from the flow. At 1013 mb this cut-off was 41 nm Feldpausch et al. (2006), but it increased with reducing ambient pressure, and a value of 100 nm was used here for the Egrett operating altitude (150 - 200 hPa). This was determined from the 200 hPa efficiency curve presented in Feldpausch et al. (2006) (figure 5.4).

5.4 Egrett Inlet

The Egrett aerosol inlet (figures 5.10 and 5.11) was mounted on the port wing of the aeroplane, protruding forward into the flow. It was built to a similar design to that used in the German CARIBIC experiment (Hermann et al., 2001), to provide isokinetic sampling (the flow speed inside the inlet tip matches the undisturbed flow past the inlet housing). All inlet systems suffer from some form of gas and

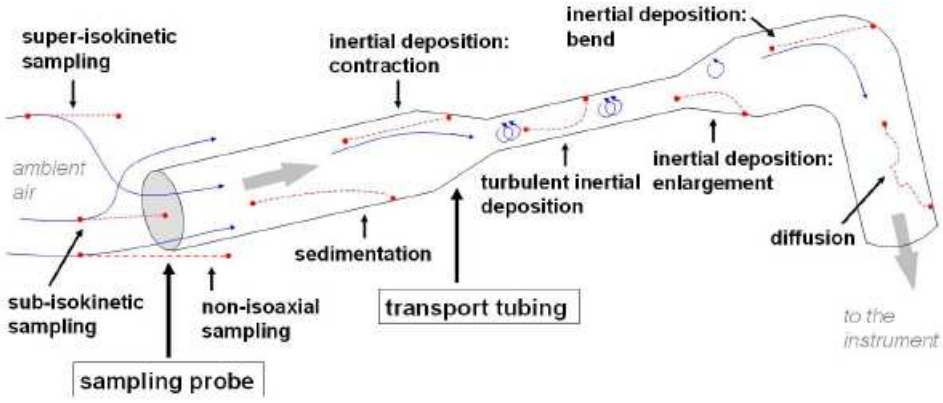

Figure 5.9: Schematic showing typical mechanisms of particle loss during flow in a pipe (Note: not representative of the inlet and pipe layout used on the Egrett during ACTIVE – see later figures 5.10 and 5.11). Figure from von der Weiden et al. (2009)

particle losses during intake; inlet designers must carefully consider the particle dynamics for the desired size range, to reduce the particle losses. Computational fluid dynamics [CFD] and laboratory studies are often used to optimise particle transport through the inlet.

There are various ways in which particles may be 'lost' during transportation and much research is focused on reducing losses. The design of the inlet and the transportation piping can have a large impact on the degree of particle losses and hence the potential for underestimating the particle population. The flow regime inside the tubing, whether laminar or turbulent, can also have an effect on particle losses. Laminar flow is usually found below a Reynolds number of 2000. The Reynolds number is given by, $Re = Ud/\nu$, where U is the flow speed, d is the characteristic length – in this case the tube diameter – and ν is the kinematic viscosity [of air]. Above Re = 4000, flow typically becomes more turbulent with the generation of eddies in the stream – this can enhance some of the particle loss mechanisms. Typical loss mechanisms for particles in tubes include laminar or turbulent diffusion, turbulent inertial deposition, inertial deposition in bends and gravitational sedimentation (e.g. Hermann et al., 2001; von der Weiden et al., 2009). Figure 5.9 shows a schematic of the some of the common particle loss mechanisms that occur in inlet and piping systems.

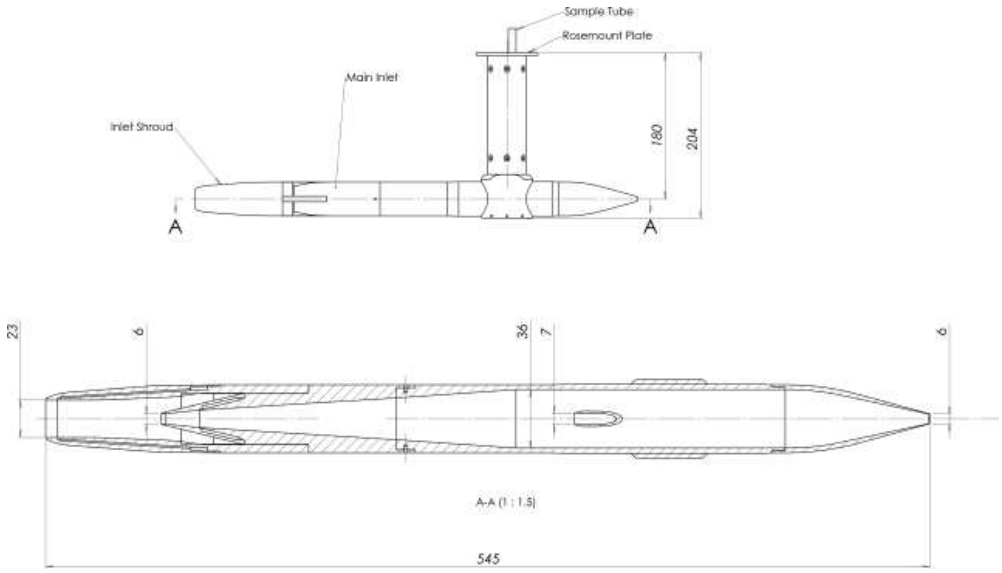

Figure 5.10: Cross-section of the Egrett Inlet (mm units); the CPCs drew air from this supply.

Gravitational settling of particles can be an important loss process for larger particles. For the two CPCs used during ACTIVE, where only submicron particles were investigated, gravitational settling can be neglected. The reduction in supermicron particles due to settling (and inertial deposition) allowed the upper detection limit to be more confidently defined as 1 μm, which was desired for the subsequent data analysis. *Diffusive deposition* (laminar or turbulent) is always present in tube flow systems. As the tube walls act as particle sinks, a radial concentration gradient is established inside the tube which results in a particle flux toward the walls through the action of Brownian motion (Hermann et al., 2001). A turbulent regime results in an increase in diffusional losses for larger sized particles. The turbulent inertial deposition is the inertial deposition loss of large particles due to the curved streamlines (eddies) in a turbulent flow. *Inertial deposition* losses manifest themselves at piping bends and contractions as a result of the straighter streamlines followed by larger particles. The larger particles continue on a straight trajectory and are deposited on the pipe walls at bends in the flow. A similar effect is also observed in *turbulent inertial deposition*. In this example, larger particles are unable to follow the curved streamlines of the flow eddies and are therefore deposited on the walls of the pipe (von der Weiden et al., 2009).

Figure 5.11: Port pylon of the Egrett. In the foreground is the CAS probe; to the rear and left (as viewed) is the aerosol inlet.

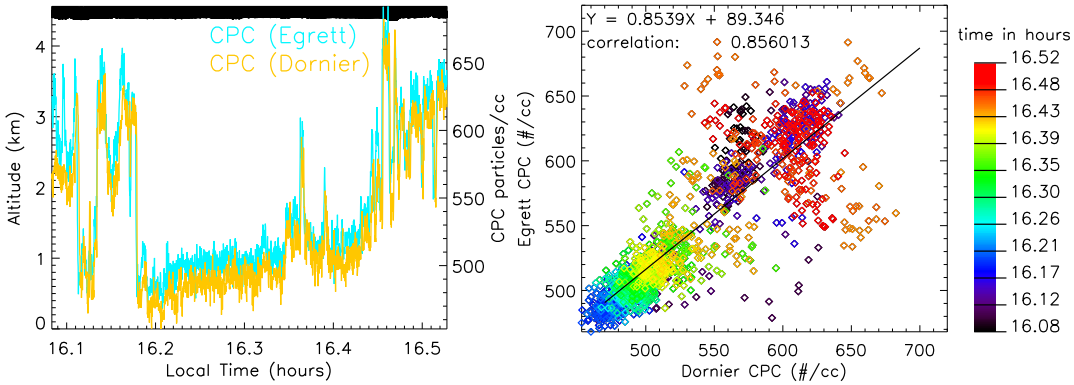

Figure 5.12: Egrett and Dornier CPC data on the intercomparison flight. *left*: time line for the two CPCs *right*: scatter plot, showing the offset between the two more clearly.

There was, however, a further 7 m of stainless steel piping leading from the inlet to the fuselage of the aircraft where the CPCs were mounted, and it is possible that some of the aerosol sample would have been lost via deposition to the walls in transit through this piping. An estimate of the severity of this loss was obtained by an intercomparison flight between the Egrett and the identical CPC on the Dornier, where the pipework was only 2 m (for details of the Dornier aerosol inlet, see Allen et al. (2008)). The two aircraft were flown 'wing-tip-to-wing-tip' to allow sampling of similar air mass; matching instrumentation from each aircraft should provided statistically identical results. The intercomparison flight took place on the 5th December 2005 (see figure 5.12). Despite the increased inlet

length, the Egrett instrument in fact measured a slightly higher concentration than the Dornier's; the scatter seems to suggest that it was a constant offset, which would indicate a slight instrumental difference between the two CPCs. These results point to minimal impact on the Egrett CPC measurement of the long pipe run. Furthermore, theoretically based calculations were made to find the expected efficiency of such an inlet and transportation system (see following section).

Examination of the data also showed that there were no spurious data spikes when the aircraft was in cirrus cloud, so we can conclude that ice shattering on the inlet, was not a significant source of particles in the 10 - 1000 nm range – this is certainly an issue for large particle detectors with Rosemount design (McFarquhar et al., 2007). However, the IAGOS D4.5 study (Petzold, priv. comm. 2009) clearly demonstrated, for DLR isokinetic and Rosemount inlet comparisons, that there were no contamination issues as a result of passage through cirrus cloud for the isokinetic set-up.

5.4.1 Inlet efficiency calculations

A particle loss calculator was used to find the efficiency of the sampling probe and the transportation piping through the Egrett. These calculations were based on a computational fluid dynamics (CFD) program by von der Weiden et al. (2009). The program allows implementation of non-isoaxial and non-isokinetic aerosol sampling (but in this study, the sampling probe was known to be of isokinetic design), aerosol diffusion, sedimentation, turbulent inertial deposition and inertial deposition in bends and contractions of tubing.

The design and layout of the Egrett sampling system were inputted into the particle loss calculator in order to determine a total transportation efficiency for particles. Based on schematics of the inlet and aircraft, such as in figures 5.10 and 5.11, the dimensions and orientations of the tubing system were entered into the calculator. The piping had a 6 mm diameter and contained four bends with an overall length of approximately 7 m; the aspiration of the inlet was 0° to the horizontal (iosaxial) for the majority of the flight time (the Egrett performed ascents and descents relatively quickly and was assumed level for this

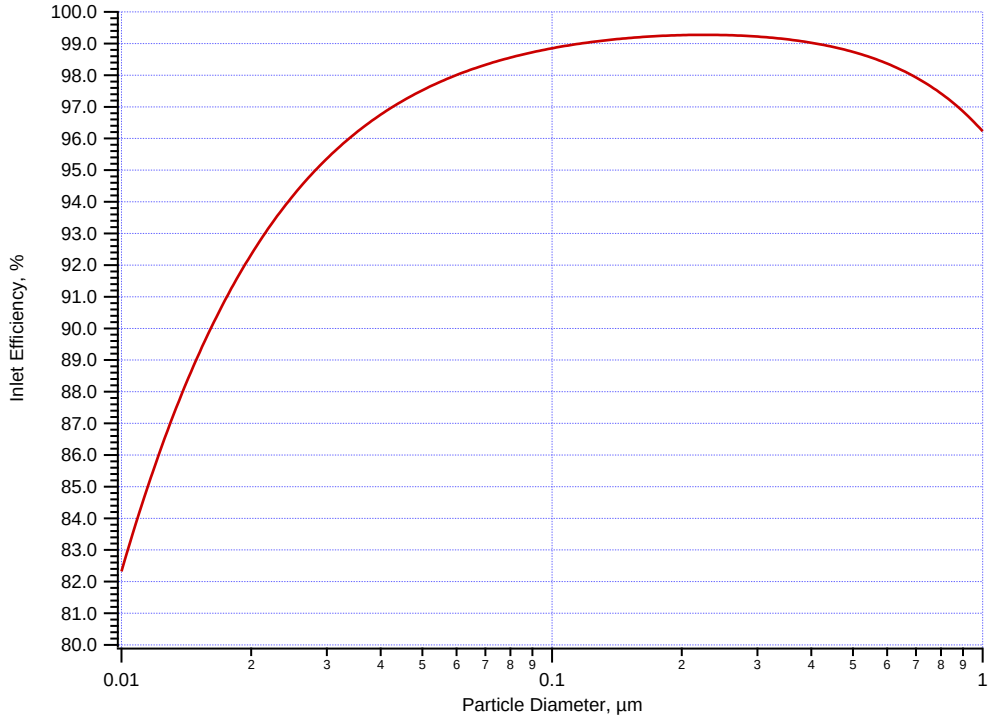

Figure 5.13: Penetration efficiency against particle diameter for the inlet and piping set-up, which transported particles to the CPC onboard the Egrett.

calculation). The flow rate in the sampling system was 10 l min^{-1}, from which the CPC drew its air supply of 1 l min^{-1}. The particle losses were calculated using this information and, incorporating the loss mechanisms described above, the overall particle efficiency for the inlet was found.

Figure 5.13 shows the penetration efficiency for the Egrett inlet and the transportation piping that leads to the CPC holding bay in the fuselage. The lower diameter particles (10 nm) have a penetration of approximately 82% with the main loss mechanism being diffusion losses to the walls; the efficiency of the inlet soon recovers as the particle size increases. Beyond 1 μm, penetration again decreases due to the effect of inertial deposition: larger particles tend to follow straight line streamlines due to inertia, resulting in wall impaction at bends and contractions. Therefore the data recorded by the two CPCs (measuring 10 to 1000 nm and 100 to 1000 nm) suffered an error of between 18% to 1% and 1% to 4%, respectively. Due to lack of a detailed size distribution across the size range, it was not possible to define the exact particle distribution. Thus it was not known where in the distribution the greatest particle loss occurred. However, there was

a relatively broad range of high efficiency seen in the inlet system (greater than 90% for most of the particle size range – 10 to 1000 nm). Ultimately, the CPC derived data (i.e. particle number concentration) had a possible particle loss error of between 1% and 18%.

5.5 Presentation of data

5.5.1 Data quality

The data in ACTIVE were analysed and inspected to check for anomalies and for general compatibility. The CPC data were standardised into digital format; a statistical method was used if data were recorded in analogue (the majority of data were recorded in both formats and only a few early flights had only analogue data: AE04, AE06, AE07). Flight data which included both analogue and digital CPC data were used to find an average offset factor (the mean of the analogue – serial difference was 0.099 ± 0.006). The offset was also tested to confirm that there was no correlation with temperature (during pressure-altitude changes in-flight). Figure 5.14 shows the affect of altitude on the offset. There was seen to be no systematic error in the offset as the instrumentation changed altitude (thus temperature and pressure) and a very low correlation coefficient. It can be seen that the offset variance was greatest beyond $\sim$11 km. It were data from these higher altitudes that helped to push the correction factor towards the $\sim$10% seen in this analysis. Therefore, the data analysis was continued with the correction factor found earlier (0.099) and the CPC aerosol dataset was standardised to the digital format.

The data were also corrected for the universal offset that exists between Coordinated Universal Time (UTC) and Global Positioning System (GPS) since data were recorded using both systems. There were two data loggers on the Egrett: one was fitted in the left fuselage the other in the right. UTC is a time standard based on International Atomic Time (TAI) with leap seconds added at irregular intervals to compensate for the Earth's slowing rotation; the GPS satellite system does not correct the time offset due to the earth's rotation. Therefore, since their inception, these two time standards have contained an offset (GPS was set to match UTC in 1980 but has since diverged). The right fuselage logger

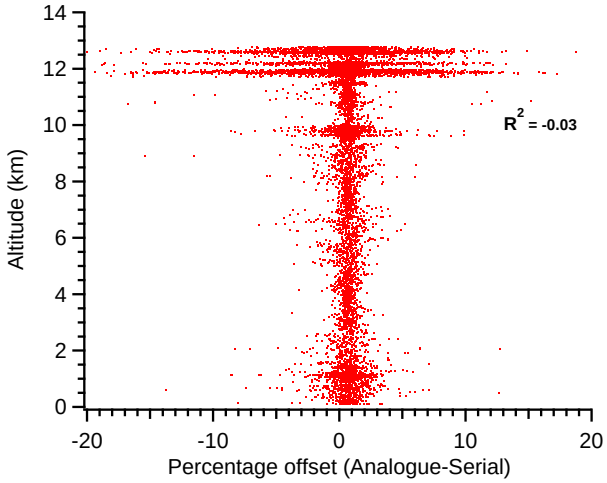

Figure 5.14: A scatter plot for the concentration offset between the analogue data and the digital (serial) data, against the altitude of the aircraft. The pearson correlation coefficient for offset and altitude was shown to be very low, -0.03. The offset was thus concluded to be uncorrelated.

recorded GPS position and velocity, attitude data (pitch, roll, etc.), analogue data (temperature, pressure, etc.) from the right wing pylon and CPCs, CR-2 and O_3 data, from the fuselage bays. The right fuselage logger recorded GPS data from 27 November and the TSI serial data. The two TSI CPCs that were used during the campaign had analogue data recorded by the right fuselage logger and serial data recorded by the left fuselage. The loggers sent 1 Hz character strings to the TSIs and the TSIs returned an ASCII string; this was then given a time stamp by the logger. The left logger used GPS satellite time and the right logger used UTC. There was a time difference of -13 seconds in 2005 and -14 seconds in 2006, between GPS and UTC time (that is, the GPS time is ahead of the UTC time) – serial data were always used where possible. This was confirmed by the intercomparison flights (see figure 5.12); the time logging difference and the additional inlet transport time were visible in the scatter plot correlation calculations (section 5.4).

During analysis, data error codes (usually defined as 'Not-a-Number' – NaN – in electronics and computing) were discarded. The codes are generated by the software involved in the data collection process and indicate when some part of the collection system is malfunctioning. The error codes could have their own channel (like an own attribute) or they could come as a part of the ordinary data. In

some instrumentation, the error codes were recorded as continuous out-of-bound values, such as negative measurements for particle concentrations. Flights AE04, AE06 and AE07 were flights that were particularly affected by excessive error codes. In these cases, sections of non-error corrupt data were extracted, if it were continuous for at least 30 minutes. This data quality assessment was undertaken with a combination of programmed algorithms and visual inspection.

5.5.2 Data presentation

Egrett data

All the particle data in this experiment were adjusted to standard temperature pressure (STP) units (equivalent to ground level measurements, 1013 hPa and 297 K) and are presented as number.cm^{-3} concentrations.

The aerosol data from the Egrett's first CPC worked in standard (referred to as CPC1 hereafter) operation and measured particles number concentrations for 10 nm at 50% efficiency (see figure 5.3) – the number concentration cm^{-3} (STP) will also be referred to by N_{10}. The second CPC (referred to as CPC2) measured 100 nm at 50% efficiency (figure 5.4) – these data concentrations cm^{-3} (STP) will also be referred to by N_{100}. The two CPCs have a theoretical upper limit of 3 μm but the CPCs were taken to have a more realistic upper detection of 1000 nm (see efficiency curve, figure 5.13). This was due to the effect of the isokinetic inlet and curved piping that were expected to have very low transportation efficiency for supermicron particles (Hermann et al., 2001). It is important to consider the wide efficiency curve of CPC2 (3 diffusion disks – see figure 5.4) and the fact that there will be some overlap with the data of CPC1 because of this – a factor that will be discussed during the analysis. The significant transport time, 7 seconds, for air to travel through the inlet and pipework was taken into account and the data time stamps were adjusted for this offset to make it compatible to other datasets.

The Cloud Particle Imager (CPI) was flown on the Egrett to detect a wide size range of cloud particles (5 - 875 μm). The CPI captures images of ice crystals (Lawson et al., 1998) and delivers a size measurement based on the image. In this

investigation, CPI number concentrations > 0.05 particle cm^{-3} in the 15 - 55 μm size range was used to define when the aircraft was in cloud. The concentration of cloud particles were also adjusted to STP conditions and were given in number cm^{-3} – the concentration herein is referred to as N_{cloud}.

Carbon monoxide was measured on the Egrett using resonance fluorescence (Volz and Kley, 1985; Gerbig et al., 1999). The instrument deployed in ACTIVE was custom-built around the fluorescence block of an AERO-Laser, Model 502. The instrument was regularly calibrated, both on the ground and during flight. Data were collected at a frequency of 1 Hz with a precision of ±2 ppbv and an accuracy of ±3 ppbv (5% at mixing ratios > 60 ppb).

Dornier data

As with Egrett data, the Dornier concentration data were also adjusted to STP levels and given in particles.cm^{-3}.

The single CPC on the Dornier worked in standard operation: 50% efficiency at 10 nm. The ASP size-binned data were used to define concentrations for the larger accumulation sized particles, 0.2 to 1.0 μm, referred to by $N_{200-1000}$. The ASP data were also used to curtail the CPC data to 200 nm; the Dornier CPC therefore defined particle concentrations for a size range of 10 to 200 nm, referred to by N_{10-200}. The Dornier and Egrett CPCs were seen to measure concentration data consistently during the intercomparison flight AE10 versus AD12 (see section 5.4 and figure 5.12).

The Dornier FSSP (Pinnick et al., 1981; Cerni, 1983) was used to define areas of cloud during the flight. A size range of 10 - 50 μm was used to define cloud particles and concentrations above 0.05 cm^{-3} were deemed to be cloud regions. These data were used to extract only aerosol data that were gathered in cloud-free air.

5.5.3 Statistical analysis

A range of statistical methods were used to analysis the data. In particular averaging and statistical dispersion (minimum, maximum, range, quartiles, etc.) were measured with box-whisker plots and histograms. Histograms are useful for giving a visual representation of the population distribution; box-whisker plots summarise many of the statistical descriptors of a distribution in a straightforward and direct manner. The median was the preferred averaging technique due to the potentially unsymmetrical (non-normal distribution) nature of in-situ geophysical data. The median gives a truer representation of the 'middle' value in cases where data spikes might occur (for whatever reason: real measurements that are short-lived and unrepresentative of the population, instrumentation artifacts, etc.) The histograms were analysed to verify the degree to which they fit normal (Gaussian) distributions. This was done with a number of methodologies, such as skewness, kurtosis, KolmogorovSmirnov test, etc. Skewness is a measure of the asymmetry of the probability distribution of a real-valued random variable. A negative skew indicates that the 'tail' on the left side of the probability density function is longer than the right side and the bulk of the values (including the median) lie to the right of the mean. A positive skew indicates that the tail on the right side is longer than the left side and the bulk of the values lie to the left of the mean. A zero value indicates that the values are relatively evenly distributed on both sides of the mean, typically but not necessarily implying a symmetric distribution. In probability theory and statistics, kurtosis is a measure of the'peakedness' of the probability distribution of a real-valued random variable. Higher kurtosis means more of the variance is the result of infrequent extreme deviations, as opposed to frequent modestly sized deviations.

The instrumentation was also smoothed depending on the time resolution of data retrieval and the degree of noise. Some instruments, such as the CO analyser, underwent regular calibration tests during the flight, resulting in spurious, periodic, spikes in the data. A moving average (median) of 20 seconds was used to smooth the data from the CO analyser, CPI and CAS instruments. These data were found to have noisy outputs at times, particularly in the case of the cloud probes at low particle concentrations. A smaller median smoothing time than that of the instruments' resolution was avoided during this study.

Furthermore, when analysing the data from the Egrett, the data were stratified

in order to extract only data obtained above an altitude of 10 km. During the analysis of Egrett data (chapters 7 and 8) and the statistical discussion and summary, all data that is termed UT/TTL is taken from 10 km and above.

For the cloud and cloud-free discussion in the Egrett data chapter (7), the data were sorted using a threshold concentration taken from the cloud probe CPI. A particle number density greater than 0.05 particle.cm^{-3} (STP) in the 15 - 55 μm size range was used to define when the aircraft was in cloud. The concentration of cloud particles are also adjusted to STP conditions and are given in number.cm^{-3} – the concentration will be referred to as N_{cloud}. This form of threshold sorting was done using a 50 second block median averaging (see section 5.5.4 below). All UT/TTL data were block averaged and then the median CPI cloud particle concentration was used to determine whether the 'data block' was in-cloud [$\geq$ than 0.05 particle cm^{-3} (STP)] or out-of-cloud [less than 0.05 particle cm^{-3} (STP)]. These median data blocks were then extracted for subsequent statistical analysis, blocks that included the median concentrations of N_{10}, N_{100}, CO, cloud particles, etc.

5.5.4 Median smoothing – wind data

During the nucleation investigation in chapter 8, wind data were an important part of the analysis due to its ability to define the trajectory of the air mass that was being sampled. The wind was recorded with a 1 second resolution by the Egrett's basic instrumentation set. Since wind strongly fluctuates over short space and times, due to turbulent small-scale eddies, the data were median smoothed in order reduce the short time period variations while still retaining the overall trend. The median smoothing operation required the specification of range over which to average. Similar to the definition of Knudsen number, $K_n = \lambda/L$, where λ defines the small-scale nature of the 'medium' in which the analysis is being done (in fluid dynamics, this would be the mean free path, of water or air, for instance) and L is the dimension of the 'object' in the medium (in fluid dynamics, this could be an aircraft aerofoil). Using this analogy for the data smoothing, the medium would be the resolution of the wind data (how much the data were smoothed) converted into a length using the aircraft flight speed; the Egrett had a typical cruising speed of 100 ms^{-1} – therefore, a 50 second smoothing would

be the equivalent of a 5 km length. The object of interest would, in this case, be the dimension of a typical anvil cloud. The aim of the Knudsen number is to find a compromise between too low and too high a number ($\lambda \ll K_n \ll L$), that is, neither too close to the small-scale structure of the medium nor on a scale of the object under investigation (this would lose much of the finer detail of the data).

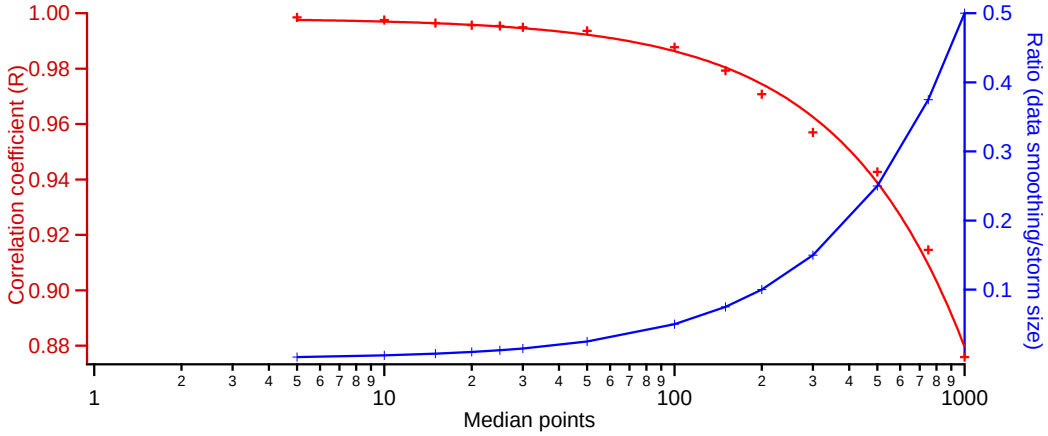

Figure 5.15: Plot (red data) showing the pearson correlation coefficient for unsmoothed U-wind data (1 sec) against the median smoothed U-wind data. The coefficient is plotted against changing median range; median points indicates how many points, either side of a data point, were involved in the median calculation. For example, a median points value of 25 would indicate that a data point would be averaged with 25 values below and 25 values above, making 50 in total. The ratio of the median smoothing (converted from time into length, using the Egrett flight speed of 100 ms^{-1}) against a typical ACTIVE storm anvil, 200 km, is shown by the blue plot.

The east-west wind data (U-wind) from the Egrett's AE19 flight were used to investigate the effect of median smoothing and to determine how much to add to the data during the wind trajectory analysis, in chapter 8. Figure 5.15 shows the wind data analysis: pearson correlation for smoothed U-wind data against unsmoothed (1 sec) data. The x-axis is the degree of median averaging applied to each data point; the value is the number of data points *either side* of a given point, over which the averaging took place. The second plot (blue) is the ratio between the smoothing 'length' (the median smoothing value converted to a length, using the Egrett flight speed of 100 ms^{-1}) and the length scale of the system under investigation: the convective anvils encountered during ACTIVE – typically $\sim$ 200 km. This pseudo-Knudsen number gives some idea of how the increased smoothing gradually reduces the fine detail of the data; as the smoothing

length approaches 1000 seconds, the data approaches a 0.5 ratio with the storm dimension – this is far too coarse to study the details of the storm. A desirable median smoothing range should retain a pearson correlation coefficient close to unity while also reducing the small-scale turbulent structure of 1 second wind data. A median smoothing range between 20 and 50 seconds appears to be the greatest possible whilst still preserving a pearson coefficient of almost unity; this should be sufficiently large to remove some of the unwanted small-scale fluctuations while still be significantly smaller than the length scale of an convective storm (almost two orders of magnitude: a ratio of $\sim$ 0.01 to 0.05). A median average of 50 seconds (25 either side), or 5 km in spatial length, was used during the wind projection analysis of chapter 8; all data that were investigate using wind trajectories as part of the analysis were also averaged into 50 second blocks.

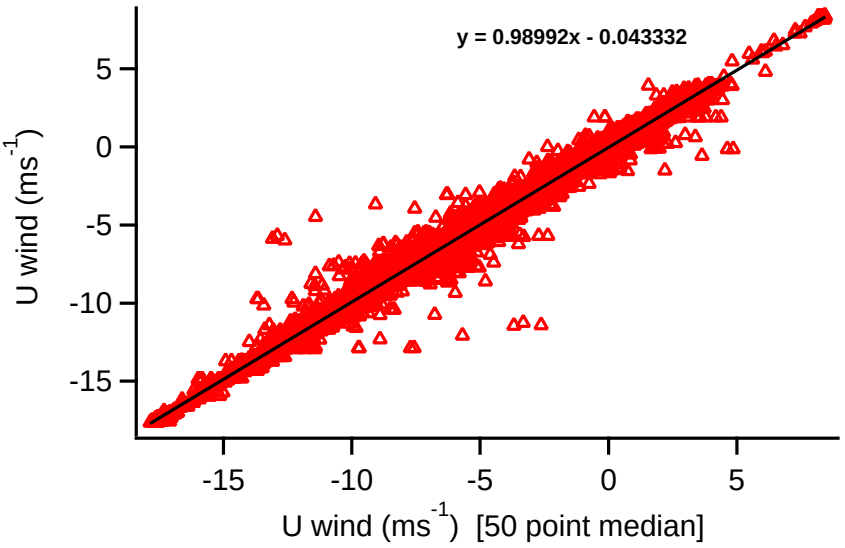

Figure 5.16: Scatter plot of the unsmoothed U-wind data (1 second) against the 50 second median smoothed U-wind data. The line of best fit is shown in black together with its linear equation.

Figure 5.16 shows the scatter plot for the unsmoothed U-wind data (1 second) against the 50 second median smoothed U-wind data, together with the best-fit line. It can be seen that the smoothed data is very well correlated with the unsmoothed data ($\sim$ 0.98).

Figure 5.17 shows the effect of the 50 second median smoothing when applied to an arbitrary section of U-wind data. The section is 500 seconds long and taken from flight AE19. It can be seen that the unsmoothed data had a lot of detail

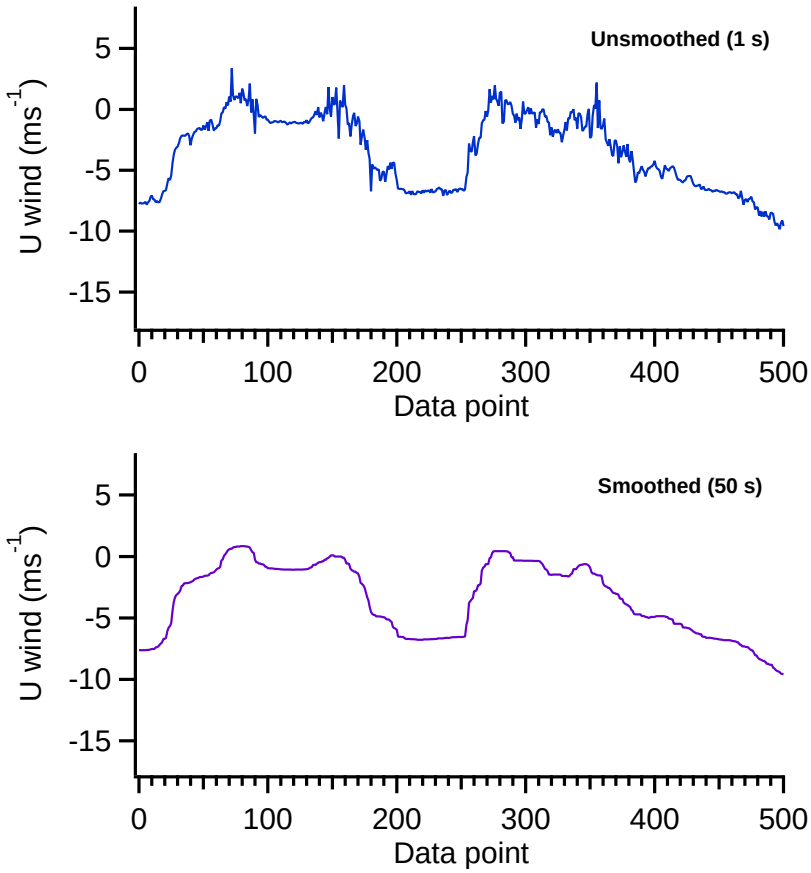

Figure 5.17: The effect of smoothing U-wind data is demonstrated by these two images. *Top:* shows a 500 second section of data from flight AE19 with no smoothing applied (1 second resolution). *Bottom:* the same 500 second section but with a 50 second median smoothing applied.

that was not particularly relevant to the study of the freestream outflow from large convective anvils: the turbulent fluctuations were unwanted characteristics that can be smoothed away. The smoothing procedure removed much of the finer detail that lasted for only seconds or tens of seconds whilst the main trend of the data was retained.

Chapter 6

Results from the PBL

6.1 Aerosol in the PBL

As convection takes place, the PBL air undergoes significant uplift into the free troposphere and beyond to the UT/TTL. This uplift can carry many aerosols and trace gases; this was discussed in detail in Allen et al. (2008) and chapter 4. It is these constituents that can play an important role in the evolution of the convective storm and the cloud particles that form. Further to the study by Allen et al. (2008), this section will present the data from the Dornier's single CPC; the CPC measures from 10 nm and above (up to ~ 3 μm) but data from the ASP were used to curtail the data range from 10 to 200 nm. The data are presented to show the typical PBL aerosol loading (data were only taken between 0.5 and 2 km) throughout the ACTIVE campaign, during the six identified climatic phases. This allowed comparisons to be made with the aerosol concentrations in the TTL. In particular, any significant changes from PBL to TTL would possibly indicate some mechanism at work. However, the simplistic view of PBL uplift transporting only the lower few kilometres of the local atmosphere to the UT/TTL is not strictly true. There is believed to be a series of levels and periods in convective generation when entrainment/detrainment occur; this can happen at all levels through the PBL and into the free troposphere. This implies that there would be a much more varied air loading signature in the UT/TTL than that expected from the local PBL alone (Mari et al., 2000; Heyes et al., 2009). Back trajectory analysis showed considerable long-range transport occurs in the free troposphere

– on an almost hemispheric scale (Allen et al., 2008; Froyd et al., 2009).

Figure 6.1 shows Dornier CPC data summarised for the six ACTIVE phases. The Dornier data were taken from the lower 2 km of the troposphere in cloud-free sections of sky – the FSSP data were used to denote cloud regions and concentration (STP) below 0.05 particles.cm^{-3} were deemed as cloud-free. These clear-sky regions were divided into 5 km (approximately 60 seconds of flight) for smoothing and averaging purposes. These sections were then median averaged and used in the general statistical analysis for the Dornier. The size range was taken to be 10 to 200 nm, by the fact that the CPC 50% efficiency detection size was 10 nm, and measured theoretically as high as 3 μm; the ASP size-binned data were then used to cut the CPC data down to a maximum detection size of 200 nm.

The histogram analysis for the mini-monsoon, premonsoon, inactive monsoon and monsoon break show the mean concentrations to be between 500 and 1000 particles cm^{-3}, with probability dropping rapidly for higher concentrations. Two notable exceptions during ACTIVE were the biomass burning period and the active monsoon. In these cases, there was a spread of the distribution into as high a concentrations as 1000 to 2000 cm^{-3} with probabilities up to 10%. It would be expected that there were an abundance of small aerosols present during the biomass burning period as a result of combustion by-products. Both primary and secondary aerosol can be readily released and formed due to the wide variety of organic compounds that are present during biomass burning (McMeeking et al., 2009). In the active monsoon the mean concentration was shifted towards 1000 cm^{-3}; the distribution also showed a much greater variability than any other phase besides the biomass period. The active monsoon has been analysed chemically and the aerosol composition has been found to be sulphate dominated with a low organic mass fraction (see figure 4.1 and Allen et al. (2008)). This suggested to Allen et al. (2008), due to the maritime wind direction, that the aerosol population in the active monsoon PBL was influenced by oceanic mechanisms such as sea spray production, DMS, cloud processing and sedimentation, and possibly coastal nucleation due to iodine and bromine compounds. The spread in the concentration distribution could reflect the range of maritime mechanism and the higher mean could be as a result of higher production rates for these

Table 6.1: Statistics for the Dornier CPC data during the six climatological phases. Aerosol size range: 10 to 200 nm. See figure 6.1 for histograms.

Period	Mean[a]	Median[a]	Standard Deviation[a]	Skew	Kurtosis	K-S test[b]	
						D value	Critical
Biomass burning	1040	714	700	2.7	10.1	0.19	0.08
Mini-monsoon	823	609	756	4.4	24.5	0.34	0.12
Premonsoon	598	518	259	3.9	26.9	0.19	0.07
Active monsoon	1240	1024	1013	5.4	47.7	0.15	0.08
Inactive monsoon	431	360	341	7.4	87.0	0.26	0.07
Monsoon break	669	492	775	6.7	56.0	0.32	0.04

[a] units are standard particles cm^{-3}.
[b] 'Kolmogorov-Smirnov test' conducted in order to test the hypothesis that the data are normally distributed. A 'D value' large than the 'critical value' indicates that the hypothesis should be rejected.

processes. The statistics (table 6.1) also confirm that the higher particle concentrations were detected in the biomass burning and active monsoon phases with much higher mean concentrations. The skewness and kurtosis are seen to show a general increase from the first campaign to the second. This suggests that there were more frequent occurrences of extreme concentration measurements during the final three phases (second campaign). This could have been due to sampling differences between the first and second campaign or if it is a real reflection of the climatology, it could reflect more varied sources of aerosols.

In figure 6.2 the 0.2 to 1.0 μm sized particles were analysed in histogram form. The data were taken from the Dornier ASP instrument that had a size range between 0.2 and 2.0 μm and adjustable size bins for categorization; the analysis was based on the same method as that used for the CPC data: 5 km size sections were median averaged. The size range 0.2 to 1.0 μm was used because it represents the typical Cloud Condensation Nuclei (CCN) range. These data therefore represented the PBL distribution for cloud forming nuclei that could be uplifted during convection – these particles are expected to play an important role on cloud particle production in convective updraughts (Wang, 2005a,b). During the first three phases (first campaign) the concentration distribution tended to have a similar mean value of $\sim$ 100 cm^{-3} but with a greater variability in the biomass burning phase – again, this probably reflects the variability in organic compounds that are released during biomass combustion. The most dramatic

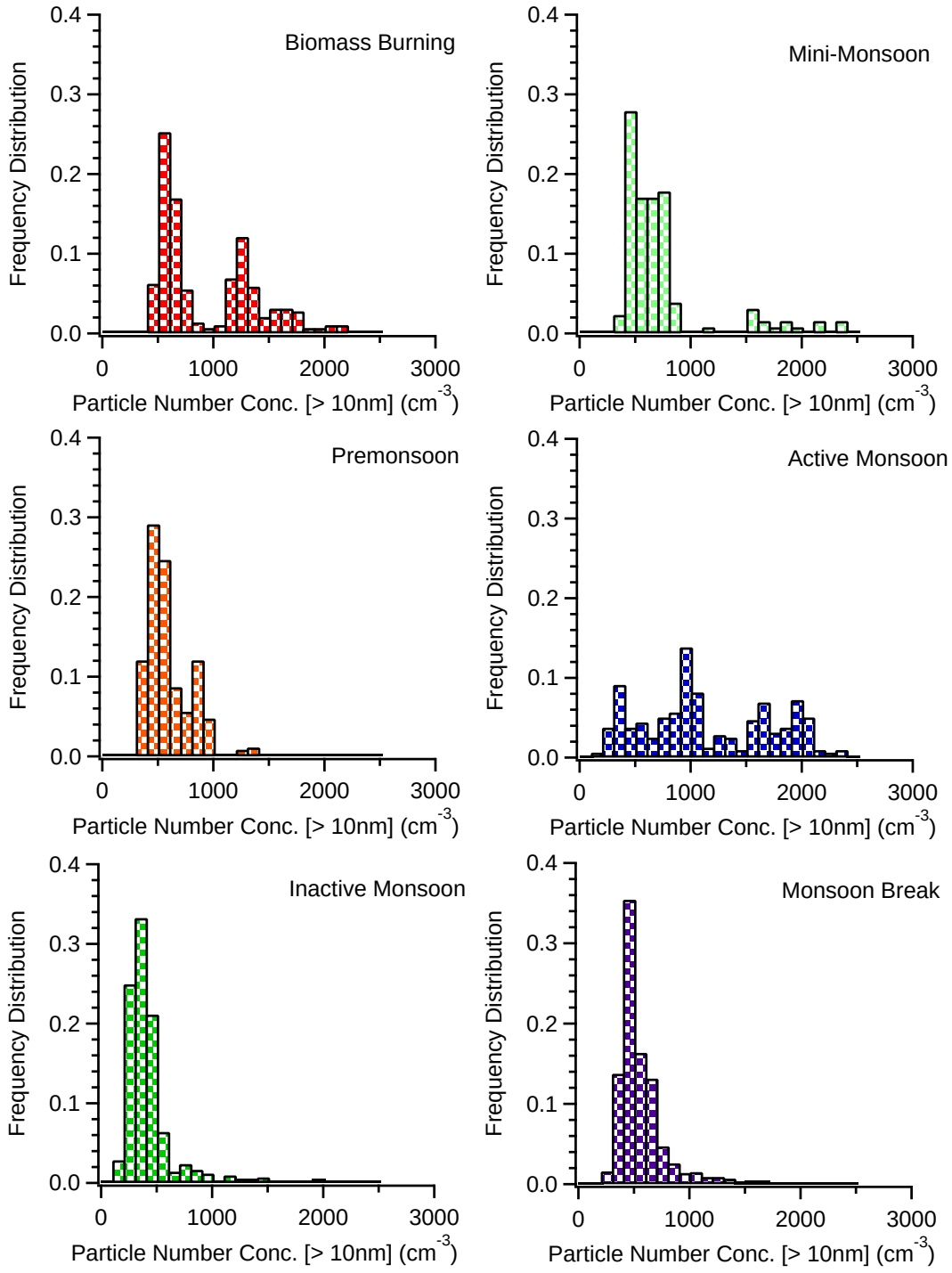

Figure 6.1: Histograms for the six climatological phases during ACTIVE. Data were taken from the Dornier CPC in the PBL (between 0.5 and 2 km); it is grouped into 60 second ($\sim$ 5 km) data bins and median averaged. These medians are then plotted as a frequency distribution, for aerosol size range 10 to 200 nm.

Table 6.2: Statistics for the Dornier APS data during the six climatological phases. Aerosol size range: 0.2 to 1.0 μm. See figure 6.2 for histograms.

Period	Mean[a]	Median[a]	Standard Deviation[a]	Skew	Kurtosis	K-S test[b]	
						D value	Critical
Biomass burning	131	90	108	2.0	4.4	0.16	0.08
Mini-monsoon	102	84	192	10	104	0.39	0.12
Premonsoon	92	90	30	0.15	-0.28	0.03	0.07
Active monsoon	44	39	21	1.6	2.4	0.22	0.08
Inactive monsoon	23	20	15	1.1	1.7	0.12	0.07
Monsoon break	51	46	26	0.7	0.4	0.08	0.04

[a] units are standard particles cm^{-3}.

[b] 'Kolmogorov-Smirnov test' conducted in order to test the hypothesis that the data are normally distributed. A 'D value' large than the 'critical value' indicates that the hypothesis should be rejected.

effect is the drop in mean concentration during the second campaign (final three phases – note the reduced x-axis scale). This would suggest that the origin of the particles was connected to continental sources, such as biomass burning, and the maritime winds in the monsoon season brought 'cleaner' air, in terms of 0.2 to 1.0 μm sized particles, into the Darwin area. Interestingly, this hypothesis (see also Allen et al. (2008)) is reinforced by the apparent recovery of the size mode during the monsoon break as the wind regime returns to a more continental influence. The statistics show that this size range had the larger mean concentrations, reflecting the biomass burning influence on particle production. Skewness and kurtosis are generally quite low, suggesting a normal distribution in the particle production and emission mechanisms. Furthermore, this unimodality reinforce the hypothesis that a single source dominates the population in the Darwin area: biomass burning.

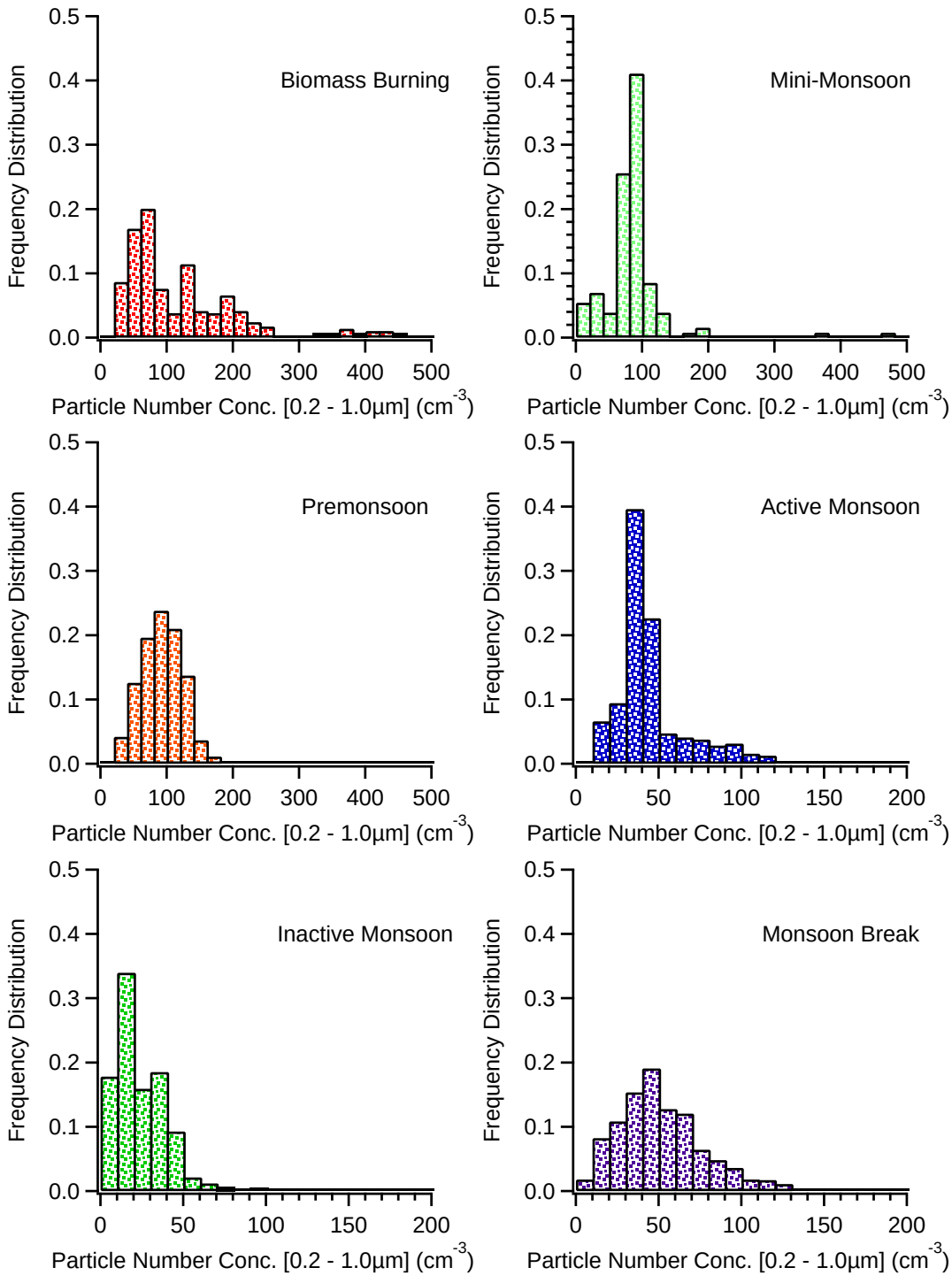

Figure 6.2: Histograms for the six climatological phases during ACTIVE. Data were taken from the Dornier APS in the PBL (between 0.5 and 2 km); it is grouped into 60 second ($\sim$ 5 km) data bins and median averaged. These medians are then plotted as a frequency distribution, for aerosol size range 0.2 to 1.0 μm. Note the reduced x-axis for the last 3 plots (second campaign).

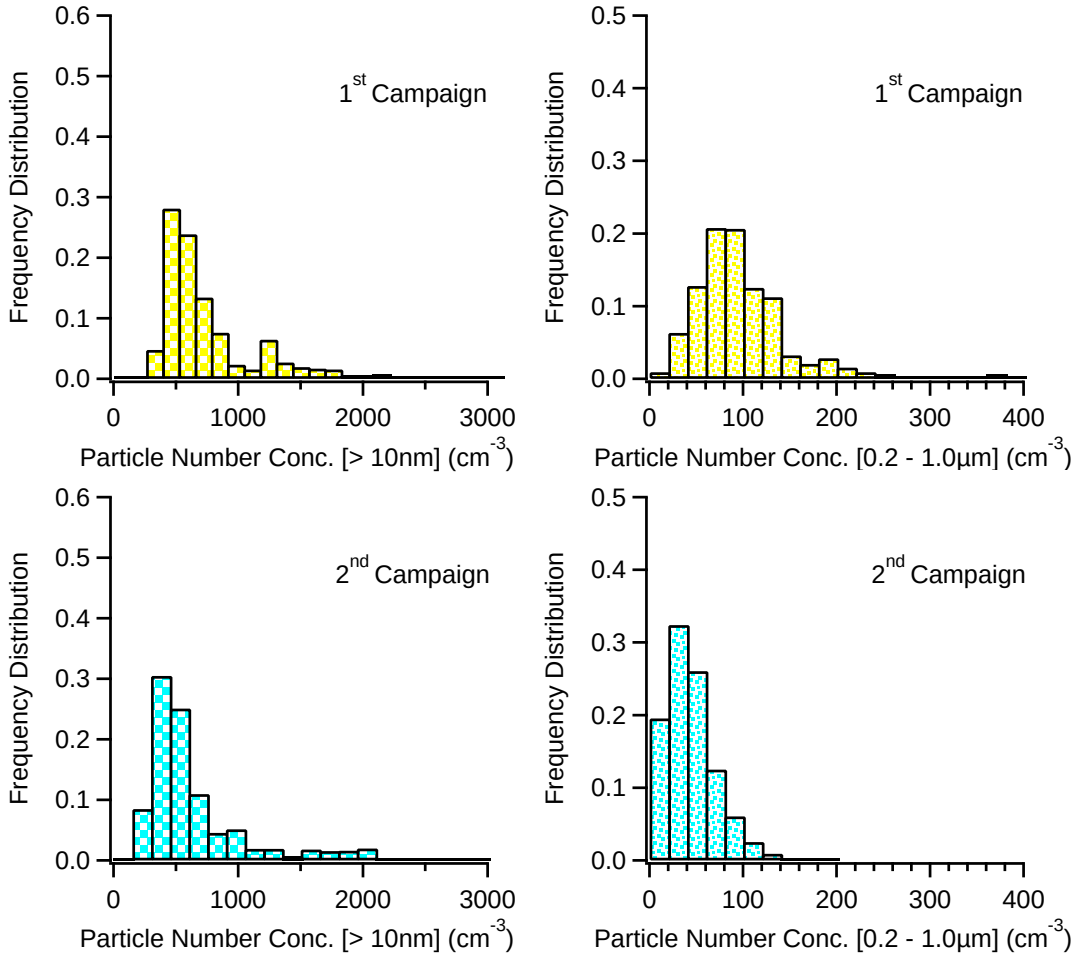

Figure 6.3: Summary for the six climatological phases averaged over the two ACTIVE campaigns. Data were taken from the Dornier CPC (10 - 200 nm) and APS (0.2 - 1.0 μm) in the PBL (between 0.5 and 2 km); it is grouped into 60 second ($\sim$ 5 km) data bins and median averaged. These medians are then plotted as a frequency distribution. Note the much reduced x-axis for the righthand plots (0.2 - 1.0 μm).

The two campaigns are summarised in figure 6.3; campaign 1 contains the data from the biomass burning phase, the mini-monsoon and the premonsoon; campaign two includes the data from the active monsoon, inactive monsoon and the monsoon break. It can be seen that on average there was little difference between the 10 - 200 nm particle mean and median concentrations in the two campaigns; most of the distinguishing features have been averaged out – in particular, the spread in the biomass burning and active monsoon data provide a similar effect when viewed over the whole of their respective campaigns. There was however a

clear spread in the data of the first campaign in the 0.2 to 1.0 μm size range; the average concentration, $\sim$ 100 cm^{-3}, was also seen to be higher throughout the first campaign. This was a result of the biomass burning and the accompanying release of aerosols and organic compounds. The organic content decreased after the biomass burning period throughout the mini-monsoon and premonsoon but organic compounds were still detected in the aerosol mass fraction and at a higher level to that seen in any of the subsequent phases of campaign 2. The reduced concentration average in the second campaign is a sign that the maritime aerosol net flux was lower for this size range than the net biomass flux.

The two box-whisker plots in figure 6.4 summarise the statistical data nicely: the high N_{10-200} concentrations in the active monsoon period can clearly be seen and the high overall dominance of the $N_{200-1000}$ during the first campaign due to the biomass combustion. The greater spread of concentrations were also observed for the N_{10-200} in the biomass burning phase and particularly the active monsoon, with values as high as 1500 to 2000 cm^{-3} and a large spread between the 50th and the 90th percentile. The biomass period can also be seen to contain greater aerosol concentrations more regularly. This reinforces the hypothesis that there is much more aerosol production occurring during the burning phase and many potential mechanisms and sources. There was also a large concentration range in the $N_{200-1000}$ data from the biomass burning period, shown by the high 75th and 90th percentiles; this variability drops considerably during the subsequent phases as combustion was suppressed – none of the other periods produced a concentration spread as great as that seen during the biomass burning phase.

During 1 - 2 February 2006 there occurred an inland flight to the centrally located town of Alice Springs (23.7° S, 133.87° E); at the time, a monsoon trough was located over the central NT region. The data from the inland flight and the return flight to Darwin are displayed in histogram form (figure 6.5). These flights occurred at a time of inactive monsoon in the Top End region and the data shows a similar distribution: the average N_{10-200} was $\sim$ 500 cm^{-3} and $N_{200-1000}$ was $\sim$ 40 cm^{-3}. There was no noticeable effect of the inland continental environment on the PBL aerosol burden, suggesting the air mass was of the same origin and composition as the maritime influenced Darwin PBL. The statistics (table 6.3)

show that there was not a great change in mean and median concentrations (CPC data) between the inactive monsoon data around Darwin and the data obtained during the flights inland to Alice Springs. On the other hand, there is a significant reduction in skewness and kurtosis in the Alice Spring data. Furthermore, a t-test* between the two datasets (Alice Springs and Inactive monsoon, 10 to 200 nm size range) a large enough t-value (5.38) to suggest that they were *different* (beyond the possibility of chance). This might be a sign of a more normal unimodal particle distribution in the inland area and hence a singular particle source or mechanism, but different distributions overall, in the case of the Alice Springs' and Darwin's (Inactive Monsoon) datasets. At first sight, the $N_{200-1000}$ particle concentrations appear to have similar mean and median with small skewness and kurtosis the statistics point to a normally, symmetrically, distributed population with a single mode of production. However, the statistical t-test again rejects the hypothesis that these datasets are 'similar' and they should be considered *different* (with a t-value of 4.65).

* The t-test assesses whether the means of two groups are statistically different from each other. The formula for the t-test is a ratio. The top part of the ratio is just the difference between the two means or averages. The bottom part is a measure of the variability or dispersion of the data. This t-value gives an indication of the similarity or difference between the two data. The acceptance level is -1.96 to 1.96, which is the area between the 2.5 and 97.5 percentiles on the Student's t distribution. If the t-test value is within this range, there is a 95% certainty (or level of significance) that the hypothesis (in this case, the two data distributions being *related*) is correct. Outside this range the hypothesis is null, with only a 5% chance of the hypothesis being wrong. In this case the distributions were deemed to be *significantly different*.

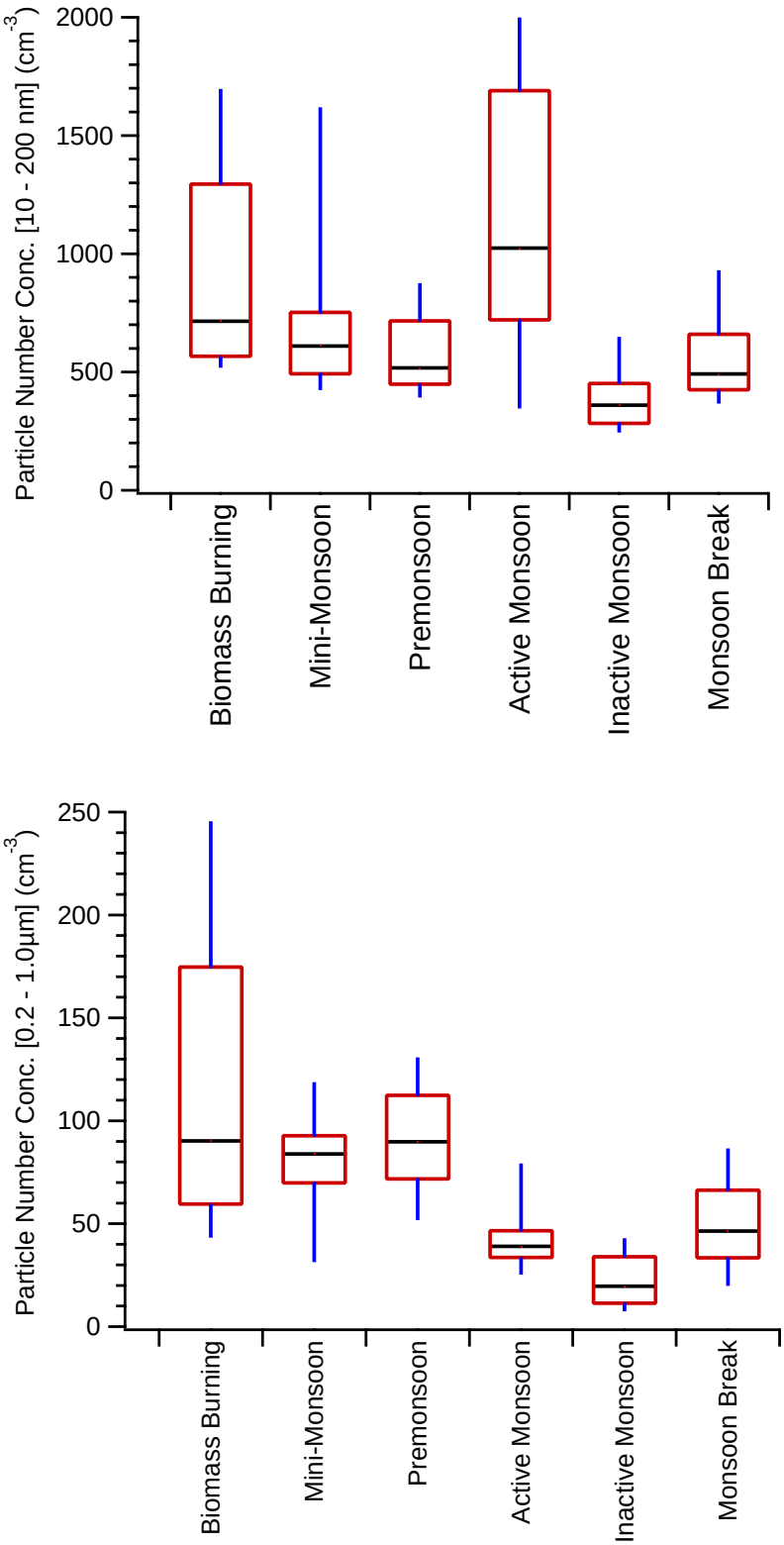

Figure 6.4: box-whisker plots for the two size ranges: 10 - 200 nm and 0.2 - 1.0 μm. The centre line is the median, the upper whisker is the 90th percentile, the upper box is the 75th percentile, the lower box the 25th percentile and the lower whisker is the 10th percentile.

Table 6.3: Statistics for the Dornier data during the inland flight to Alice Springs (1-2 February 2006). See figure 6.5 for histograms.

Size Range	Mean[a]	Median[a]	Standard Deviation[a]	Skew	Kurtosis	K-S test[b]	
						D value	Critical
10-200 nm	539	538	174	0.6	3.1	0.06	0.09
0.2-1.0 μm	31	23	24	2.3	6.6	0.26	0.09

[a] units are standard particles cm^{-3}.
[b] 'Kolmogorov-Smirnov test' conducted in order to test the hypothesis that the data are normally distributed. A 'D value' large than the 'critical value' indicates that the hypothesis should be rejected.

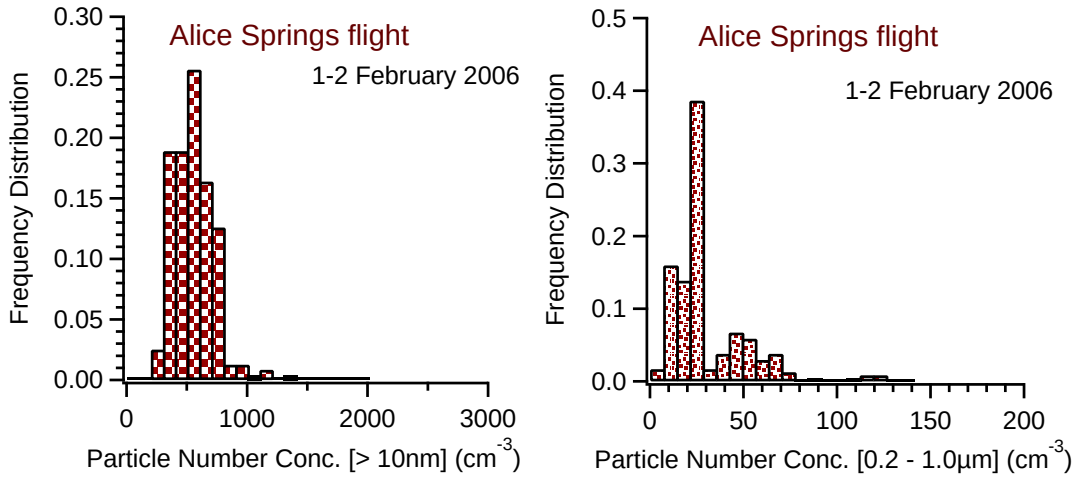

Figure 6.5: Histograms for the inland flight to Alice Springs (1-2 February 2006) in the central region of Australia where a large storm formed. Data were taken from the Dornier CPC (10 - 200 nm) and APS (0.2 - 1.0 μm) in the PBL (between 0.5 and 2 km); it is grouped into 60 second ($\sim$ 5 km) data bins and median averaged. These medians are then plotted as a frequency distribution.

Another set of exploratory flights towards Indonesia occurred on the 30 January and 3 February to investigate the possible influence of the northern hemisphere on the southern hemispheric air mass. The objective of these flights was to answer a number of important questions: were there any traces of Northern Hemisphere pollution in the southern hemisphere, to what degree did the air masses contrast and where might the chemical boundary be? These flights found that there were major influences from the more polluted northern hemisphere on the southern hemisphere and a chemical boundary existed to the south of the equator. The histograms (figure 6.6) show the effect of the northern pollution plume on the

Table 6.4: Statistics for the Dornier data during the northward flights (30 January and 3 February 2006). See figure 6.6 for histograms.

Size Range	Mean[a]	Median[a]	Standard Deviation[a]	Skew	Kurtosis	K-S test[b]	
						D value	Critical
10-200 nm	1009	921	768	1.3	2.6	0.12	0.07
0.2-1.0 μm	43	31	39	1.4	1.2	0.20	0.07

[a] units are standard particles cm^{-3}.
[b] 'Kolmogorov-Smirnov test' conducted in order to test the hypothesis that the data are normally distributed. A 'D value' large than the 'critical value' indicates that the hypothesis should be rejected.

aerosol loading in the PBL. The concentration average is significantly higher than that in the Darwin area, with a mean between 1000 - 1500 cm^{-3} for N_{10-200} however the skewness and kurtosis are lower in the northern plume data, meaning the distribution looks symmetric about the mean. This however does not tell the full story: the Kolmogorov-Smirnov test (see table 6.4) indicates that the distribution is not normal and the t-test again shows that there is *'significant difference'* between the northern plume data and the data collected in the Darwin locale at the same period. The distribution in fact shows signs of bimodality with two peaks either side of the mean value. This could point to possible differing air mass mixing, with various particle production mechanisms and sources. The t-value was much higher than Alice Springs, at 13.8, highlighting the variability between the Darwin climatology, inland climatology and the northern hemisphere pollution plume.

The larger 200 - 1000 μm particles also show higher concentrations than that found around Darwin during the inactive monsoon; the mean and median are both higher and the variability is also greater in the northern plume – both concentration datasets are significantly non-normal (indicated by the Kolmogorov-Smirnov tests in tables 6.2 and 6.4). With a t-value of 9.29, there is again little statistical resemblance to the 'inactive monsoon', 200 to 1000 μm data.

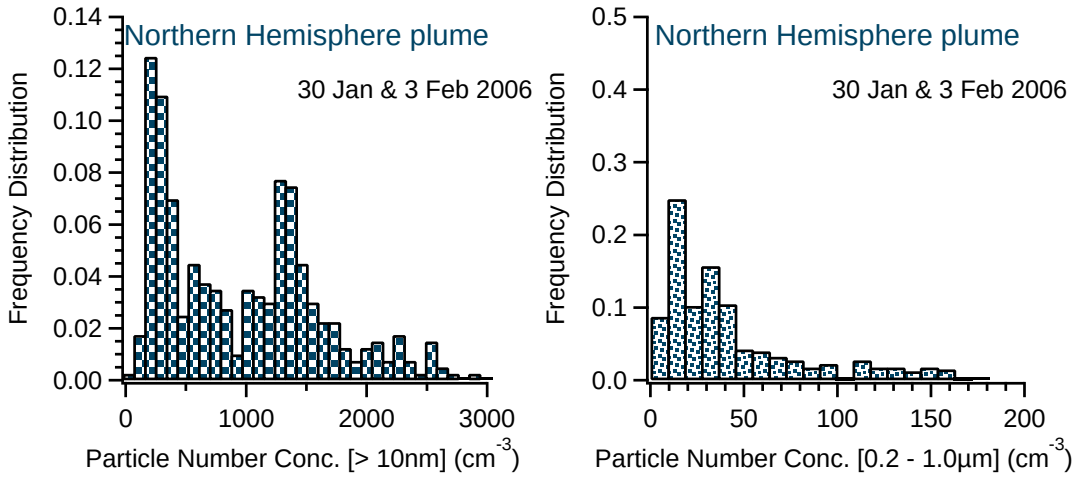

Figure 6.6: Histograms for northward flights (30 January and 3 February 2006) across the ocean to assess the extent of the Northern Hemispheric pollution south of the equator. Data were taken from the Dornier CPC (10 - 200 nm) and APS (0.2 - 1.0 μm) in the PBL (between 0.5 and 2 km); it is grouped into 60 second ($\sim$ 5 km) data bins and median averaged. These medians are then plotted as a frequency distribution.

Chapter 7

Results from the TTL

7.1 Aerosol in the UT/TTL

The Egrett flights were all unique in their aims and objectives and the results show a wide range of phenomena at work. This section will attempt to describe the UT/TTL data (taken from 10 km and above) that were observed during ACTIVE in a more general sense; the thesis will move on to more specific cases in later sections. However, to begin this section, an example of a specific flight will be presented to give some impression of the mode of operation and data retrieval. As an example of the data retrieved from ACTIVE, figure 7.2 shows the data timeline for flight AE12, figure 7.1 indicates the flight track over the Darwin area. This flight shows some of the very highest concentrations of N_{10} and N_{100} particles (10 to 1000 nm and 100 to 1000 nm, respectively). It can be seen that higher aerosol concentrations tend to occur in lower cloud particle concentrations, N_{cloud}, and *vice versa*. At approximately 16:00 LT there is a large peak in both N_{10} and N_{100} during cloud-free conditions. These high concentrations were not seen anywhere in the local Darwin PBL (see section 6.1) or even in the case of the pollution plume flights towards the equator (figure 6.6). This could possibly indicate in situ production of particles in the outflows: *aerosol nucleation*. There are also spikes of CO that correlate with corresponding peaks of cloud particles and aerosol particles. This tracer could indicate a possible origin for the high particle concentrations – not necessarily local, as discussed in section 4.3. These peaks would indicate elevated CO against the background and an influence of

convection; this convection could have occurred in relatively distant regions with varied sources (Heyes et al., 2009). The long lifetime of CO in the troposphere ($\sim$ 1 month) means there was significant timespan over which convective uplift could have occurred and produced chemical tracer spikes in the background. However, in places that are convectively active such as the Tropical Warm Pool and the Northern Territory, one must take into account the effect of mixing, advection and entrainment/detrainment at all levels; this makes the task of disentangling the source region more difficult.

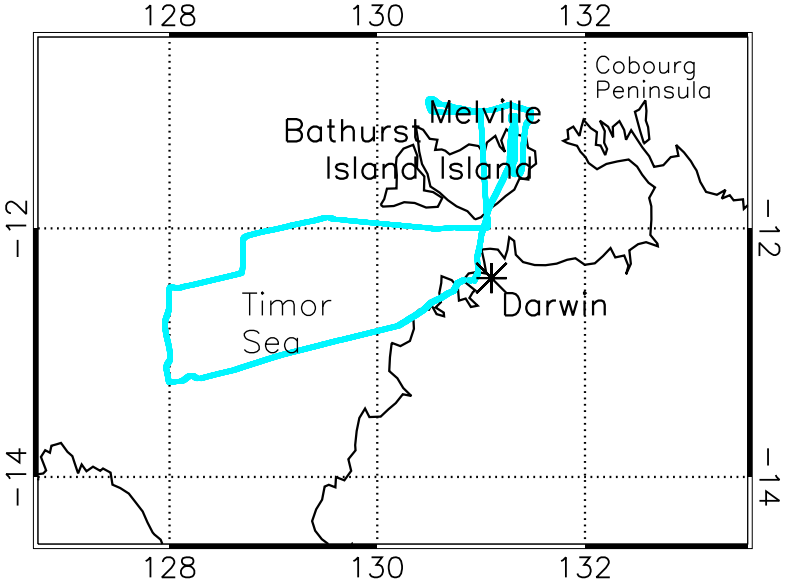

Figure 7.1: Flight AE12 took place on 8 December 2005 during the decay of a large storm anvil that had been active throughout the previous night. The light blue line indicates the flight track over the local topography.

There were other cases of extreme N_{10} concentrations detected in the UT/TTL during ACTIVE. These flights typically coincided with very large storms. The high N_{10} aerosol concentrations again occurred in the outflows of the convective cells in cloud-free air. Figure 7.3 shows another example of high aerosol concentrations during the ACTIVE project. Flight AE19 (23 January 2006) and AE12 produced the largest median N_{10} concentrations during the whole experiment and were closely linked with the outflows of very large and widespread convective systems.

Figure 7.4 gives a general statistical overview of the whole 10 - 1000 nm, N_{10}, ACTIVE concentration dataset. A few of the flights, AE12, AE18 and AE19 stand out with particularly high concentration maxima and wide ranges. These

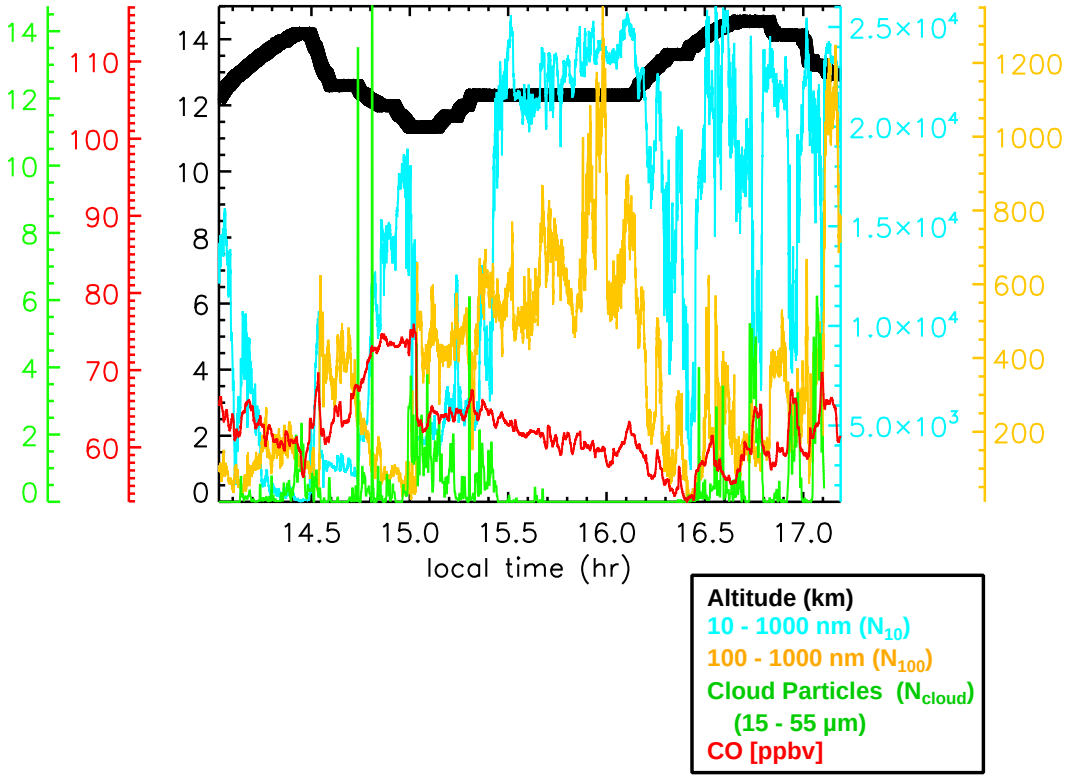

Figure 7.2: A data time line for the flight AE12, showing aircraft altitude (km, black), particle number concentration in number.cm^{-3} (STP) and carbon monoxide [ppbv].

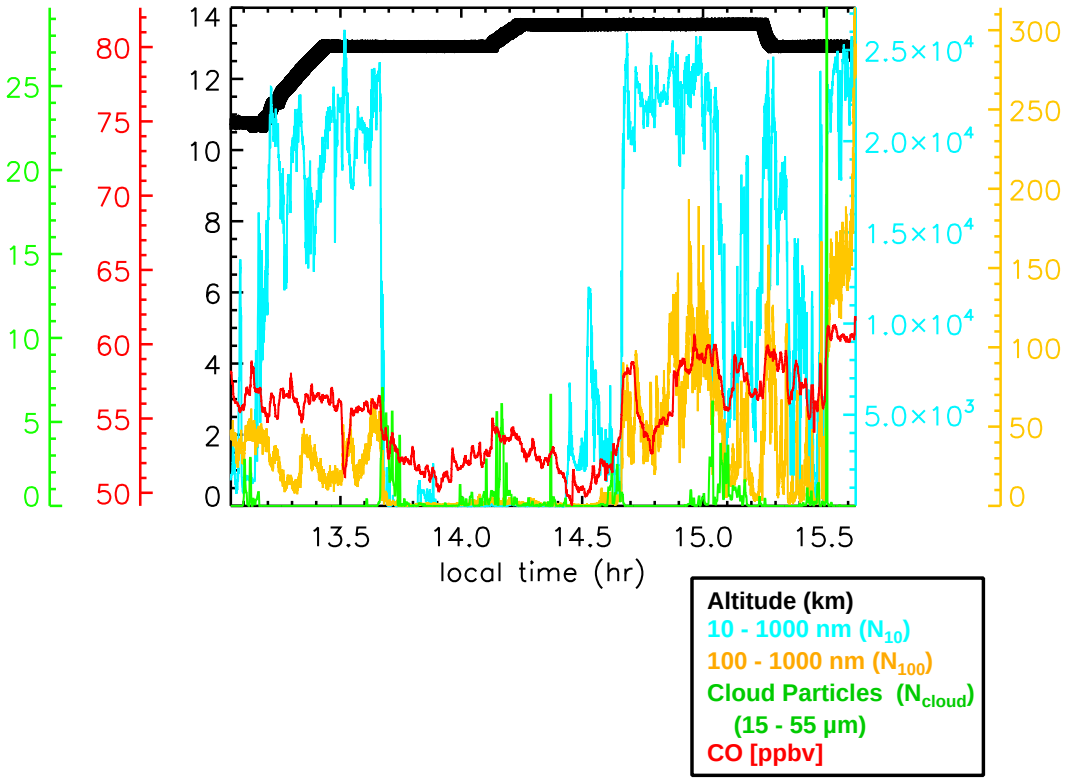

Figure 7.3: Showing aircraft altitude (km, black), particle number concentration in number cm^{-3} (STP) and carbon monoxide. AE19, 23 January 2006. An example of some of the high N_{10} and N_{100} concentrations encountered during ACTIVE.

three flights also show consistently higher concentrations throughout the flight, demonstrated by their high median and interquartile values. The spread in data, for individual flights, appears to reflect the generality of the statistical survey: N_{10} data were taken from both cloud and cloud-free regions, regions with close convective influence and others with more 'background' conditions. Nevertheless, this plot shows that something significant happened in the flights: AE12, AE18 and AE19. This will be investigated in more detail later. It is worth mentioning, however, that the storms that occurred during, or shortly before, these flights were exceptionally large, with widespread convection taking place. Also the first 3 flights, AE04, AE06, AE07 were early in the campaign before widespread continental convection took place.

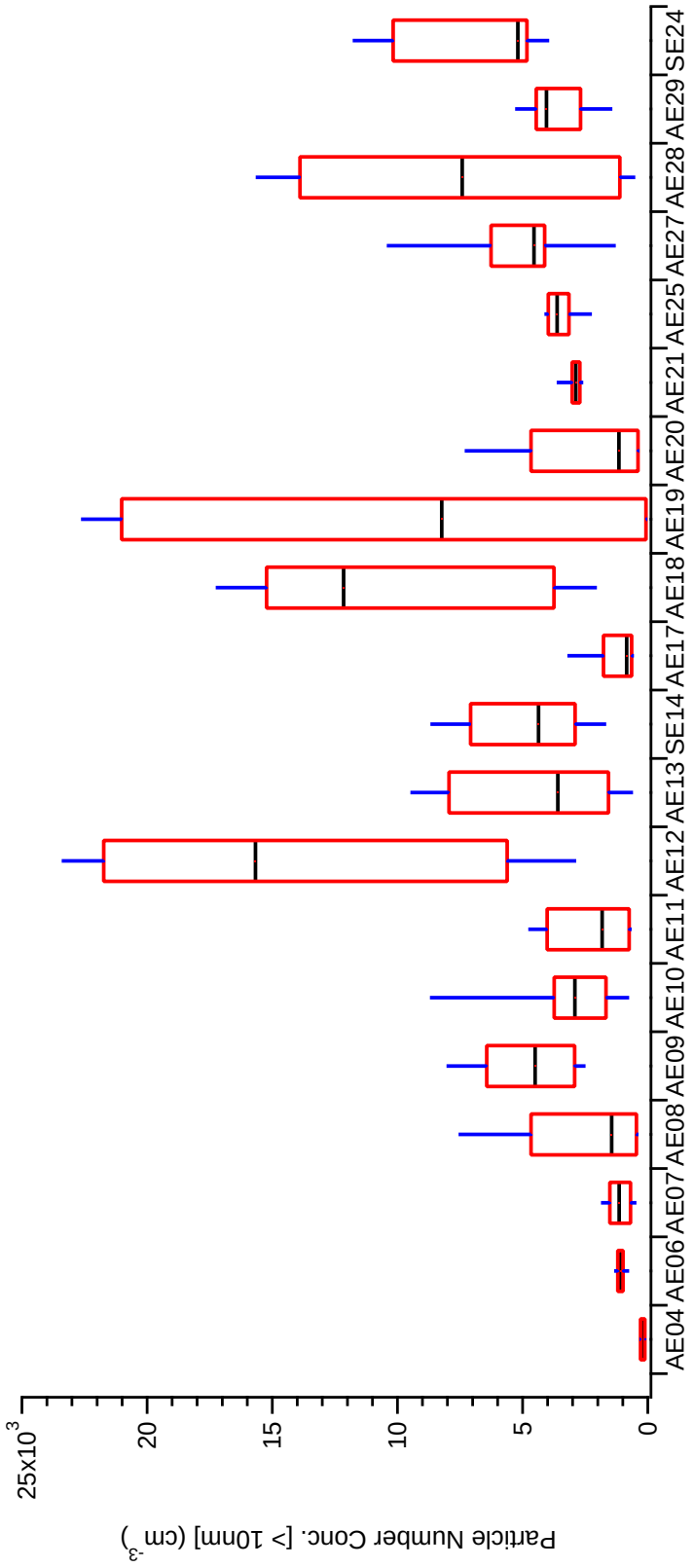

Figure 7.4: Box-whisker plots for the size range: 10 to approximately 1000 nm. The concentrations, N_{10}, are taken for all conditions (cloud and cloud-free) above 10 km. The centre line is the median, the upper whisker is the 90th percentile, the upper box is the 75th percentile, the lower box the 25th percentile and the lower whisker is the 10th percentile.

Many of the ACTIVE data timelines showed a strong anticorrelation between high N_{cloud} and high N_{10} and N_{100}. As the aircraft enters cloud there is a sudden reduction in the number of aerosol particles, both N_{10} and N_{100}. Figure 7.5 shows the scatter plots of CPC1 (N_{10}) against cloud (N_{cloud}) concentration data. The scatter shows that the majority of the high concentration N_{10} data lie in low N_{cloud} concentrations regions; a few outliers however had significant N_{10} concentrations whilst in cloud ($N_{cloud} > 0.05$ cm^{-3}).

This anticorrelation suggests that the presence of high cloud particle concentrations is inhibitive to high aerosol concentrations. Scavenging of aerosols and aerosol gas precursors by cloud particles has been seen in other campaigns (e.g. Strom et al., 1999; Twohy et al., 2002) and model studies (e.g. Wang, 2005a,b). The larger 100 to 1000 nm aerosols also show the anticorrelation (figure 7.6) behaviour that was seen in the N_{10} data; the N_{100} data seem to obey the hypothesis more closely, with fewer outliers. This would suggest that it is increasingly more difficult for larger aerosols to survive interstitially in cloud. It is known that the Kelvin effect decreases (surface tension) as radii increases with an accompanying increase in the probability of activation to CCN (cloud condensation nuclei). This in effect removes the aerosols from their population; as their size increases, they become cloud droplets (supermicron). This is the most likely scavenging mechanism for the accumulation mode ($\sim$ 100 to 1000 nm); for the smaller Aitken mode deposition through Brownian motion onto larger aerosols and cloud particles is a quite effective mechanism for reducing the number concentration (approximately 10 to 100 nm).

7.2 Satellite data

Satellite data become integral to the analysis of the ACTIVE dataset, proving to be an invaluable resource for the project in general. For this investigation, infrared data become an important aid in determining the meteorological and convective conditions in the vicinity of the aircraft and the larger picture across Darwin and the Tropical Warm Pool. Infrared (IR) data exists in a range that makes it temperature dependent; this provides a useful method for detecting cloud particles and in particular rising convective columns. The Infrared data were provided by the Multifunctional Transport Satellite (MTSAT). This collects hourly data from most of the Indian Ocean and western Pacific, including all of Australia. It should be noted that the satellite scan-records data, from the north-pole to the south-pole, and therefore takes an additional 20 minutes, from the file's time stamp, to reach the Darwin area. There are three Infrared bands: 1) measuring 10.3 - 11.3 μm, 2) 11.5 - 12.5 μm and 3) 6.5 - 7.0 μm, and a visible wavelength band; the MTSAT has a resolution of 4 km at sub-satellite point. Figure 7.7 shows an example of MTSAT data overlaid with an Egrett fight track and aerosol data from the earlier AE12 example (8 December 2005 – timeline given by figure 7.2). The AE12 flight track is colour-coded to the Egrett N_{10} data, overlaid onto the MTSAT channel 2 data, represented with grayscale. Since the typical cloud droplet has a diameter of > 10 μm, the radiation will be related to cloud particle emissions. Infrared radiation is temperature dependent and can provide information about cloud top temperature and cloud height (basically the colder the temperature, the higher the cloud top). The IR data in this work is grayscaled to give a visual indication of the cloud location and temperature. Figure 7.7 also shows quite clearly the sections of flight that coincided with high N_{10} particle number concentrations and there relation to the cloud. The cloud clearing above Melville Island was seen to contain high particle concentrations, supporting the hypothesis of out-of-cloud nucleation.

7.3 Cloud and aerosols

The distinction between low N_{10} in cloud regions ($N_{cloud} > 0.05$ cm^{-3}) and high N_{10} in cloud-free regions was commonly seen during ACTIVE flights, although

exceptions did occur. The two flight timelines in figure 7.8 show the consecutive bands of N_{cloud} peaks and then N_{10} peaks that were observed in much of the recent convective data.

7.3.1 Cloud-free regions

Egrett data were collected into 5 km segments; the data were then median averaged. This median N_{cloud} value was used to determine if the segment was cloud or cloud-free, with > 0.05 cm^{-3} denoting cloud and < 0.05 cm^{-3} denoting cloud-free air. These 5 km data segments were then separated in order to investigate any differences that might exist between the 2 states. Figures 7.9 and 7.10 show box-whisker plots for N_{10} and N_{100} concentrations, respectively. Compared to the complete dataset box-whisker for N_{10} (figure 7.4), it can be seen that the medians, 10th, 25th, 75th and 90th percentiles in general increase in the cloud-free environment and the interquartile range is reduced, with few exceptions. This again illustrates the higher aerosol concentrations found in out-of-cloud regions and the possibility that aerosols were being generated in convective outflows.

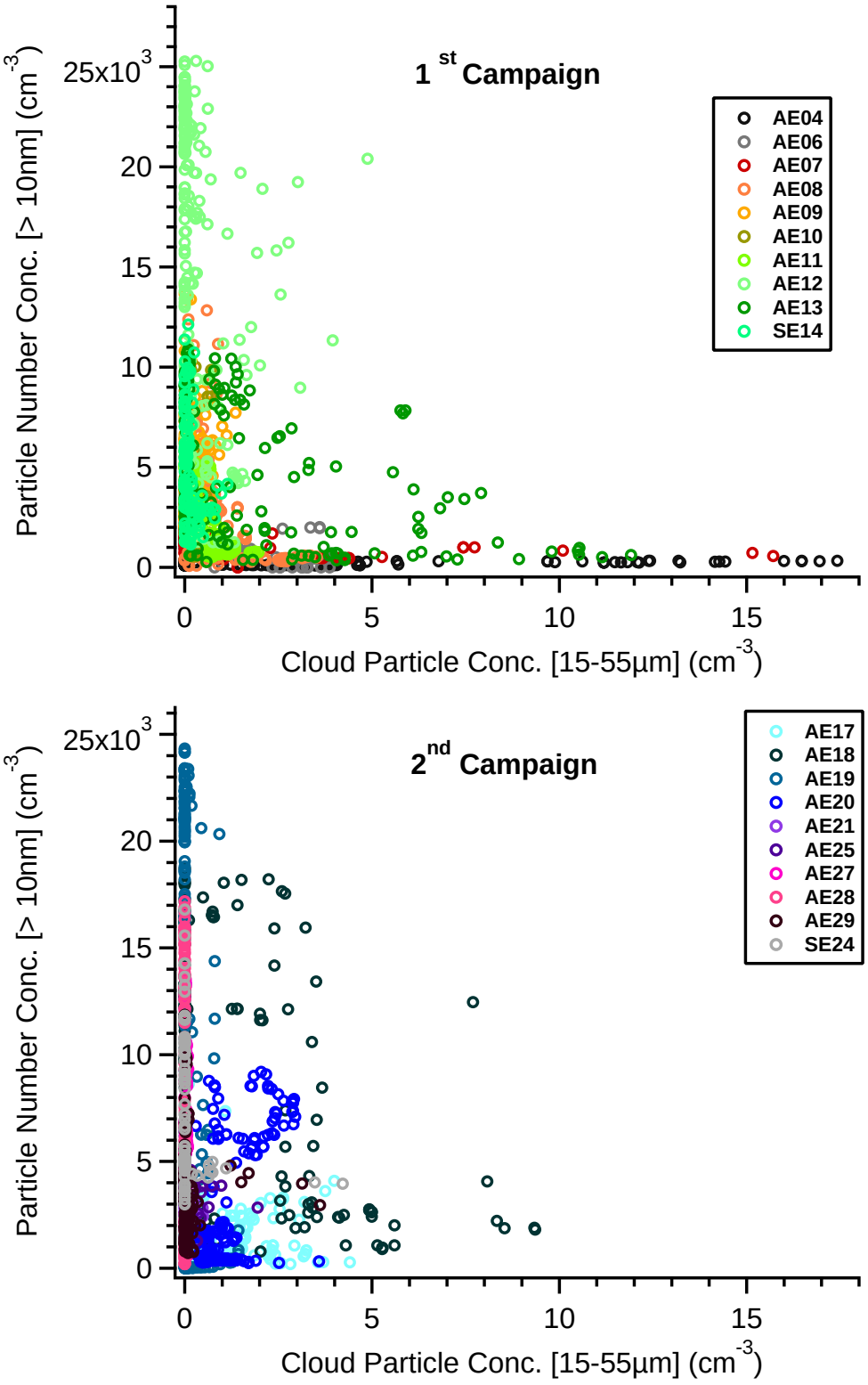

Figure 7.5: Scatter plot of CPC1 concentrations, N_{10}, against cloud particle concentrations, N_{cloud}. Each marker represents the median average of a 50 second bin from the Egrett dataset. The two ACTIVE campaigns are shown separately here.

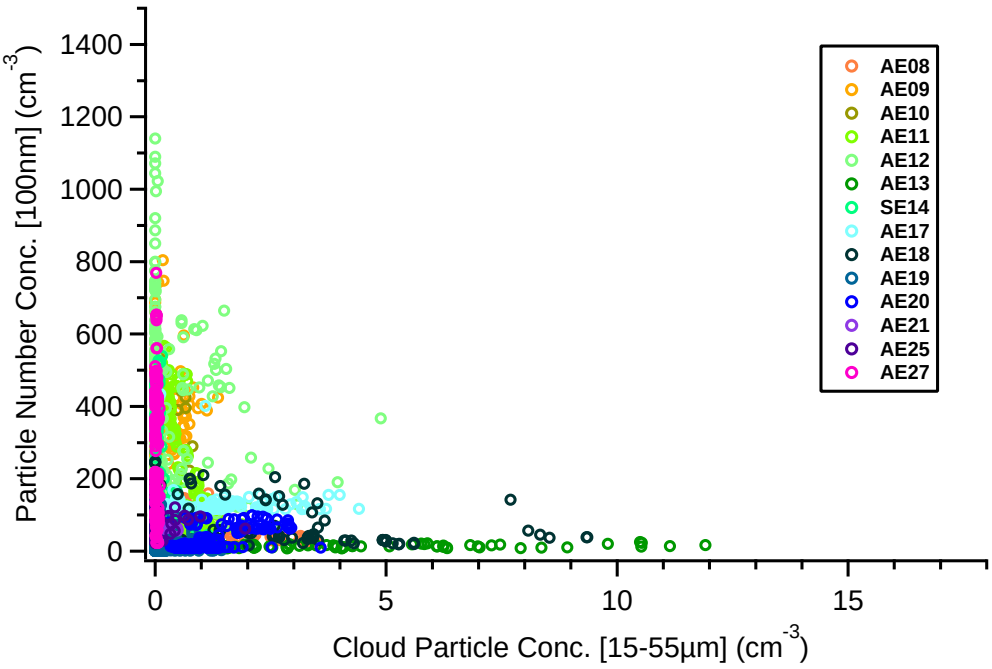

Figure 7.6: Scatter plot of CPC2 concentrations, N_{100}, against cloud particle concentrations, N_{cloud}. Each marker represents the median average of a 50 second bin from the Egrett dataset. The whole ACTIVE campaign is shown in one plot here.

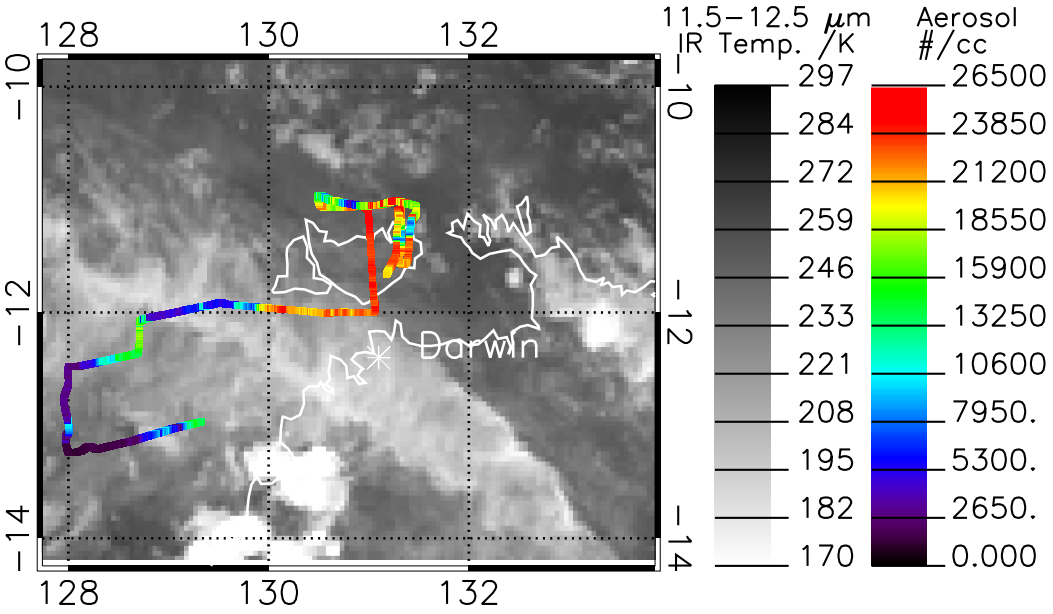

Figure 7.7: Infrared satellite image, overlaid with a section of flight data. The flight track is colour-coded with aerosol, N_{10}, concentration data (see coloured bar). Only flight data above 10 km is shown.

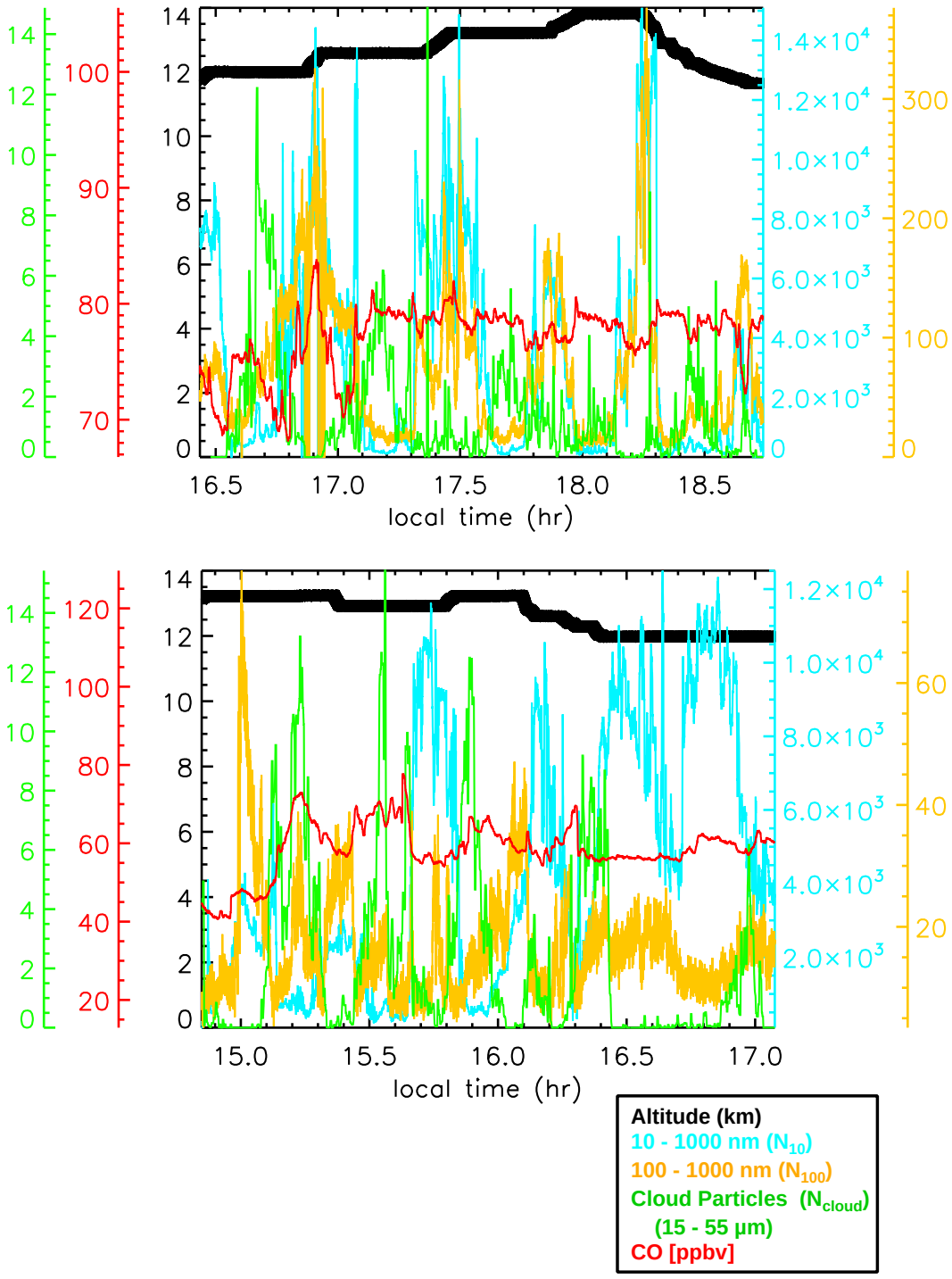

Figure 7.8: Showing aircraft altitude (km, black), particle number concentration in number cm^{-3} (STP) and carbon monoxide. *Top:* AE08, 3 December 2005, *bottom:* AE13, 9 December 2005. An example of N_{10} and N_{cloud} anticorrelation encountered during ACTIVE.

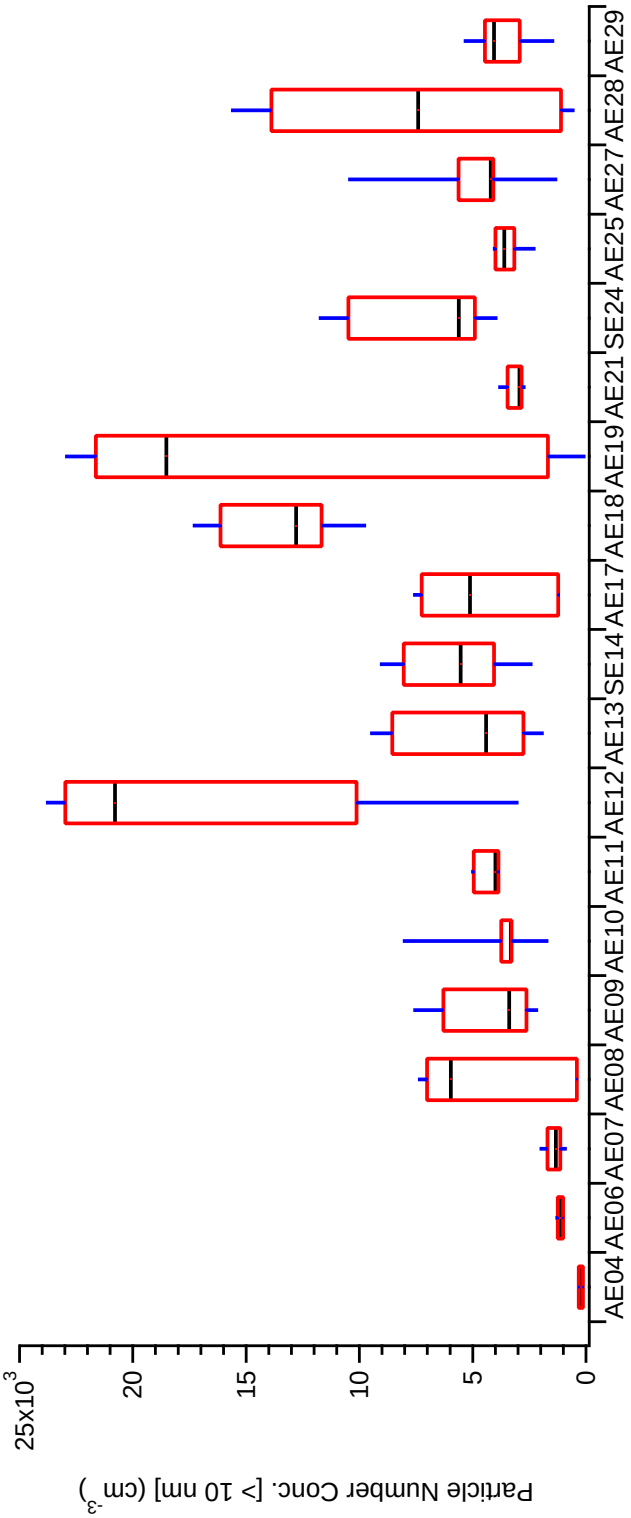

Figure 7.9: Box-whisker plots for the size range: 10 to approximately 1000 nm. The concentrations, N_{10}, are taken for cloud-free conditions above 10 km. The centre line is the median, the upper whisker is the 90th percentile, the upper box is the 75th percentile, the lower box the 25th percentile and the lower whisker is the 10th percentile.

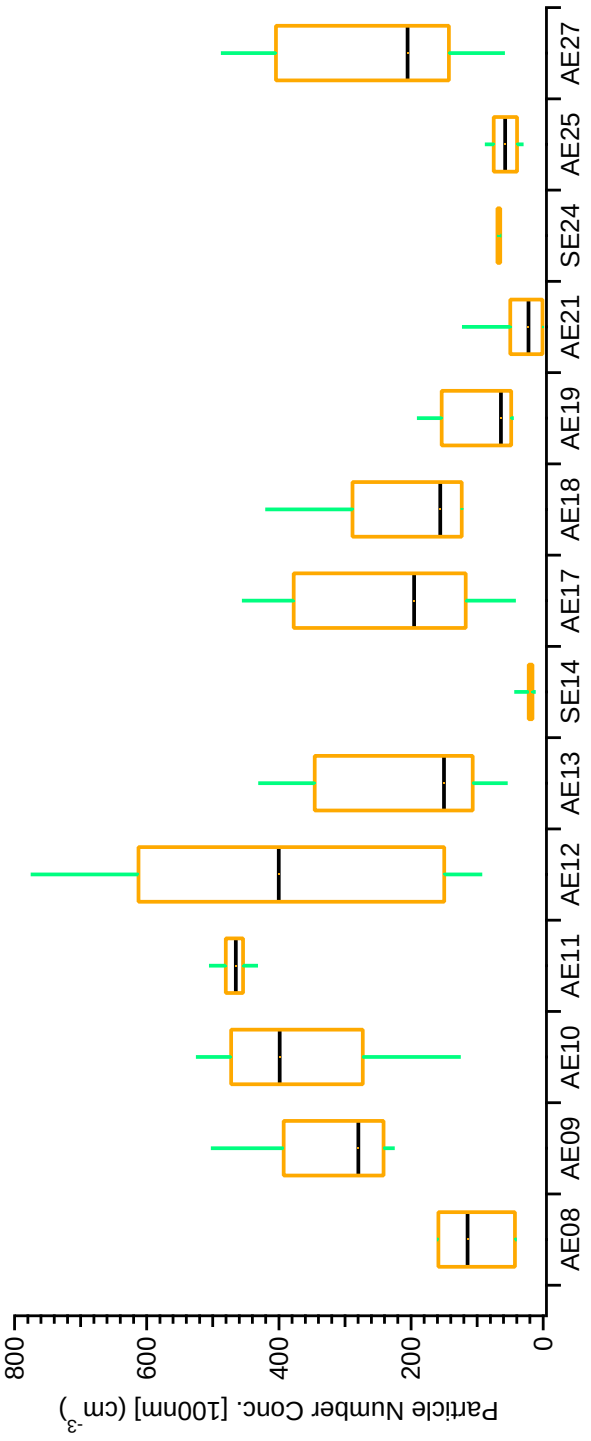

Figure 7.10: Box-whisker plots for the size range: 100 to approximately 1000 nm. The concentrations, N_{100}, are taken for cloud-free conditions above 10 km. The centre line is the median, the upper whisker is the 90th percentile, the upper box is the 75th percentile, the lower box the 25th percentile and the lower whisker is the 10th percentile.

7.3.2 Cloud and aerosol mixing?

The statistical data do show however that there were exceptions to the cloud and aerosol anticorrelation. In a number of cases (for example AE13, AE18) very high N_{10} were found in cloudy regions. Some hypotheses exist that suggest in-cloud or interstitial nucleation (or aerosol survivability in cloud) is possible (Lee et al., 2004; Kulmala et al., 2006b; Kazil et al., 2007); low uptake rates of precursor gases by ice crystals (possibly SO_2) are proposed as a possible mechanism. Kulmala et al. (2006b) suggested a role for insoluble organic compounds that exist interstitially in cloud and act as aerosol nuclei.

A section of flight AE13 (9 December 2005) was analysed to determine the source of the cloud and aerosol correlation (figure 7.11). The figure shows that there was a maximum N_{10} concentration of $\sim$ 6000 cm^{-3} in very thick cloud ($N_{cloud} \sim 80$ cm^{-3}); furthermore, the 2 concentrations correlated. Wind and satellite data were used to assess the possible origin of the high aerosol (see the following section). There is some evidence to suggest that these correlation episodes occurred due to mixing of air masses and in particular when the outflow of one storm is intercepted by another anvil. This occurred quite commonly during the convectively active periods: premonsoon, active monsoon and monsoon break. It would be possible for nucleation to occur in the outflow of one storm which is then mixed into the anvil or column of another storm. This was seen in the case of the AE13 flight segment when the wind data were analysed (see figure 7.12) and an outflow from an earlier storm (*bottom*, figure 7.12) was intercepted by a more recent storm to the west of the Tiwi Islands (*top*, figure 7.12). The aerosol survivability in-cloud would depend on its coagulation efficiency and this is determined by the size of the particle. The presence of in-cloud nucleation could also be a contributing factor to the interstitial aerosol concentrations. However, the theories are tentative and require more investigation; insoluble organics (Kulmala et al., 2006b) are one of the recent proposals for in cloud nucleation.

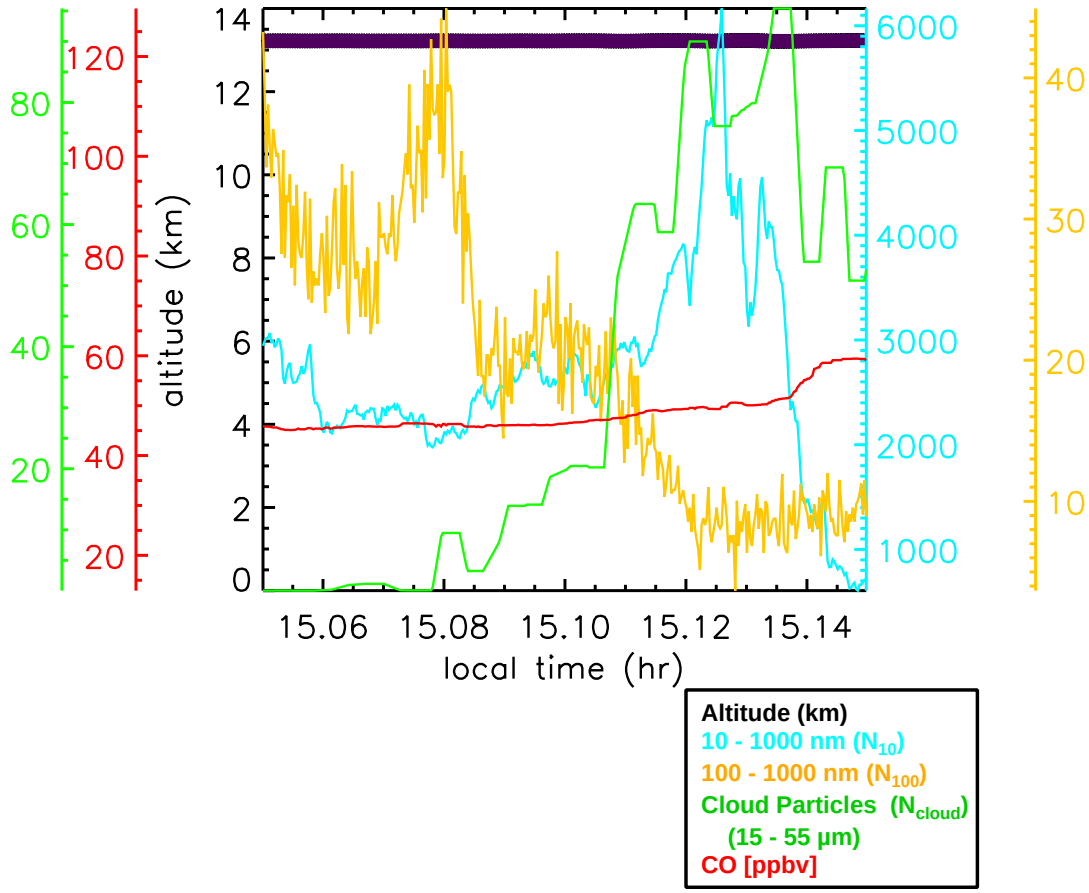

Figure 7.11: A data time line for the flight AE13, showing aircraft altitude (km, black), particle number concentration in number.cm^{-3} (STP) and carbon monoxide [ppbv]. This flight shows a section of cloud that contains significant numbers of 10 - 1000 nm particles.

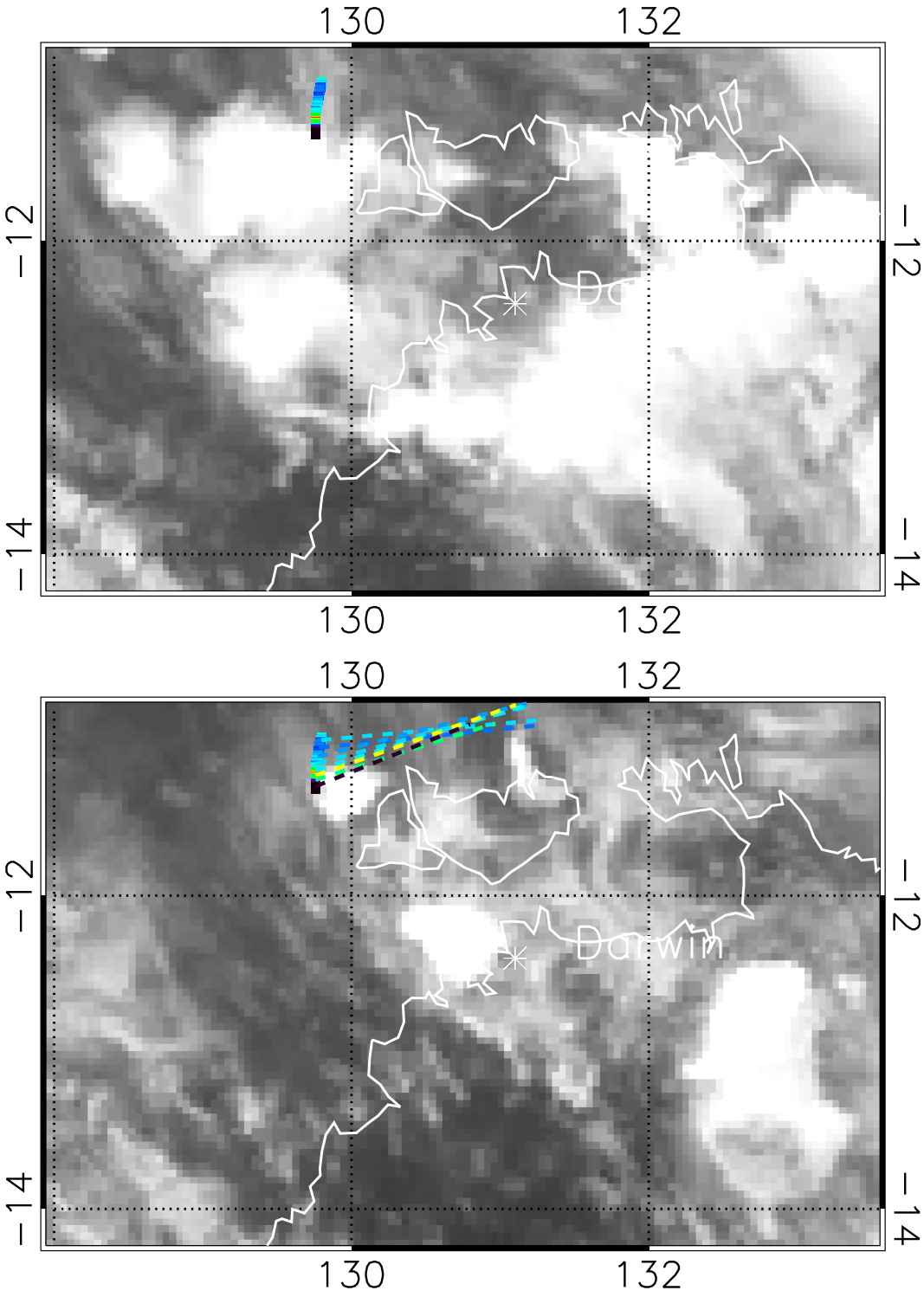

Figure 7.12: Two satellite images showing the evolution of the AE13 flight section shown in figure 7.11. *Top:* IR data at the time of flight, showing in-cloud conditions *bottom:* IR data from 3 hours previously. The dashed lines also indicate the wind projections and the origin of the air parcel 3 hours before.

7.4 Air mass history

7.4.1 Local-scale wind projections

The ability to track an air parcel through time is a very powerful tool for determining its compositional evolution. The simplest technique involved using the aircraft wind data; the aircraft three-way pitot tube provided 3-dimensional air velocity data. A combination of the wind, aircraft GPS and satellite data allowed air mass projections to be made into the past and hence the air mass history to be determined. The wind data were found to be more accurate, without losing too much detail, if they were median smoothed over 5 km regions – this is why all the Dornier and Egrett data were median averaged over 5 km (50 seconds) segments, for the purpose of uniformity throughout this investigation (see section 5.5.4 for wind smoothing discussion). The air mass spatial position could then be ascertain for hourly points in the past. This technique was accurate back to 10 hours; beyond this point the instantaneous wind measurements diverged from the true global wind field due to the linear nature of the projection. For longer back projections modelling calculations were necessary; based on networks of wind measurements, 4-dimensional streamlines can to be constructed throughout atmosphere. This techniques was used to assess the time since air exited the cloud and how long had it been cloud-free; it is discussed in the case study of AE19, in chapter 8.

7.4.2 Synoptic-scale back trajectories

Together with the MTSAT data, calculated back trajectories were employed in order to assess air mass history. The combination of aircraft, satellite infrared and back trajectory data allowed timescales to be determined, since the air was last influenced by convective uplift. The method was similar to that used for the wind projections: aircraft data were overlaid onto satellite data together with the relevant back trajectory. Trajectories also allowed the probable climatic conditions to be determined at the time of uplift. This was used in Allen et al. (2008) and Heyes et al. (2009) to find if the air had a strong maritime or biomass burning influence, for example. Heyes et al. (2009) used trajectories to explain the high CO and ozone levels found over Darwin; the trajectories indicated a source that typically

originated over Indonesia – areas that are either highly populated and polluted or effected by forest and other biomass fires. The trajectories use convective parameterisation in the European Centre for Medium-range Weather Forecasting (ECMWF) Integrated Forecasting System model. The ECMWF operational analyses, from the Integrated Forecasting System (IFS Cycle 29r2), outputs data on a 2.5°×2.5° grid, and were performed using the trajectory server at the British Atmospheric Data Centre (BADC) using wind-fields derived from ECMWF operational data. The validity of the results is to a large degree dependent on the accuracy of the ECMWF wind fields. These were checked against wind measurements aboard the Egrett and were found to agree (section 8.6.1 discusses the use of both wind and trajectories in the same analysis). The background analysis in the following section shows the example of SE24 and the application of back trajectories to satellite data (see figure 7.13).

7.5 Background aerosol

Determining the background level of aerosol in the UT/TTL allowed the areas of elevated aerosol concentration to be categorised and studied. However, since the ACTIVE project took place in an area and at a time of intense convective activity, it was difficult to find areas of cloud-free air that had been uninfluenced by convection for over a day. The inactive monsoon offered a period in which air was unperturbed for almost 5 days in the Darwin region. There were some large storms over Indonesia and the monsoon trough over central NT (Alice Springs – see figure 6.5) generated convection, with anvil cirrus reaching as far as Darwin (flights AE20 and AE21 detected some of this aged cirrus as it reached the Top End). The initial sections of flight SE24 provided data from air which had been up to 4 days without any convective influence. This was determined from MTSAT IR data over the previous 5 days. Figure 7.13 shows an example of the use of back trajectories and regular MTSAT records to determine the history of the air parcels in question. In this example, it can be seen that for the previous 24 hours there had been no convective activity in the vicinity of the trajectories. Between -36 and -48 hours there appeared a large system which intercepted the trajectories at the same altitude as the trajectories. The cloud top temperature was used to infer the cloud top height; this was then used to find the point of intersection with

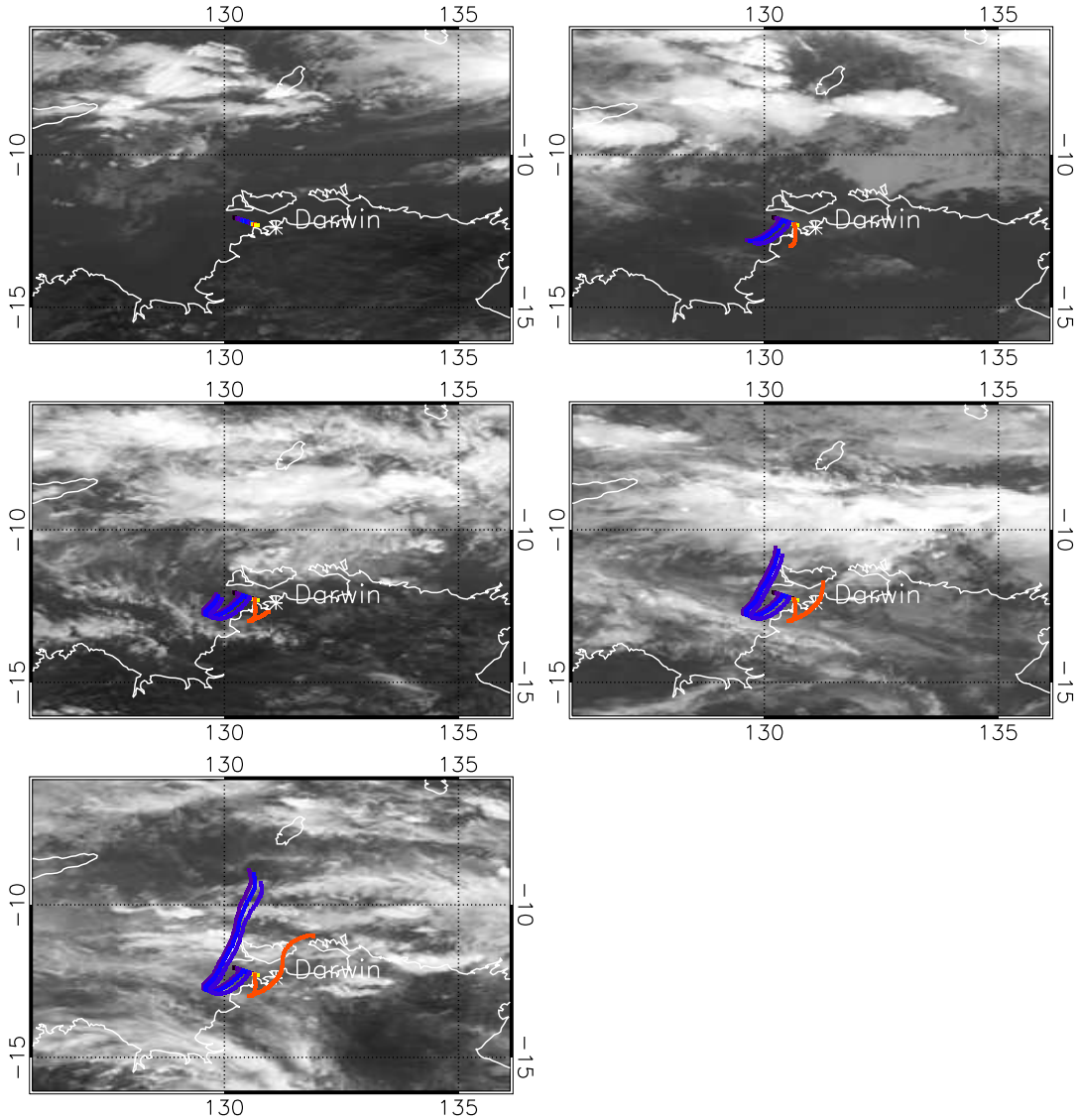

Figure 7.13: An example of combined Egrett, MTSAT infrared and back trajectory data (coloured) in order to determine the period of last convective influence. The plots progress in 12 hour intervals: *top left:* 0 hour (aircraft measurement), *top right:* -12 hours, *middle left:* -24 hours, *middle right:* -36 hours, *bottom left:* -48 hours.

the trajectory (see chapter 8 for a case study example of an integrated trajectory and satellite analysis to find cloud top heights and the point of outflow). This would suggest that there passed approximately 36 to 48 hour since the air was last influenced by convection. The winds also fluctuated significantly during the course of the trajectories, indicating a higher possibility of mixing and dilution in the air's constitution.

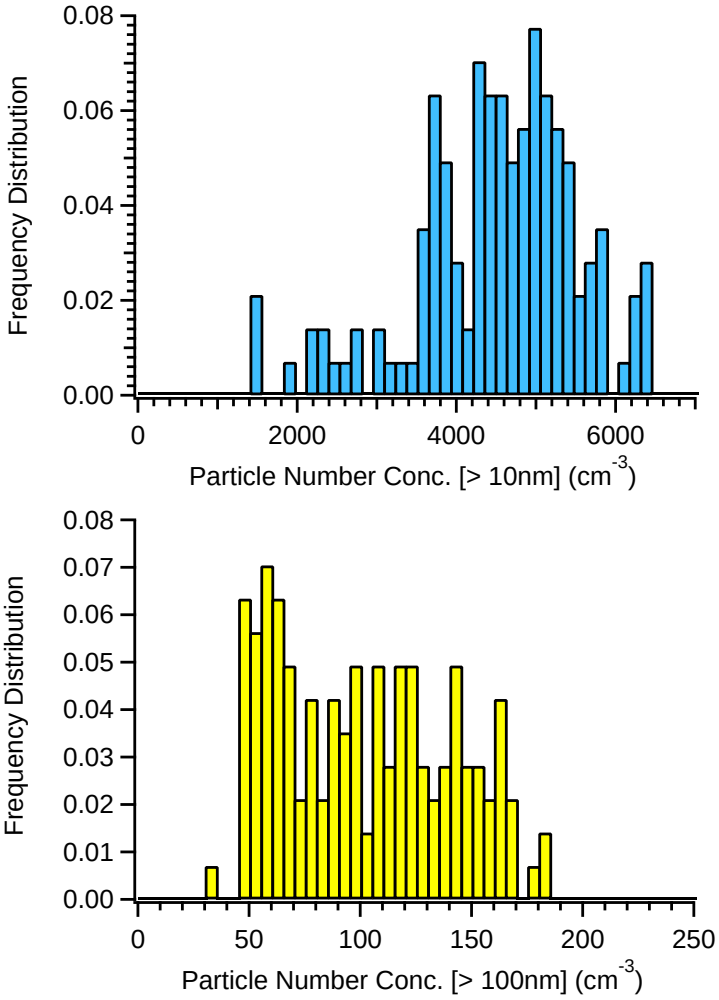

Figure 7.14: Histograms for background aerosol population measured during the inactive monsoon on flight SE24. Data were grouped into 5 km sections and then the data were median averaged. The top plot represents the N_{10} data and the bottom, the N_{100} data.

The cloud-free regions that had at least 24 hours of non-contact with convective activity were selected for analysis. These areas were grouped in to 5 km regions,

as before, and then median averaged. These 5km segments were then statistically analysed with histograms (figure 7.14) and box-whisker plots (figure 7.15) to give an impression of the typical background aerosol population. The data suggests that there was a median N_{10} aerosol population of $\sim$ 4,500 cm^{-3}. The N_{100} concentrations are quite spread, with a median of about 100 cm^{-3} and an interquartile range between 60 and 130 cm^{-3}. An N_{100} concentration anywhere between 50 and 150 cm^{-3} seems equally likely from this plot (90% probability). These data were obtained after 1 - 4 days of convective inactivity and lack of influence on the air mass. The spread of the data is typically between 3,000 and 6,000 cm^{-3} suggesting some inhomogeneity in the sources. Also some of the lower aerosol concentrations found in the cloud-free data (see figure 7.9) were typically between 3,000 and 6,000 cm^{-3}, for example AE21, AE25 and AE29 which all occurred at or near the inactive monsoon period. This data gives some indication as which events are more exceptional than the norm and which might indicate possible nucleation.

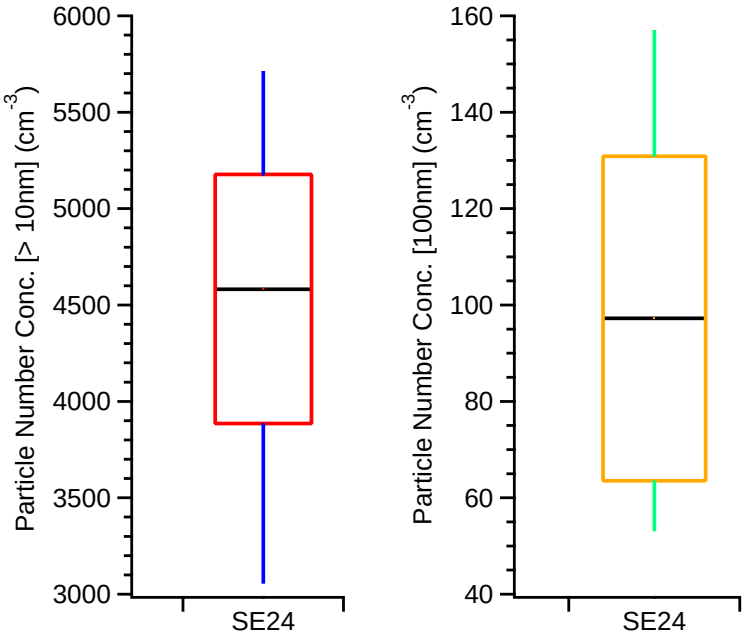

Figure 7.15: Box-whisker plot for background aerosol population (N_{10}, *left* and N_{100}, *right*) measured during the inactive monsoon on flight SE24. The centre line is the median, the upper whisker is the 90th percentile, the upper box is the 75th percentile, the lower box the 25th percentile and the lower whisker is the 10th percentile.

Chapter 8

Nucleation - a case study

8.1 Nucleation in the Tropical Tropopause Layer (TTL)

This case study aimed to find and quantify areas of suspected nucleation during ACTIVE. It has been seen in earlier campaigns that high number densities of aerosol have been seen in convective outflow (e.g. Strom et al., 1999; Twohy et al., 2002); it was suspected by the authors that nucleation was occurring downstream of the storm anvil, in areas of high moisture and precursor gases (such as SO_2). The statistical survey of ACTIVE also pointed to a number of cases of very elevated aerosol concentrations, in comparison to the PBL and the TTL background (see chapter 7); these flights, AE12, AE18, AE19 and AE29 all stood out from the typical aerosol concentrations seen across the ACTIVE flight campaign (compared with other flights – see figures 7.4, 7.9 and 7.10). This required further investigation to determine the cause of the enhanced aerosol concentrations, N_{10} in particular, and to confirm if nucleation could have occurred in the UT/TTL region. This investigation will focus on the flight of AE19 on the 23 January 2006 but the methodology was also transferable to other ACTIVE flights.

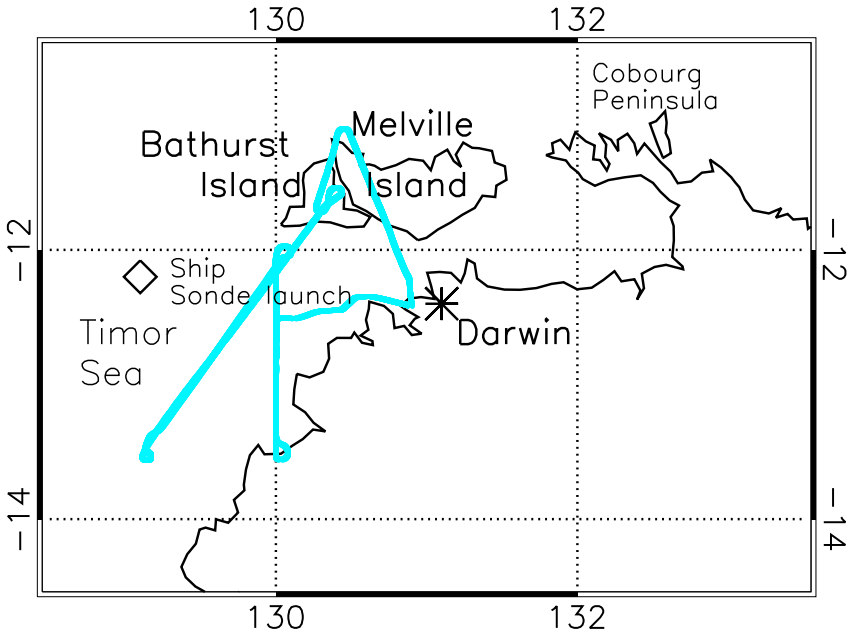

Figure 8.1: AE19 flight track (blue line) as it passes over the Darwin topography. The ship is the location of the regular sonde launches which were used for temperature profiling.

8.2 Experimental details

The ACTIVE experiment is explained in detail in chapter 5. This case study looks at the situation on the 23 January 2006 and the meteorology over the preceding days. This study also uses data from the M-55 Geophysica aircraft acquired during the concurrent SCOUT-O3 campaign in Darwin (Vaughan et al., 2008). The flight of the 23 January 2006 took place during the dissipation of a large monsoon system that spawned the previous day over central Northern Territory and then moved to the coast (a large mesoscale convective system [MCS] developed later in the day, as this storm decayed).

8.3 AE19 flight details

The Egrett flight of AE19 took place on the day a monsoon storm formed on the coastal region of the Northern Territory. The storm cells then moved towards the sea, where they intensified. The flight of the Egrett took place as the anvils were beginning to dissipate; the anvil over the Cobourg peninsula, east of the Tiwis,

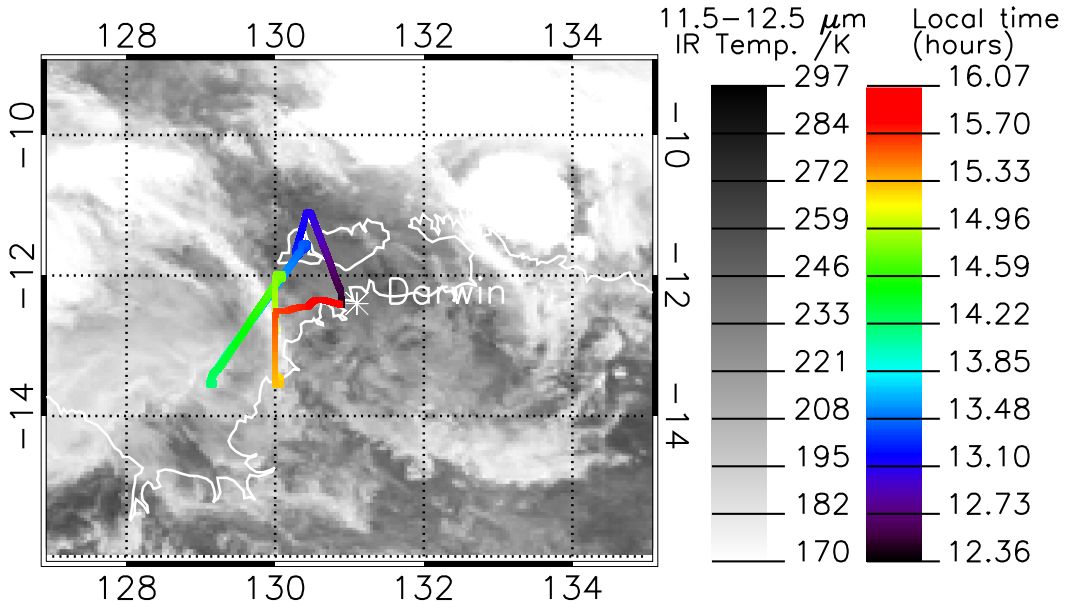

Figure 8.2: Egrett flight is colour-coded with the local time. The MTSAT image is mapped using the IR channel 2 (IR-2, 11.5 - 12.5 μm), scaled black-white. The MTSAT image, over the Darwin area, was taken at approximately 13:20 local time.

dissipated sooner than the Timor Sea storm, to the west of Bathurst Island. The Egrett flight path is superimposed over a contemporaneous satellite image in figure 8.2. After ascending to 10.7 km altitude to the north of Bathurst Island, the plane flew south-west to 13.0° S, 129.4° W, then traced its path as far as 12.0° S, 130.1° W, before flying south to 13.3° S, 130.0° W, then returning via 12.5° S, 130.0° W to Darwin. The flight was designed to study the dissipating anvil over the Timor Sea, beginning in clear air and flying into cloud.

8.4 SO_2 measurements

There were SO_2 measurements made in the first campaign as part of the SCOUT-O3 campaign collaboration. The Falcon aircraft was able to operate up to an 11 km ceiling and contained a chemical ionization mass spectroscopy that could detect SO_2 (Speldel et al., 2007). There were not any SO_2 measurements available for the second campaign but General Circulation Models with chemical modules, such as pTOMCAT – a three-dimensional [3-D] off-line chemical transport model

[CTM] (Chipperfield, 2006) – were able to provide data for this period of ACTIVE. The model data were found to give similar values to those which were measured directly during the first campaign.

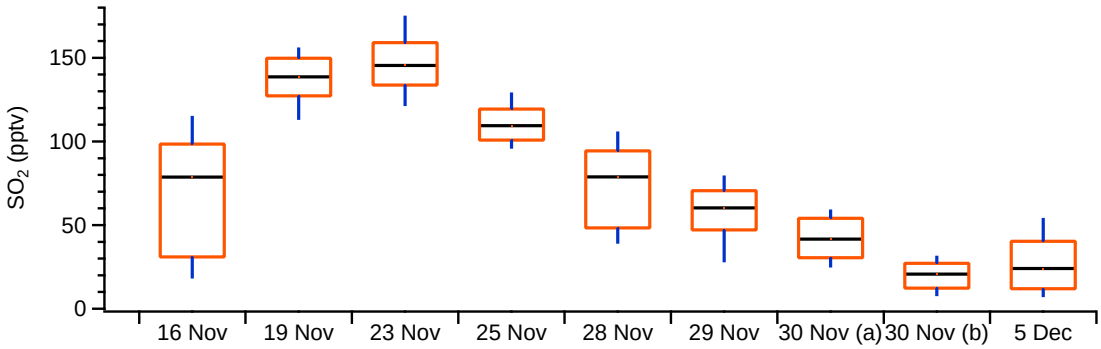

Figure 8.3: SO_2 data from the first campaign, in the upper troposphere above Darwin, presented in box-whisker format. The centre line is the median, the upper whisker is the 90th percentile, the upper box is the 75th percentile, the lower box the 25th percentile and the lower whisker is the 10th percentile.

The SO_2 measurements from the first campaign are summarised in box-whisker form in figure 8.3. The pTOMCAT models, performed as part of the ACTIVE analysis, found the concentration minima to be 5 pptv, the median to be 10 pptv and a 90th percentile of 40 pptv (personnel communications, Olivier Dessens, University of Cambridge), for 23 January 2006 at 200 hPa. This range, together with the first campaign data, meant there was some variability of SO_2 in the convective outflow region ($\sim$ 10 km) above Darwin, during the ACTIVE period. This could be a result of variability in convective activity or changes in the climatology, in particular the boundary layer chemical burden (DMS, SO_2, biomass burning species, etc.). However, it can be seen that there was a trend towards lower SO_2 concentrations (lower median and 90th percentiles) throughout the first campaign and together with the model data for the 23 January 2006 it seems probable that the SO_2 concentrations (background) for January 2006 were below 50 pptv (90th percentile).

8.5 Aerosol measurements

Figure 8.4 shows a section of flight as the aircraft flew south-west from Bathurst Island. The aerosol data show a distinct change in number concentration as the flight progresses. A clear boundary is seen between a region of high Aitken aerosol (N_{10}, light blue line), in cloud-free air (< 0.05 cm^{-3} in the 15 - 55 μm size range, green line), and a corresponding low particle number concentration in more cloudy regions, in the latter section of flight. The accumulation mode aerosol concentration is also noticeable higher in the cloud-free region, though not as enhanced as the Aitken mode. This is consistent with the scavenging of aerosols and precursor gases in cloud (Twohy et al., 2002). Note the change in CO as the aircraft entered cloud, denoting a change in airmass - suggesting that the contrast in particle concentrations might not be purely due to the edge of a dissipating anvil. Nevertheless, the very high concentration of small particles do suggest air that has recently been in cloud, followed by particle nucleation when the cloud dissipated. Figure 8.5 shows the flight segment of figure 8.4 overlaid on the satellite image of figure 8.2. The boundary between the high and low particle number concentrations and their relation to the surrounding cloud can be clearly seen in this image.

To identify possible nucleation events, sections of flight AE19 that were above 10 km and out of cloud were divided into 5 km sections. 5 km was chosen because the BADC trajectory service had a limited resolution for initiation coordinate points. 5 km was approximately the greatest resolution possible with this ECMWF model service. Furthermore, the Egrett wind data, which were used in concert with the air mass trajectory service, were found to favour a 50 second, or 5 km, median block averaging (see section 5.5.4). The criterion for identifying possible nucleation event was taken to be at least 2000 Aitken mode particles cm^{-3}; this latter value exceeded boundary-layer measurements made by the Dornier during this period thus excluding any possible boundary-layer source for the observed particles. The flight track was superimposed on to the nearest MTSAT satellite data file (infrared channel 2, 11.5-12 μm), to within the nearest half hour (since MTSAT data was recorded hourly); the additional 20 minute MTSAT scanning time required to reach Darwin was also taken into account.

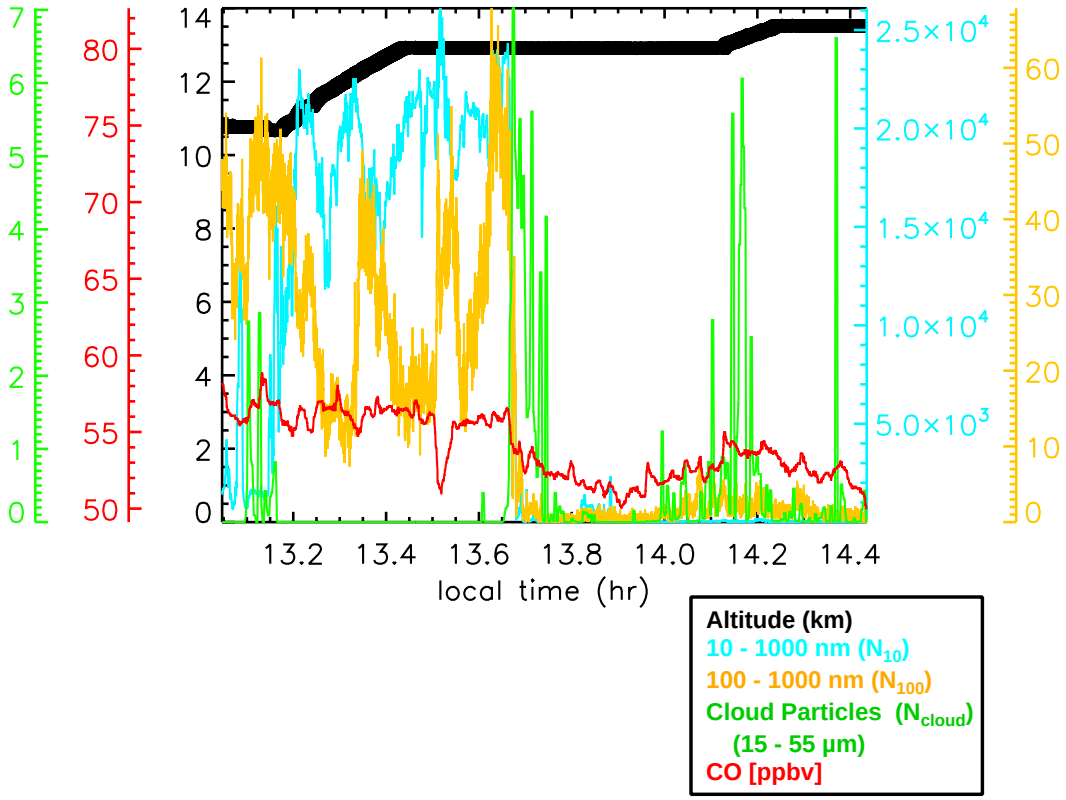

Figure 8.4: Showing aircraft altitude (km, black), particle number concentration in number cm^{-3} (STP) and carbon monoxide. Note the dramatic fall in aerosol concentration as the aircraft enters cloud (13.65 hr).

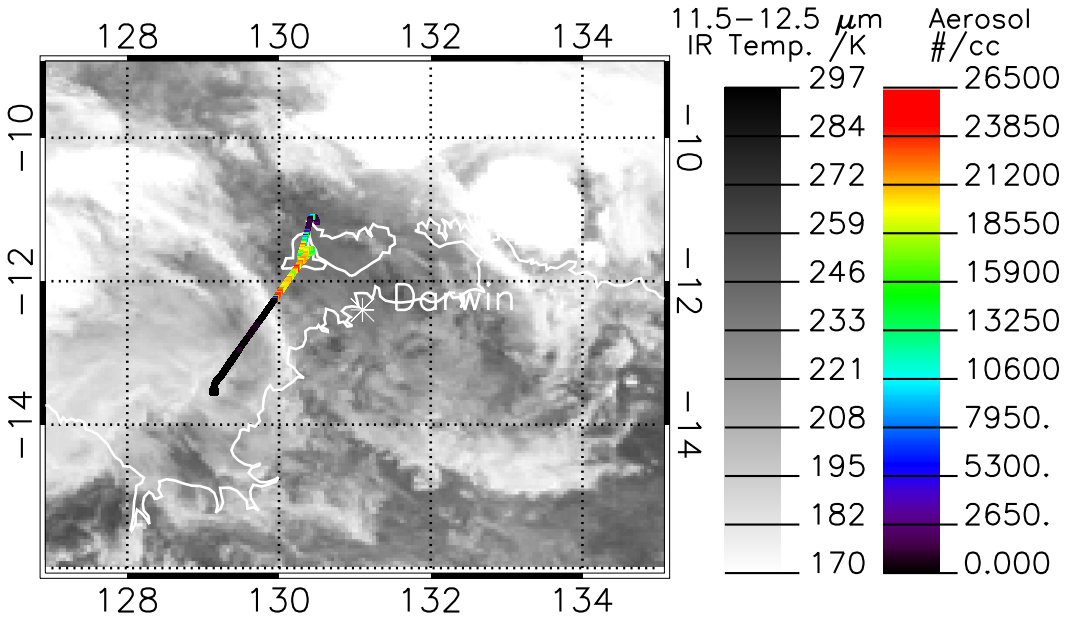

Figure 8.5: Infrared satellite image, overlaid with a section of flight data, satellite image is the same as in figure 8.2. The flight track is colour coded with aerosol concentration data (see coloured bar), for the N_{10}.

8.6 Interpretation of nucleation events

8.6.1 Applying trajectories to satellite imagery

Having identified a number of cases of recent nucleation events, we now turn to the question of time scale - how long was it since the air was in cloud? To answer this question we use wind data and back-trajectory analysis combined with satellite images. The wind data and back trajectories were used separately in order to assess the consistency of the 2 methods. The wind data were taken from the Egrett 3-way pitot tube. The back-trajectories were calculated using the British Atmospheric Data Centre (BADC) trajectory server, based on ECMWF analysis at a resolution of 2.5° × 2.5 ° - for further details see Allen et al. (2009). The validity of the results is to a large degree dependent on the accuracy of the ECMWF wind fields. These were checked against wind measurements aboard the Egrett and were found to agree. The wind data were used for the AE19 case and the back trajectories were used for AE12 and AE18, due to the longer timescales and distances involved.

The wind projections were initiated at the centre of the 5 km segments and were a

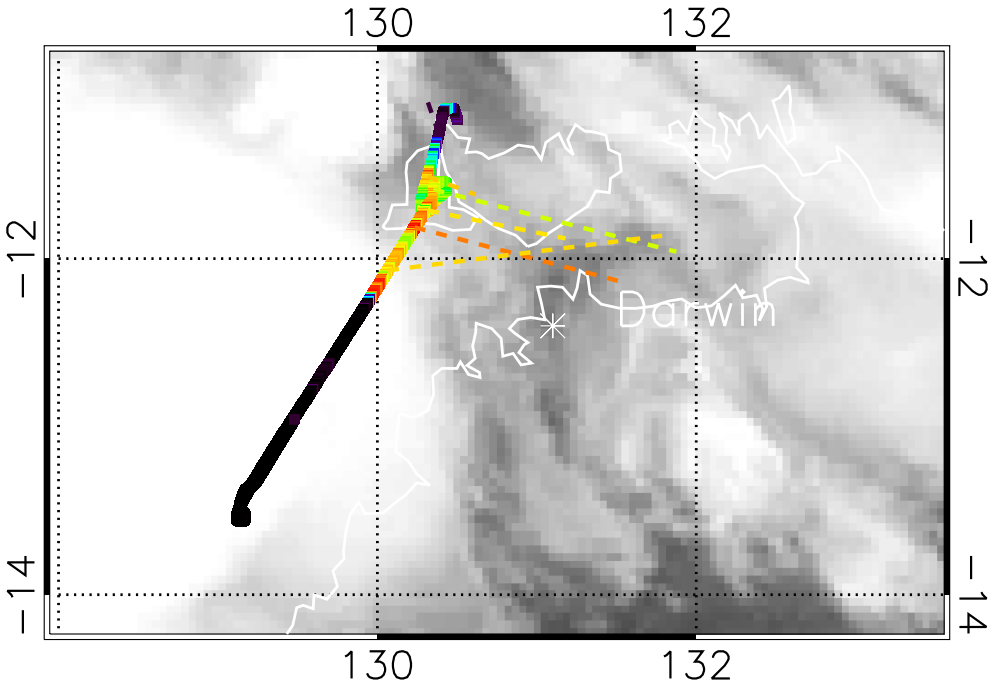

Figure 8.6: Wind data projections overlaid on to MTSAT satellite image; dashed lines indicate the wind trajectory. The dotted lines are coloured to the same N_{10} colour-scale (see figure 8.5) found at their origin. This figure shows an example of 6 initiation points, whereas in reality there were many more 5 km sections. This was done to show the method more clearly and to compare to the BADC back trajectories, which used the same start points. This is the same AE19 section seen in figures 8.4 and 8.5. The wind end points show the air mass location 4 hours previously; the MTSAT data also shows the conditions 4 hours before the aircraft measurements were made.

median of the wind velocity within that segment. The wind data were then used to project the air mass into the past; by making use of the hourly MTSAT data, the location and origin of the air could be tracked retrospectively (see example in figure 8.6).

Back-trajectories were initiated at 0600 UTC (15:30 local time) from the centre of a selection of 5 km flight sections. The computations provided half hourly information about the latitude, longitude, pressure level and temperature. This information, together with the availability of hourly MTSAT data, allowed the suspected nucleation events to be tracked onto earlier satellite images, as with the wind projection method. An example of this method is shown in figure 8.7, for the same section of flight AE19 shown above (figures 8.4 and 8.5). The flight

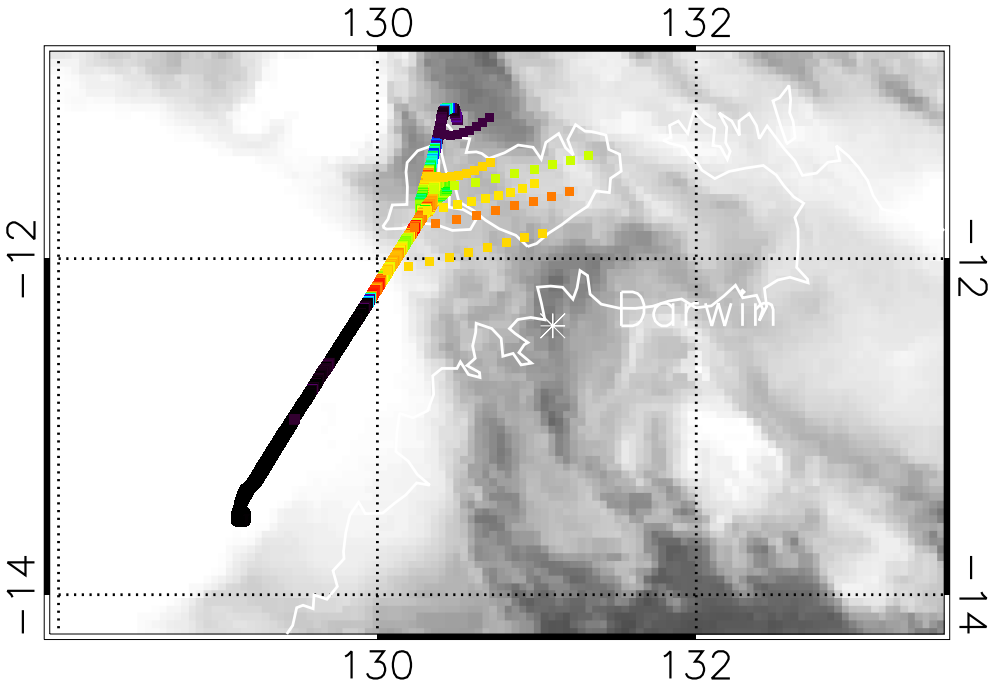

Figure 8.7: Back trajectories overlaid on to MTSAT satellite image; dashed lines indicate the trajectories. The dotted lines are coloured to the same N_{10} colour-scale (see figure 8.5) found at their origin. Each dot shows the air's location at half hourly points. This is the same AE19 section seen in figures 8.4 and 8.5. This example is 4 hours back.

track is coloured with the same N_{10} scale as above and the hourly regression into the past is indicated by the dashed extension of the trajectories and earlier MTSAT images (note that the colour of the trajectories merely indicates the N_{10} concentration at the back trajectory initiation point on the Egrett flight track). It can be seen that the trajectories emanated from a convective cloud system 3 - 4 hours previously. The methodology was continued by taking IR temperature (11.5 - 12.5 μm) medians, over a 5 km radius, at the end points of the trajectories. This provided hourly data for the cloud IR temperature in the vertical plane of the trajectory. Temperature and altitude were related using a radiosonde profile measured from a ship located beneath the Egrett path at 14:27 LT.

Fig. 8.8 shows an example of the variation of cloud top temperature and height derived along a trajectory. The time at which the air was last in cloud was determined by the altitude of the Egrett - in this case 11.2 km, corresponding to a time of around 2.4 hours since the air was last in cloud. This methodology was

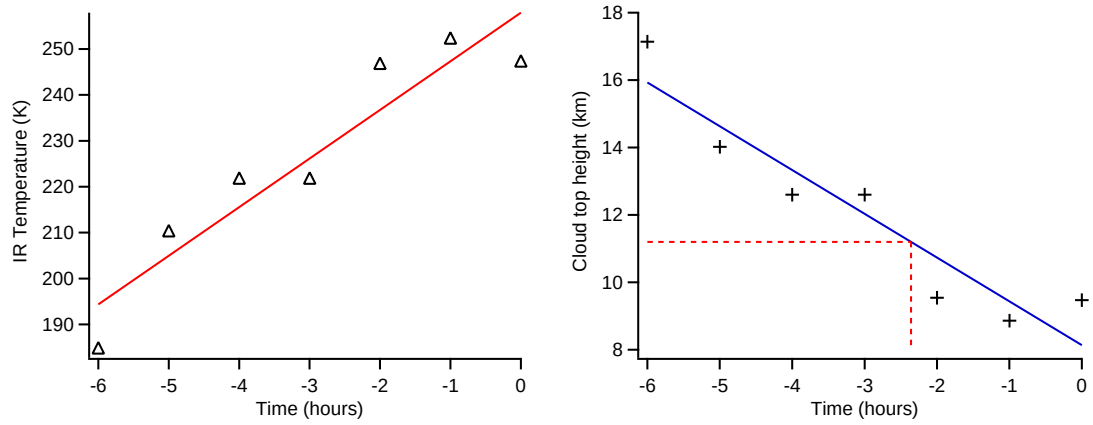

Figure 8.8: A trajectory taken from the above section (figure 8.5). The left-hand plot shows the infrared temperature at the trajectory end-point against time. The right-hand plot is for the same trajectory shown as the corresponding cloud top height against time - the red dashed-line indicates the Egrett altitude and the corresponding time.

applied to all the nucleation events.

8.6.2 Compatibility of cloud top temperature and MT-SAT IR: Geophysica

The reliability of this method depends on the compatibility of cloud top temperature and the remotely sensed satellite temperatures, which are inferred from IR radiation. The altitude of the nucleation event, the pressure level of the trajectory and its relation to cloud height must be investigated. Firstly, the use of back trajectory data requires the calculated pressure level to be consistent with the aircraft pressure level for the duration of the analysis. It was found on investigation that ECMWF calculated no significant descent (below a 10 km level), back to 48 hours, for the all of the trajectories used in this ACTIVE study (AE12, AE18, AE19 and SE24). Wind projections were regressed less in time so had very little descent (wind data were used back to -12 hours). Therefore, the trajectories and wind data have been assumed to have followed a constant pressure level throughout the investigation. A further consideration was that the MTSAT provided IR data calibrated to blackbody temperature distributions; these temperature algorithms need to be tested for their ability to infer actual cloud top temperatures. The high-altitude M-55 Geophysica (21 km ceiling) allowed the

sampling of the highest of the cloud tops from convective storms.

The M-55 Geophysica flight and FSSP data (Vaughan et al., 2008) were used from first campaign flights: 28, 29 and 30 November 2005. During these flights, the Geophysica spent time investigating the cloud top boundary of convective storms and the thinner cirrus that resulted from anvil dissipation. The Geophysica's high ceiling allowed it to circle above the storm anvil and then descend into the cloud. The dispersing anvil cloud was very similar to that which was observed during 23 January 2006 (AE19).

The Geophysica cloud and temperature data and MTSAT satellite IR temperatures were combined in a similar method to that used in the aerosol data analysis. Sections of Geophysica data that crossed the cloud top boundary – cloud marked by concentrations of 0.05 cm^{-3} and greater – were first extracted. These data points, including temperature, were overlaid onto the nearest contemporaneous IR data map. The IR temperature was found by taking MTSAT data medians 5 km around the Geophysica data coordinates; this was done for all the extracted data points on the cloud top boundary. The scatter plot (figure 8.9) shows the IR channel 2 data plotted against Geophysica measured temperatures, at cloud top. The straight line has been forced through at gradient 1. The R^2 value shows the correlation coefficient for the data. It can be seen that at very low temperatures (high altitudes), about 180 K, the IR-2 measurements slightly underestimate the true temperature. However, the overall correlation shows a good correlation between the remote satellite retrieval method and the in situ measurements. This allowed the MTSAT data to be used with some confidence when remotely sampling cloud tops during the ACTIVE project.

Hourly radiosonde data, from an observation ship in the Timor Sea located at approximately (12.2 S, 129.1 W), provide atmospheric temperature profiles. The sondes produced altitude, temperature, latitude, longitude, etc. data. There was a radiosonde released at 2:37 p.m. local time, at the approximate mid-point of the AE19 flight (see figure 8.1). These date were then used to determine the temperature with altitude for the cloud tops observed during this flight. The equivalent IR temperature was converted into altitude using the sonde profile data and was plotted hourly as in figure 8.8.

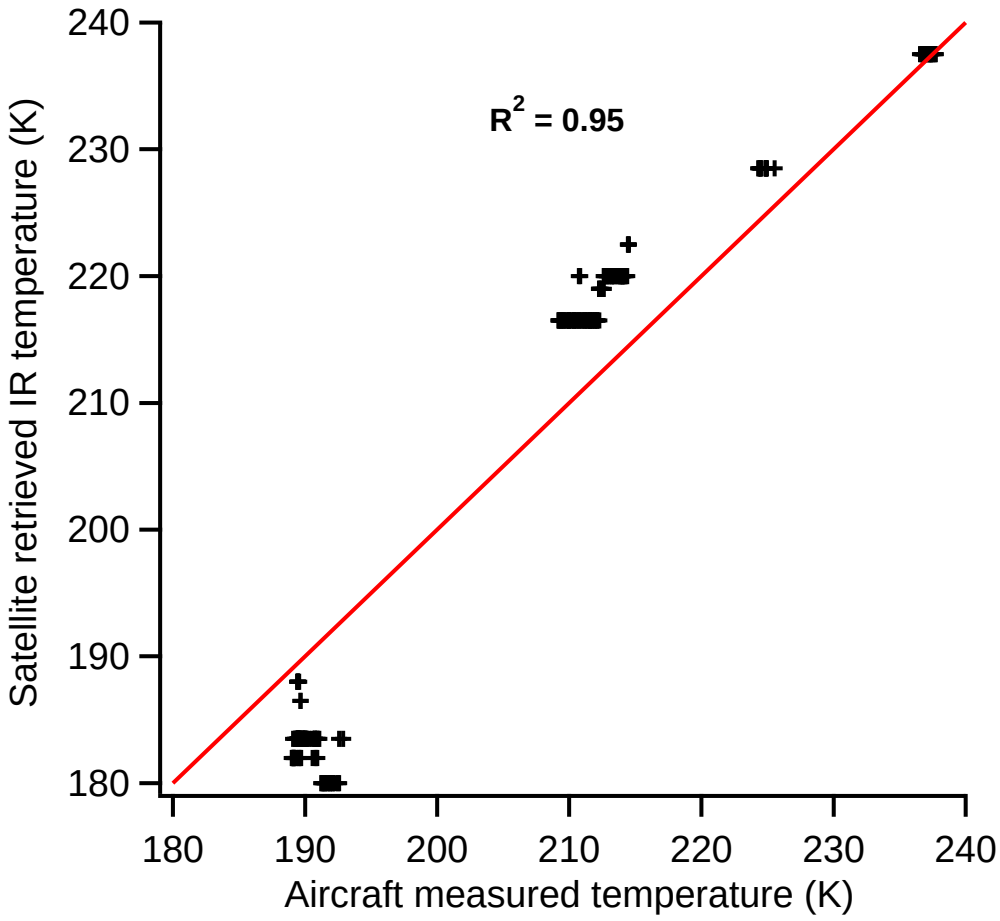

Figure 8.9: Scatter of infrared temperature (MTSAT) against the Geophysica measured temperature, for cloud tops. The line indicates a gradient of 1.

8.6.3 Error analysis

For the case of the wind data, the propagation of errors were calculated by first finding a standard deviation of the wind velocity vectors within the 5 km segments. Since the MTSAT satellite scanned hourly, a further error was considered to be the time offset between the aircraft and IR data. The satellite data were chosen so as to be only a maximum of 0.5 hour away from the Egrett measurement but an unavoidable error occurred due to the time resolution available. The final error propagation came from the Geophysica and IR-2 temperature calibration (see section 8.6.2 and figure 8.9). The standard deviation was calculated from the scatter calibration fit. These error were propagated to the final result and expressed as an uncertainty in the outflow time.

The back trajectory error analysis was the same except for the calculation of the trajectory variance. The BADC trajectories were initiated with clustering enabled. This allowed every coordinate point (trajectory) to have a 4-point cluster simultaneously defined at a set separation from the centre. The cluster separation from the centre was chosen to be 5 km since this was the standard averaging region used throughout this investigation. The divergence of the cluster trajectories away from the centre (defined) trajectory was calculated for each hour and used to calculate a standard deviation.

8.7 Results: Nucleation in the TTL

The sensitivity of the result was tested by adding a + 5 K and a - 5 K offset to the temperature-altitude relationship and then recalculating the cloud outflow time.

The Aitken mode aerosol (N_{10}) reached a concentration of 25,000 cm^{-3} after 2 - 4 hours. The constraints of the available data and fitted sigmoid line seem to suggest that the concentration stays at a maximum and does not decrease. Loss mechanisms, such as coagulation, would be expected to reduce the aerosol population with increasing time, as nucleation and sulphuric acid production rates drop (Clement et al., 2002, 2006). The accumulation mode (N_{100}) showed a slower increase in number; the exponentially fitted trendlines indicated a more rapid growth in number concentration between 3.8 - 6 hours, as the Aitken mode

was reaching its maximum concentration.

The accumulation mode aerosol is expected to be produced by vapour deposition and coagulation of Aitken mode particles. The almost exponential increase in accumulation mode number concentration could be a sign of increased coagulation from an already highly populated Aitken size range. Ekman et al. (2006) found that simulations of aerosol growth in the upper troposphere showed a preference for coagulation growth, rather than H_2SO_4 deposition, particularly for the accumulation mode. It must be noted however that the efficiency curve of CPC2 (figure 5.4) is wide enough to overlap with the CPC1 efficiency and potentially produce significant number of 'double-counts'. The maximum N_{10} concentrations were as high as 25,000 cm^{-3}; as the nucleation mode (3 - 9 nm) particles grow from 10 nm and beyond they begin to be detected by the CPC1. With continued growth, it is plausible that the CPC2 will begin to detect particles in the CPC1 range – a 50 nm is detected by the CPC2 with 20% efficiency. Tellingly, the efficiency curve (between approximately 0 and 50%) resembles an exponential curve, as seen in the 8.10. This might point to an overlaying of the two datasets as one efficiency curve convolves with the other. Nevertheless, the CPC1 data still strongly supports the production of large numbers of Aitken mode aerosols, of the order of 10 nm.

In the present hypothesis, the storm anvil outgassed SO_2 (from the PBL and/or entrained in the mid and upper troposphere) which was oxidised by radicals such as OH (Ekman et al., 2004) and further reacted with water and oxygen to produce sulphuric acid. Sulphuric acid and water molecules then form clusters that begin the aerosol nucleation process; some models suggest TTL conditions are conducive to almost barrierless sulphuric acid nucleation (Kulmala et al., 1998; Clement et al., 2002).

Clement et al. (2006) showed that numbers of aerosol produced in TTL simulations, were typically 10^3 - 10^4 cm^{-3}, for sizes above 20 nm, with the total aerosol concentration (sized over 3 nm) between 10^4 - 10^6 cm^{-3} - this was from a H_2SO_4 production rate of 10^5 $cm^{-3}s^{-1}$. Both the current study and the Clement et al. (2006) study showed a sudden increase in the aerosol concentration (for the lowest size range in each: N_{10} in this study and > 20 nm in Clement et al. (2006)) that then levelled out. The simulation also showed that the maximum was attained at about 4 - 5 hours, similar to this study. Due to the constraints of the data,

it was not possible to reproduce the slow decrease in the aerosol concentration with time, after approximately 5 - 6 hours in Clement et al. (2006). However, it is believed that their simulation included a dry deposition factor for the boundary layer. The relevance of this is debatable considering the height of the data obtained (above 10 km) and the roughness factor used in the model (e.g. grass, marine, concrete) (Schack et al., 1985). On the other hand, it is expected that the aerosol concentration would decrease with time as coagulation of aerosol takes effect. However, at these altitudes coagulation is not as effective as at higher temperatures (see chapter 3).

In comparing measurement and model, consideration must be given to the likely H_2SO_4 production rate in the Darwin area. SO_2 concentrations were measured during the SCOUT-O3 campaign on the Falcon aircraft using Chemical Ionisation mass spectrometry (Speldel et al., 2007). In the outflow of a large storm in the TTL on the 30 November 2005 (see Vaughan et al. (2008) for more details) this measured a median of 15 pptv of SO_2. For OH, we take the median upper troposphere OH concentration of 0.85 pptv, taken from pTOMCAT simulations for the 23 January 2006. Using the H_2SO_4 production rate of Clement et al. (2006):

$$P = 10^{-18}[OH][SO_2]\mathrm{m}^{-3}\mathrm{s}^{-1},$$

with 0.23 pptv OH and 15 pptv of SO_2 at a pressure of 200 hPa and temperature of 223 K gives P = 5.29×10^8 $\mathrm{m}^{-3}\mathrm{s}^{-1}$, or P = 529 $\mathrm{cm}^{-3}\mathrm{s}^{-1}$. This is of the order of 2 magnitudes lower than that of Clement et al. (2006) due to the much lower SO_2 detected over Darwin compared to Twohy et al. (2002).

The expression for P also provides an estimate of the SO_2 photochemical lifetime in the TTL which is of order 1 day (the actual lifetime is longer as OH is not present in the dark).

A further test of the results can be made by considering the number of sulphur atoms required to produce the maximum concentration, 2.5×10^4 cm^{-3} (STP), of Aitken mode aerosol. The STP data must first be converted back into in situ data:

$$N = 0.27N(\mathrm{stp\ cm}^{-3}), \tag{8.1}$$

for a pressure of 200 hPa and temperature of 215 K. This gives an approximate ACTIVE maximum of 6,750 cm^{-3}.

To simplify the analysis and provide an upper limit, the Aitken mode (N_{10}) will be taken as monodisperse with a diameter, D_p, of 10 nm. The aerosol will be modelled as spherical and containing purely H_2SO_4 – not strictly realistic, but it provides an upper limit on the level of sulphur required,

$$\text{mass/cm}^3 = \frac{4}{3}\pi\left(\frac{D_p}{3}\right)\rho N,$$

where ρ is the density of sulphuric acid, 1830.5 kg m^{-3}, and N is the number of particles cm^{-3}. Using the mass of a single sulphur atom, 5.31×10^{-26} kg, the total number of required sulphur is:

$$1.22 \times 10^8 \text{atoms of S cm}^{-3}.$$

Using an SO_2 concentration of 15 pptv, produces 9.66×10^7 *S atoms* cm^{-3}, which is slightly lower than the required value. This simple calculation involves a number of assumptions, such as, one SO_2 molecule yields one H_2SO_4 molecule and that the aerosol is 100% sulphuric acid. The uncertainty in the assumptions and the SO_2 measurements are probably sufficient to explain the small discrepancy. However, a more detailed numerical method, introduced in chapter 3 will be presented later to test the hypothesis further. This leaves open the possibility that there was some other compound(s) involved, such organics. The lower organic loading, compared to the first campaign (see chapter 4 and figure 4.1), would seem to discount this possibility for the case of flight AE19 – however, there were still many potential sources of organics, such as long-range transport from Indonesia. Ion assisted nucleation could be an influence, especially in the photoactive TTL. The possible deficit in SO_2 would still pose the question of which chemical species were involved in the aerosol production. As Clement et al. (2006) stated in their study, the final aerosol concentration was independent of the initial nucleation number but depended on the production rate of acid – i.e. the presence of sufficient condensable material is the most important factor.

8.8 Summary of nucleation events

This study has found that convective storms, in the tropics, populate the TTL with aerosol, with much higher concentrations observed in the TTL than the boundary layer. In-cloud and cloud-free data showed large differences in aerosol population: in-cloud, N_{10} concentrations were < 100 cm^{-3}; out-cloud, levels were as high as 25,000 cm^{-3}. This suggests that nucleation occurred readily in the cloud outflow: wind projections and BADC back trajectories showed that these nucleation bursts had originated from convective uplift regions. The common hypothesis is of convective storms outgassing SO_2 (from the PBL and entrained by the storm from the free troposphere) which is then oxidised to H_2SO_4; sulphuric acid and water then act as the primary nucleation precursors. Cold TTL temperatures, and a clean cloud-free environment – as outgassed air is generally low in pre-existing aerosol (Perry and Hobbs, 1994; Clement et al., 2002; Twohy et al., 2002) – allowed for ideal nucleation conditions. However, the SO_2 concentrations in the Darwin TTL were not exceptional (8 - 15 pptv median) and were possibly too low to produce such high numbers of Aitken mode particles. This leaves open the possibility of organic nucleation/growth and ion recombination as methods of aerosol production in the TTL.

The upper troposphere CARIBIC study (Heintzenberg et al., 2003) found concentrations of aerosol of diameter, 4 to 12 nm, between 10,000 and 30,000 cm^{-3} (STP) and 12 to 18 nm of 9000 cm^{-3} (STP). Twohy et al. (2002) found levels of nucleation that reached 45,000 cm^{-3} (aerosol $\geq$ 20 nm), downwind of a mid-latitude mesoscale storm. The present study found aerosol concentrations intermediate between these two: Aitken mode (10 - 100 nm) up to 25,000 /cm^3 (STP) and accumulation mode (100 - 1000 nm) up to $\sim$ 220 /cm^3 (STP).

A time frame of 2 - 4 hours is deduced for the Aitken aerosol to reach population levels approaching 25,000 cm^{-3} (STP) - similar to the Clement et al. (2006) simulation study; the accumulation mode reaches values of $\sim$ 220 cm^{-3} (STP) after 5 - 6 hours but with the likelihood being that, due to the wide efficiency curve, the CPC2 is in fact detecting particles smaller than 100 nm. Interestingly, the sigmoid fit-line shows remarkable similarity to the aerosol concentration timelines in the Clement et al. (2006) paper.

8.9 Nucleation: further cases

This methodology was also applied to two other cases with suspected nucleation events – flights that showed very enhanced aerosol concentrations: AE12 and AE18. It was found that in these two cases the outflow from the storms occurred earlier than 12 hours back; as a consequence, only BADC calculated back trajectories were used, for accuracy.

The N_{10} data seems to show similar behaviour across the 3 cases, with a sudden increase in concentration (within 1 - 4 hours) up to a maximum of order 10^4 particles.cm^{-3}. The N_{100} data again shows the exponential type increase which could be a sign of data convolution (CPC2 counting CPC1 data as it grows into detectable range). The Aitken mode, N_{10}, shows that small aerosol particles could be quite persistent. Aitken sized (10 - 100 nm) particles could remain in UT/TTL for considerable time, provided scavenging was not a problem – i.e. reduced convection and limited mixing with moist anvil cloud would allow aerosols to survive (Ekman et al., 2006). This appeared to be the case in AE12; air was transported for a considerable length of time and distance without contact with further convection.

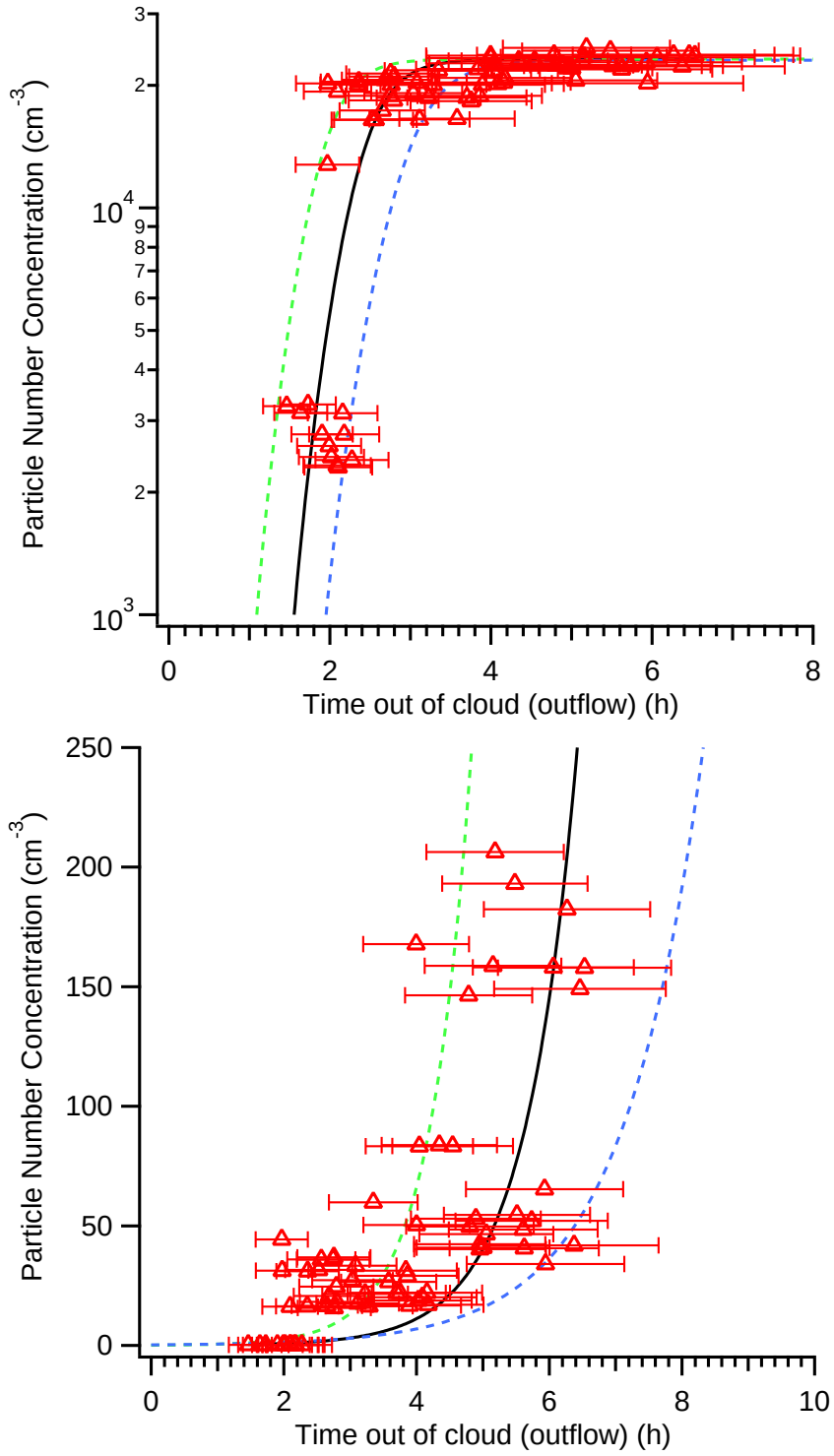

Figure 8.10: These show the particle number concentration (STP) for the Aitken mode, N_{10} (upper plot) and the accumulation mode aerosol, N_{100}, (lower plot), against the time since cloud outflow – this was calculated using wind data. The markers indicate the median particle number concentration for the 5 km flight sections. The cloud evaporation threshold was tested with a $\pm$ 5 K sensitivity; these are shown with the dashed lines. Note that the upper plot has a log-scale y-axis and the lower has a linear scale.

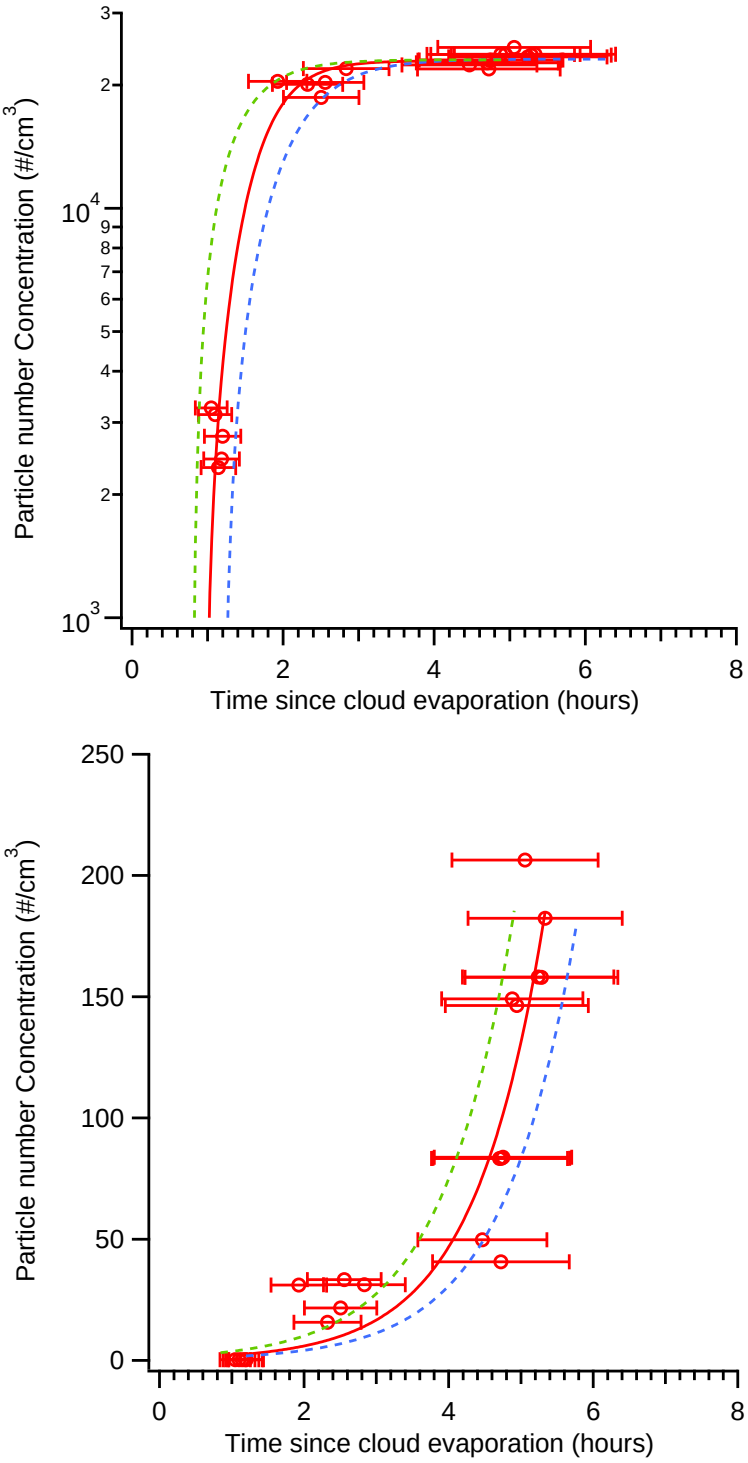

Figure 8.11: These show the particle number concentration (STP) for the Aitken mode, N_{10} (upper plot) and the accumulation mode aerosol, N_{100}, (lower plot), against the time since cloud outflow – this was calculated using BADC back trajectories. The markers indicate the median particle number concentration for the 5 km flight sections. The cloud evaporation threshold was tested with a $\pm$ 5 K sensitivity; these are shown with the dashed lines. Note that the upper plot has a log-scale y-axis and the lower has a linear scale.

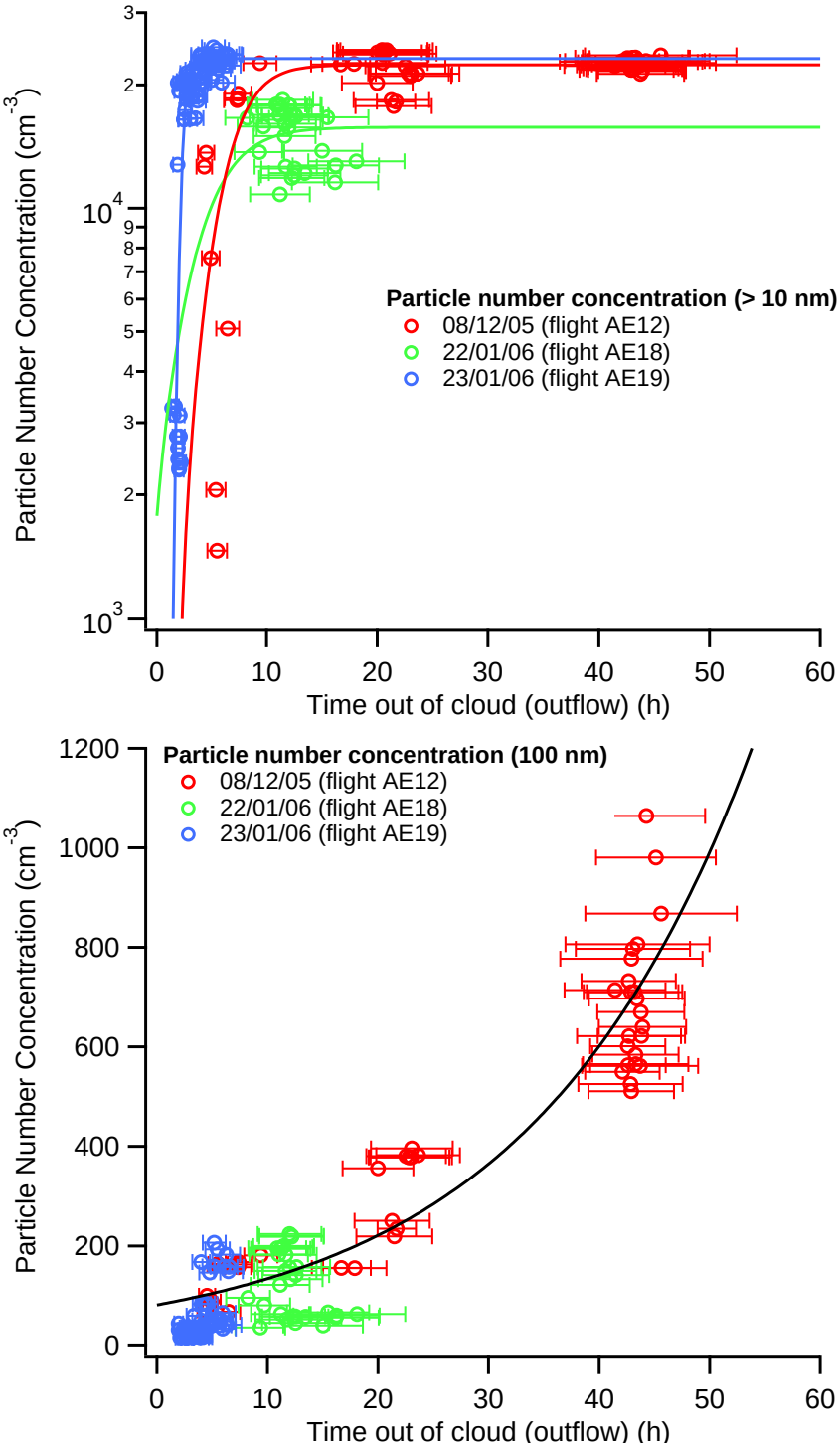

Figure 8.12: N_{10} (*top*) and N_{100} (*bottom*) data are plotted against time (from cloud outflow). Each marker represents a 5 km segment, median averaged. Note the log-scale y-axis in the N_{10} plot and linear y-axis in the N_{100} plot.

Chapter 9

Nucleation model

This modelling exercise was undertaken in order to investigate the nucleation and growth hypothesis presented throughout this study. If freshly nucleated particles, which grow into observable sizes, were to be produced in convective outflow there would need to be a sufficient source of condensable material in the storm region. SO_2 is one of the prime candidates for aerosol precursor gases; via oxidation to H_2SO_4, and together with water, it is believed to form stable aerosol nuclei through the binary nucleation mechanism (see section 2.3 for a background discussion and chapter 3 for the theoretical approach). The following model study allowed an assessment of the required concentration of SO_2 to be made; furthermore, if SO_2 were not present in sufficient amounts, it can give a constraint on the necessary concentration of another, unknown, condensable (for example, the role of organic gases is not fully known and could play a part in the ACTIVE climatology and aerosol production mechanism). Chapter 3 explains the numerical model and the theory and parameterisations that were used. The SO_2 data that were obtained during the first campaign are presented in section 8.4; figure 8.3 shows the box-whisker plot for the first campaign data and clearly shows a trend towards lower concentrations: below 50 pptv (90th percentile). The only available SO_2 data for the second campaign (the period in which the ACTIVE aerosol nucleation data were analysed [chapter 8]) were produced by the pTOMCAT model. The 23 January model run produced a minimum of 5 pptv, a 10 pptv median and a 90th percentile of 40 pptv. However, this data tends to describe the average background level rather than the concentrations in storm outflow. This is also a factor with the first campaign Falcon data because the

aircraft was not primarily tasked with outflow sampling. This uncertainty factor, in SO_2 concentration, could temper any conclusions that were derived from the ACTIVE nucleation study. Nevertheless, the first campaign aircraft data and the model data for the 23 January 2006 gave some limits to the possible SO_2 concentrations above Darwin during ACTIVE.

Simulations were made using an AEROFOR based model (Pirjola and Kulmala, 1998), with some slight adjustments to some of the parameterisations (to reflect more recent work, for example, Kuuluvainen et al. (2010)). The model is a 27 section representation of an aerosol distribution, from 0.5×10^{-9} m to 1.0×10^{-6} m. The model fully represents nucleation, condensational growth and coagulation and uses sulphuric acid as the primary condensable.

Runs were performed with both constant acid production rate and with a semi-sinusoidal variation to model daylight hours and variability of the Sun's intensity. Simulations were made with varying levels of background SO_2 to find the sensitivity of binary nucleation to the precursor gases. The UT pressure level was chosen to be 200 hPa and a corresponding temperature of 220 K; H_2O mixing ration was set to 30 ppmv, as a typical ACTIVE moisture level. Table 9.1 summarises the model runs that were performed for this study, together with their initialisation parameters.

Figure 9.1 shows the base test, where an SO_2 concentration of 1 ppbv was used, as in Clement et al. (2006). The results from Clement et al. (2006) are shown in figure 2.6 and the 25 nm and greater aerosol data are extracted and overlaid onto the current data (shown as a green line in figure 9.1). With the information available in Clement et al. (2006), it was not possible to run an exact replica. Parameterisations and some initialisations are expected to be different during the two simulations, such as the H_2O concentrations/relative humidity, chemical scheme and also the lack of deposition loses in the present model. However, it can be seen that the two simulations produce consistent results, with 25 nm particle production rates of the same magnitude and within approximately $\pm$ 2 hours of each other. The Clement et al. (2006) result does show the result of including deposition in the model and the rate of particle loss; this was not included in the current study because the prime motivation for the experiment was to simulated the nucleation and growth of submicron particles [deposition losses could be included at a possible future investigation]. The similarities in

Table 9.1: This table shows the model runs that were completed for this study and the main programme parameters and initialisations.

SO_2[a] (pptv)	OH (pptv)	H_2O[b] (ppmv)	Temp.[c] (K)	P[d] (hPa)	Sine[e]	Initiation[f] (h)	Time-step[g] (sec)	Runtime (h)	Method[h]
40	0.8	30	220	200	Y	6	0.1	20	Euler forward
100	0.8	30	220	200	Y	6	0.01	20	Euler forward
200	0.8	30	220	200	Y	6	0.01	20	Euler forward
300	0.8	30	220	200	Y	6	0.01	20	Euler forward
1000	0.8	30	220	200	N	–	0.01	20	Euler forward

[a] The SO_2 level remained constant throughout the simulation. The H_2SO_4 production level was based on a kinematic rate-equation (3.3). If daylight variation was enabled, this rate factor was modulated by a semi-sinusoidal function.

[b] H_2O concentrations were considered to be of such high concentration relative to SO_2 that is was assumed to be constant throughout the simulation.

[c] Temperature was typical of the UT/TTL, in the Egrett operational area of 10 to 15 km.

[d] Pressure was typical of the UT/TTL, in the Egrett operational area of 10 to 15 km.

[e] Y (Yes) means that semi-sinusoidal variation was applied to the H_2SO_4 production rate; N (No) if not. The daylight hours for Darwin during 23 January 2005 were 0637 to 1920. The semi-sinusoidal factor was modulated to this time region; the nighttime used a zero production rate.

[f] The initiation point is the defined as the time (h) after sunrise at which the model simulation begins. This result affects the point on the semi-sinusoidal curve at which the daylight modulation begins.

[g] The time-step determines the number of iterative steps required to complete the simulation (together with the *runtime*). Programme stability is largely dependent on the numerical method used but generally the smaller the time-step the more stable the programme. The time-step was adjusted manually until runtime crashes ceased.

[h] *Numerical methodology*: the mathematical solver used to run the model. In the case of this study, an Euler forward differencing method was used (see section 3.4.3) without exception. The time-step is the main parameter for controlling programme stability, when using this methodology.

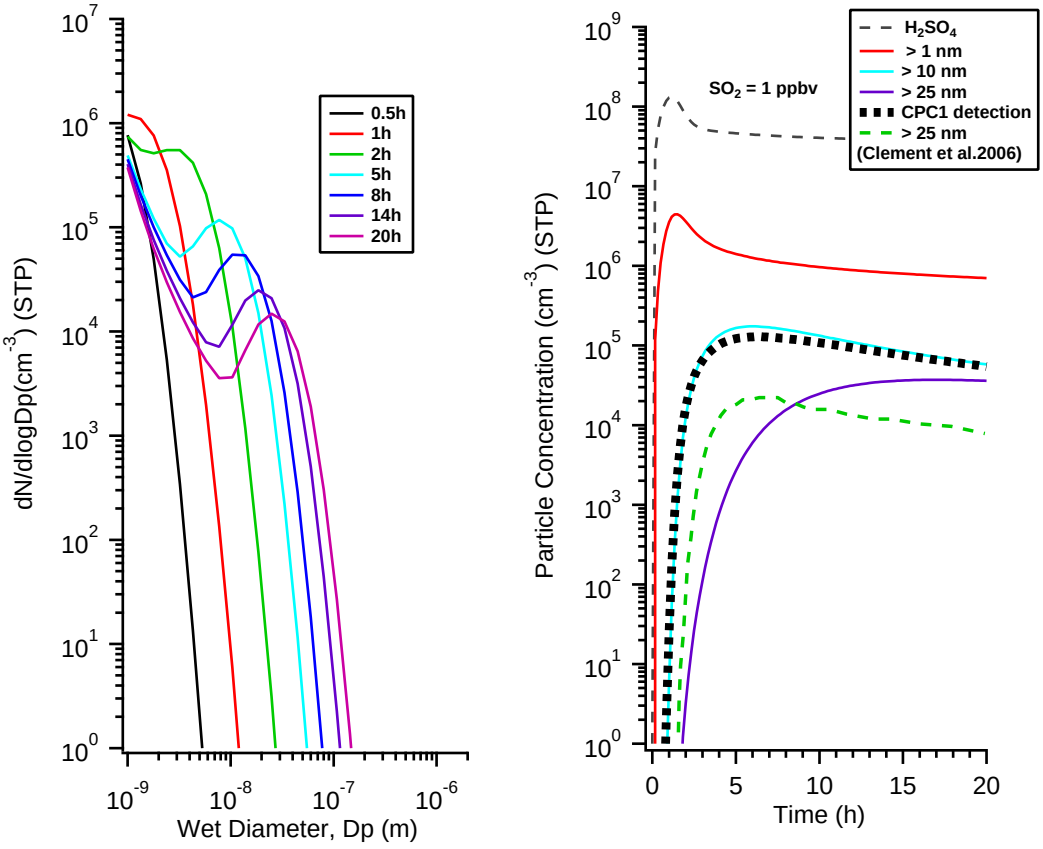

Figure 9.1: *left:* Aerosol size distribution as a function of wet diameter, Dp. The background SO_2 concentration was set at 1 ppbv (1000 pptv) and the acid production was semi-sinusoidally varied to replicate daylight hours. Concentration is adjusted to STP units. *Right:* Concentrations calculated numerically as functions of time for molecular sulphuric acid (H_2SO_4), total aerosol number (above 0.5 nm), and aerosol numbers with diameters over 10 nm and 25 nm. For comparison, the data for 25 nm aerosols and greater from (Clement et al., 2006) are given by the green line.

the comparison allowed the model to be used with confidence in the following aerosol nucleation simulations.

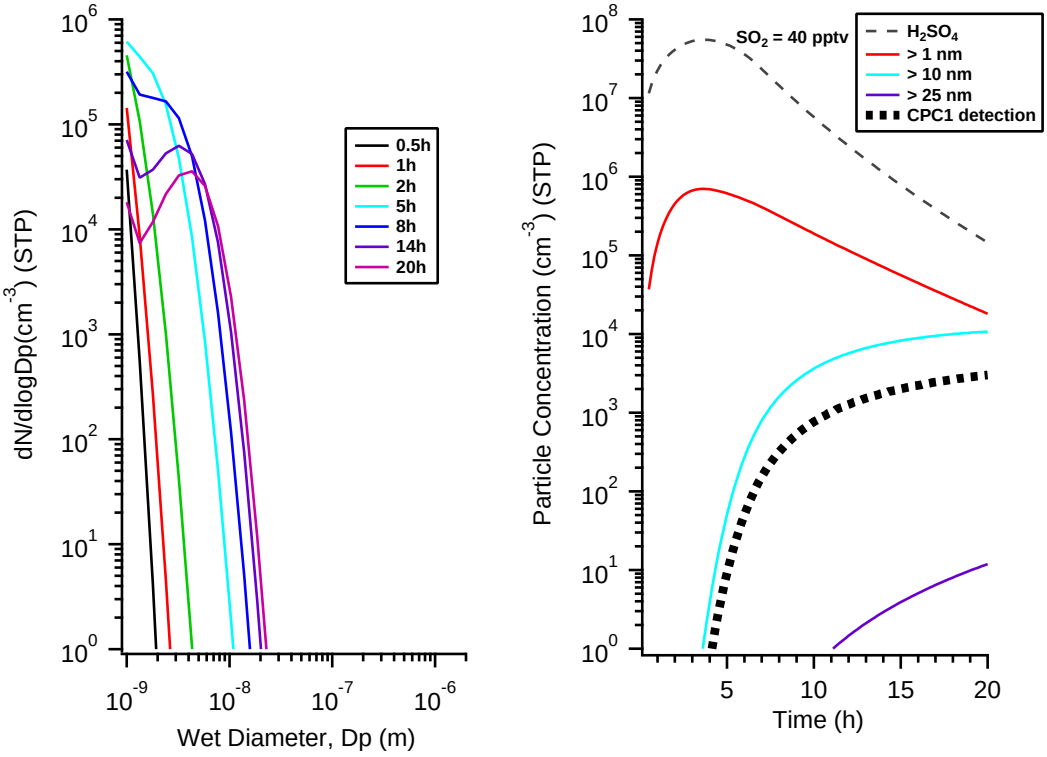

Figure 9.2: *left:* Aerosol size distribution as a function of wet diameter, Dp. The background SO_2 concentration was set at 40 pptv and the acid production was semi-sinusoidally varied to replicate daylight hours. Concentration is adjusted to STP units. *Right:* Concentrations calculated numerically as functions of time for molecular sulphuric acid (H_2SO_4), total aerosol number (above 0.5 nm), and aerosol numbers with diameters over 10 nm and 25 nm.

Figure 9.2 shows an example using the upper limit of the Falcon detected and pTOMCAT calculated SO_2 concentration: 40 pptv; the OH concentration was also taken from pTOMCAT: 0.8 pptv. Sunlight intensity was modulated with a semi-sinusoidal function to replicate daylight hours; the simulation was commenced 6 hours after sunrise – most convective activity intensified around noon local time. It can be seen that the sulphuric acid and total aerosol concentration (> 0.5 nm) increase rapidly to a maximum within 2 - 4 hours (*right*, figure 9.2), as nucleation begins. The sulphuric acid concentration then drops as the rate of condensation increases onto the ever larger population of particles; the total particle concentration also decreases due to the coagulation of smaller particles

into larger. A large nucleation mode exists up to 5 hours (see 0.5, 1, 2 and 5 hour curves); the effect of particle coagulation can be seen at 8 hours and beyond, as a 'shoulder' appears in the size distribution. This simulation demonstrates that there is some inconsistency between the measured data and the simulated data, using an SO_2 value that has been measured and predicted (40 pptv – maximum). Particles greater than 9 nm do not reach significant figures until 5 hours and then, only of the order of 10^2. The Aitken mode ($>$ 10 nm) does not grow into the order of 10^4 until 15 hours – this was commonly encountered during a number of exceptional ACTIVE flights (AE12, AE18 and AE19). Possible causes could be uncertainty in the SO_2 measurements or an increased H_2SO_4 production rate via other pathways – however this seems unlikely since all currently known chemical pathways involve SO_2 as the precusor. If the H_2SO_4 production rate is correct then there might have been a different mechanism involved, such as an ion recombination, organic nucleation and growth or association of other unknown species. The dashed black line indicates how CPC1 would behave if it were detecting this aerosol population in real-time; the curve is based on the CPC1 efficiency equations that were discussed in section 5.3.1 (see also equation 5.1).

Figure 9.3 shows the situation if a higher SO_2 concentration of 100 pptv were used in the model. The 100 pptv value was measured in the Darwin UT/TTL only at the 90th percentile in the early biomass burning period (early November 2005), but the likelihood of an SO_2 concentration of 100 pptv decreases throughout the first campaign (see figure 8.3) and into the second campaign (from the pTOMCAT model). During this simulation the aerosol grew much more rapidly into higher size ranges, although the sudden peak in the nucleation mode and the sulphuric acid occurred in a similarly short time frame. The Aitken mode approaches concentrations of the order 10^4, found during AE12, AE18 and AE19, sooner ($\sim$ 12 hours) than the previous simulation but not to the degree found in the ACTIVE analysis (see chapter 8). Again this reinforces the conclusion that there was either other condensable species present or a different mechanism was involved: some unknown binary or ternary process, organic nucleation/growth and/or ion recombination.

Figures 9.4 and 9.5 show the model run for an SO_2 of 200 pptv and 300 pptv respectively. The H_2SO_4 production rate is again modulated by daylight hours; the simulation is initiated 6 hours after sunrise. It can be seen that the aerosol

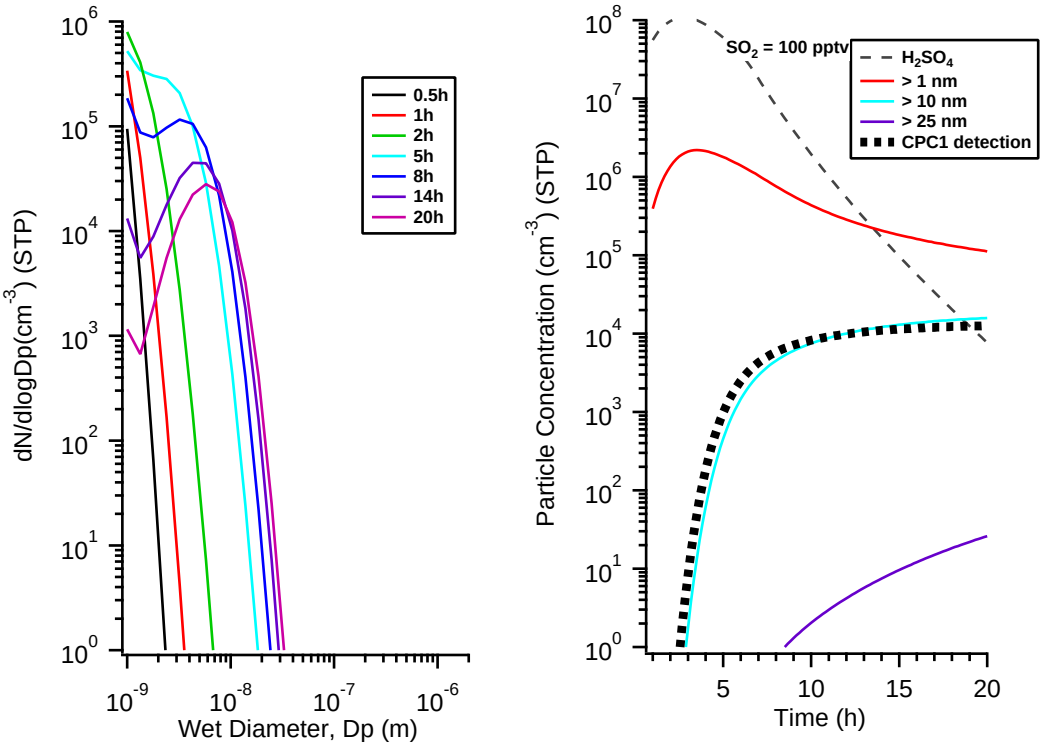

Figure 9.3: *left:* Aerosol size distribution as a function of wet diameter, Dp. The background SO_2 concentration was set at 100 pptv and the acid production was semi-sinusoidally varied to replicate daylight hours. Concentration is adjusted to STP units. *Right:* Concentrations calculated numerically as functions of time for molecular sulphuric acid (H_2SO_4), total aerosol number (above 0.5 nm), and aerosol numbers with diameters over 10 nm and 25 nm.

concentrations and production rates are now beginning to approach that seen during the ACTIVE field campaign (see section 8.7 for the ACTIVE aerosol nucleation data). However, this level of SO_2 was unlikely to have been present in the Darwin area during ACTIVE. The analysis in section 8.4 has already revealed that SO_2 was higher in November 2005, during the first campaign, coinciding with the biomass burning phase. Even the higher SO_2 concentrations of the first campaign only registered a 90th percentile of $\sim$ 170 pptv. Furthermore the interquartile range was typically less than 50 pptv, demonstrating SO_2 levels were quite homogeneous throughout the Darwin area and few, if any, exceptionally high concentrations (above 200 pptv). This leads to a conclusion that there was still insufficient SO_2 to explain the aerosol population seen in convective outflows. However, this study does give some indication of the necessary condensable concentration required: 300 pptv or higher. What this condensable was remains a

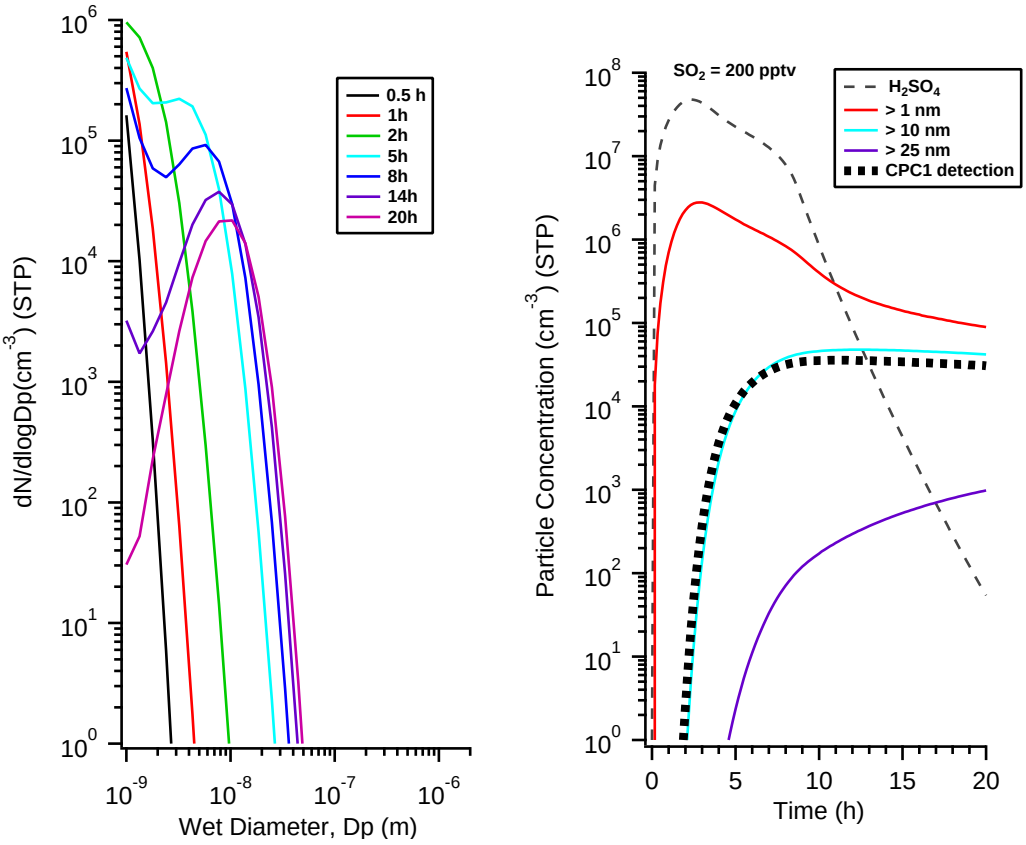

Figure 9.4: *left:* Aerosol size distribution as a function of wet diameter, Dp. The background SO_2 concentration was set at 200 pptv and the acid production was semi-sinusoidally varied to replicate daylight hours. Concentration is adjusted to STP units. *Right:* Concentrations calculated numerically as functions of time for molecular sulphuric acid (H_2SO_4), total aerosol number (above 0.5 nm), and aerosol numbers with diameters over 10 nm and 25 nm.

mystery. There were possible candidates in the biomass compounds that were seen in the first campaign (e.g. Allen et al., 2008) and the long-range transport of organic compounds from further afield. Long-range transport of certain trace gases (ozone, CO, etc.) was confirmed in the Darwin region, during ACTIVE, by air mass back trajectory calculations (Allen et al., 2008; Heyes et al., 2009). In conclusion, there could still be a role for binary nucleation of H_2SO_4-H_2O, with the involvement of some other condensable (organic compounds – for example, alpha-pinene, isoprene, toluene, alkanes and aromatics). Additional processes, such as ternary nucleation, organic nucleation/growth or ion recombination/nucleation could also play a role in the overall aerosol population generation. Despite these

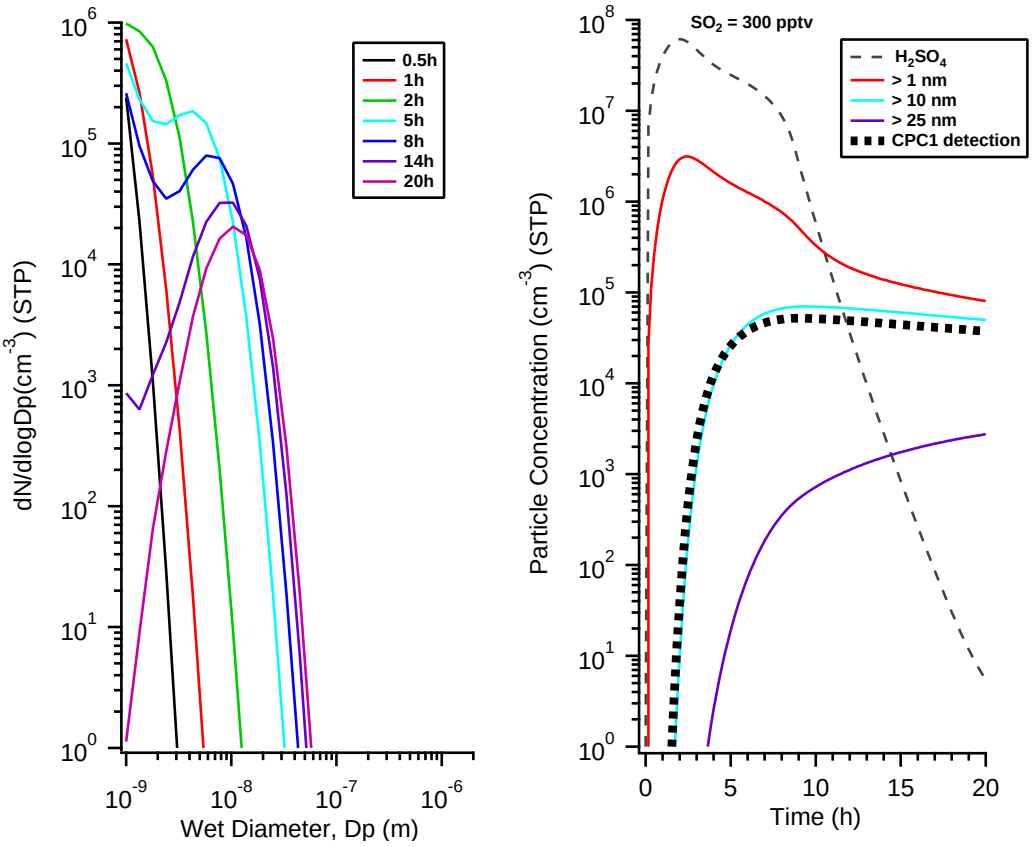

Figure 9.5: *left:* Aerosol size distribution as a function of wet diameter, Dp. The background SO_2 concentration was set at 300 pptv and the acid production was semi-sinusoidally varied to replicate daylight hours. Concentration is adjusted to STP units. *Right:* Concentrations calculated numerically as functions of time for molecular sulphuric acid (H_2SO_4), total aerosol number (above 0.5 nm), and aerosol numbers with diameters over 10 nm and 25 nm.

possibilities, there is still uncertainty in any potential theory for organic compounds role in nucleation and growth and ion mediated nucleation. Much of the literature is contradictory in terms of results and conclusions and the ability for unknown compounds to provide such large vapour masses concentrations, with which to produce high numbers of observable aerosols, is debatable. This does however provide motivation for future research.

Chapter 10

Discussion and conclusions

ACTIVE was a major success, with a large range of quality data collected from aircraft, sondes and ground-based systems. Many phenomena were observed in the data and a number of publications have resulted from it (e.g. Allen et al., 2008; Vaughan et al., 2008; Chemel et al., 2009; Heyes et al., 2009; Labrador et al., 2009; May et al., 2009). This experiment has undoubtedly increased the knowledge of the tropics and the influence it has on global climatology.

This research project has provided some important additions to the understanding of atmospheric aerosol and the origin of aerosol particles. Some of the notable research topics covered by this PhD and presented in this thesis include:

- A detailed description of the instrumentation used and a thorough quality assessment and control for all the data used. Data reliability was proved statistically.
- Climatological discussion of the Darwin region during the ACTIVE project of 2005/2006, including trace gas (CO) analysis and relevance to convection and long-range transport in the tropics.
- Presented extensive aerosol data for the PBL around Darwin and farther afield. Data were presented in a comprehensive statistical analysis. Data will be of great value for the atmospheric study of tropical climatology.
- The TTL data were analysed and assessed in order to find overall trends, which were presented in statistical plots, and unique events. Large aerosol populations were identified and were proven to originate from convective

anvil clouds. These events were investigated and were found to nucleate over a certain timescale that was determined from wind data. This provided a unique result that will be of great importance for the theoretical and modelling studies of aerosol nucleation and growth.

- A complete aerosol nucleation and growth model was written in order to investigate the ACTIVE aerosol populations detected. SO_2 (which is a sulphuric acid, H_2SO_4, precursor) measurements from ACTIVE indicated a range of between 5 and 150 pptv. The modelling exercise proved a binary mechanism of sulphuric acid and water nucleation to be insufficient for the production of the large particle concentrations seen in the ACTIVE data. Alternatives, such as organic compounds and ion mediation, were discussed.

The prime motivation for this thesis was to find the influence of tropical convection on the aerosol population in the Tropical Tropopause layer (TTL). The TTL is important due the exchange that exists between the tropopause and the stratosphere (see section 1.4), followed by possible transportation in the Brewer-Dobson circulation. This circulation provides a link between the photochemically active tropics and the cold polar regions; it was used to explain the higher than expected ozone levels in the polar troposphere (e.g. Holton et al., 1995; Fueglistaler et al., 2009). Due to its global connectivity, it is of great importance to understand the effect of tropical convection on the TTL's chemical and particulate composition. Furthermore, the intense convective activity in the tropics provide a large percentage of the world's overall cloud coverage – global cirrus coverage is approximately 20% and 45% in the tropics (e.g. Hong et al., 2007). Cirrus, like all cloud, has reflective properties in the visible wavelength; cirrus cloud can also absorb and re-emit terrestrial infrared radiation, providing a significant radiation forcing. The sign and magnitude of this forcing is not fully known but it is believed to effect the global energy budget (IPCC, 2007). Aerosols ability to act as Cloud Condensation Nuclei (CCN) provides an important pathway for cloud formation. Aerosols in the TTL can directly and indirectly (through cloud formation) affect the radiative energy balance in the tropics and ultimately the global energy budget.

The boundary layer around Darwin was surveyed with the Dornier aircraft. The data were statistically analysed and presented in section 6.1. The influences changed throughout the ACTIVE campaign: initially there was a prevalence of

organic aerosols due to the biomass burning in November 2005. This gradually decreased throughout the first campaign until it reached a low during the monsoon period of the second ACTIVE campaign. The monsoon winds introduced a marine influence to the Darwin PBL which reduced the organic loading in the region. The high sulphate percentage of the aerosol was the dominant feature of the active monsoon period; the sulphate was likely a result of the marine influence and biogenic breakdown, such as DMS, MSA and H_2S.

Profile studies, including the work of Heyes et al. (2009), have shown the origin of UT/TTL air to have a complex and varied number of sources. Despite regular convective activity across the Darwin region, the TTL signature often indicated long-range sources of origin. Darwin TTL was founded to have influences from all across the Tropical Warm Pool region and in particular from the Indonesian archipelagoes – where high biomass and pollution markers in the Darwin TTL were traced back to this region (Heyes et al. (2009) used ozonesondes and back trajectory analysis to reach this conclusion). The CO profiles also showed a transition from the first ACTIVE campaign to the second campaign. In the biomass burning period there was a high concentration of CO, correlated with the combustion, in the PBL of the Northern Territory. The concentration reduced with altitude up to the TTL, which was found to have a background level influenced by long-range transport rather than local sources. Air is also believed to be entrained and detrained at many levels within the convective storm (Mari et al., 2000); therefore, the air can be lifted from throughout the free troposphere and not solely from the surface. The high PBL to low TTL CO gradient continues into the premonsoon (with slightly lower PBL concentrations compared to the biomass burning phase); the variability of the TTL CO concentrations increased during this phase indicating a number of possible influences on the UT/TTL composition, including local convection. The transition occured when the active monsoon period began, during the second campaign; the profiles showed little change with altitude but much more variability above 10 km. The PBL concentration also showed the effect of the cessation of biomass combustion and a cleansing of the PBL by maritime monsoon winds. A greater impact from local convection seemed more evident in this period as the mean CO concentration was similar throughout the troposphere. Long-range transport still had an effect on the TTL composition, demonstrated by the high variability in the concentrations (figure 4.5).

The aerosol concentrations varied from flight to flight and even within each mission. Figure 7.4 shows the high degree of variability within the ACTIVE aerosol, N_{10}, dataset. The statistical surveys of the Planetary Boundary Layer (PBL section 6.1) and the UT/TTL revealed a significant discrepancy between the two. The Dornier PBL survey found median N_{10-200} values of between 500 - 1000 cm^{-3} and rarely any maxima higher than 2000 cm^{-3}. The UT/TTL concentrations are consistently higher than those found in the PBL, suggesting an origin of particles other than direct uplift from the local boundary layer. Maxima as high as 25,000 particles cm^{-3} were seen during some missions (AE12 and AE19, for example); minima as low as 1000 particles cm^{-3} were also seen in most flights but the medians were typically larger than the PBL values. These low N_{10} concentrations were commonly found in cloud , ($N_{cloud} > 0.05$ cm^{-3}); this was a common theme in the ACTIVE data: regions of cloud tended to have lower N_{10} and N_{100}. Conversely, cloud regions, particularly 'fresh' cloud (from recent convection – within $\sim$ 4 hours) showed depletion of N_{10} and N_{100} (for example, see figures 7.5 and 7.6). This yielded another conclusion: cloud was indeed scavenging aerosol particles (by wet deposition or by aerosol 'activation' to cloud droplets) and depleting their population stock (e.g. Clement et al., 2002; Twohy et al., 2002).

The cloud and aerosol anticorrelation effect was investigated with wind data and back trajectories to see the origin of the effect. The low N_{10} and N_{100} were found in convective anvil cloud, suggesting cloud scavenging of aerosols or at the least, the suppression of aerosol nucleation in cloud. The high aerosol concentrations (greater than 6000 cm^{-3}) were also analysed for their evolution. As mentioned previously, these high aerosol concentrations were found in cloud-free air ($N_{cloud} < 0.05$ cm^{-3}); wind projections found that the air emanated from convective outflows. Namely, the air was at one time cloudy but then was outgassed into cloud-free air – chapter 8 discusses this in detail for flight AE19. This study had already found there to be very low aerosol concentrations in cloud (seen very clearly during flight AE19), with contrasting areas of low N_{10} ($\lesssim$ 1000 cm^{-3}) and high N_{10} concentrations (up to 25,000 cm^{-3}). This points to a mechanism of in situ aerosol production in storm outflow regions (for example, Twohy et al., 2002). The background levels found in SE24 and other areas unperturbed by convection showed concentrations between 2000 and 6000 cm^{-3} with an SE24 median of 4500 cm^{-3} after approximately 2 days in fluctuating winds (figure 7.13).

Aerosol nucleation occurs through 4 possible mechanisms: binary, ternary, ion recombination and organic nucleation (section 2.3). It is also possible that these processes do not just work in isolation but can also aid or impede the other mechanisms. Organic compounds in particular are suspected of playing a varied role in aerosol nucleation and growth (e.g. Laaksonen et al., 2008b; Kulmala et al., 2006b). Organic nucleation is an area which requires continual investigation, particularly in the UT/TTL, in order to find its significance to the high aerosol number concentrations seen in field campaigns, such as ACTIVE.

The nucleation investigation (section 8.7 and chapter 9 discuss this in detail) began with the hypothesis that binary (H_2O-H_2SO_4) would be the most likely candidate for aerosol production in the TTL (Clement and Ford, 1999a,b; Clement et al., 2002; Twohy et al., 2002). The low temperatures and high moisture in the outflow are considered to be ideal conditions for almost barrierless nucleation to occur (Clement et al., 2002). Furthermore, the pollutant SO_2, which oxidises to H_2SO_4 in the UT/TTL, is commonly detected during atmospheric aircraft campaigns in sufficient concentrations to initiate binary nucleation (1 ppbv was detected by Clement et al. (2002) and Twohy et al. (2002)). SO_2 is a pollutant that is emitted in many industrial combustion processes and, due to its partial solubility, it is able to reach the UT/TTL through convective uplift with an approximate 10% survivability (Clement et al., 2002). However, during pTOMCAT simulations of the second campaign, there was only a maximum SO_2 concentration of 40 pptv and a median of between 8 and 15 pptv in the UT/TTL above Darwin. This range of SO_2 was insufficient to produce the H_2SO_4 required for N_{10} concentrations of the order 10^4 cm^{-3} – not for at least 15 hours (see chapter 9). The data available points to enough available SO_2 for nucleation to occur but not enough for the rapid and high Aitken, N_{10}, concentrations seen during ACTIVE – using the standard binary nucleation mechanism. There was the possibility of other chemical pathways to H_2SO_4 besides SO_2; DMS and H_2S are able to oxidise to H_2SO_4 (e.g. Berglen et al., 2004). However, the role of DMS in nucleation is still uncertain; a number of campaigns have come to opposite conclusions: Thornton et al. (1997) found that DMS, during the west Pacific Ocean campaign (PEM-West), was not a high source of SO_2 in the UT and the majority of SO_2 was due to volcanic emission and anthropogenic. Whereas, O'Dowd et al. (2007) and Froyd et al. (2009) consider it to be an substantial factor in aerosol nucleation, especially in maritime and coastal environments, which is relevant

to the Darwin area. Marine boundary layer nucleation was found to be closely correlated to DMS concentrations, by Pandis et al. (1994). Coastal nucleation is also believed to be driven by VOC and/or alkyl halide derivatives (O'Dowd et al., 1999); H_2S ia also a natural (e.g. bacterial breakdown) and anthropogenic source for H_2SO_4 (Berglen et al., 2004) – methanesulphonic acid (MSA) also plays a role in the sulphur cycle.

Organic compounds (Kulmala et al., 2006b) and ion recombination could provide mechanisms with which to produce the necessary aerosol concentrations seen during ACTIVE. However, the lack of a suitable condensable vapour candidate is still an obstacle to a complete explanation. The profile and trajectory work (Allen et al., 2008; Heyes et al., 2009) showed there were widespread and long-range origins for the TTL composition; Indonesia and the wider Tropical Warm Pool were typical sources for the Darwin TTL. Forests cover much of Indonesia and together with the many biomass fires (Allen et al., 2008), organic compounds and aerosols would undoubtedly have been present in the TTL over Darwin due to the long-range transport that exists (Heyes et al., 2009). Ion nucleation was also a possibility, especially considering the photoactivity that exists in the stratosphere and upper troposphere (Kazil et al., 2007). Unfortunately, the theories are still uncertain and the data is still inadequate to assess the true impact on aerosol nucleation and growth. This is an area of research that requires a lot more work but could provide some high impact results: the origin of atmospheric aerosol.

10.1 Summary

This study has achieved a number of unique and original scientific results that will be of importance to the atmospheric science community:

- The climatology of the tropical troposphere, in particular, the Planetary Boundary Layer (PBL) and the Upper Troposphere/Tropical Troposphere Layer (UT/TTL), was described in detail during important climatological phases. This study revealed the particle and trace gas loadings during distinct periods: biomass burning, a breaking Rossby wave, premonsoon, active monsoon, inactive monsoon and the monsoon break. There are few studies available with such a broad scoping and comprehensive dataset.

These data were presented using a thorough graphical and tabular statistical analysis, for ease of reference.

- The tropical PBL aerosol population was studied, using the low level Dornier aircraft, and categorised using statistics and data visualisation. The tropical PBL loading and climatology play a major role in determining the nature of convective activity in the free tropopause and the clouds that are formed in the UT. The 10 to 200 nm and 200 nm to 1000 nm aerosol populations were presented in this thesis and the potential effect they had on the tropical climatology and meteorology. Again, this is vital additional literature for the study of tropical climate and its wider implications for the globe; an unprecedented quantity of data were collected and analysed for this experiment.

- The UT/TTL was the focal point of the ACTIVE campaigns in order to find the effect of tropical convection on the aerosol and chemical composition of the upper troposphere. This is an area where cloud cover is of great importance to the global energy budget. Cloud production in the tropics typically results in high altitude cirrus (above ~ 12 km), which have a strong influence on upwelling and downwelling longwave and shortwave radiation (IR and visible). The global energy budget is believed to be affected by this radiation forcing from cirrus cloud. Therefore, a thorough investigation of cirrus and the TTL environment was undertaken by ACTIVE, SCOUT-O3 and TWP-ICE in order to quantify and understand this vital region that is insufficiently represented in the literature. ACTIVE and this project yielded a wealth of aerosol data (10 to 1000 nm and 100 to 1000 nm) for a broad period of the tropical premonsoon and monsoon seasons that is of great value to UT/TTL understanding. This study presented solid evidence for the relationship between high particle number concentrations and convective activity. These high number density particle populations were found to originate from convective anvils. Anvil cloud was also shown to suppress large aerosol concentrations while out-of-cloud regions were conversely seen to be the source of high particle number densities. Furthermore, this study tested a hypothesis of aerosol nucleation occurring in the outflow of convective anvils in regions of no-cloud. Wind and trajectory data were used to confirm the origin of numerous high aerosol concentration events in the

anvil. This led to the conclusion that aerosols were being nucleated in convective outflow regions. This has been discussed in other papers but the evidence is limited; this work provides compelling evidence to support the theory of aerosol nucleation in the TTL due to convective activity.

- A nucleation time frame was derived from in-situ aerosol and wind data. The wind data provided a timescale since the air mass exited the convective anvil and the aerosol instrumentation (CPC) recorded the particle concentrations, allowing a relationship to be derived for TTL aerosol concentration against time. This was quite a unique approach that will provide an important reference for theoretical studies and computational modelling of aerosol generation and growth.

- A thorough modelling project was also undertaken to complement the in-situ data. The model worked from a hypothesis of SO_2 as the driver for binary homogeneous nucleation. SO_2 was measured in the Darwin region during ACTIVE but was typically low in concentration: 10 to 150 pptv. Using the SO_2 measurements available as the model's initiation parameters, it was found that there was insufficient SO_2 to H_2SO_4 conversion for the required aerosol nucleation and growth rates. The lack of SO_2 indicated that there was potentially some other condensable and/or mechanism involved in UT/TTL nucleation (e.g. organic nucleation, ion-ion nucleation). Organic compounds were found in the Darwin boundary layer and in the surrounding Tropical Warm Pool (TWP) area (such as alpha-pinene, isoprene, toluene, alkanes and aromatics). Long-range transport was also found to be a major influence on the Darwin troposphere climatology (both PBL and UT/TTL). Therefore, it was shown through the ACTIVE study that there were both local and long-range influences on the aerosol and trace gas loading in the Darwin region, with the potential to effect the particle number and composition in UT/TTL. This project provided evidence for the possible role of trace gases (SO_2, inorganic and organic compounds) in the tropospheric nucleation process in regions of convective activity. This is an area of literature that has insufficient coverage and this study adds valuable knowledge to the field of atmospheric and climate science.

There are a number of areas that would require further investigation. ACTIVE was a major success, acquiring a great deal of data and furthering the knowledge

of the tropics. However, there are still uncertainties about the mechanism of nucleation in the TTL and of the composition of the aerosols. Future campaigns need to continue analysing the TTL, the aerosol concentrations and their composition, in particular, organics in the TTL need to be studied in more detail, with possible additions of mass spectrometers and chemical samplers to the aircraft data. It would be ideal to have as many CPC as possible for this type of field study; when nucleation is being investigated it would be of great benefit to have a nucleation mode (< 9 nm) detector. A range of CPCs with varying diameter detection cut-offs would be very useful for observing possible nucleation and particle growth. Personally, it would have been nice to have had more time to test the model more thoroughly and maybe improve it to include organic parameterisation. Modelling work would complement the ACTIVE aerosol data and possibly help explain the nucleation mechanism and aerosol growth rates – it could be pursued in the future as an expansion to the aerosol investigation herein.

Appendix A

Aerosol model – Fortran 90 code

```
PROGRAM Aerosol_nucl_cond_coag1

IMPLICIT NONE

      double precision  pi
      parameter        (pi = 3.14159265358979323846264643d0)

  INTEGER, PARAMETER :: QUAD = SELECTED_REAL_KIND(10,100)

  !Constants

  REAL(KIND=QUAD) :: Avo_N,Vw,Va,Diff_vol_acid,Diff_vol_air
      REAL(KIND=QUAD) :: mol_mass_acid
      REAL(KIND=QUAD) :: mol_mass_air,m_h2so4,m_h2o,mass_air
      REAL(KIND=QUAD) :: D_collision_air
      REAL(KIND=QUAD) :: k,R_gas,c_light,h_planck,Sun_temp,Sun_radius
      REAL(KIND=QUAD) :: Sun_area
      REAL(KIND=QUAD) :: Sun_dist,Sun_sphere,Day_length,a_factor_oh
      REAL(KIND=QUAD) :: E_R_oh
      REAL(KIND=QUAD) :: a_factor_o2,E_R_o2,a_factor_n2,E_R_n2
      REAL(KIND=QUAD) :: n_h2o_clusters
      REAL(KIND=QUAD) :: m_h2o_clusters,sticking,moler_volume_a,alpha1
      REAL(KIND=QUAD) :: alpha2
      REAL(KIND=QUAD) :: alpha3
      REAL(KIND=QUAD) :: n_test,t_max,exp_begin

!Variables

  REAL(KIND=QUAD) :: mu_coag
  REAL(KIND=QUAD) :: k0_hoso2
      REAL(KIND=QUAD) :: kinf_hoso2
      REAL(KIND=QUAD) :: Temp,P,Altitude
      REAL(KIND=QUAD) :: n_air,m_air
      REAL(KIND=QUAD) :: mx_h2o,p_h2o
      REAL(KIND=QUAD) :: Q,Q_m3,Q_max,mx_oh,mx_so2,n_oh,n_so2
      REAL(KIND=QUAD) :: n_so2_cm3,n_air_sq,m_air_cm3,n_air_cm3
      REAL(KIND=QUAD) :: n_h2o,n_h2o_cm3,n_h2so4,n_h2so4_cm3
      REAL(KIND=QUAD) :: n_h2so4_old,n_h2so4_old_cm3
      REAL(KIND=QUAD) :: p_h2o_sat,rh,hydrate_ratio
      REAL(KIND=QUAD) :: n_hydrates,n_hydrates_cm3
      REAL(KIND=QUAD) :: p_h2o_sat1,R_min,R_max
      REAL(KIND=QUAD) :: x_ini,x_end,x_grad
      REAL(KIND=QUAD) :: st_drop1,st_drop2,st_drop3
      REAL(KIND=QUAD) :: log_r1,drop_density1
      REAL(KIND=QUAD) :: day_sec,t_sec,power_coeff,day_num
      REAL(KIND=QUAD) :: RK_step1,RK_step2
      REAL(KIND=QUAD) :: p_h2so4,p_h2so4_sat,RA,x_h2o,x_h2so4
```

```
      REAL(KIND=QUAD) :: A11,A12,B11,B12,Log_act_w,Log_act_a
      REAL(KIND=QUAD) :: Act_h2so4_co,Act_h2o_co,A_h2so4,A_h2o
      REAL(KIND=QUAD) :: p_a_sol,chem_potn_acid,sigma_tension_pt1
      REAL(KIND=QUAD) :: sigma_tension_pt2,sigma_tension,m_frac_h2so4
      REAL(KIND=QUAD) :: density_pt1,density_pt2,density,V_avg,R_crit
      REAL(KIND=QUAD) :: m_crit,N_crit_h2so4
      REAL(KIND=QUAD) :: F_molecules,B_a,B_w,B_h,Area_crit,growth_angle
      REAL(KIND=QUAD) :: Z_factor,B_num,B_denom,B_AV,delta_G,exp_term,J_rate
      REAL(KIND=QUAD) :: Diffusion_coeff,mfp
      REAL(KIND=QUAD) :: cond_Acid_term,sum_acid,n_a_RK_adder
      REAL(KIND=QUAD) :: cond_part1,cond_part2,coag_part1,coag_part2,coag_part3,i_term
      REAL(KIND=QUAD) :: sum_coag1,sum_coag2,sum_coag3,pop_ini,pop_end,pop_grad, p_i_real
      REAL(KIND=QUAD) :: t_step,t_float

      INTEGER :: Q_choice,n_bin
      INTEGER :: b_i,c_i,c_j,c_k,RK,count,i_acid,d_i,p_i
      INTEGER*4 :: t_number,t,t_print,t_10min

      REAL(KIND=QUAD), DIMENSION(27) :: N,N_cm3,N_old,log_R,R_size,drop_x_frac
  REAL(KIND=QUAD), DIMENSION(27) :: drop_density,s_tension_drop,mass
      REAL(KIND=QUAD), DIMENSION(27) :: N_acid_drop
      REAL(KIND=QUAD), DIMENSION(27) :: Cond_denom1,Cond_denom2 !coagulation and condensation terms
      REAL(KIND=QUAD), DIMENSION(27) :: kron_delta_I1,kron_delta_I2
      REAL(KIND=QUAD), DIMENSION(27) :: Coag_coeffs_I1,Coag_coeffs_I2
      REAL(KIND=QUAD), DIMENSION(27) :: Knudsen,beta_factor,cond_coeff,p_kelvin
      REAL(KIND=QUAD), DIMENSION(27) :: D_1,c_rms,gamma_coag,cunningham
      REAL(KIND=QUAD), DIMENSION(27) :: N_RK_adder

      REAL(KIND=QUAD), DIMENSION(27,27) :: k_coag,kcb,R_coag,c_coag,D_coag,omega_coag
      REAL(KIND=QUAD), DIMENSION(27,27) :: sigma_coag,K_denom1,K_denom2

      REAL(KIND=QUAD), DIMENSION(27,27,27) :: kron_delta1,kron_delta2,kron_delta3
      !kronecker deltas for coagulation terms
      REAL(KIND=QUAD), DIMENSION(27,27,27) :: Coag_coeffs1,Coag_coeffs2,Coag_coeffs3

      !Constants
  Avo_N = 6.022142D23     !Avogadro's number

Vw = 8.8032D-31     !volume of water molecule! taken from arm dimensions
Va = 8.844D-29   !volume of sulphuric acid molecule, taken from density considerations

Diff_vol_acid = 51.66D0
Diff_vol_air = 19.7D0    !diffusion volume - Kuuluvainen 2009

mol_mass_acid = 98.0D0
mol_mass_air = 28.97D0

m_h2so4 = 0.098/Avo_N     !mass of a single sulphuric acid molecule
m_h2o = 0.018/Avo_N        !mass of a single water molecule
mass_air = 0.02897/Avo_N     !average mass of an air molecule

D_collision_air = 3.69D-10     !collisional diameter of average air molecule

k = 1.3806503D-23     !Boltzmann constant
R_gas = 8.314472D0       !Universal Gas constant

c_light = 2.99792D8     !speed of light
h_planck = 6.626D-34    !Planck's constant
Sun_temp = 5778.0        !Sun's temperature

Sun_radius = 6.955D8
Sun_area = 4.*pi*(Sun_radius**2)   !surface area of the Sun
Sun_dist = 1.496D11     !average Sun-Earth distance
Sun_sphere = 4.*pi*(Sun_dist**2)    !surface area of Sun-Earth sphere

Day_length = 12.72      !Length of time (h) of a day, Darwin (23/01/06)
                !Sunrise:0637, Sunset: 1920

a_factor_oh = 1.63D-10   !A-factor OH production JPL k derivation
E_R_oh = -60.          !E/R OH

a_factor_o2 = 3.3D-11     !A_factor O(1D) de-excited by O2
```

```
E_R_o2 = - 110          !E/R O(1D) by O2

a_factor_n2 = 2.15D-11   !A_factor O(1D) de-excited by N2
E_R_n2 = -110      !E/R O(1D) by N2

n_h2o_clusters = 2    !number of water molecules in hydrates - may change to test - typically no more than 10
m_h2o_clusters = m_h2so4 + n_h2o_clusters*m_h2o

sticking = 1       !sticking coefficient for condensation assumed 1 here, may change

moler_volume_a = 5.3261D-5          !molar volume of LIQUID sulphuric acid - MAY INVESTIGATE
 !- used in Kelvin pressure calculation
alpha1 = 1.142
alpha2 = 0.558
alpha3 = 0.999          !Constants used to find Cunningham correction factor
!-----------------------------------------------------------------------------------------
!enter some of the environmental variables
      print *, 'Enter the temperature (K)'
      read  *, Temp

      print *,'Enter the pressure (hPa)'
      read  *, P
      P = 100*P     !convert hPa to Pa

      Altitude = -(Temp - 324.23)/8.15  !in km; this is taken from
                                        !23/01/06 AE19 ship sonde data - change for other flights

      m_air = P*1./(R_gas*Temp)     !number of moles of air, in 1 m^3
      n_air = m_air*Avo_N   !number of molecules of air, in 1 m^3

      print *, 'Enter the initial molar ratio of water vapour, in ppmv'
      read *, mx_h2o
      mx_h2o = mx_h2o*1D-6
      p_h2o = mx_h2o*P  !xi = pi/P; the molar fraction is ratio of partial pressure to total pressure

!+++++++++++++++++++++++++++++++++++++++++++++++++++++
!gas dynamic viscosity - used in coagulation section

  mu_coag =(18.27D-6*(291.15D0+120.D0)/(Temp+120.D0))*(Temp/291.15D0)**1.5

!+++++++++++++++++++++++++++++++++++++++++++++++++++++
!factors used in hoso2 production

  k0_hoso2 = 3D-31*(Temp/300)**(-3.3)
      kinf_hoso2 = 1.5D-12
!-----------------------------------------------------------------------------------------

        !-----------------------------------------------------------------------------------------
        !Find the sulphuric acid concentration

      print *,'Choose the sulphuric acid production/loss mechanism '
      print *,'and rate (1) Define a steady rate, self defined; (2) Use'
      print *,'P = k1[oh][so2]; (3) as before but with sinusoidal'
      print *,'variability'

        !++++++++++++++++++++++++++++++
read *, Q_choice

        !++++++++++++++++++++++++++++++

      select case(Q_choice)
!;;;;;;;;;;;;;;;;;;;;;;;;;;;;;;;;;;;;;;;;;;;;;;;;;;;;;;;;;;;;;;;;;;;;;;;;;;;;;;;;;;;;;;;;;;;;
!;;;;;;;;;;;;;;;;;;;;;;;;;;;;;;;;;;;;;;;;;;;;;;;;;;;;;;;;;;;;;;;;;;;;;;;;;;;;;;;;;;;;;;;;;;;;
      case(1)

      print *, 'Choose a rate, Q (m-3.s-1)'
      read *, Q_m3
!;;;;;;;;;;;;;;;;;;;;;;;;;;;;;;;;;;;;;;;;;;;;;;;;;;;;;;;;;;;;;;;;;;;;;;;;;;;;;;;;;;;;;;;;;;;;
!;;;;;;;;;;;;;;;;;;;;;;;;;;;;;;;;;;;;;;;;;;;;;;;;;;;;;;;;;;;;;;;;;;;;;;;;;;;;;;;;;;;;;;;;;;;;

      case(2)
```

```
      print *, 'Input oh and so2 molar ratios (pptv): '

      read  *, mx_oh, mx_so2     !this is molar/volume ratio

      mx_oh = mx_oh*1D-12
      mx_so2 = mx_so2*1D-12

      n_oh = n_air*mx_oh   !change to concentration m^-3
      n_so2 = n_air*mx_so2

      !In CM^-3

      n_so2_cm3 = n_so2/1D6

      n_air_sq = (n_air)**2

      Q_m3 = (1.296D-18*mx_oh*mx_so2)*n_air_sq   !production rate, m^-3, from Berglen et al. 2004
!;;;;;;;;;;;;;;;;;;;;;;;;;;;;;;;;;;;;;;;;;;;;;;;;;;;;;;;;;;;;;;;;;;;;;;;;;;;;;;;;;;;;;;;;;;
!;;;;;;;;;;;;;;;;;;;;;;;;;;;;;;;;;;;;;;;;;;;;;;;;;;;;;;;;;;;;;;;;;;;;;;;;;;;;;;;;;;;;;;;;;;

      case(3)
      print *,'Input oh and so2 molar ratios (pptv): '

      read  *, mx_oh, mx_so2     !this is molar/volume ratio

      mx_oh = mx_oh*1D-12
      mx_so2 = mx_so2*1D-12

      n_oh = n_air*mx_oh  !change to concentration m^-3
      n_so2 = n_air*mx_so2

!In CM^-3

      n_so2_cm3 = n_so2/1D6

      n_air_sq = (n_air)**2

      Q_max = (1.296D-18)*mx_oh*mx_so2*n_air_sq  !production rate, m^-3, from Berglen et al. 2004
!;;;;;;;;;;;;;;;;;;;;;;;;;;;;;;;;;;;;;;;;;;;;;;;;;;;;;;;;;;;;;;;;;;;;;;;;;;;;;;;;;;;;;;;;;;
!;;;;;;;;;;;;;;;;;;;;;;;;;;;;;;;;;;;;;;;;;;;;;;;;;;;;;;;;;;;;;;;;;;;;;;;;;;;;;;;;;;;;;;;;;;

      end select

!;;;;;;;;;;;;;;;;;;;;;;;;;;;;;;;;;;;;;;;;;;;;;;;;;;;;;;;;;;;;;;;;;;;;;;;;;;;;;;;;;;;;;;;;;;
!;;;;;;;;;;;;;;;;;;;;;;;;;;;;;;;;;;;;;;;;;;;;;;;;;;;;;;;;;;;;;;;;;;;;;;;;;;;;;;;;;;;;;;;;;;
!;;;;;;;;;;;;;;;;;;;;;;;;;;;;;;;;;;;;;;;;;;;;;;;;;;;;;;;;;;;;;;;;;;;;;;;;;;;;;;;;;;;;;;;;;;
!;;;;;;;;;;;;;;;;;;;;;;;;;;;;;;;;;;;;;;;;;;;;;;;;;;;;;;;;;;;;;;;;;;;;;;;;;;;;;;;;;;;;;;;;;;
! Common variables

      m_air_cm3 = m_air/1D6     !number air moles per cm^3
      n_air_cm3 = n_air/1D6     !number of air molecules per cm^3


      n_h2o = n_air*mx_h2o     !in m^-3
      n_h2o_cm3 = n_h2o/1.D6    !number of H2O molecules per cm^3
!--------------------------------------
!initial H2SO4

      n_h2so4 = 1D6            !m^-3 arbitrary initial value
      n_h2so4_cm3 = n_h2so4/1D6

      n_h2so4_old = 0.
      n_h2so4_old_cm3 = 0.         !used in Runke-Kutta method
!+++++++++++++++++++++++++++++++++++++++++++++++++++++
      p_h2o_sat1=77.3449-(7235.4247/Temp)-8.2*LOG(Temp)+Temp*5.7113D-3
      p_h2o_sat=exp(p_h2o_sat1)    !saturation pressure of water
                                                !parameterized from Kulmala et al. 1998
      rh = p_h2o/p_h2o_sat       !relative humidity
!+++++++++++++++++++++++++++++++++++++++++++++++++++++

      !print *, 'The number of water molecules and relative humidity: '
      !print *, n_h2o_cm3, rh
```

```
      !print *, 'Enter the fraction of which are hydrates '
      !print *, '(0.001 for example) it is higher for higher RH '
      !print *,'For example 50% to 100% is an almost 10^2 higher number.'
      !print *, 'Suggest 1D-6 - 1D-8. Enter: '
      !read *, hydrate_ratio

      hydrate_ratio = 1.D-6

      n_hydrates = hydrate_ratio*n_h2o
      n_hydrates_cm3 = hydrate_ratio*n_h2o_cm3         !the number of hydrate clusters
!-------------------------------------------------------------------------------------------
!-------------------------------------------------------------------------------------------
!-------------------------------------------------------------------------------------------
!-------------------------------------------------------------------------------------------
!Set up the initial values of variables
! - Common to all cases - vary if want to investigate other cases

  n_bin=27
     !+++++++++++++++++++++++++++++++++++++++++++++++++++++++++++++++++++++++++++++
!set up population for drops

      !pop_ini = 1D10
      !pop_end = 1D1 !arbitrary h2so4 fractions initially (r_min) and at end (r_max)

  !pop_grad = (pop_end - pop_ini)/(n_bin)

      !N(1) = pop_ini
      !N(n_bin) = pop_end


      !DO p_i = 2, n_bin-1

      !p_i_real = real(p_i)

      !N(p_i) = pop_ini + pop_grad*p_i_real

      !END DO
!+++++++++++++++++++++++++++++++++++++++++++++++++++++++++++++++++++++++++++++++++++
  N = 0.D0

      N_cm3 = N/1.D6
!*********************************************************************

!For full programme - from Pirjola 1999

      R_min = 0.5D-9
      R_max = 1.0D-6        !Use for full equation
!+++++++++++++++++++++++++++++++++++++++++++++++++++++++++++++++++++++++++++++++++++

      DO b_i = 1, n_bin

  log_R1 = ((LOG10(R_max)-LOG10(R_min))/(n_bin-1))*(b_i-1)
      log_R(b_i)=LOG10(R_min)+ log_R1

      R_size(b_i) = 10**(log_R(b_i))   !lower bound of bin

      !drop_x_frac(b_i) = x_grad*R_size(b_i) + x_ini
  drop_x_frac(b_i) = 1.D0

      drop_density1 = ((1.0-drop_x_frac(b_i))*1000.)
      drop_density(b_i) = (drop_x_frac(b_i)*1830.5)+drop_density1


      st_drop1 = 3.7628*LOG(drop_x_frac(b_i)+0.1)
      st_drop2 = 4.51915*((LOG(drop_x_frac(b_i)+0.1))**2)
      st_drop3 = 2.93893*((LOG(drop_x_frac(b_i)+0.1))**3)

      s_tension_drop(b_i) = 1D-3*(51.777-st_drop1-st_drop2-st_drop3)

      !This is parameterization from Hoppel 1987, may change mole fraction
```

```
      END DO    !end of lower bound calculator
!*******************************************************************************

      mass = ((4/3.)*pi*R_size**3)*drop_density   !mass of a particle in a given size bin

      N_acid_drop = (4/3.)*pi*(R_size**3)*drop_x_frac*1830.5/m_h2so4
!the number of acid molecules in a drop, each bin size
!+++++++++++++++++++++++++++++++++++++++++++++++++++++++++++++++++++++++++++++++
!+++++++++++++++++++++++++++++++++++++++++++++++++++++++++++++++++++++++++++++++
!+++++++++++++++++++++++++++++++++++++++++++++++++++++++++++++++++++++++++++++++
!+++++++++++++++++++++++++++++++++++++++++++++++++++++++++++++++++++++++++++++++
!now for the kronecker deltas and coefficients used in the coagulation equations

DO c_i =1, n_bin
DO c_j=1, n_bin
DO c_k = 1, n_bin

if (c_j == c_k) then
kron_delta1(c_i, c_j, c_k) = 1
else
kron_delta1(c_i, c_j, c_k) = 0
endif

Coag_coeffs1(c_i, c_j, c_k) = 1/(1.+ kron_delta1(c_i, c_j, c_k))

END DO   !end c_k loop
END DO   !end c_j loop
END DO   !end c_i loop

!first loop covers all i, 1 -> n
!-------------------------------------------------------------------------------
!second loop doesn't require 1st bin

kron_delta2(1, :, :) = 0.
Coag_coeffs2(1, :, :) = 0.
Cond_denom1(1) = 1./N_acid_drop(1)

DO c_i =2, n_bin

Cond_denom1(c_i) = 1./(N_acid_drop(c_i) - N_acid_drop(c_i-1))

DO c_j=1, n_bin
DO c_k = 1, n_bin

n_test = N_acid_drop(c_j) + N_acid_drop(c_k)

if ((n_test > N_acid_drop(c_i-1)).and.(n_test <= N_acid_drop(c_i))) then
kron_delta2(c_i, c_j, c_k) = 1
else
kron_delta2(c_i, c_j, c_k) = 0
endif

Coag_coeffs2(c_i, c_j, c_k) = (n_test - N_acid_drop(c_i-1))/(N_acid_drop(c_i)-N_acid_drop(c_i-1))*kron_delta2(c_i, c_j, c_k)

END DO   !end c_k loop
END DO   !end c_j loop
END DO   !end c_i loop
!-------------------------------------------------------------------------------
!third loop doesn't require last bin

kron_delta3(n_bin, :, :) = 0.
Coag_coeffs3(n_bin, :, :) = 0.
Cond_denom2(n_bin) = -1./N_acid_drop(n_bin)

DO c_i=1, n_bin-1

Cond_denom2(c_i) = 1./(N_acid_drop(c_i+1) - N_acid_drop(c_i))

DO c_j=1, n_bin
DO c_k =1, n_bin

n_test = N_acid_drop(c_j) + N_acid_drop(c_k)
```

```
if ((n_test > N_acid_drop(c_i)).and.(n_test <= N_acid_drop(c_i+1))) then
kron_delta3(c_i, c_j, c_k) = 1
else
kron_delta3(c_i, c_j, c_k) = 0
endif

Coag_coeffs3(c_i, c_j, c_k) = (N_acid_drop(c_i+1) - n_test)/(N_acid_drop(c_i+1)-N_acid_drop(c_i))*kron_delta3(c_i, c_j, c_k)

END DO   !end c_k loop
END DO   !end c_j loop
END DO   !end c_i loop
!++++++++++++++++++++++++++++++++++++++++++++++++++++++++++++++++++++++++++++++++++++
!-----------------------------------------------------------------------------------------
!-----------------------------------------------------------------------------------------

print *, 'Choose the time step, in seconds: '

read *, t_step

print *, 'Choose the end time, in HOURS: '

read *, t_max

t_number = ceiling(t_max/(t_step/3600D0))     !finds the number of iterations the code will produce

t_print = ceiling(600/t_step)

print *, 'What time after Sunrise (0000) to begin experiment, in hours: '
read *, exp_begin
!-----------------------------------------------------------------------------------------
!open a file for saving data
OPEN(UNIT=10,FILE='Aerosol_nucl_cond_coag1.dat')

WRITE(10,*) 'Time steps (s): ', t_step
WRITE(10,*) 'End time in hours: ', t_max
WRITE(10,*) 'Time after Sunrise at which experiment began: ', exp_begin

WRITE(10,*) 'Temperature: ', Temp
WRITE(10,*) 'Pressure (hPa): ', P
WRITE(10,*) 'H2O conc (ppmv): ', mx_h2o*1D6
WRITE(10,*) 'OH conc (pptv): ', mx_oh*1D12
WRITE(10,*) 'SO2 conc (pptv): ', mx_so2*1D12
WRITE(10,*)
WRITE(10,*)'-----------------------------------------------------------------------------------------'
WRITE(10,*) 'Radii (m): '
WRITE(10,99) R_size
99 FORMAT(27(E18.11,1x))

WRITE(10,*) 'time elapsed (s), h2so4 (cm^-3),  N (CM^-3)'
WRITE(10,*)'-----------------------------------------------------------------------------------------'
WRITE(10,102) 0,n_h2so4_cm3,N_cm3 !print initial, 0 time, values


102 FORMAT(I10,1x,E18.11,1x,27(E18.11,1x)) !print format
!-----------------------------------------------------------------------------------------

!Iterative
!*****************************************************************************************************
!+++++++++++++++++++++++++++++++++++++++++++++++++++++++++++++++++++++++++++++++++++++++++++++++++++++++
!*****************************************************************************************************
DO t=1, t_number    !++++++++++++++++++++++++++++++++++++++++++++++++++++++++++++++++++++++++++++++MAIN LOOP

N_old = N
n_h2so4_old = n_h2so4
!*****************************************************************************************************
!+++++++++++++++++++++++++++++++++++++++++++++++++++++++++++++++++++++++++++++++++++++++++++++++++++++++

!Find Q for sinusoidal Earth rotation

day_sec = Day_length*3600.D0     !now use sunrise/set to define daylight
!*******************************************************************************************
```

```
if (q_choice == 3) then            !*************************************************************Q=3

t_sec = t*t_step                !convert step into a time (s)

day_num = FLOOR(t_sec/86400)         !find number of days passed

t_sec = t_sec + exp_begin*3600.

Power_coeff = 0.

if ((t_sec > day_num*86400).and.(t_sec < ((day_num*86400)+day_sec))) then
  Power_coeff = SIN((PI/180.)*(180./day_sec)*t_sec) !sin wt only for daylight times
endif

Q_m3 = Power_coeff*Q_max

endif                   !*********************************************************************Q=3
!*****************************************************************************************

!*************************************************************************************************
!+++++++++++++++++++++++++++++++++++++++++++++++++++++++++++++++++++++++++++++++++++++++++++++++++
p_h2so4_sat = exp(27.7849D0 - 10156.D0/Temp)
!saturation pressure of sulphuric acid - parameterized from Kulmala 1998

p_h2so4 = (n_h2so4/n_air)*P   !find molar fraction of acid, then times by ambient pressure
                                !to find partial pressure
ra = p_h2so4/p_h2so4_sat          !Relative acidity

x_h2so4 = 1.2233 - (0.0154D0*ra/(ra + rh)) + 0.0102D0*LOG(n_h2so4_cm3) - 0.0415D0*LOG(n_h2o_cm3) + 0.0016D0*Temp
                            !Parameterized from Kulmala et al. 1998; acid molar fraction

!if finite(x_h2so4) ne 1 then x_h2so4 = 1.D
!if (x_h2so4 lt 0.D) then x_h2so4 = 0.D
!if (x_h2so4 gt 1.D) then x_h2so4 = 1.D

x_h2o = 1.D0 - x_h2so4           !water molar fraction in critical cluster
!+++++++++++++++++++++++++++++++++++++++++++++++++++++++++++++++++++++++++++++++++++++++++++++++++
!*************************************************************************************************

!*************************************************************************************************
!+++++++++++++++++++++++++++++++++++++++++++++++++++++++++++++++++++++++++++++++++++++++++++++++++
!Evaluate Activities and chemical potential difference

A11 = 2.989D3 - (2.147D6/Temp) + (2.33D8/(Temp**2))
                                 !2 activity parameters
A12 = 5.672D3 - (4.074D6/Temp) + (4.421D3/(Temp**2))

B11 = 0.527D0
B12 = 1.8975D0         !2 more parameters

Log_act_w = (A11*x_h2so4**2)/(((x_h2so4 + x_h2o*B11)**2)*Temp)
Log_act_a = (A12*x_h2o**2)/(((x_h2o + x_h2so4*B12)**2)*Temp)

Act_h2so4_co = 10**Log_act_a
Act_h2o_co = 10**Log_act_w      !Activity coefficients

!Activity, A = A_coeff*molar_fraction

A_h2so4 = Act_h2so4_co*x_h2so4
A_h2o = Act_h2o_co*x_h2o          !Activities for sulphuric acid and water

p_a_sol = A_h2so4*p_h2so4_sat      !This pressure above mixed solution; needed for chemical potential

chem_potn_acid = -1.0D0*k*Temp*ALOG(p_h2so4/p_a_sol)      !chemical potential for H2SO4
!+++++++++++++++++++++++++++++++++++++++++++++++++++++++++++++++++++++++++++++++++++++++++++++++++
!*************************************************************************************************

!*************************************************************************************************
!+++++++++++++++++++++++++++++++++++++++++++++++++++++++++++++++++++++++++++++++++++++++++++++++++
!Use parameterization to find surface tension and density - Kulmala et al. 1998
```

```
if (x_h2so4 < 0.16D0) then

sigma_tension_pt1 = 74.00296 + 7.68634*x_h2so4 + (625.86132*x_h2so4**2) - &   !parameters of surface tension
(5117.53488*x_h2so4**3) + (10646.24244*x_h2so4**4)

else

sigma_tension_pt1 = 77.04932 + 9.73321*x_h2so4 - (59.4238*x_h2so4**2) + &
(5.6594*x_h2so4**3) + (19.78486*x_h2so4**4)

endif

if (x_h2so4 < 0.25D0) then

sigma_tension_pt2 = 67.822 + 78.97377*x_h2so4 - (207.81448*x_h2so4**2) - &
(165.6474*x_h2so4**3) + (654.16827*x_h2so4**4)

else

sigma_tension_pt2 = 72.55489 + 32.99004*x_h2so4 - (115.88314*x_h2so4**2) + (62.0346*x_h2so4**3)

endif

sigma_tension = 0.001*sigma_tension_pt1 + (sigma_tension_pt2 - sigma_tension_pt1)*((Temp - 283.15)/40000.)
!Surface tension in N/m
!++++++++++++++++++++++++++++++++++++Density parameterization - Kulmala et al. 1998

m_frac_h2so4 = (x_h2so4*98)/((x_h2so4*98) + (x_h2o*18))     !Mass fraction of sulphuric acid in critical cluster

if (m_frac_h2so4 < 0.6D0) then

density_pt1 = 998.94 + 748.23*m_frac_h2so4 - (4.07622*m_frac_h2so4**2) + (317.88*m_frac_h2so4**3)

density_pt2 = 982.99 + 608.19*m_frac_h2so4 + (233.26*m_frac_h2so4**2) + (154.19*m_frac_h2so4**3)

else

density_pt1 = 473.52 + 4903.99*m_frac_h2so4 - (11916.5*m_frac_h2so4**2) + &      !Parameters for density
(15057.6*m_frac_h2so4**3) - (6668.37*m_frac_h2so4**4)

density_pt2 = 250.52 + 5733.14*m_frac_h2so4 - (13138.14*m_frac_h2so4**2) + &
(15565.78*m_frac_h2so4**3) - (6618.7*m_frac_h2so4**4)

endif

density = density_pt1 + (density_pt2 - density_pt1)*((Temp-273.15)/60.)     !density in kg/m3

!++++++++++++++++++++++++++++++++++++Average molecular volume - Pirjola 1998

V_avg = x_h2so4*Va + x_h2o*Vw
!++++++++++++++++++++++++++++++++++++++++++++++++++++++++++++++++++++++++++++++++++++++++++++++++++++++++++++++++++++
!******************************************************************************************************************

!******************************************************************************************************************
!++++++++++++++++++++++++++++++++++++++++++++++++++++++++++++++++++++++++++++++++++++++++++++++++++++++++++++++++++++
!Find critical cluster size

R_crit = (-2.D0*sigma_tension*Va)/chem_potn_acid          !critical radius from Kulmala et al. 1998

if (R_crit < (Va**(0.333D0))) then
  R_crit = (Va**(0.333D0))   !if it is found to be less than 1 acid molecule
endif                                                 !then re-set to 1 acid molecule: barrierless
!++++++++++++++++++++++++++++++++++++++++++++++++++++++++++++++++++++++++++++++++++++++++++++++++++++++++++++++++++++
!******************************************************************************************************************

!******************************************************************************************************************
!++++++++++++++++++++++++++++++++++++++++++++++++++++++++++++++++++++++++++++++++++++++++++++++++++++++++++++++++++++
!Find number of acid molecules in critical cluster and mass of cluster - Pirjola 1998

m_crit = ((4/3.)*pi*(R_crit**3.)*density)       !mass of cluster
```

```
N_crit_h2so4 = ((4/3.)*pi*(R_crit**3.)*density)/(m_h2so4 + (x_h2o/x_h2so4)*m_h2o)
!+++++++++++++++++++++++++++++++++++++++++++++++++++++++++++++++++++++++++++++++++++++++++++++++++++++++++++++++++++++
!*****************************************************************************************************************

!*****************************************************************************************************************
!+++++++++++++++++++++++++++++++++++++++++++++++++++++++++++++++++++++++++++++++++++++++++++++++++++++++++++++++++++++
!Calculate the initiation Kronecker deltas - Pirjola 1999

kron_delta_I1(1) = 1
Coag_coeffs_I1(1) = N_crit_h2so4/N_acid_drop(1)
kron_delta_I2(n_bin) = 0                                !initial and final bins
Coag_coeffs_I2(n_bin) = N_crit_h2so4/N_acid_drop(n_bin)

DO c_i = 2, n_bin

if ((N_crit_h2so4 > N_acid_drop(c_i-1)).and.(N_crit_h2so4 <= N_acid_drop(c_i))) then
kron_delta_I1(c_i) = 1
else
kron_delta_I1(c_i) = 0
endif

Coag_coeffs_I1(c_i) = ((N_crit_h2so4 - N_acid_drop(c_i-1))/(N_acid_drop(c_i) - N_acid_drop(c_i-1)))*kron_delta_I1(c_i)
END DO

DO c_i = 1, n_bin-1

if ((N_crit_h2so4 > N_acid_drop(c_i)).and.(N_crit_h2so4 <= N_acid_drop(c_i+1))) then
kron_delta_I2(c_i) = 1
else
kron_delta_I2(c_i) = 0
endif

Coag_coeffs_I2(c_i) = ((N_acid_drop(c_i+1) - N_crit_h2so4)/(N_acid_drop(c_i+1) - N_acid_drop(c_i)))*kron_delta_I2(c_i)
END DO
!+++++++++++++++++++++++++++++++++++++++++++++++++++++++++++++++++++++++++++++++++++++++++++++++++++++++++++++++++++++
!*****************************************************************************************************************

!*****************************************************************************************************************
!+++++++++++++++++++++++++++++++++++++++++++++++++++++++++++++++++++++++++++++++++++++++++++++++++++++++++++++++++++++
!Calculate nucleation rate - Kulmala et al. 1998 and Pirjola 1998

F_molecules = n_h2o        !since water molecules conc. is much higher n_h2so4 and clusters are neglected

B_a = n_h2so4*sqrt(((k*Temp)/(2.D0*pi))*((1.D0/m_h2so4) - (1.D0/m_crit)) )    !acid parameter - Kulmala et al. 1998

B_w = n_h2o*sqrt(((k*Temp)/(2.D0*pi))*((1.D0/m_h2o) - (1.D0/m_crit)) )       !water parameter

B_h = n_hydrates*sqrt(((k*Temp)/(2.D0*pi))*((1.D0/m_h2o_clusters) - (1.D0/m_crit)) )     !hydrate parameter

Area_crit = 4.D0*pi*(R_crit)**2        !surface area of the nucleus

growth_angle = ATAN(x_h2so4/x_h2o)   !growth angle of steepest descent on Gibbs free energy surface

Z_factor = sqrt(sigma_tension/(k*Temp))*(V_avg)/(2.D0*pi*R_crit**2)   !Zeldovich factor

B_num = B_w*B_a - B_h**2
B_denom = (B_w*(sin(growth_angle))**2) + (B_a*(cos(growth_angle))**2) - 2.D0*B_h*sin(growth_angle)*cos(growth_angle)

B_AV = B_num/B_denom       !average growth rate

delta_G = (1.333D0)*pi*(R_crit**2)*sigma_tension

exp_term = -1.0D0*delta_G/(K*Temp)

J_rate = F_molecules*Area_crit*B_AV*Z_factor*exp(exp_term)
!+++++++++++++++++++++++++++++++++++++++++++++++++++++++++++++++++++++++++++++++++++++++++++++++++++++++++++++++++++++
!*****************************************************************************************************************

!*****************************************************************************************************************
!+++++++++++++++++++++++++++++++++++++++++++++++++++++++++++++++++++++++++++++++++++++++++++++++++++++++++++++++++++++
!Calculate condensation rate - Pirjola 1998
```

```
Diffusion_coeff = (0.00143*(Temp**(1.75))*sqrt((1.D0/mol_mass_air)+(1.D0/mol_mass_acid))/ &
((P/1.D5)*(((Diff_vol_acid)**(0.333D0)) + ((Diff_vol_acid)**(0.333D0)))**2))*1.D-4

!from Kuuluvainen 2009; Reid 1989
!D is in cm^2 s^-1; P is bars
!so 1D-4 is to convert to m^2 s^-1

mfp = ((pi*m_h2so4/(8.D0*k*Temp))**(0.333D0))*Diffusion_coeff    !mean free path

DO count=1, n_bin

Knudsen(count) = mfp/R_size(count) !knudsen number: mfp/R

beta_factor(count) = (Knudsen(count)+1.D0)/((0.377D0*Knudsen(count)) & ! fuchs correction factor
 + 1.D0 + ((1.333D0)*(sticking**(-1.D0))*Knudsen(count)**2.D0) + ((1.333D0)*(sticking**(-1.D0))*Knudsen(count)))

cond_coeff(count) = (4.D0*pi*R_size(count)*beta_factor(count)*Diffusion_coeff) !condensation coefficient

!if (cond_coeff(count) == -1) then
!   cond_coeff(count) = 0.D0 !Test for TRUE statement
!endif

END DO
!++++++++++++++++++++++++++++++++++++++++++++++++++++++++++++++++++++++++++++++++++++++++++++++++++++++++++++++++++++
!**************************************************************************************************************

!**************************************************************************************************************
!++++++++++++++++++++++++++++++++++++++++++++++++++++++++++++++++++++++++++++++++++++++++++++++++++++++++++++++++++++
!Calculate coagulation rate - Pirjola 1998

cunningham = 1.D0 + Knudsen*(alpha1 + alpha2*exp(-1.D0*alpha3/Knudsen))

D_1 = k*Temp*cunningham/(6.*pi*mu_coag*R_size)

c_rms = sqrt(8.*k*Temp/(pi*mass))

gamma_coag = 8.*D_1/(pi*c_rms)

DO c_i =1, n_bin

DO c_j=1, n_bin

D_coag(c_i, c_j) = D_1(c_i) + D_1(c_j)

R_coag(c_i, c_j) = R_size(c_i) + R_size(c_j)

c_coag(c_i, c_j) = sqrt((c_rms(c_i)**2) + (c_rms(c_j)**2))

omega_coag(c_i, c_j) = ( ( ( R_coag(c_i, c_j) + gamma_coag(c_i) )**3 - ( (R_coag(c_i, c_j))**2.D0 + &
 (gamma_coag(c_i))**2)**(1.33D0))/(3.D0*(R_coag(c_i, c_j)*gamma_coag(c_i))) ) - R_coag(c_i, c_j)

kcb(c_i, c_j) = 4.D0*pi*R_coag(c_i, c_j)*D_coag(c_i, c_j)

END DO   !end c_j loop

END DO   !end c_i loop

DO c_i=1, n_bin

DO c_j=1, n_bin

sigma_coag(c_i, c_j) = sqrt(omega_coag(c_i, c_j)**2 + omega_coag(c_j, c_i)**2)

K_denom1(c_i, c_j) = R_coag(c_i, c_j)/(R_coag(c_i, c_j) + sigma_coag(c_i, c_j))

K_denom2(c_i, c_j) = 4.D0*D_coag(c_i, c_j)/(c_coag(c_i, c_j)*R_coag(c_i, c_j))

k_coag(c_i, c_j) = kcb(c_i, c_j)/(K_denom1(c_i, c_j) + K_denom2(c_i, c_j))

k_coag(c_i, c_j) = k_coag(c_i, c_j)

END DO   !end c_j loop
```

```
END DO   !end c_i loop
!++++++++++++++++++++++++++++++++++++++++++++++++++++++++++++++++++++++++++++++++++++++++++++++++++++++++++++++++++++++
!**********************************************************************************************************************
cond_Acid_term = 0.D0
DO i_acid = 1, n_bin
!----------------------------------------------------------------------------------------------------------------------
sum_acid = (n_h2so4)*cond_coeff(i_acid)*N(i_acid)
!----------------------------------------------------------------------------------------------------------------------
cond_acid_term = cond_acid_term + sum_acid
END DO

n_h2so4 = (Q_m3 - N_crit_h2so4*J_rate - cond_acid_term)

n_h2so4 = n_h2so4_old + t_step*n_h2so4

n_h2so4_cm3 = n_h2so4/1.D6
!**********************************************************************************************************************
!++++++++++++++++++++++++++++++++++++++++++++++++++++++++++++++++++++++++++++++++++++++++++++++++++++++++++++++++++++++
!Reckon number of particles in each bin

DO c_i = 1, n_bin

cond_part1 = 0.D0
cond_part2 = 0.D0

coag_part1 = 0.D0
coag_part2 = 0.D0
coag_part3 = 0.D0
!-------------------------------------------------
DO c_j=1, c_i
DO c_k = c_j, c_i
!----------------------------------------------------------------------------------------------------------------------
sum_coag1 = Coag_coeffs1(c_i, c_j, c_k)*k_coag(c_j, c_k)*N(c_j)*N(c_k)*Coag_coeffs2(c_i, c_j, c_k)
!----------------------------------------------------------------------------------------------------------------------
sum_coag2 = Coag_coeffs1(c_i, c_j, c_k)*k_coag(c_j, c_k)*N(c_j)*N(c_k)*Coag_coeffs3(c_i, c_j, c_k)
!----------------------------------------------------------------------------------------------------------------------
coag_part1 = coag_part1 + sum_coag1

coag_part2 = coag_part2 + sum_coag2
!-------------------------------------------------
END DO    !end c_k loop
END DO   !end c_j loop

!----------------------------------------------------------------------------------------------------------------------
i_term = J_rate*Coag_coeffs_I1(c_i)*kron_delta_I1(c_i) + J_rate*Coag_coeffs_I2(c_i)*kron_delta_I2(c_i)
!----------------------------------------------------------------------------------------------------------------------
if (c_i == 1) then
cond_part1 = 0.D0
else
cond_part1 = Cond_denom1(c_i)*N(c_i-1)*(n_h2so4)*cond_coeff(c_i-1)
endif
!----------------------------------------------------------------------------------------------------------------------
cond_part2 = Cond_denom2(c_i)*N(c_i)*(n_h2so4)*cond_coeff(c_i)
!----------------------------------------------------------------------------------------------------------------------

!----------------------------------------------------------------------------------------------------------------------
DO c_j = 1, n_bin
sum_coag3 = k_coag(c_i, c_j)*N(c_j)
!----------------------------------------------------------------------------------------------------------------------
coag_part3 = coag_part3 + sum_coag3
!coag_part3 = 0.D0 !JUST TO TEST EFFECT! REMOVE AFTER
!-------------------------------------------------
END DO !end of coag_coeff3 loop

N(c_i) = N_old(c_i) + t_step*(i_term + cond_part1 - cond_part2 + coag_part1 + coag_part2 - N(c_i)*coag_part3)

END DO   !end of c_i loop - for all bins

N_cm3 = N/1.D6
!++++++++++++++++++++++++++++++++++++++++++++++++++++++++++++++++++++++++++++++++++++++++++++++++++++++++++++++++++++++
!++++++++++++++++++++++++++++++++++++++++++++++++++++++++++++++++++++++++++++++++++++++++++++++++++++++++++++++++++++++
```

```
!++++++++++++++++++++++++++++++++++++++++++++++++++++++++++++++++++++++++++++++++++++++++++++++++++++++++++++++++++++++++
!++++++++++++++++++++++++++++++++++++++++++++++++++++++++++++++++++++++++++++++++++++++++++++++++++++++++++++++++++++++++
!++++++++++++++++++++++++++++++++++++++++++++++++++++++++++++++++++++++++++++++++++++++++++++++++++++++++++++++++++++++++
!++++++++++++++++++++++++++++++++++++++++++++++++++++++++++++++++++++++++++++++++++++++++++++++++++++++++++++++++++++++++

t_float = t*t_step

if  (mod(t,t_print) == 0) then !print, every 10 minutes

t_10min = ceiling(t_float)

WRITE(10,101) t_10min,n_h2so4_cm3, N_cm3

101 FORMAT(I10,1x,E18.11,1x,27(E18.11,1x)) !print format, if needs adjusting

endif

END DO         !++++++++++++++++++++++++++++++++++++++++++++++++++++++++++++++++++++++++++++++++++++++++++++++END MAIN LOOP
!++++++++++++++++++++++++++++++++++++++++++++++++++++++++++++++++++++++++++++++++++++++++++++++++++++++++++++++++++++++++
!++++++++++++++++++++++++++++++++++++++++++++++++++++++++++++++++++++++++++++++++++++++++++++++++++++++++++++++++++++++++
CLOSE(UNIT=10)

END PROGRAM Aerosol_nucl_cond_coag1
```

Bibliography

M. R. Alfarra, D. Paulsen, M. Gysel, A. A. Garforth, J. Dommen, A. S. H. Prevot, D. R. Worsnop, U. Baltensperger, and H. Coe. A mass spectrometric study of secondary organic aerosols formed from the photooxidation of anthropogenic and biogenic precursors in a reaction chamber. *Atmospheric Chemistry and Physics*, 6:5279–5293, 2006.

G. Allen, G. Vaughan, K. N. Bower, P. I. Williams, J. Crosier, M. Flynn, P. Connolly, J. F. Hamilton, J. D. Lee, J. E. Saxton, N. M. Watson, M. Gallagher, H. Coe, J. Allan, T. W. Choularton, and A. C. Lewis. Aerosol and trace-gas measurements in the darwin area during the wet season. *Journal of Geophysical Research-Atmospheres*, 113(D6), 2008.

G. Allen, G. Vaughan, D. Brunner, P. T. May, W. Heyes, P. Minnis, and J. K. Ayers. Modulation of tropical convection by breaking rossby waves. *Quarterly Journal of the Royal Meteorological Society*, 135(638):125–137, 2009.

M. O. Andreae and P. Merlet. Emission of trace gases and aerosols from biomass burning. *Global Biogeochemical Cycles*, 15(4):955–966, 2001.

M. O. Andreae, P. Artaxo, H. Fischer, S. R. Freitas, J. M. Gregoire, A. Hansel, P. Hoor, R. Kormann, R. Krejci, L. Lange, J. Lelieveld, W. Lindinger, K. Longo, W. Peters, M. de Reus, B. Scheeren, Mafs Dias, J. Strom, P. F. J. van Velthoven, and J. Williams. Transport of biomass burning smoke to the upper troposphere by deep convection in the equatorial region. *Geophysical Research Letters*, 28(6):951–954, 2001.

C. Andronache, L. J. Donner, C. J. Seman, V. Ramaswamy, and R. S. Hemler. Atmospheric sulfur and deep convective clouds in tropical pacific: A model study. *Journal of Geophysical Research-Atmospheres*, 104(D4):4005–4024, 1999.

T. Anttila, H. Vehkamaki, I. Napari, and M. Kulmala. Effect of ammonium bisulphate formation on atmospheric water-sulphuric acid-ammonia nucleation. *Boreal Environment Research*, 10(6):511–523, 2005.

F. Arnold, L. Pirjola, H. Aufmhoff, T. Schuck, T. Lahde, and K. Hameri. First gaseous sulfuric acid measurements in automobile exhaust: Implications for volatile nanoparticle formation. *Atmospheric Environment*, 40(37):7097–7105, 2006.

R. Atkinson and A. C. Lloyd. Evaluation of Kinetic and Mechanistic Data for Modeling of Photochemical Smog. *Journal of Physical and Chemical Reference Data*, 13(2):315–444, 1984.

R. Atkinson, S. M. Aschmann, A. M. Winer, and J. N. Pitts. Kinetics of the Gas-Phase Reactions of NO3 Radicals with a Series of Dialkenes, Cycloalkenes, and Monoterpenes at 295 +/- 1-K. *Environmental Science and Technology*, 18(5): 370–375, 1984.

R. Atkinson, S. M. Aschmann, and J. N. Pitts. Rate Constants for the Gas-Phase Reactions of the Oh-Radical with a Series of Monoterpenes at 294 +/- 1-K. *International Journal of Chemical Kinetics*, 18(3):287–299, 1986.

R. Atkinson, D. L. Baulch, R. A. Cox, R. F. Hampson, J. A. Kerr, and J. Troe. Evaluated Kinetic and Photochemical Data for Atmospheric Chemistry .3. Iupac Subcommittee on Gas Kinetic Data Evaluation for Atmospheric Chemistry. *Journal of Physical and Chemical Reference Data*, 18(2):881–1097, 1989.

R. Atkinson, S. M. Aschmann, and J. Arey. Rate Constants for the Gas-Phase Reactions of OH and NO3 Radicals and O-3 with Sabinene and Camphene at 296 +/-2K. *Atmospheric Environment Part a-General Topics*, 24(10):2647–2654, 1990.

R. Atkinson, D. L. Baulch, R. A. Cox, R. F. Hampson, J. A. Kerr, and J. Troe. Evaluated Kinetic and Photochemical Data for Atmospheric Chemistry - Introduction. *Atmospheric Environment Part a-General Topics*, 26(7):1187–1230, 1992.

F. C. Bahe, W. N. Marx, and U. Schurath. Determination of the Absolute Photolysis Rate of Ozone by Sunlight, O3+hv-O(1d)+O2(1[delta]G), at Ground-Level. *Atmospheric Environment*, 13(11):1515–1522, 1979.

P. A. Baron and K. Willeke. *Aerosol measurement: principles, techniques, and applications*. The University of Michigan, A Wiley-Interscience publication, Wiley (2001), 2nd edition, 2001.

R.G. Barry and R. J. Chorley. *Atmosphere, Weather and Climate*. Routledge, 11 New Fetter Lane, London, EC4P 4EE, 8th edition, 2003.

M. C. Barth, A. L. Stuart, and W. C. Skamarock. Numerical simulations of the july 10, 1996, stratospheric-tropospheric experiment: Radiation, aerosols, and ozone (sterao)-deep convection experiment storm: Redistribution of soluble tracers. *Journal of Geophysical Research-Atmospheres*, 106(D12):12381–12400, 2001.

T. F. Berglen, T. K. Berntsen, I. S. A. Isaksen, and J. K. Sundet. A global model of the coupled sulfur/oxidant chemistry in the troposphere: The sulfur cycle. *Journal of Geophysical Research-Atmospheres*, 109, 2004.

J. Beringer, N. J. Tapper, and T. D. Keenan. Evolution of maritime continent thunderstorms under varying meteorological conditions over the tiwi islands. *International Journal of Climatology*, 21(8):1021–1036, 2001.

T. Berndt, O. Boge, F. Stratmann, J. Heintzenberg, and M. Kulmala. Rapid formation of sulfuric acid particles at near-atmospheric conditions. *Science*, 307(5710):698–700, 2005.

M. Boy, T. Karl, A. Turnipseed, R. L. Mauldin, E. Kosciuch, J. Greenberg, J. Rathbone, J. Smith, A. Held, K. Barsanti, B. Wehner, S. Bauer, A. Wiedensohler, B. Bonn, M. Kulmala, and A. Guenther. New particle formation in the front range of the colorado rocky mountains. *Atmospheric Chemistry and Physics*, 8(6):1577–1590, 2008.

C. A. M. Brenninkmeijer, P. Crutzen, F. Boumard, T. Dauer, B. Dix, R. Ebinghaus, D. Filippi, H. Fischer, H. Franke, U. Friess, J. Heintzenberg, F. Helleis, M. Hermann, H. H. Kock, C. Koeppel, J. Lelieveld, M. Leuenberger, B. G. Martinsson, S. Miemczyk, H. P. Moret, H. N. Nguyen, P. Nyfeler, D. Oram, D. O'Sullivan, S. Penkett, U. Platt, M. Pupek, M. Ramonet, B. Randa, M. Reichelt, T. S. Rhee, J. Rohwer, K. Rosenfeld, D. Scharffe, H. Schlager, U. Schumann, F. Slemr, D. Sprung, P. Stock, R. Thaler, F. Valentino, P. van Velthoven, A. Waibel, A. Wandel, K. Waschitschek, A. Wiedensohler, I. Xueref-Remy,

A. Zahn, U. Zech, and H. Ziereis. Civil aircraft for the regular investigation of the atmosphere based on an instrumented container: The new CARIBIC system. *Atmospheric Chemistry and Physics*, 7(18):4953–4976, 2007.

C. A. Brock, P. Hamill, J. C. Wilson, H. H. Jonsson, and K. R. Chan. Particle formation in the upper tropical troposphere - a source of nuclei for the stratospheric aerosol. *Science*, 270(5242):1650–1653, 1995.

K. A. Browning, A. M. Blyth, P. A. Clark, U. Corsmeier, C. J. Morcrette, J. L. Agnew, S. P. Ballard, D. Bamber, C. Barthlott, L. J. Bennett, K. M. Beswick, M. Bitter, K. E. Bozier, B. J. Brooks, C. G. Collier, F. Davies, B. Deny, M. A. Dixon, T. Feuerle, R. M. Forbes, C. Gaffard, M. D. Gray, R. Hankers, T. J. Hewison, N. Kalthoff, S. Khodayar, M. Kohler, C. Kottmeier, S. Kraut, M. Kunz, D. N. Ladd, H. W. Lean, J. Lenfant, Z. Li, J. Marsham, J. McGregor, S. D. Mobbs, J. Nicol, E. Norton, D. J. Parker, F. Perry, M. Ramatschi, H. M. A. Ricketts, N. M. Roberts, A. Russell, H. Schulz, E. C. Slack, G. Vaughan, J. Waight, D. P. Wareing, R. J. Watson, A. R. Webb, and A. Wieser. The convective storm initiation project. *Bulletin of the American Meteorological Society*, 88(12):1939–1955, 2007.

D. Brunner, P. Siegmund, P. T. May, L. Chappel, C. Schiller, R. Muller, T. Peter, S. Fueglistaler, A. R. MacKenzie, A. Fix, H. Schlager, G. Allen, A. M. Fjaeraa, M. Streibel, and N. R. P. Harris. The SCOUT-O3 darwin aircraft campaign: rationale and meteorology. *Atmospheric Chemistry and Physics*, 9(1):93–117, 2009.

T. A. Cerni. Determination of the size and concentration of cloud drops with an fssp. *Journal of Climate and Applied Meteorology*, 22(8):1346–1355, 1983.

C. Chemel, M. R. Russo, J. A. Pyle, R. S. Sokhi, and C. Schiller. Quantifying the Imprint of a Severe Hector Thunderstorm during ACTIVE/SCOUT-O3 onto the Water Content in the Upper Troposphere/Lower Stratosphere. *Monthly Weather Review*, 137(8):2493–2514, 2009.

M. P. Chipperfield. New version of the TOMCAT/SLIMCAT off-line chemical transport model: Intercomparison of stratospheric tracer experiments. *Quarterly Journal of the Royal Meteorological Society*, 132(617):1179–1203, 2006.

C. Chou and J. D. Neelin. Cirrus detrainment-temperature feedback. *Geophysical Research Letters*, 26(9):1295–1298, 1999.

T. W. Choularton, K. N. Bower, E. Weingartner, I. Crawford, H. Coe, M. W. Gallagher, M. Flynn, J. Crosier, P. Connolly, A. Targino, M. R. Alfarra, U. Baltensperger, S. Sjogren, B. Verheggen, J. Cozic, and M. Gysel. The influence of small aerosol particles on the properties of water and ice clouds. *Faraday Discussions*, 137:205–222, 2008.

C. F. Clement and I. J. Ford. Gas-to-particle conversion in the atmosphere: I. evidence from empirical atmospheric aerosols. *Atmospheric Environment*, 33 (3):475–487, 1999a.

C. F. Clement and I. J. Ford. Gas-to-particle conversion in the atmosphere: II. analytical models of nucleation bursts. *Atmospheric Environment*, 33(3): 489–499, 1999b.

C. F. Clement, M. Kulmala, and T. Vesala. Theoretical consideration on sticking probabilities. *Journal of Aerosol Science*, 27(6):869–882, 1996.

C. F. Clement, I. J. Ford, C. H. Twohy, A. Weinheimer, and T. Campos. Particle production in the outflow of a midlatitude storm. *Journal of Geophysical Research-Atmospheres*, 107(D21), 2002.

C. F. Clement, L. Pirjola, C. H. Twohy, I. J. Ford, and M. Kulmala. Analytic and numerical calculations of the formation of a sulphuric acid aerosol in the upper troposphere. *Journal of Aerosol Science*, 37(12):1717–1729, 2006.

H. Coe, P. I. Williams, G. McFiggans, M. W. Gallagher, K. M. Beswick, K. N. Bower, and T. W. Choularton. Behavior of ultrafine particles in continental and marine air masses at a rural site in the united kingdom. *Journal of Geophysical Research-Atmospheres*, 105(D22):26891–26905, 2000.

T. Corti, B. P. Luo, M. de Reus, D. Brunner, F. Cairo, M. J. Mahoney, G. Martucci, R. Matthey, V. Mitev, F. H. dos Santos, C. Schiller, G. Shur, N. M. Sitnikov, N. Spelten, H. J. Vössing, S. Borrmann, and T. Peter. Unprecedented evidence for deep convection hydrating the tropical stratosphere. *Geophys. Res. Lett.*, 35, 2008.

N. A. Crook. Sensitivity of moist convection forced by boundary layer processes to low-level thermodynamic fields. *Monthly Weather Review*, 124(8):1767–1785, 1996.

J. Curtius. Nucleation of atmospheric aerosol particles. *Comptes Rendus Physique*, 7(9-10):1027–1045, 2006.

J. Curtius, B. Sierau, F. Arnold, M. de Reus, J. Strom, H. A. Scheeren, and J. Lelieveld. Measurement of aerosol sulfuric acid 2. pronounced layering in the free troposphere during the second aerosol characterization experiment (ACE 2). *Journal of Geophysical Research-Atmospheres*, 106(D23):31975–31990, 2001.

D. Davis, G. Chen, P. Kasibhatla, A. Jefferson, D. Tanner, F. Eisele, D. Lenschow, W. Neff, and H. Berresheim. DMS oxidation in the antarctic marine boundary layer: Comparison of model simulations and field observations of DMS, DMSO, DMSO2, H2SO4(g), MSA(g), and MSA(p). *Journal of Geophysical Research-Atmospheres*, 103(D1):1657–1678, 1998.

D. Davis, G. Chen, A. Bandy, D. Thornton, F. Eisele, L. Mauldin, D. Tanner, D. Lenschow, H. Fuelberg, B. Huebert, J. Heath, A. Clarke, and D. Blake. Dimethyl sulfide oxidation in the equatorial pacific: Comparison of model simulations with field observations for DMS, SO2, H2SO4(g), MSA(g), MS, and NSS. *Journal of Geophysical Research-Atmospheres*, 104(D5):5765–5784, 1999.

M. De Reus, J. Strom, M. Kulmala, L. Pirjola, J. Lelieveld, C. Schiller, and M. Zoger. Airborne aerosol measurements in the tropopause region and the dependence of new particle formation on preexisting particle number concentration. *Journal of Geophysical Research-Atmospheres*, 103(D23):31255–31263, 1998.

M. De Reus, J. Strom, J. Curtius, L. Pirjola, E. Vignati, F. Arnold, H. C. Hansson, M. Kulmala, J. Lelieveld, and F. Raes. Aerosol production and growth in the upper free troposphere. *Journal of Geophysical Research-Atmospheres*, 105 (D20):24751–24762, 2000.

A. E. Dessler. The effect of deep, tropical convection on the tropical tropopause layer. *Journal of Geophysical Research-Atmospheres*, 107(D3), 2002.

B. M. Dinelli, E. Castelli, B. Carli, S. Del Bianco, M. Gai, L. Santurri, B. P. Moyna, M. Oldfield, R. Siddans, D. Gerber, W. J. Reburn, B. J. Kerridge, and C. Keim. Technical note: Measurement of the tropical utls composition in presence of clouds using millimetre-wave heterodyne spectroscopy. *Atmospheric Chemistry and Physics*, 9(4):1191–1207, 2009.

J. Duplissy, M. Gysel, M. R. Alfarra, J. Dommen, A. Metzger, A. S. H. Prevot, E. Weingartner, A. Laaksonen, T. Raatikainen, N. Good, S. F. Turner, G. McFiggans, and U. Baltensperger. Cloud forming potential of secondary organic aerosol under near atmospheric conditions. *Geophysical Research Letters*, 35 (3), 2008.

D. R. Durran, T. Dinh, M. Ammerman, and T. Ackerman. The mesoscale dynamics of thin tropical tropopause cirrus. *Journal of the Atmospheric Sciences*, 66(9):2859–2873, 2009.

D. P. Edwards, G. Petron, P. C. Novelli, L. K. Emmons, J. C. Gille, and J. R. Drummond. Southern hemisphere carbon monoxide interannual variability observed by terra/measurement of pollution in the troposphere (MOPITT). *Journal of Geophysical Research-Atmospheres*, 111(D16):9, 2006.

F.L. Eisele and D. R. Hanson. First measurements of prenucleation molecular clusters. *Journal of Physical Chemistry*, 104:830–836, 2000.

A. M. L. Ekman, C. Wang, J. Wilson, and J. Strom. Explicit simulations of aerosol physics in a cloud-resolving model: a sensitivity study based on an observed convective cloud. *Atmospheric Chemistry and Physics*, 4:773–791, 2004.

A. M. L. Ekman, C. Wang, J. Strom, and R. Krejci. Explicit simulation of aerosol physics in a cloud-resolving model: Aerosol transport and processing in the free troposphere. *Journal of the Atmospheric Sciences*, 63(2):682–696, 2006.

Philipp Feldpausch, Markus Fiebig, Lutz Fritzsche, and Andreas Petzold. Measurement of ultrafine aerosol size distributions by a combination of diffusion screen separators and condensation particle counters. *Journal of Aerosol Science*, 37(5):577–597, 2006.

R. Ferretti and S. Gentile. A study of the triggering mechanisms for deep convection in the tropics using a mesoscale model: Hector events during SCOUT-O-3 and TWP-ICE campaigns. *Atmospheric Research*, 93(1-3):247–269, 2009.

V. Fiedler, M. Dal Maso, M. Boy, H. Aufmhoff, J. Hoffmann, T. Schuck, W. Birmili, M. Hanke, J. Uecker, F. Arnold, and M. Kulmala. The contribution of sulphuric acid to atmospheric particle formation and growth: a comparison between boundary layers in northern and central europe. *Atmospheric Chemistry and Physics*, 5:1773–1785, 2005.

F. Flocke, R. L. Herman, R. J. Salawitch, E. Atlas, C. R. Webster, S. M. Schauffler, R. A. Lueb, R. D. May, E. J. Moyer, K. H. Rosenlof, D. C. Scott, D. R. Blake, and T. P. Bui. An examination of chemistry and transport processes in the tropical lower stratosphere using observations of long-lived and short-lived compounds obtained during STRAT and POLARIS. *Journal of Geophysical Research-Atmospheres*, 104(D21):26625–26642, 1999.

K. Frederick and C. Schumacher. Anvil characteristics as seen by C-POL during the Tropical Warm Pool International Cloud Experiment (TWP-ICE). *Monthly Weather Review*, 136(1):206–222, 2008.

K. D. Froyd, D. M. Murphy, T. J. Sanford, D. S. Thomson, J. C. Wilson, L. Pfister, and L. Lait. Aerosol composition of the tropical upper troposphere. *Atmospheric Chemistry and Physics*, 9(13):4363–4385, 2009.

N.A. Fuchs. *The mechanics of aerosols*. Macmillan, 1964.

S. Fueglistaler, A. E. Dessler, T. J. Dunkerton, I. Folkins, Q. Fu, and P. W. Mote. Tropical tropopause layer. *Reviews of Geophysics*, 47, 2009.

M. W. Gallagher, P. J. Connolly, J. Whiteway, D. Figueras-Nieto, M. Flynn, T. W. Choularton, K. N. Bower, C. Cook, R. Busen, and J. Hacker. An overview of the microphysical structure of cirrus clouds observed during EMERALD-1. *Quarterly Journal of the Royal Meteorological Society*, 131(607):1143–1169, 2005.

C. Gerbig, S. Schmitgen, D. Kley, A. Volz-Thomas, K. Dewey, and D. Haaks. An improved fast-response vacuum-UV resonance fluorescence CO instrument. *Journal of Geophysical Research-Atmospheres*, 104(D1):1699–1704, 1999.

B. W. Golding. A numerical investigation of tropical island thunderstorms. *Monthly Weather Review*, 121(5):1417–1433, 1993.

D. L. Hartmann, J. R. Holton, and Q. Fu. The heat balance of the tropical tropopause, cirrus, and stratospheric dehydration. *Geophysical Research Letters*, 28(10):1969–1972, 2001a.

D. L. Hartmann, L. A. Moy, and Q. Fu. Tropical convection and the energy balance at the top of the atmosphere. *Journal of Climate*, 14(24):4495–4511, 2001b.

J. Heintzenberg, M. Hermann, and D. Theiss. Out of africa: High aerosol concentrations in the upper troposphere over africa. *Atmospheric Chemistry and Physics*, 3:1191–1198, 2003.

O. Hellmuth. Columnar modelling of nucleation burst evolution in the convective boundary layer - first results from a feasibility study - part i: Modelling approach. *Atmospheric Chemistry and Physics*, 6:4175–4214, 2006.

B. F. Henson. An adsorption model of insoluble particle activation: Application to black carbon. *Journal of Geophysical Research-Atmospheres*, 112(D24), 2007.

M. Hermann, F. Stratmann, M. Wilck, and A. Wiedensohler. Sampling characteristics of an aircraft-borne aerosol inlet system. *Journal of Atmospheric and Oceanic Technology*, 18(1):7–19, 2001.

M. Hermann, J. Heintzenberg, A. Wiedensohler, A. Zahn, G. Heinrich, and C. A. M. Brenninkmeijer. Meridional distributions of aerosol particle number concentrations in the upper troposphere and lower stratosphere obtained by Civil Aircraft for Regular Investigation of the Atmosphere Based on an Instrument Container (CARIBIC) flights. *Journal of Geophysical Research-Atmospheres*, 108(D3), 2003.

W. J. Heyes, G. Vaughan, G. Allen, A. Volz-Thomas, H. W. Patz, and R. Busen. Composition of the TTL over Darwin: local mixing or long-range transport? *Atmospheric Chemistry and Physics*, 9(20):7725–7736, 2009.

N. S. Holmes. A review of particle formation events and growth in the atmosphere in the various environments and discussion of mechanistic implications. *Atmospheric Environment*, 41(10):2183–2201, 2007.

J. R. Holton, P. H. Haynes, M. E. McIntyre, A. R. Douglass, R. B. Rood, and L. Pfister. Stratosphere-troposphere exchange. *Reviews of Geophysics*, 33(4): 403–439, 1995.

G. Hong, P. Yang, B. C. Gao, B. A. Baum, Y. X. Hu, M. D. King, and S. Platnick. High cloud properties from three years of MODIS Terra and Aqua collection-4 data over the Tropics. *Journal of Applied Meteorology and Climatology*, 46(11): 1840–1856, 2007.

H. Huntrieser, C. Feigl, H. Schlager, F. Schroder, C. Gerbig, P. van Velthoven, F. Flatoy, C. Thery, A. Petzold, H. Holler, and U. Schumann. Airborne measurements of NOx, tracer species, and small particles during the European lightning nitrogen oxides experiment. *Journal of Geophysical Research-Atmospheres*, 107(D11), 2002.

H. Huntrieser, H. Schlager, M. Lichtenstern, A. Roiger, P. Stock, A. Minikin, H. Holler, K. Schmidt, H. D. Betz, G. Allen, S. Viciani, A. Ulanovsky, F. Ravegnani, and D. Brunner. NOx production by lightning in Hector: first airborne measurements during SCOUT-O3/ACTIVE. *Atmospheric Chemistry and Physics*, 9(21):8377–8412, 2009.

K. Iida, M. R. Stolzenburg, P. H. McMurry, and J. N. Smith. Estimating nanoparticle growth rates from size-dependent charged fractions: Analysis of new particle formation events in mexico city. *Journal of Geophysical Research-Atmospheres*, 113(D5), 2008.

IPCC. Le Treut, H., Somerville, R., Cubasch, U., Ding, Y., Mauritzen, C., Mokssit, A., Peterson, T., Prather, M. 2007: Historical Overview of Climate Change. In: Climate Change 2007: The Physical Science Basis. Contribution of Working Group I to the Fourth Assessment Report of the Intergovernmental Panel on Climate Change [Solomon, S., D. Qin, M. Manning, Z. Chen, M. Marquis, K.B. Averyt, M. Tignor and H.L. Miller (eds.)]. *Cambridge University Press, Cambridge, United Kingdom and New York, NY, USA.*, 2007.

A. Jaecker-voirol and P. Mirabel. Nucleation rate in a binary mixture of sulfuric-acid and water-vapor. *Journal of Physical Chemistry*, 92(12):3518–3521, 1988.

A. Jaecker-voirol, P. Mirabel, and H. Reiss. Hydrates in supersaturated binary

sulfuric acid-water vapor - a reexamination. *Journal of Chemical Physics*, 87 (8):4849–4852, 1987.

L. Jaeglé, D. J. Jacob, W. H. Brune, and P. O. Wennberg. Chemistry of HOx radicals in the upper troposphere. *Atmospheric Environment*, 35(3):469–489, 2001.

E. J. Jensen, W. G. Read, J. Mergenthaler, B. J. Sandor, L. Pfister, and A. Tabazadeh. High humidities and subvisible cirrus near the tropical tropopause. *Geophysical Research Letters*, 26(15):2347–2350, 1999.

N. B. Jones, C. P. Rinsland, J. B. Liley, and J. Rosen. Correlation of aerosol and carbon monoxide at 45 degrees S: Evidence of biomass burning emissions. *Geophysical Research Letters*, 28(4):709–712, 2001.

C. E. Junge, J. E. Manson, and C. W. Chagnon. A world-wide stratospheric aerosol layer. *Science*, 133(346):1478–1479, 1961.

J. Kazil, E. R. Lovejoy, M. C. Barth, and K. O'Brien. Aerosol nucleation over oceans and the role of galactic cosmic rays. *Atmospheric Chemistry and Physics*, 6:4905–4924, 2006.

J. Kazil, E. R. Lovejoy, E. J. Jensen, and D. R. Hanson. Is aerosol formation in cirrus clouds possible? *Atmospheric Chemistry and Physics*, 7:1407–1413, 2007.

T. Keenan, S. Rutledge, R. Carbone, J. Wilson, T. Takahashi, P. May, N. Tapper, M. Platt, J. Hacker, S. Sekelsky, M. Moncrieff, K. Saito, G. Holland, A. Crook, and K. Gage. The Maritime Continent Thunderstorm Experiment (MCTEX): Overview and some results. *Bulletin of the American Meteorological Society*, 81(10):2433–2455, 2000.

J. T. Kiehl and K. E. Trenberth. Earth's annual global mean energy budget. *Bulletin of the American Meteorological Society*, 78(2):197–208, 1997.

E. O. Knutson. History of diffusion batteries in aerosol measurements. *Aerosol Science and Technology*, 31(2-3):83–128, 1999.

M. Kulmala. Condensational growth and evaporation in the transition regime - an analytical expression. *Aerosol Science and Technology*, 19(3):381–388, 1993.

M. Kulmala, V. M. Kerminen, and A. Laaksonen. Simulations on the effect of sulfuric-acid formation on atmospheric aerosol concentrations. *Atmospheric Environment*, 29(3):377–382, 1995.

M. Kulmala, A. Laaksonen, and L. Pirjola. Parameterizations for sulfuric acid/water nucleation rates. *Journal of Geophysical Research-Atmospheres*, 103(D7):8301–8307, 1998.

M. Kulmala, H. Vehkamaki, T. Petaja, M. Dal Maso, A. Lauri, V. M. Kerminen, W. Birmili, and P. H. McMurry. Formation and growth rates of ultrafine atmospheric particles: a review of observations. *Journal of Aerosol Science*, 35 (2):143–176, 2004.

M. Kulmala, K. E. J. Lehtinen, and A. Laaksonen. Cluster activation theory as an explanation of the linear dependence between formation rate of 3nm particles and sulphuric acid concentration. *Atmospheric Chemistry and Physics*, 6:787–793, 2006a.

M. Kulmala, A. Reissell, M. Sipila, B. Bonn, T. M. Ruuskanen, K. E. J. Lehtinen, V. M. Kerminen, and J. Strom. Deep convective clouds as aerosol production engines: Role of insoluble organics. *Journal of Geophysical Research-Atmospheres*, 111(D17), 2006b.

H. Kuuluvainen, J. Kannosto, A. Virtanen, J. M. Mäkelä, M. Kulmala, P. Aalto, and J. Keskinen. Technical Note: Measuring condensation sink and ion sink of atmospheric aerosols with the electrical low pressure impactor (ELPI). *Atmospheric Chemistry and Physics*, 10(3):1361–1368, 2010.

L. Laakso, J. M. Makela, L. Pirjola, and M. Kulmala. Model studies on ion-induced nucleation in the atmosphere. *Journal of Geophysical Research-Atmospheres*, 107(D20), 2002.

L. Laakso, M. Kulmala, and K. E. J. Lehtinen. Effect of condensation rate enhancement factor on 3-nm (diameter) particle formation in binary ion-induced and homogeneous nucleation. *Journal of Geophysical Research-Atmospheres*, 108(D18), 2003.

L. Laakso, S. Gagne, T. Petaja, A. Hirsikko, P. P. Aalto, M. Kulmala, and V. M. Kerminen. Detecting charging state of ultra-fine particles: instrumental

development and ambient measurements. *Atmospheric Chemistry and Physics*, 7:1333–1345, 2007.

A. Laaksonen, L. Pirjola, M. Kulmala, K. H. Wohlfrom, F. Arnold, and F. Raes. Upper tropospheric SO_2 conversion into sulfuric acid aerosols and cloud condensation nuclei. *Journal of Geophysical Research-Atmospheres*, 105(D1):1459–1469, 2000.

A. Laaksonen, M. Kulmala, T. Berndt, F. Stratmann, S. Mikkonen, A. Ruuskanen, K. E. J. Lehtinen, M. Dal Maso, P. Aalto, T. Petaja, I. Riipinen, S. L. Sihto, R. Janson, F. Arnold, M. Hanke, J. Ucker, B. Umann, K. Sellegri, C. D. O'Dowd, and Y. Viisanen. SO_2 oxidation products other than H_2SO_4 as a trigger of new particle formation. part 2: Comparison of ambient and laboratory measurements, and atmospheric implications. *Atmospheric Chemistry and Physics*, 8(23):7255–7264, 2008a.

A. Laaksonen, M. Kulmala, C. D. O'Dowd, J. Joutsensaari, P. Vaattovaara, S. Mikkonen, K. E. J. Lehtinen, L. Sogacheva, M. Dal Maso, P. Aalto, T. Petaja, A. Sogachev, Y. J. Yoon, H. Lihavainen, D. Nilsson, M. C. Facchini, F. Cavalli, S. Fuzzi, T. Hoffmann, F. Arnold, M. Hanke, K. Sellegri, B. Umann, W. Junkermann, H. Coe, J. D. Allan, M. R. Alfarra, D. R. Worsnop, M. L. Riekkola, T. Hyotylainen, and Y. Viisanen. The role of VOC oxidation products in continental new particle formation. *Atmospheric Chemistry and Physics*, 8 (10):2657–2665, 2008b.

L. Labrador, G. Vaughan, W. Heyes, D. Waddicor, A. Volz-Thomas, H. W. Patz, and H. Holler. Lightning-produced NO_x during the northern australian monsoon; results from the ACTIVE campaign. *Atmospheric Chemistry and Physics*, 9(19):7419–7429, 2009.

L. J. Labrador, R. von Kuhlmann, and M. G. Lawrence. Strong sensitivity of the global mean OH concentration and the tropospheric oxidizing efficiency to the source of NO_x from lightning. *Geophysical Research Letters*, 31(6), 2004.

I. K. Larin and A. N. Yermakov. Participation of hydrogen peroxide in halogen activation in the low stratosphere. *International Journal of Remote Sensing*, 31(2):531–542, 2010.

R. P. Lawson, A. J. Heymsfield, S. M. Aulenbach, and T. L. Jensen. Shapes, sizes and light scattering properties of ice crystals in cirrus and a persistent contrail during success. *Geophysical Research Letters*, 25(9):1331–1334, 1998.

R. P. Lawson, B. Pilson, B. Baker, Q. Mo, E. Jensen, L. Pfister, and P. Bui. Aircraft measurements of microphysical properties of subvisible cirrus in the tropical tropopause layer. *Atmospheric Chemistry and Physics*, 8(6):1609–1620, 2008.

S. H. Lee, J. C. Wilson, D. Baumgardner, R. L. Herman, E. M. Weinstock, B. G. LaFleur, G. Kok, B. Anderson, P. Lawson, B. Baker, A. Strawa, J. V. Pittman, J. M. Reeves, and T. P. Bui. New particle formation observed in the tropical/subtropical cirrus clouds. *Journal of Geophysical Research-Atmospheres*, 109(D20), 2004.

H. Levy. Normal atmosphere - large radical and formaldehyde concentrations predicted. *Science*, 173(3992):141–143, 1971.

X. H. Liu, J. E. Penner, and M. Herzog. Global modeling of aerosol dynamics: Model description, evaluation, and interactions between sulfate and nonsulfate aerosols. *Journal of Geophysical Research-Atmospheres*, 110(D18), 2005.

J. P. Lopez, A. M. Fridlind, H. J. Jost, M. Loewenstein, A. S. Ackerman, T. L. Campos, E. M. Weinstock, D. S. Sayres, J. B. Smith, J. V. Pittman, A. G. Hallar, L. M. Avallone, S. M. Davis, and R. L. Herman. CO signatures in subtropical convective clouds and anvils during CRYSTAL-FACE: An analysis of convective transport and entrainment using observations and a cloud-resolving model. *Journal of Geophysical Research-Atmospheres*, 111(D9), 2006.

A. A. Lushnikov and M. Kulmala. Source-enhanced condensation in monocomponent disperse systems. *Physical Review E*, 52(2):1658, 1995.

C. Mari, D. J. Jacob, and P. Bechtold. Transport and scavenging of soluble gases in a deep convective cloud. *Journal of Geophysical Research-Atmospheres*, 105 (D17):22255–22267, 2000.

P. T. May and A. Ballinger. The statistical characteristics of convective cells in a monsoon regime (darwin, northern australia). *Monthly Weather Review*, 135 (1):82–92, 2007.

P. T. May, J. H. Mather, G. Vaughan, C. Jakob, G. M. McFarquhar, K. N. Bower, and G. G. Mace. The tropical warm pool international cloud experiment. *Bulletin of the American Meteorological Society*, 89(5):629–645, 2008.

P. T. May, G. Allen, G. Vaughan, and P. Connolly. Aerosol and thermodynamic effects on tropical cloud systems during twpice and active. *Atmospheric Chemistry and Physics*, 9(1):15–24, 2009.

G. M. McFarquhar, J. Um, M. Freer, D. Baumgardner, G. L. Kok, and G. Mace. Importance of small ice crystals to cirrus properties: Observations from the Tropical Warm Pool International Cloud Experiment (TWP-ICE). *Geophysical Research Letters*, 34(13), 2007.

G. R. McMeeking, S. M. Kreidenweis, S. Baker, C. M. Carrico, J. C. Chow, J. L. Collett, W. M. Hao, A. S. Holden, T. W. Kirchstetter, W. C. Malm, H. Moosmuller, A. P. Sullivan, and C. E. Wold. Emissions of trace gases and aerosols during the open combustion of biomass in the laboratory. *Journal of Geophysical Research-Atmospheres*, 114, 2009.

Y. Mebarki, V. Catoire, N. Huret, G. Berthet, C. Robert, and G. Poulet. More evidence for very short-lived substance contribution to stratospheric chlorine inferred from hcl balloon-borne in situ measurements in the tropics. *Atmospheric Chemistry and Physics*, 10(2):397–409, 2010.

J. Merikanto, I. Napari, H. Vehkamaki, T. Anttila, and M. Kulmala. New parameterization of sulfuric acid-ammonia-water ternary nucleation rates at tropospheric conditions. *Journal of Geophysical Research-Atmospheres*, 112(D15), 2007.

S. Mertes, F. Schroder, and A. Wiedensohler. The particle detection efficiency curve of the TSI- 3010 CPC as a function of the temperature difference between saturator and condenser. *Aerosol Science and Technology*, 23(2):257–261, 1995.

D. M. Murphy, D. J. Cziczo, P. K. Hudson, and D. S. Thomson. Carbonaceous material in aerosol particles in the lower stratosphere and tropopause region. *Journal of Geophysical Research-Atmospheres*, 112(D4), 2007.

I. Napari, M. Kulmala, and H. Vehkamaki. Ternary nucleation of inorganic acids, ammonia, and water. *Journal of Chemical Physics*, 117(18):8418–8425, 2002a.

I. Napari, M. Noppel, H. Vehkamaki, and M. Kulmala. An improved model for ternary nucleation of sulfuric acid-ammonia-water. *Journal of Chemical Physics*, 116(10):4221–4227, 2002b.

I. Napari, M. Noppel, H. Vehkamaki, and M. Kulmala. Parametrization of ternary nucleation rates for H_2SO_4-NH_3-H_2O vapors. *Journal of Geophysical Research-Atmospheres*, 107(D19), 2002c.

C. Nishita, K. Osada, M. Kido, K. Matsunaga, and Y. Iwasaka. Nucleation mode particles in upslope valley winds at mount norikura, japan: Implications for the vertical extent of new particle formation events in the lower troposphere. *Journal of Geophysical Research-Atmospheres*, 113(D6), 2008.

C. O'Dowd, G. McFiggans, D. J. Creasey, L. Pirjola, C. Hoell, M. H. Smith, B. J. Allan, J. M. C. Plane, D. E. Heard, J. D. Lee, M. J. Pilling, and M. Kulmala. On the photochemical production of new particles in the coastal boundary layer. *Geophysical Research Letters*, 26(12):1707–1710, 1999.

C. D. O'Dowd, Y. J. Yoon, W. Junkerman, P. Aalto, M. Kulmala, H. Lihavainen, and Y. Viisanen. Airborne measurements of nucleation mode particles I: coastal nucleation and growth rates. *Atmospheric Chemistry and Physics*, 7(6):1491–1501, 2007.

S. N. Pandis, L. M. Russell, and J. H. Seinfeld. The relationship between DMS flux and CCN concentration in remote marine regions. *Journal of Geophysical Research-Atmospheres*, 99(D8):16945–16957, 1994.

K. D. Perry and P. V. Hobbs. Further evidence for particle nucleation in clear-air adjacent to marine cumulus clouds. *Journal of Geophysical Research-Atmospheres*, 99(D11):22803–22818, 1994.

R. G. Pinnick, D. M. Garvey, and L. D. Duncan. Calibration of knollenberg FSSP light-scattering counters for measurement of cloud droplets. *Journal of Applied Meteorology*, 20(9):1049–1057, 1981.

L. Pirjola. Effects of the increased UV radiation and biogenic VOC emissions on ultrafine sulphate aerosol formation. *Journal of Aerosol Science*, 30(3):355–367, 1999.

L. Pirjola and M. Kulmala. Modelling the formation of H_2SO_4-H_2O particles in rural, urban and marine conditions. *Atmospheric Research*, 46(3-4):321–347, 1998.

W. H. Press. *Numerical recipes: the art of scientific computing*. Cambridge University Press, 3rd edition, 2007.

H. R. Pruppacher and J. D. Klett. *Microphysics Of Clouds And Precipitation*. Springer, 1st edition, 1997.

F. Raes and A. Janssens. Ion-induced aerosol formation in a H_2O-H_2SO_4 system .2. numerical-calculations and conclusions. *Journal of Aerosol Science*, 17(4): 715–722, 1986.

G. C. Reid and K. S. Gage. The tropical tropopause over the western pacific: Wave driving, convection, and the annual cycle. *Journal of Geophysical Research-Atmospheres*, 101(D16):21233–21241, 1996.

I. Riipinen, S. L. Sihto, M. Kulmala, F. Arnold, M. Dal Maso, W. Birmili, K. Saarnio, K. Teinila, V. M. Kerminen, A. Laaksonen, and K. E. J. Lehtinen. Connections between atmospheric sulphuric acid and new particle formation during QUEST III-IV campaigns in Heidelberg and Hyyti. *Atmospheric Chemistry and Physics*, 7(8):1899–1914, 2007.

J. M. Rosen, D. J. Hofmann, and S. P. Singh. Steady-state stratospheric aerosol model. *Journal of the Atmospheric Sciences*, 35(7):1304–1313, 1978.

L. M. Russell, S. N. Pandis, and J. H. Seinfeld. Aerosol production and growth in the marine boundary-layer. *Journal of Geophysical Research-Atmospheres*, 99(D10):20989–21003, 1994.

C. J. Schack, S. E. Pratsinis, and S. K. Friedlander. A general correlation for deposition of suspended particles from turbulent gases to completely rough surfaces. *Atmospheric Environment*, 19(6):953–960, 1985.

F. Schröder and J. Ström. Aircraft measurements of sub micrometer aerosol particles (>7 nm) in the midlatitude free troposphere and tropopause region. *Atmospheric Research*, 44(3-4):333–356, 1997.

M. Seifert, J. Strom, R. Krejci, A. Minikin, A. Petzold, J. F. Gayet, H. Schlager, H. Ziereis, U. Schumann, and J. Ovarlez. Aerosol-cirrus interactions: a number based phenomenon at all? *Atmospheric Chemistry and Physics*, 4:293–305, 2004a.

M. Seifert, R. Tiede, M. Schnaiter, C. Linke, O. Mohler, U. Schurath, and J. Strom. Operation and performance of a differential mobility particle sizer and a TSI 3010 condensation particle counter at stratospheric temperatures and pressures. *Journal of Aerosol Science*, 35(8):981–993, 2004b.

J.H. Seinfeld. *Atmospheric Chemistry and Physics of Air Pollution.* Wiley-Interscience publication, John Wiley & Sons, New York, 1986.

G. J. Sem. Design and performance characteristics of three continuous-flow condensation particle counters: a summary. *Atmospheric Research*, 62(3-4):267–294, 2002.

S. C. Sherwood, V. Ramanathan, T. P. Barnett, M. K. Tyree, and E. Roeckner. Response of an atmospheric general-circulation model to radiative forcing of tropical clouds. *Journal of Geophysical Research-Atmospheres*, 99(D10):20829–20845, 1994.

S. L. Sihto, M. Kulmala, V. M. Kerminen, M. Dal Maso, T. Petaja, I. Riipinen, H. Korhonen, F. Arnold, R. Janson, M. Boy, A. Laaksonen, and K. E. J. Lehtinen. Atmospheric sulphuric acid and aerosol formation: implications from atmospheric measurements for nucleation and early growth mechanisms. *Atmospheric Chemistry and Physics*, 6:4079–4091, 2006.

D. Simpson. Long-period modeling of photochemical oxidants in europe - model-calculations for july 1985. *Atmospheric Environment Part a-General Topics*, 26(9):1609–1634, 1992.

S. Sjogren, M. Gysel, E. Weingartner, U. Baltensperger, M. J. Cubison, H. Coe, A. A. Zardini, C. Marcolli, U. K. Krieger, and T. Peter. Hygroscopic growth and water uptake kinetics of two-phase aerosol particles consisting of ammonium sulfate, adipic and humic acid mixtures. *Journal of Aerosol Science*, 38(2): 157–171, 2007.

J. A. Smith, A. S. Ackerman, E. J. Jensen, and O. B. Toon. Role of deep convection in establishing the isotopic composition of water vapor in the tropical transition layer. *Geophysical Research Letters*, 33(6), 2006.

R. Sorjamaa and A. Laaksonen. The effect of H_2O adsorption on cloud drop activation of insoluble particles: a theoretical framework. *Atmospheric Chemistry and Physics*, 7(24):6175–6180, 2007.

A. Sorokin and F. Arnold. Laboratory study of cluster ions formation in H_2SO_4-H_2O system: Implications for threshold concentration of gaseous H_2SO_4 and ion-induced nucleation kinetics. *Atmospheric Environment*, 41(18):3740–3747, 2007.

A. Sorokin, F. Arnold, and D. Wiedner. Formation and growth of sulfuric acid-water cluster ions: Experiments, modelling, and implications for ion-induced aerosol formation. *Atmospheric Environment*, 40(11):2030–2045, 2006.

R. Spang, L. Hoffmann, A. Kullmann, F. Olschewski, P. Preusse, P. Knieling, S. Schroeder, F. Stroh, K. Weigel, and M. Riese. High resolution limb observations of clouds by the CRISTA-NF experiment during the SCOUT-O3 tropical aircraft campaign. *Advances in Space Research*, 42(10):1765–1775, 2008.

M. Speldel, R. Nau, F. Arnold, H. Schlager, and A. Stohl. Sulfur dioxide measurements in the lower, middle and upper troposphere: Deployment of an aircraft-based chemical ionization mass spectrometer with permanent in-flight calibration. *Atmospheric Environment*, 41(11):2427–2437, 2007.

J. Strom, H. Fischer, J. Lelieveld, and F. Schroder. In situ measurements of microphysical properties and trace gases in two cumulonimbus anvils over western europe. *Journal of Geophysical Research-Atmospheres*, 104(D10):12221–12226, 1999.

A. Thomas, S. Borrmann, C. Kiemle, F. Cairo, M. Volk, J. Beuermann, B. Lepuchov, V. Santacesaria, R. Matthey, V. Rudakov, V. Yushkov, A. R. MacKenzie, and L. Stefanutti. In situ measurements of background aerosol and subvisible cirrus in the tropical tropopause region. *Journal of Geophysical Research-Atmospheres*, 107(D24), 2002.

D. C. Thornton, A. R. Bandy, B. W. Blomquist, J. D. Bradshaw, and D. R. Blake. Vertical transport of sulfur dioxide and dimethyl sulfide in deep convection and its role in new particle formation. *Journal of Geophysical Research-Atmospheres*, 102(D23):28501–28509, 1997.

W. K. Tobiska, T. Woods, F. Eparvier, R. Viereck, L. Floyd, D. Bouwer, G. Rottman, and O. R. White. The SOLAR2000 empirical solar irradiance model and forecast tool. *Journal of Atmospheric and Solar-Terrestrial Physics*, 62(14):1233–1250, 2000.

TSI. Model 3010 condensation particle counter instruction manual. *TSI. Incorporated, Shoreview, MN, USA*, P/N 1933010, Revision F, 2002.

A. F. Tuck, S. J. Hovde, K. K. Kelly, S. J. Reid, E. C. Richard, E. L. Atlas, S. G. Donnelly, V. R. Stroud, D. J. Cziczo, D. M. Murphy, D. S. Thomson, J. W. Elkins, F. L. Moore, E. A. Ray, M. J. Mahoney, and R. R. Friedl. Horizontal variability 1-2 km below the tropical tropopause. *Journal of Geophysical Research-Atmospheres*, 109(D5), 2004.

C. H. Twohy, C. F. Clement, B. W. Gandrud, A. J. Weinheimer, T. L. Campos, D. Baumgardner, W. H. Brune, I. Faloona, G. W. Sachse, S. A. Vay, and D. Tan. Deep convection as a source of new particles in the midlatitude upper troposphere. *Journal of Geophysical Research-Atmospheres*, 107(D21), 2002.

G. Vaughan, C. Schiller, A. R. MacKenzie, K. Bower, T. Peter, H. Schlager, N. R. P. Harris, and P. T. May. SCOUT-03/ACTIVE - high-altitude aircraft measurements around deep tropical convection. *Bulletin of the American Meteorological Society*, 89(5):647–662, 2008.

H. Vehkamäki, M. Kulmala, I. Napari, K. E. J. Lehtinen, C. Timmreck, M. Noppel, and A. Laaksonen. An improved parameterization for sulfuric acid-water nucleation rates for tropospheric and stratospheric conditions. *Journal of Geophysical Research-Atmospheres*, 107(D22), 2002.

Y. Viisanen, M. Kulmala, and A. Laaksonen. Experiments on gas-liquid nucleation of sulfuric acid and wafer. *Journal of Chemical Physics*, 107(3):920–926, 1997.

A. Volz and D. Kley. A resonance-fluorescence instrument for the insitu measurement of atmospheric carbon-monoxide. *Journal of Atmospheric Chemistry*, 2 (4):345–357, 1985.

S. L. von der Weiden, F. Drewnick, and S. Borrmann. Particle loss calculator - a new software tool for the assessment of the performance of aerosol inlet systems. *Atmospheric Measurement Techniques*, 2(2):479–494, 2009.

C. Wang. A modeling study of the response of tropical deep convection to the increase of cloud condensation nuclei concentration: 1. dynamics and microphysics. *Journal of Geophysical Research-Atmospheres*, 110(D21), 2005a.

C. Wang. A modeling study of the response of tropical deep convection to the increase of cloud condensation nuclei concentration: 2. radiation and tropospheric chemistry. *Journal of Geophysical Research-Atmospheres*, 110(D22), 2005b.

C. Wang and R. G. Prinn. On the roles of deep convective clouds in tropospheric chemistry. *Journal of Geophysical Research-Atmospheres*, 105(D17): 22269–22297, 2000.

Y. Wang, C. N. Long, L. R. Leung, J. Dudhia, S. A. McFarlane, J. H. Mather, S. J. Ghan, and X. Liu. Evaluating regional cloud-permitting simulations of the WRF model for the Tropical Warm Pool International Cloud Experiment (TWP-ICE), Darwin, 2006. *Journal of Geophysical Research-Atmospheres*, 114, 2009.

J. Whiteway, C. Cook, M. Gallagher, T. Choularton, J. Harries, P. Connolly, R. Busen, K. Bower, M. Flynn, P. May, R. Aspey, and J. Hacker. Anatomy of cirrus clouds: Results from the Emerald airborne campaigns. *Geophysical Research Letters*, 31(24), 2004.

G. Wilemski. Composition of the critical nucleus in multicomponent vapor nucleation. *Journal of Chemical Physics*, 80(3):1370–1372, 1984.

S. Wilhelm, S. Eichkorn, D. Wiedner, L. Pirjola, and F. Arnold. Ion-induced aerosol formation: new insights from laboratory measurements of mixed cluster ions HSO_4-(H_2SO_4)(a)(H_2O)(w) and H+(H_2SO_4)(a)(H_2O)(w). *Atmospheric Environment*, 38(12):1735–1744, 2004.

P. I. Williams. *Construction and validation of a DMPS for aerosol characterisation.* PhD thesis, The University of Manchester, 1999.

L. H. Young, D. R. Benson, W. M. Montanaro, S. H. Lee, L. L. Pan, D. C. Rogers, J. Jensen, J. L. Stith, C. A. Davis, T. L. Campos, K. P. Bowman, W. A. Cooper, and L. R. Lait. Enhanced new particle formation observed in the northern midlatitude tropopause region. *Journal of Geophysical Research-Atmospheres*, 112(D10), 2007.

F. Q. Yu and R. P. Turco. Ultrafine aerosol formation via ion-mediated nucleation. *Geophysical Research Letters*, 27(6):883–886, 2000.

F. Q. Yu and R. P. Turco. From molecular clusters to nanoparticles: Role of ambient ionization in tropospheric aerosol formation. *Journal of Geophysical Research-Atmospheres*, 106(D5):4797–4814, 2001.

Y. Zaizen, K. Okada, M. Ikegami, Y. Sawa, and Y. Makino. Number-size distributions of aerosol particles in the free troposphere over the northwestern pacific ocean-influence of asian outflow and tropical air transport. *Journal of the Meteorological Society of Japan*, 82(4):1147–1160, 2004.